LOW LOAD OPERATION IN A LIGHT-DUTY DIESEL ENGINE USING HIGH OCTANE FUELS AND ADDITIVES

By

Bishwadipa Das Adhikary

A dissertation submitted in partial fulfillment of

the requirements for the degree of

Doctor of Philosophy

(Mechanical Engineering)

at the

UNIVERSITY OF WISCONSIN – MADISON

2014

Date of final oral examination: 11/21/2014

The dissertation is approved by the following members of the Final Oral Committee:

Rolf Reitz, Professor, Mechanical Engineering
Christopher Rutland, Professor, Mechanical Engineering
Jaal Gandhi, Professor, Mechanical Engineering
David Rothamer, Associate Professor, Mechanical Engineering
Tracey Holloway, Associate Professor, Atmospheric & Oceanic Sciences

Abstract

The present study focuses on multi-cylinder, light-duty engine operation at light load conditions while maintaining efficiency and emissions. It is required that the same engine should be able to run at high load conditions as well. Thus, the choice of fuel and combustion strategy should support over a wide range of speed-load operation. This is achieved by utilizing partially premixed combustion [PPC] of gasoline, which is a combination of homogeneous mixture operation of the fully premixed charge and a direct injection, where the fuel is injected during or slightly before the combustion event, like in standard diesel combustion. The engine load in gasoline PPC operation is controlled by limiting the injected fuel amount, whereas desirable combustion phasing is achieved by controlling the injection timing. The effect of injector included angle was also studied in the present work with the objective of operating at the lowest possible load in this type of combustion.

The number of injections was found to play a major role in this type of combustion, since it provides flexibility for load extension while achieving better combustion efficiency. Fuel effects also significantly alter the combustion behavior due to changes in the auto-ignition characteristics. Fuels with lower Research Octane Numbers [RON] provide better auto-ignitability, minimizing the hurdle of achieving stable engine operation at lighter load. Thus, the current study focused on low load operation using various RON gasoline fuels in a multi-cylinder engine.

The use of a cetane improver is also emphasized in this research for operation at light load conditions with lower octane fuels. By changing the amount of cetane improver in standard gasoline, it is possible to alter the octane number of the fuel and potentially resolve engine startability issues. In the present research 2-EthylHexyl Nitrate [EHN] is considered as a potential cetane improver. A reaction kinetics model for EHN was developed and used to study HCCI

operation in a light-duty, single-cylinder engine at light load conditions. 96 RON gasoline was used as the base fuel.

The results indicate that the current EHN mechanism predicts combustion phasing and nitrogen oxides [NO_x] and carbon-monoxide [CO] emission trends of available HCCI experiments fairly well. Direct injection engine experiments performed at the Argonne National Laboratory with 87 AKI gasoline and 0.4% by volume of EHN additive were also used to validate the newly developed EHN mechanism. An additive-PRF map was generated that provides information about the effective PRF number of mixtures of gasoline and EHN additive.

Acknowledgments

This thesis is dedicated to those who made the path for my journey and believed I can reach the destination. Among them, I can only mention few names here. But the unspoken names are also worth of thousand words and my gratitude will always remain for them.

First, I would like to thank my advisor, Professor Rolf Reitz, for giving me the opportunity to be a part of such a great research facility. Each weekly meeting was a pillar added to the foundation and at times the structure seemed to fall down. But his endless patience and guidance always encouraged me to put some more effort to understand the advanced engine combustion concept. I will always be grateful for that. Along with him I would like to acknowledge Dr. Youngchul Ra, without whom this thesis would have been incomplete. His tolerance and support helped me understand the chemical phenomenon of low temperature combustion and the additive chemistry.

This project would not have existed without the funding support from Dr. Steve Ciatti, at Argonne National Laboratory. Apart from his contribution with experimental data, he acted like a friend, philosopher and guide to me, which I will embrace for the rest of my life.

I would like to thank Prof. Chris Rutland, Prof. Dave Rothamer, Prof. Jaal Gandhi and Prof. Tracey Holloway for agreeing to be in my committee.

A very special ‘thank you’ remains for Josh for his prompt attention when computers, servers and simulations behaved strangely. He also helped me debugging the KIVA code while transferring it from Hades to Elephant cluster.

I will always be indebted to the ERC students for the insightful discussions and the fun-times we had. I am obliged to Dr. Jessica Brakora, Dr. Gokul Viswanathan, Dr. Adam Dempsey and Dr. Siddhartha Banerjee for helping me to start with KIVA-3V. I also appreciate the help of Dr. Randy Hessel on the RCM study, and Dr. Federico Perini for implementing SpeedChem in my KIVA

code. I enjoyed and benefited from many research-related discussions with Jessica, Gokul, Siddhartha, Adam, Jae, Hu, Ben, Michael, Qi, Wonah, Lu and Peng. I will also cherish their friendship for the rest of my life along with many other ERCers, who made this journey a memorable one.

Interaction and experiences with Professor Amitava Datta at Jadavpur University, have been instrumental in defining my research interests. I owe a lot to him for his inspiring words and the interests he showed in my future.

Finally, I would like to thank my parents, and my brother for their continuous encouragement. My husband, Subhamoy, needs a special mention, without whom I could not have achieved my goals.

Table of Contents

List of Figures

List of Tables

Nomenclature

Abbreviations

AKI	Anti Knock Index
ATDC	After Top Dead Center
BDC	Bottom Dead Center
BMEP	Brake Mean Effective Pressure
C_2H_2	Acetylene
CA50	Crank Angle at 50% Burn
CDC	Conventional Diesel Combustion
CFD	Computational Fluid Dynamics
CH_2O	Formaldehyde
CI	Compression Ignition
CN	Cetane Number
CO	Carbon-Monoxide
CO_2	Carbon-di-Oxide
COV	Coefficient of Variance
CR	Compression Ratio
DI	Direct Injection
DICI	Direct Injection Compression Ignition
DMC	Discrete Multi-Component
DTBP	Di-Tertiary Butyl Peroxide
EGR	Exhaust Gas Recirculation
EHN	EthylHexyl Nitrate
ERC	Engine Research Center
EVO	Exhaust Valve Open
FSN	Filter Smoke Number
GA	Genetic Algorithm
GDICI	Gasoline Direct Injection Compression Ignition
GM	General Motors
GRI	Gas Research Institute
HC	Hydro-carbon
HCCI	Homogeneous Charge Compression Ignition
IMEP	Indicated Mean Effective Pressure
ISFC	Indicated Specific Fuel Consumption
IVC	Intake Valve Closure
LDEF	Lagrangian Droplet Eulerian Fluid
LLNL	Lawrence Livermore National Laboratory
MOGA	Multi Objective Genetic Algorithm
MON	Motored Octane Number
NO_x	Oxides of Nitrogen

NSGAII	Non-dominated Sorting Genetic Algorithm II
O_2	Oxygen
OI	Octane Index
ON	Octane Number
PCCI	Premixed Charge Compression Ignition
PCI	Premixed Compression Ignition
PON	Pump Octane Number
PPC	Partially Premixed Combustion
PPRR	Peak Pressure Rise Rate
PRF	Primary Reference Fuel
RANS	Reynolds Averaged Navier Stokes
RCCI	Reactivity Controlled Compression Ignition
RI	Ringing Intensity
ROI	Rate of Injection
RON	Research Octane Number
SI	Spark Ignition
SOI	Start of Injection
SOI2	Second Injection Timing
S1	Premixed Fuel Amount
S2	Fuel Amount in Second Pulse
TDC	Top Dead Center
UHC	Unburned Hydro Carbon

Greek Letters

ϕ	Equivalence Ratio
γ	Ratio of Specific Heats

Chapter 1 Introduction

1.1 Motivation

With the gradual imbalance of the supply and demand chain of petroleum fuel, the demand for more fuel-efficient engines leads to growing interest in the compression ignition [CI] engine. While pumping and throttling losses are the two major issues in a spark ignition [SI] engine, generating high load by using a high compression ratio without the fear of knocking is the advantage of the CI engine. However, due to the mixing controlled combustion in a diesel engine, maintaining both soot and NO_x emissions has been a challenge. Diesel engine combustion involves highly complex and coupled processes of fuel injection, atomization, vaporization, fuel-air mixing, ignition and the establishment of a flame. In a typical direct injection compression ignition [DICI] engine fueled with conventional diesel, the fuel is injected at the end of the compression stroke, very close to top dead center [TDC]. As the injected fuel atomizes, followed by the vaporization and the mixing of fuel vapor and air, ignition occurs in a fuel rich mixture region [$\Phi \sim 4.0$]. The subsequent combustion process is characterized by a dual burning mode, involving first a rich premixed flame and then a diffusion combustion process [Dec *et al.*, 1998]. The rich fuel burning in the so called premixed mode initiates soot formation, whereas the NO_x, mostly consisting of NO, is formed either in the diffusion combustion regime or in the remaining hot gases at the end of combustion [Heywood, 1988]. The emission consequences of conventional diesel combustion [CDC] are best illustrated in an equivalence ratio-temperature diagram, which is shown in Figure 1-1 [Neely *et al.*, 2005]. As can be observed in the figure, mixing-controlled combustion often leads to high NO_x formation at stoichiometric conditions, whereas high soot can be formed in regions with $2 < \Phi < 4$ and $T \sim 2000K$.

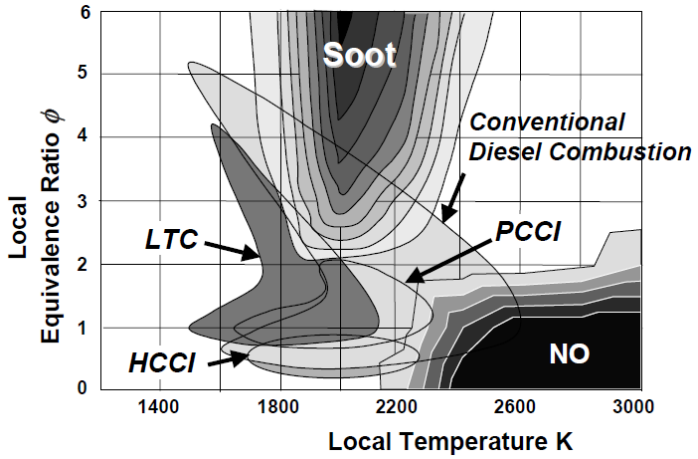

Figure 1.1: Operating regimes for CDC, HCCI, LTC and PCCI plotted in a local equivalence ratio – local temperature space [Neely *et al.*, 2005]

In 2010 the United States Environmental Protection Agency [EPA, 2007] tightened exhaust emission regulations at 0.268 g/kW-hr and 0.013 g/kW-hr, for NO_x and soot respectively, for new on-highway, heavy-duty diesel engines. Similar regulation applies for light-duty engines as well.

One way to control the engine-out emissions is to use an after-treatment system. It has been observed that soot can be effectively reduced by the use of diesel particulate filters [DPF]. However, this requires periodic removal of the collected soot, which affects fuel economy [Kodama *et al.*, 2005]. In order to burn off the soot from the filter wall the DPF inlet needs a temperature of ~600^{o}C [Johnson, 2011], leading to diesel burning during the late-cycle or in the exhaust stream, which increases fuel consumption. Additionally, NO_x can be controlled by various means, such as using a three-way catalyst [TWC] [Odaka *et al.*, 1998], lean NO_x trap [LNT] [Theis *et al.*, 2003] or selective catalytic reduction [SCR] [Saito *et al.*, 2003] techniques. An SCR system requires a secondary fluid, known as diesel exhaust fluid [DEF], an aqueous urea solution. Once it is injected into the exhaust system it vaporizes and decomposes to NH_3 and CO_2, and helps in NO_x decomposition into N_2 and H_2O in presence of a catalyst. Current SCR technology reports the DEF consumption to be 1% of the total fuel consumption for 1.0 g/kW-hr of NO_x reduction [Johnson, 2011]. A LNT helps in reducing the NO_x by up to 70%. However, usage of precious

metals makes them relatively expensive. Also, it requires periodic rich engine operation to produce hydrocarbons and carbon-monoxide to regenerate the LNT, which reduces fuel economy [Neely *et al.*, 2007]. As the fuel economy gets affected by these complicated and expensive after-treatment systems, which is the primary benefit of the diesel engine, a great deal of interest has been devoted to studies with a variety of fuels and different combustion strategies, while maintaining the diesel-like efficiency in the CI engine. In general, soot can be reduced by introducing more premixing, whereas NO_x can be controlled by lowering the combustion temperature. Thus, low temperature combustion [LTC] with more premixing becomes a promising direction for advanced combustion strategy research.

LTC operation with diesel fuel is typically limited by early knocking at higher loads [Okude *et al.*, 2004], but conventional gasoline with a high octane number appears as a solution. The higher resistance of gasoline to auto-ignition allows premixing as well as direct injection, and it provides controllability over injection strategies in order to minimize soot and NO_x at high load operation. However, gasoline LTC is often limited by misfiring at lower loads [Kalghatgi *et al.*, 2007]. This leads to the study of fuel effects, which indicates that by using a lower octane fuel with its lower auto-ignition characteristics, there will be fewer hurdles to operate the engine at low load. Obtaining a gasoline-like fuel with various octane ratings is not always feasible, whereas by adding a small amount of cetane improver to a standard gasoline, the fuel's auto-ignitability can be altered [Hara *et al.*, 1999]. Chemicals, such as alkyl nitrates, ether nitrates, nitroso compounds and certain peroxides have been identified as effective cetane improvers. However, low production cost and good response with wide range fuels have identified EHN as one of the most promising cetane improvers.

1.2 Objectives

The primary objective of this research is to explore low load engine operation using a partially premixed combustion strategy. As the auto-ignition characteristics of the fuel have a significant impact on engine performance, use of a lower octane fuel is desirable to achieve ignition at light load conditions. The hurdle of obtaining various octane fuels can be overcome by introducing a cetane improver, which can change the auto-ignition characteristics of the base fuel by altering its octane rating. As EHN has been considered as potential cetane improver by researchers, another objective of the present research is to develop an EHN reaction mechanism and to observe its impact on the auto-ignition characteristics of the base fuel.

1.3 Approach

Low load triple-injection experiments were conducted in a multi-cylinder CI engine at the Argonne National Laboratory [ANL] using various octane gasolines. Simulations were performed using the KIVA-3V CFD code [Amsden, 1997] coupled with detailed chemistry solvers in order to validate the experimental data and to provide insights on the ignition behavior of different octane number fuels. All the simulations in this study were conducted using $1/7^{th}$ sector mesh from IVC to EVO with the assumption of sector symmetry. Considering the complexity of a multiple-injection strategy, use of a simpler single injection strategy was followed in the experiments using 93 RON or 87 AKI gasoline at different injection timings to achieve minimum load at each timing while maintaining the COV of IMEP less than 3%. Simulations were carried out to understand the in-cylinder combustion behavior of these single-injection experiments. Additional experiments were performed at ANL using 93 RON gasoline and 0.4% EHN by volume in order to minimize the possible operating load even further. At this point the focus was shifted to EHN reaction kinetics development in order to compare the engine performance data provided by ANL and also

to establish effective PRF number correlations while using gasoline and the EHN additive. Dempsey *et al.* [2013] performed HCCI experiments using both PRF fuels and additives at two different equivalence ratios - 0.26 and 0.3, using different intake temperatures. The present newly developed EHN mechanism was validated using Dempsey's HCCI experiments and also with spray experiments performed using 87 AKI gasoline and 0.4% EHN by volume at ANL. The EHN mechanism was then used for HCCI simulations using 87 AKI gasoline fuel chemistry with a 15-component surrogate fuel model, coupled with the validated EHN model, to predict the effective PRF number due to the addition of EHN with gasoline.

Chapter 2 Literature Review

2.1 Advanced Combustion Strategies

2.1.1 HCCI Combustion

In order to achieve clean combustion while maintaining high thermal efficiency, many combustion strategies have been proposed over the years. The primary focus of many current combustion strategies is to achieve more premixed low-temperature combustion. HCCI operation was first introduced by Onishi *et al.* [1979] for reducing unburned hydrocarbon in a 2-stroke engine and later demonstrated by Najt and Foster [2002] in a four-stroke CI engine. The fuel was inducted in the cylinder very early in the cycle and a completely premixed, lean fuel/air mixture was burned at an equivalence ratio of ~0.5. HCCI has been shown to yield very clean combustion with a very high thermal efficiency due to the lower heat losses and shorter combustion duration [Tsurushima *et al.*, 2002]. However, the start of ignition and combustion duration controllability issue are major problems in terms of engine noise control.

Ignition is controlled by the spark timing in the SI engine, and by the start of fuel injection in the CI engine. The rate of fuel injection dictates the combustion duration in the CI engine, whereas turbulent flame propagation is the parameter in the SI engine. In contrast to the ignition control in CI and SI engines, combustion parameters for HCCI operation completely depend on the initial conditions of the mixture and the auto-ignition characteristics of the fuel, which can lead to very high heat release and peak pressure rise rates. Moreover, as diesel fuel has a high cetane number, HCCI operation conducted using diesel fuel needs to have a low compression ratio [CR] engine and should be operated at low load to control the engine noise. Also, unburned hydrocarbon [UHC] and CO emissions from the partially combusted gases in the engine's crevice volumes has been noticed to be an issue.

2.1.2 PCCI Combustion

To achieve more control HCCI has been extended to premixed charge compression ignition [PCCI] operation, where the problems of lack of combustion phasing control and excessive peak pressure rise rate [PPRR] can be reduced by the use of retarded injection timings [Kimura *et al.*, 1999]. This enables engine operation at a higher load. As a hybrid between HCCI and DICI combustion, being partially premixed the PPRR is reduced compared to the HCCI strategy, allowing high load operation. Engines using the PREDIC [Takeda *et al.*, 1996], Nissan MK [Kimura *et al.*, 2001] and Toyota UNIBUS [Hasegawa *et al.*, 2003] systems utilize this type of combustion. In the Nissan MK system, delayed combustion at a low temperature is achieved by introducing a high level of cooled EGR, whereas a multiple injection strategy is used in the Toyota UNIBUS system to control combustion. High swirl and high injection pressure also promote mixing prior to ignition. However, excessive delay in the heat release can lead to unstable combustion, reducing engine efficiency.

The flame luminosity visualization shown in Figure 2-1 [Mueller, 2005] indicates that in CDC the typical path of a fuel element passes through the soot formation and oxidation zones, which is clearly visible from the orange flame, whereas HCCI combustion avoids these regimes. When mixing-controlled LTC conditions are achieved with high rates of EGR, high temperatures are avoided to keep the combustion process away from the soot and NO_x formation zones. Therefore, no soot luminosity is observed in Figure 2.1c, despite some high local equivalence ratios observed in the experiments. However, as research at Lund University discovered when operating fully premixed diesel combustion, maintaining low NO_x and PM emissions simultaneously requires high levels of EGR, which negatively affect combustion stability at higher loads.

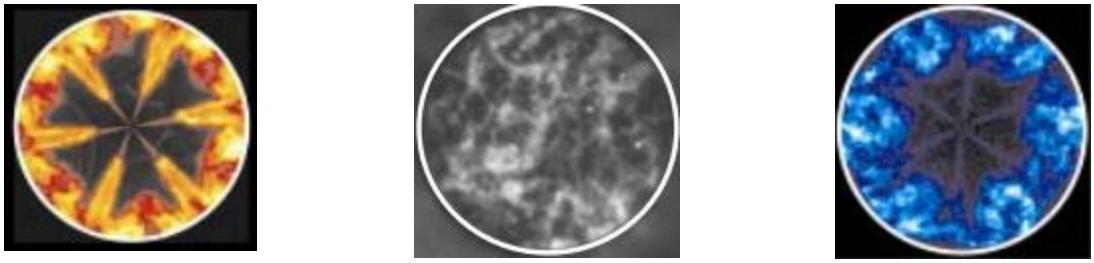

(a) (b) (c)

Figure 2.1: Flame luminosity visualization for (a) Conventional diesel combustion (b) HCCI combustion and (c) Dilute clean diesel combustion [DCDC] [Mueller, 2005]

2.1.3 Gasoline PPC

Fuel properties can have a profound impact on the performance and emissions of engines employing LTC, especially in premixed LTC approaches where ignition occurs well after the air and fuel are mixed. Two important characteristics of fuels that can affect the performance of an engine employing premixed LTC are how well the fuel and air mix, and how easily the mixture ignites. Fuel-air mixing is determined not only by the mixture temperature and flow conditions, but by fuel volatility as well, which is determined by its distillation characteristics. The more volatile the fuel is, the faster are the evaporation and mixing processes. The volatility characteristics of a typical gasoline and a diesel fuel are shown in Figure 2.2, which indicates that gasoline is more volatile compared to diesel. The ignitability of a fuel reflects the chemical kinetic characteristics of that fuel when it is mixed with air. Common measures of a fuel's ignitability are the cetane number [CN] for diesel fuels and the octane number [ON] for gasoline. The Cetane number has been shown to correlate reasonably well with the combustion phasing of diesel-like fuels, whereas the RON and MON do not characterize the combustion phasing of gasoline-like fuels uniquely. In 2005 Kalghatgi proposed another measure of fuel ignitability, known as the Octane Index [OI], which is defined as OI = (1-K)*RON+K*MON, where K is a constant which depends on the pressure and temperature of the unburned mixture.

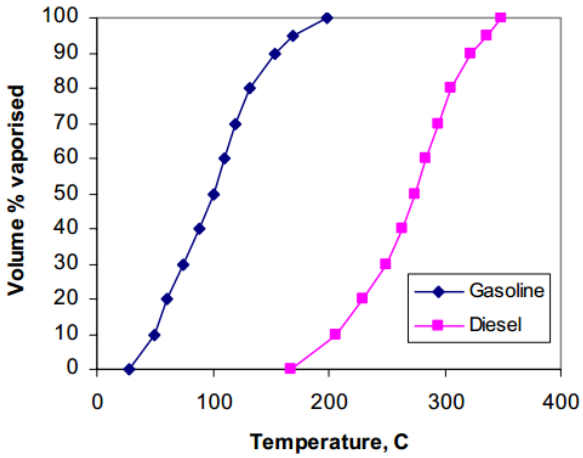

Figure 2.2: Volatility characteristics of a typical gasoline and a diesel fuel [Kalghatgi, 2005]

2.1.3.1 Single and Double Injection Strategies

Research done by Shimazaki *et al.* [2003] and Kalghatgi *et al.* [2005, 2006] shows that gasoline-like fuels, having lower cetane or higher octane numbers, delay the ignition, resulting in more premixing, which generates lower NO_x and soot. Kalghatgi *et al.* also showed that for a given intake pressure and EGR level, gasoline can provide much higher IMEP with very low NO_x and PM emissions compared to diesel. The experiments for their study were conducted on a SCANIA D12 single-cylinder engine, having a CR of 14, operated at 1200 rev/min. Another Kalghatgi *et al.* [2007] paper demonstrated that early gasoline injection reduces the maximum heat release for a given IMEP. They were able to operate the engine at ~16 bar IMEP with a very low level of soot and NO_x.

In addition to high load engine performance studies, Sellnau *et al.* [2012] operated a light-duty single-cylinder engine at 2 bar and 3 bar IMEP using 91 RON gasoline. Single and double injection strategies were followed, respectively, for 2 bar and 3 bar IMEP conditions. In that study, an exhaust rebreathing strategy was considered to provide the charge heating by means of hot exhaust gases. The results indicated very low levels of soot [<0.1 FSN] and NO_x [0.2 g/kW-hr] emissions with 67% residuals at 2 bar IMEP and 23% residuals at 3 bar IMEP. An impressive

ISFC of ~230 g/kW-hr was achieved at these low load conditions. In another study, Weall *et al.* [2009] experimented with low load operating conditions using multi-cylinder engine. A 2L 4-cylinder Ford engine was operated at extremely light load conditions [1 bar BMEP at 1000 rev/min and 2 bar BMEP at 1200 rev/min] using 95 RON gasoline. That study demonstrated the importance of intake pressure, temperature and fuel stratification for a light load multi-cylinder engine operation. Manente *et al.* [2009] achieved 1 bar IMEP load which required significant amount of boost and intake air heating using higher than ~70 AKI fuel. Borgqvist *et al.* [2012] performed low load operation in a single-cylinder 16.5 CR light-duty engine using 69 and 87 RON gasoline. They could attain as low as 2 bar gross IMEP using 87 RON fuel, but the combustion efficiency was less than 80%. Even after using a 180 degree negative valve overlap, they found it difficult to attain more than 80% combustion efficiency at a light load condition. Loeper [2013] operated a GM 1.9L 4-cylinder engine using a multiple injection strategy to vary the load from 3 bar to 17.8 bar net IMEP with less than 1 g/kgf NO_x and PM emissions. The intake temperature and pressure, injection pressure and intake O_2 concentration was altered in order to generate an engine speed-load operating map.

2.1.3.2 Triple Injection Strategies

While the double-injection strategy has been widely investigated, Kalghatgi *et al.* [2010] successfully carried out high load triple injection experiments on a light-duty single cylinder CI engine, and demonstrated the controllability of the heat release rate with improved engine performance using 84 RON gasoline. Manente *et al.* [2012] performed light-duty single-cylinder engine experiments using 98 RON gasoline at 2000 rev/min, producing 6 bar gross IMEP. A triple pulse injection took place at -90, -55 and -25 deg ATDC using a 120^o umbrella included angle 7-hole nozzle injector. This strategy produced more than 48% gross indicated efficiency at 6 bar

IMEP with very low soot and NO_x emissions. Ciatti *et al.* [2011] performed 2 bar and 5 bar BMEP operation using 84 RON gasoline in a GM 1.9L 4-cylinder diesel engine. The study revealed that controlled combustion in a multi-cylinder engine could be achieved with a proper split-injection strategy, and low emissions could be attained by proper combustion phasing, which was a function of both the fuel properties and EGR usage. Improved fuel economy in a light-duty diesel has also been demonstrated by Sellnau *et al.* [2010], where the engine was operated at 6 bar IMEP and 1500 rev/min. The fuel-air stratification achieved by the various multiple injection strategies was proven to minimize heat loss, resulting in high thermal efficiency.

2.1.3.3 Engine Modeling

Multi-dimensional engine modeling has proven to be an essential complement to successful engine experiments for more than a decade. Ra *et al.* [2009] reported a numerical study of multiple injection gasoline sprays in a heavy-duty CI engine, where it was found that enhanced fuel/air mixing prior to ignition affects the CO and UHC emissions, and the fuel split ratio turned out to be very effective in reducing PPRR, but at the expense of slightly increased indicated specific fuel consumption (ISFC). Dempsey *et al.* [2011] performed a numerical optimization study in a Caterpillar heavy-duty Gasoline Direct Injection Compression Ignition [GDICI] engine at medium and high load conditions by varying 9 engine design parameters, including the injector spray included angle and number of nozzle holes, and found a set of optimum mid-load design parameters leading to two-stage combustion, while maintaining a low level of engine-out emissions. But controlling the PPRR was a challenge at high load for this 16.1 compression ratio engine. Another study by Ra *et al.* [2011] explored the characteristics of GDICI operation along with its sensitivity to engine operating parameters in detail. The study was conducted on GM 1.9L engine, operated at a high speed (2500 rev/min) and full load (~16bar IMEP) condition. One of

the primary focuses of that research was to reveal the effect of multiple injections and the fuel split among the pulses on stable engine operation and emissions.

2.1.4 Other Advanced Combustion Strategies

Other than gasoline PPC, dual fuel combustion strategies are also evolving as a promising technique to improve engine performance while achieving high thermal efficiency. In 1949, when the development of the dual-fuel engines was in its infancy, Boyer [1949] explained the term 'dual fuel' saying that dual-fuel engines are not ones which use more than one fuel, but ones which feature the necessity of using two fuels. In dual fuel combustion strategies a high volatility fuel is used to generate sufficient premixing in the combustion chamber, while a direct injected fuel is used as the ignition trigger. Tomita *et al.* [2002] used methane as the premixed fuel and diesel as the ignition source to achieve clean combustion. The diesel fuel amount, equivalence ratio, EGR amount and injection timing were altered to monitor the NO_x, CO and UHC emissions. This study showed that early diesel injection reduced the peak heat release resulting in a lower NO_x and slightly higher thermal efficiency.

Inagaki *et al.* [2006] performed dual-fuel PCI operation using high-octane gasoline and diesel fuels as a means of reducing the EGR usage. The operable load range was extended to 12 bar IMEP by introducing an intake air boosting system along with dual-fuel usage. Kokjohn *et al.* [2011] further extended the dual-fuel concept to a so-called Reactivity Controlled Compression Ignition [RCCI] concept where the premixed fuel was defined as low reactivity fuel and the direct injected fuel was defined as the high reactivity fuel, which was used to create the reactivity gradient in the cylinder to perform LTC operation. In their study the high reactivity fuel was injected twice – the first injection was termed the 'Squish Conditioning' pulse, which targeted the fuel in the squish region for complete combustion of the premixed gasoline, and the second injection was

termed the ‘Ignition Source’ which targeted the bowl region of the combustion chamber and generated a relatively high reactivity region from where the combustion started. The RCCI combustion strategy reduced the NO_x, CO and UHC emissions over a range of speed, load and fuel characteristics [Splitter *et al.*, 2011; Hanson *et al.*, 2011; Nieman *et al.*, 2012; Lim *et al.*, 2014] and showed a path towards clean combustion. However, the current research study focuses only on gasoline PPC.

2.2 Fuel Effects on IC Engine Operation

While gasoline and diesel are widely used fuels for IC engine operation, considering the importance of fuel effects on low temperature combustion, cetane improvers have been found to be effective in altering the fuel reactivity, and therefore mitigating the need for reactivity fuels.

Cetane improvers, mixed with diesel fuel, are widely studied under mixing limited conditions, where the equivalence ratio is high. Hara *et al.* [1999] found improved engine startability of a single-cylinder Deutz engine by using iso-octyl nitrate [ION] as a cetane improver. Aradi *et al.* [1995] studied the effect of cetane number on diesel fuel ignition delay. Experiments were performed in a constant volume combustion apparatus maintaining minimal fuel/wall interactions. Two different diesel fuels were used with different aromatic and sulfur contents. 0.25% by volume of EthylHexyl Nitrate [EHN] and Di-Tertiary Butyl Peroxide [DTBP] were used as cetane improvers in these experiments, which indicated that EHN was more effective as a cetane improver than DTBP. The effect of EHN on the diesel spray ignition process was studied by Higgins *et al.* [2001] in a constant volume vessel under direct-injection, heavy-duty-type diesel engine conditions. By blending three different single-component hydrocarbons, two fuels were prepared with cetane numbers of 45 and 55. The third fuel was a blend of 4000 ppm EHN and CN-45 fuel providing an effective cetane number of 55. This study revealed that the EHN doped fuel

had a pronounced effect on the first stage ignition chemistry. However, at higher load conditions the differences in the development of the ignition process using the above fuels was greatly reduced.

Even though both EHN and DTBP have been used as a cetane improver, there are concerns about the nitrate group in additives, such as in EHN and its effect on NO_x emissions. Some studies indicate that the nitrate group contributes to higher NO_x emission [Liotta, 1993; Nandi *et al.*, 1994], whereas others indicate [Lange, 1997; Schwab, 1999] that the NO_x emission is independent of the additive type. Schwab *et al.* [1999] studied the effect of EHN and DTBP on two different diesel fuels and found EHN to be more reactive than DTBP, as indicated in Figure 2.3a. Figure 2.3b, also from the same study, shows that both EHN and DTBP reduce emissions with the increase in cetane number, but no significant difference in the NOx emission was observed due to the presence of the nitrate group in EHN.

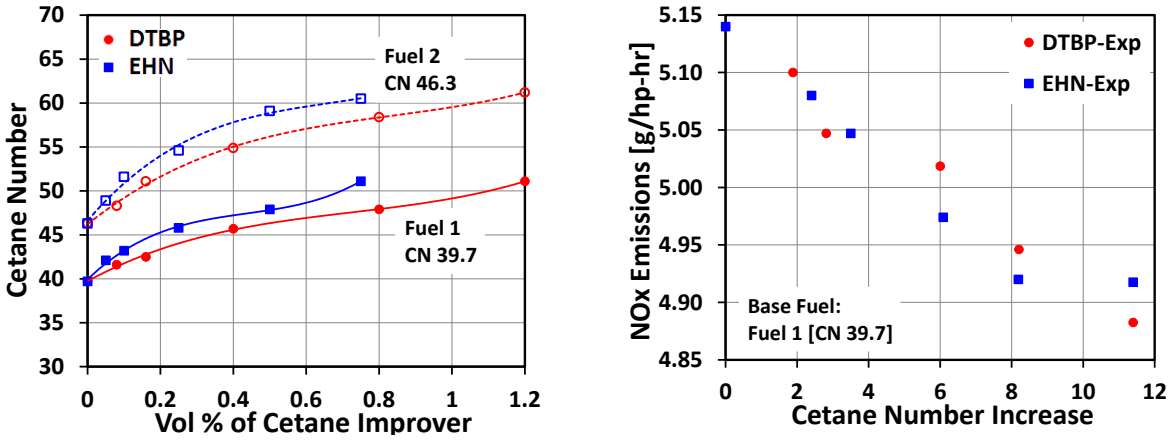

(a) (b)

Figure 2.3: Effect of EHN and DTBP (a) on cetane number of diesel fuel under conventional diesel combustion (b) on NO_x emission where 39.7 CN fuel is used as base fuel [Schwab *et al.*, 1999]

In addition to diesel fuel, cetane improvers added to other fuels are also of much interest. Eng *et al.* [2003] performed HCCI experiments using gasoline doped with DTBP in order to extend the low-load limit. Further reduction of the minimum fueling level was achieved in that study by using

DTBP. The effect of DTBP and EHN addition was studied by Tanaka *et al.* [2003] considering iC_8H_{18} and PRF90 as the base fuels. The experiments were performed in a Rapid Compression Machine having a compression ratio of 16:1. Ignition promoters were added in levels up to 2% by volume. DTBP was found to be more effective in their study in reducing the ignition delay of both iC_8H_{18} and PRF90 fuels, which is contradictory to the study of Schwab *et al.* [1999]. Kaddatz *et al.* [2012] performed some dual fuel RCCI experiments with gasoline/diesel and E10/E10+EHN, where gasoline and E10 were used as the low reactivity fuels and diesel and E10+EHN were used as the high reactivity fuels. They showed that RCCI operation with gasoline/diesel resulted in an essentially zero NO_x if the direct injection timing was sufficiently advanced, i.e., -36 deg ATDC or earlier. With E10/E10+EHN fuel the NO_x emission converged to about $1/3^{rd}$ of the fuel-bound NO from EHN. Premixed low temperature diesel combustion experiments by Ickes *et al.* [2009] and gasoline/EHN HCCI experiments by Dempsey *et al.* [2013] also found similar observations as Kaddatz.

All the above studies indicate that the behavior of cetane improvers is not very well understood and there is a need for fundamental shock-tube and pyrolysis studies in order to understand the chemistry better.

Chapter 3 Engine Specification and Modeling Approach

This chapter briefly describes the engines used in this study for conducting the experiments and the CFD modeling approach to predict the combustion process.

3.1 Engine Specification

Low load experiments with different octane number fuels were performed at the Argonne National Laboratory using 1.9L 4-cylinder GM engine, whereas the HCCI additive experiments were performed at the ERC using a single-cylinder version of the same engine by Dempsey *et al.* [2013]. The base engine geometry and injector specifications are shown in Table 3.1.

Table 3.1: Engine and injector specifications

GM 1.9L Engine Specifications	
Stock Compression Ratio [CR]	17.5
Bore [mm]	82
Stroke [mm]	90.4
Connectiong Rod Length [mm]	145.4
Intake Valve Closing [deg ATDC]	-132
Exhaust Valve Opening [deg ATDC]	116
Swirl Ratio	2.2
Injector Specifications	
Injector Type	Bosch Common Rail
Number of nozzle holes	7
Hole Diameter [µm]	141
Included Angle [deg]	148

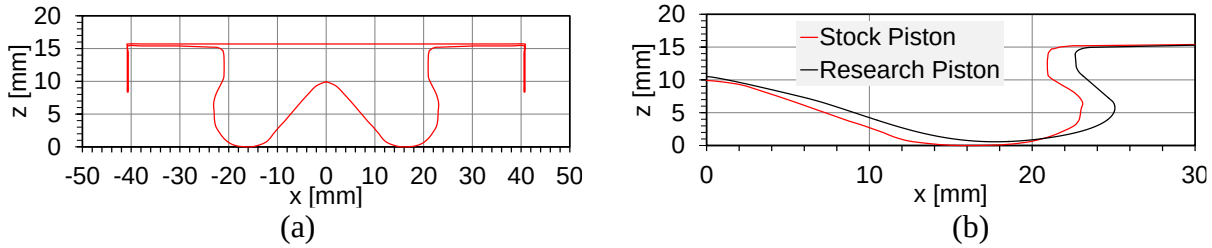

Figure 3.1: (a) Stock piston geometry and (b) Difference between stock and research piston

Figure 3.1a indicates the stock piston geometry, whereas Figure 3.1b shows the difference in bowl geometry between the stock piston and the research piston for the same base engine. The bowl geometry of the research piston was originally designed to perform optical engine experiments at the Sandia National Laboratory. Later a similar metal engine was used by Loeper [2013] to perform LTC experiments. The research piston bowl geometry was used for the genetic algorithm (GA) optimization study in the present work, the details of which are presented in Chapter 4.

3.2 Computational Model Description

For simulating the spray and combustion processes the KIVA3V-ERC-Chemkin CFD code was used, which is originally based on KIVA3V Release 2 [Amsden, 1997 & 1999]. The code is based on the Lagrangian-Drop Eulerian-Fluid [LDEF] approach, where the sprayed liquid fuel is treated as Lagrangian parcels, and the surrounding gas phase is spatially discretized into Eulerian cells. The Reynolds Averaged Navier Stokes [RANS] modeling approach is used for the gas phase flow field. The code has been improved with several sub-models, which include droplet break-up, collision and coalescence, droplet deformation, evaporation, wall impingement and vaporization, and turbulence modeling.

3.2.1 Spray Models

For engine modeling it is desirable to use a relatively coarse computational mesh for numerical efficiency due to the detailed chemistry model requirement to capture the combustion phenomenon. However, it has been observed that the standard LDEF approach has a severe grid size dependency. In 1997, Abraham showed that accurate modeling of the near nozzle region required a grid resolution on the order of the injector nozzle orifice diameter, which is not very feasible from the computational time standpoint. In order to reduce the grid size dependency and

preserve accurate spray simulations, Abani *et al.* [2008] introduced the Gasjet model, which computes the relative velocity between the liquid droplets and the gas phase fluid in the near nozzle region. In this approach the relative velocity between the droplet and the gas phase is assumed to be the same as the relative velocity between liquid droplet and a turbulent gas jet with the same mass and momentum of that of the injected fuel. According to this theory the axial component of the gas phase velocity can be modeled as

$$V_{gas} = \min\left[U_{inj}, \frac{3U_{inj}^2 d_{noz}\sqrt{\frac{\rho_l}{\rho_g}}}{K_{entr} z\left[1+\frac{12r^2}{K_{entr}^2 z^2}\right]}\right] \quad (1)$$

where U_{inj} is the injection velocity of the liquid jet, d_{noz} is the effective nozzle diameter, ρ_l and ρ_g are the liquid and gas phase densities, r is the radial distance of the droplet from the spray axis, z is the axial distance of the droplet from the injector tip and K_{entr} is a model constant, the value of which is 0.75 according to Abani *et al.*

The code uses the computationally efficient and comprehensive hybrid primary break-up model developed by Beale and Reitz [1999]. In this model, primary break-up of the injected spray parcels occurs based on Kelvin-Helmholtz [KH] instability theory, whereas the secondary break-up processes are resolved by the Kelvin-Helmholtz [KH]-Rayleigh-Taylor [RT] hybrid model. The concept of the KH-RT break-up model is illustrated in Figure 3.2.

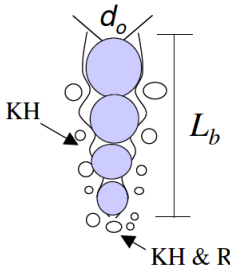

Figure 3.2: Illustration of KH-RT break-up model [CONVERGE_V1.3]

In the primary break-up process the radius of the child droplet [r_c] is calculated by using Equation (2), whereas the primary break-up time is evaluated using Equation (3), where B_1 is an adjustable model constant and Ω_{KH} and Λ_{KH} are the calculated frequency and wavelength of the fastest growing wave, respectively. r in Equation (3) is the radius of the droplet participating in the break-up process.

$$r_c = B_0 \Lambda_{KH} \tag{2}$$

$$\tau_{KH} = \frac{3.726 B_1 r}{\Omega_{KH} \Lambda_{KH}} \tag{3}$$

A break-up length, L_b, is calculated using Equation (4), where d_0 is the parent droplet diameter, ρ_f and ρ_a are the fluid and air densities, respectively, and C_b is an adjustable model constant.

$$L_b = C_b d_0 \sqrt{\frac{\rho_f}{\rho_a}} \tag{4}$$

When the wavelength of the fastest growing wave on a given droplet is smaller than the droplet diameter, RT waves grow on the droplet surface. When the wave growth time is greater than the break-up time, the droplet breaks up into child droplets. The radius of the child droplet is given by Equation (5), where K_{RT} is the calculated wave number and C_{RT} is the model constant.

$$r_c = \frac{\pi C_{RT}}{K_{RT}} \tag{5}$$

To improve the original O'Rourke droplet collision model, a new radius-of-influence method was implemented to further reduce the grid dependency of the collision model [Abani *et al.*, 2008]. More comprehensive range of collision outcomes was further introduced by Munnannur [2007]. Droplet distortion and deformation phenomena are described by the model of Liu *et al.* [1999],

which considers the momentum exchange between the droplet and ambient gas to monitor the droplet break-up and evaporation processes. An advanced droplet vaporization model was implemented by Ra and Reitz [2009] that considers a Discrete Multi-Component [DMC] fuel approach for the spray droplets, which is applicable over a wide range of temperatures. Spray/wall interaction is treated using the model of O'Rourke *et al.* [2000]. A modified k-ε RNG method [Han and Reitz, 1995] was used for the turbulence calculation.

3.2.2 Combustion Models

The modeling results in Chapter 4 include simulations with the CHEMKIN chemistry solver, whereas the later results used an advanced Jacobian chemistry solver, SpeedChem [Perini *et al.*, 2012]. The CHEMKIN II chemistry solver [Kee *et al.*, 1989] had been integrated into the KIVA3V Release 2 code for solving detailed chemistry mechanisms for multi-dimensional CFD simulations. In the computations each CFD cell is treated as a homogeneous reactor. At each time step the KIVA CFD model provides the chemistry solver the thermodynamic conditions and the mixture composition. The mixture composition and the energy information are updated in the chemistry solver, which is then received by the KIVA code. The present research neither considers flame propagation model nor turbulence/chemistry interaction phenomena. The model validations are presented in Chapter 5.

If a chemical kinetic mechanism involves n_s number of species and n_r number of reactions, the k^{th} reaction can be expressed as

$$\sum_{i=1}^{n_s} \nu'_{k,i} M_i \Leftrightarrow \sum_{i=1}^{n_s} \nu''_{k,i} M_i \qquad \text{where } k=1,2,\ldots\ldots,n_r \tag{6}$$

where ν' and ν'' are the forward and reverse stoichiometric coefficients, respectively. M_i identifies the chemical species in the mechanism. Generally, the stoichiometric coefficients are stored as

sparse matrices of n_r rows and n_s columns. Therefore, a Jacobian formulation was introduced, based on the aforementioned sparsity matrices, which shows a significant reduction in computational time [Perini *et al.*, 2012]. The sparse analytical Jacobian chemistry solver, SpeedChem, was found to reduce the computational time by 3-4 times without any noticeable change in the computational results.

This general reaction kinetics framework leads to n_s ODEs expressing mass conservation for the system, as

$$\frac{dY_i}{dt} = \frac{W_i}{\rho}\sum_{k=1}^{n_r}\left(\nu''_{k,i} - \nu'_{k,i}\right) q_k\left(\overline{Y},T\right) \qquad \text{where } i=1,2,\ldots\ldots,n_s \tag{7}$$

In the above equation Y_i is the species mass fraction, W_i is the species molecular weight, ρ is the average system density and q_k is the rate of progress variable. The rate of progress variable is given by

$$q_k\left(\overline{Y},T\right) = k_{f,k}\prod_{i=1}^{n_s}\left(\frac{\rho Y_i}{W_i}\right)^{\nu'_{k,i}} - k_{b,k}\prod_{i=1}^{n_s}\left(\frac{\rho Y_i}{W_i}\right)^{\nu''_{k,i}} \tag{8}$$

where $k_{f,k}$ and $k_{b,k}$ are the forward and backward reaction rate constants. The temperature dependent forward and backward reaction rates follow the modified Arrhenius kinetic law which can be expressed as

$$k_{f,k}(T) = A_k T^{b_k}\exp\left(-\frac{E_k}{RT}\right) \tag{9}$$

where A_k is the pre-exponential factor, b_k is the temperature exponent and E_k is the activation energy. The backward reaction rates can be expressed in similar manner, but are usually derived from the equilibrium constant of each reaction.

3.2.3 Emission Models

NO_x emissions are predicted using a reduced NO_x formation mechanism consisting of 4 species and 12 reactions [Sun, 2007]. The mechanism is based on the Gas Research Institute [GRI] NO_x mechanism. Reactions 10-21 are the extended Zeldovich pathways for the NO_x mechanism.

$$N + NO \Leftrightarrow N_2 + O \quad (10)$$
$$N + O_2 \Leftrightarrow NO + O \quad (11)$$
$$N + OH \Leftrightarrow NO + H \quad (12)$$
$$N_2O + O \Leftrightarrow N_2 + O_2 \quad (13)$$
$$N + O_2 \Leftrightarrow 2NO \quad (14)$$
$$N_2O + H \Leftrightarrow N_2 + OH \quad (15)$$
$$N_2O + OH \Leftrightarrow N_2 + HO_2 \quad (16)$$
$$N_2O + M \Leftrightarrow N_2 + O + M \quad (17)$$
$$HO_2 + NO \Leftrightarrow NO_2 + OH \quad (18)$$
$$NO + O + M \Leftrightarrow NO_2 + M \quad (19)$$
$$NO_2 + O \Leftrightarrow NO + O_2 \quad (20)$$
$$NO_2 + H \Leftrightarrow NO + OH \quad (21)$$

A two-step phenomenological soot model [Kong *et al.*, 2007] is used for soot prediction, which is originally based on the Hiroyasu soot model [Hiroyasu & Kadota, 1976]. The rate of change of soot mass within a computational cell, $\dot{M}_s$, is determined by a competition between the soot formation, $\dot{M}_{sf}$, and the oxidation, $\dot{M}_{so}$, processes.

$$\dot{M}_s = \dot{M}_{sf} - \dot{M}_{so} \quad (22)$$

Equation (23) shows the Arrhenius expression for the soot formation rate, where C_2H_2 is considered as the soot inception species.

$$\dot{M}_{sf} = \frac{dM_s}{dt} = A_{sf} M_{C_2H_2} P^n \exp\left(-\frac{E_{sf}}{RT}\right) \quad (23)$$

The soot oxidation rate is based on the Nagle and Strickland-Constable model [1962] which is given by Equation (24). In this equation M_s, ρ_s and D_s indicate the soot mass in the computational cell, the soot density and the soot particle diameter, respectively, whereas R_{oxid} is a function of temperature and the partial pressure of oxygen. This model has been discussed thoroughly by Liu *et al.* [2005].

$$\dot{M}_{s_o} = \frac{dM_{so}}{dt} = \frac{6MW_c}{\rho_s D_s} M_s R_{oxid} \tag{24}$$

Two model constants in Equation (23), the soot formation pre-exponential factor, A_{sf}, and the activation energy, E_{sf}, were tuned in the present simulations in order to compare with the experimental soot level. However, LTC operation usually does not produce much soot.

3.2.4 Fuel Chemistry

Real fuels are composed of many different components. But for simplicity, the ignition characteristics of automotive fuels are often represented by a blend of two hydrocarbons, i.e., iso-octane [iC_8H_{18}] and n-heptane [nC_7H_{16}], known as the primary reference fuel [PRF]. A well-validated skeletal reaction mechanism for PRF oxidation, with 41 species and 130 reactions was developed at ERC [Ra and Reitz, 2008] and was used to study the high-load, multi-cylinder engine operation in Chapter 4.

An extensively validated and improved reduced PRF mechanism was developed by Wang *et al.* [2013] based on a detailed mechanism from Lawrence Livermore National Laboratory [LLNL] with 1550 species and ~6000 reactions, and was used for the rest of the study in order to capture the fuel chemistry and the cool flame effects more accurately. This reduced PRF mechanism consists of 73 species and 296 reactions. The skeletal mechanism developed at ERC will be

referred as the ERC-PRF mechanism, whereas the one reduced from the LLNL will be referred as the PRF2 mechanism throughout the present study.

3.3 Genetic Algorithm Optimization Technique

The genetic algorithm [GA] is a search technique to find the "fittest" gene in a pre-defined design space. The criteria for the 'fittest' needs to be decided based on the problem definition, also known as objectives, which are engine-out emissions and noise level reduction for the current study. Originally based on the study of Senecal *et al.* [2000], the GA is considered to be a global optimization technique because of its ability to explore the entire design space [Shi *et al.*, 2011].

Different multi-objective genetic algorithms [MOGA] have been assessed before [Shi *et al.*, 2008 & 2011], among which the Non-dominated Sorting Genetic Algorithm II (NSGA II) of Deb *et al.* [2002] has been shown to give the best performance in approaching the optimal solution over all the objectives. The algorithm randomly creates 32 citizens in each generation, which are solved by KIVA runs. Once the computations for all citizens are finished for one specific generation, the NSGA II code is called for the evaluation of the objectives and only the best solution gets retained [Shi *et al.*, 2008]. In the next generation more random citizens are created while retaining the best citizens from the previous solution, to make the total number of citizens as 32. The optimal solution in one generation is known as Pareto optimal, for which no other solution set exists in a particular generation which will reduce all the objectives simultaneously. The Pareto surface can be explained by referring to Figure 3.3.

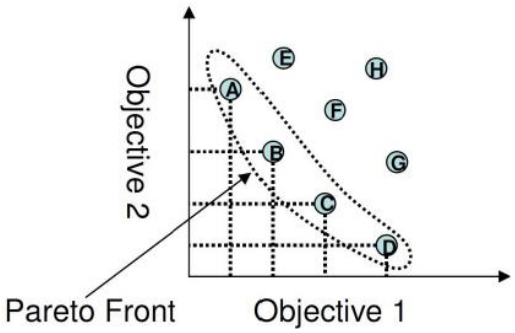

Figure 3.3: Concept of Pareto Optimal Solution [Shi *et al.*, 2008]

Figure 3.3 shows the Pareto optimal solutions A-D in a two objective space, which provide a simultaneous decrease of two objectives compared to the solutions E-H. The front is known as the Pareto front, which also illustrates convergence of the solution. Quantification of the convergence has been done by Kokjohn and Reitz [2008], and this procedure is used in the current study as well.

Chapter 4 High Load Operation in a Multi-Cylinder Light-Duty CI Engine Using Gasoline

Prior to investigating low load operation, high load [~16 bar IMEP] operating conditions were studied. This ensures that the engine exhibits reasonable combustion behavior over the entire range of speed and load. The current chapter focuses on triple injection strategies and reveals optimized high-load operating conditions for the GM 1.9L light-duty engine with the research piston, as mentioned in Chapter 3. The optimization study was conducted with the primary concern of revealing an optimized triple injections condition and comparison with double injection strategies. The simulations were performed using the KIVA-3V code with the improved ERC sub-models and the Chemkin library described in Chapter 3. The fuel oxidation chemistry was the ERC-PRF mechanism [Ra & Reitz, 2008], which was chosen to match the ignition characteristics of the gasoline fuel used for the experiments by Ra *et al.*, 2011.

Six engine design parameters were selected to vary, which were the premixed fuel percentage, the start of the second and third pulse timings, the second and third pulse fuel amounts, the EGR ratio and the boost pressure. The objective was to minimize NO_x, soot, CO, UHC, ISFC and PPRR.

4.1 Justification for Using Coarse Grid

A $1/7^{th}$ sector [~54.43 degree] mesh was used for the simulations considering the 7-hole injector used in the engine and runs were conducted from IVC to EVO timing. Computational grids with two different resolutions (see Table 4.1) were considered, as shown in Figure 4.1. The coarse grid with ~10,500 cells at IVC was used for the optimization simulations in order to save computational time, while the refined grid (~32,600 cells) was used to assess the differences with the use of a coarse grid.

(a) (b)

Figure 4.1: Computational grids at TDC [51.43 degree sector mesh] - (a) Coarse (b) Refined

Table 4.1: Coarse and refined grid comparison

	Coarse	**Refined**
Cells at IVC	~10500	~32600
Average Cell Size [mm]	~1.6	~0.6

The EGR gas composition was calculated using a burned gas analysis routine that assumes a constant ratio of CO and CO_2 [Ra *et al.*, 2011]. Figure 4.2 shows the simulated variation of gas composition at IVC with respect to EGR amount. With increasing EGR ratio, CO_2 increases, while the O_2 mole fraction decreases, resulting in an increase in global equivalence ratio. The amount of CO at IVC was maintained at a relatively small level.

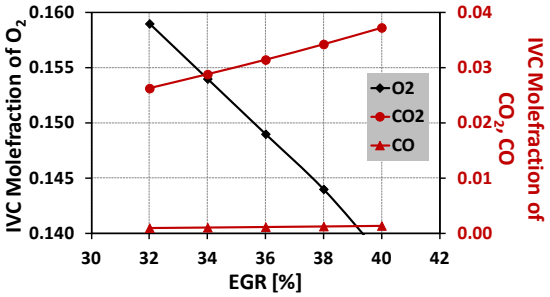

Figure 4.2: O_2, CO_2 and CO mole fractions at IVC with EGR

Figure 4.3 shows comparisons of the predicted in-cylinder pressure and heat release rate profiles between the coarse and refined grids for engine operation at 47% EGR ratio. The chosen case was the optimized high load condition of Ra et al. [2011] using the triple injection strategy. In order to match the compression pressures and temperatures between the coarse and the refined grids, the geometric compression ratio of the coarse grid was slightly adjusted by increasing the crevice region height, as can be seen from Figure 4.1. It is observed that the combustion phasings

of the two cases are in good agreement, although the pressure rise rate is slightly over-predicted in the coarse grid case. The corresponding predicted emissions are compared in Table 4.2, which show good agreement between the two grid cases, while the computing time is 3 times less using the coarse grid. Thus, the use of the coarse grid in the computationally demanding optimization study is well justified. This case was chosen to be the baseline case in the GA study which acted as a seed towards obtaining the optimum condition using less computational time. All simulation results in this Chapter correspond to the coarse grid case, unless mentioned otherwise.

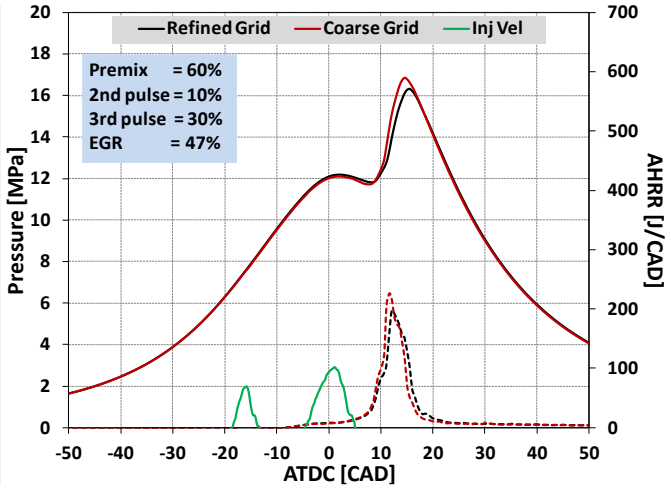

Figure 4.3: Pressure and apparent heat release rate (AHRR) comparison between coarse and refined grid cases

Table 4.2: Emission comparison for the coarse and refined grid cases

	Coarse	**Refined**
Soot @ EVO [g/kW-hr]	0.045	0.040
NO_x @ EVO [g/kW-hr]	0.017	0.028
CO @ EVO [g/kW-hr]	37.086	38.159
UHC @ EVO [g/kW-hr]	10.817	10.323

4.2 Optimization Parameters

In the present optimization study, the variation of six engine design parameters was considered. The list of the parameters and their variability ranges are shown in Table 4.3.

Table 4.3: Engine design parameters

IVC Pressure [bar]	2 to 5
Premixed Fuel Fraction	0 to 1
Ratio of fuel fraction in 2nd & 3rd pulse	0 to 1
Start of 2nd Pulse [deg ATDC]	-80 to +30
Start of 3rd Pulse [deg ATDC]	-80 to +30
%EGR	10 to 55

The IVC pressure was chosen to vary from 2 to 5 bar, with the IVC pressure of 3.25 bar used in the previous extensive study of Ra *et al.*, 2011, which is in the middle of the considered range. Also, the high end of the EGR ratio range was set to 55% such that the EGR variation included a much higher level than that of the study of Ra *et al.* [2011], which explored double-pulse injections. The minimum EGR ratio was selected to be low enough to compensate for the reduced reactivity of the lower bound of the IVC pressure range. The GA optimization was also intended to explore both double and triple pulse strategies by allowing overlaps of the injection timings of the 2nd and 3rd pulses. Note that this implies the use of two independent injection systems to enhance the controllability of the spray injection strategies. However, at the same time this also indicates that an increase in injection pressure might be necessary to allow more injected fuel amounts for a given injection duration when only a single injector system is considered. Thus, the injection pressure does not need to be considered as an explicit variable in the study.

In order to estimate the noise level related to the peak pressure rise rate (PPRR), the ringing intensity (RI) was monitored. RI is a correlation based on fundamental wave dynamics [Eng, 2002], defined as

$$RI\left[\frac{kW}{m^2}\right] \cong \frac{1}{2\gamma}\frac{\left(\beta\left.\frac{dP}{dt}\right|_{max}\right)^2}{P_{max}}\sqrt{\gamma RT_{max}} \qquad (25)$$

In the above equation, γ is the ratio of the specific heats, $(dP/dt)_{max}$ is the peak pressure rise rate in [kPa/ms], P_{max} is the peak cylinder pressure in [kPa], R is the universal gas constant, T_{max} is the peak in-cylinder temperature in [K] and β is a constant with a value of 0.05 in [ms]. It has been found that the higher the PPRR, the higher the ringing intensity, whose threshold value is about 5 MW/m^2 to have smooth engine operation [Dec *et al.*, 2010]. Note that the RI is a function of engine speed, which makes it difficult to set an universal constraint value of RI for a wide range of engine operating conditions. For this reason, PPRR was chosen as one of the objectives to be minimized in this study, but the corresponding RI value will be presented as well.

4.3 Optimization Results

This section presents the optimal designs revealed by the GA optimization simulations and their detailed analysis. As shown in Figure 4.4, the Pareto front stopped advancing after the 15th generation, but the GA optimization was allowed to run until the 30th generation to confirm that convergence was achieved. The total run time was ~20days on the University of Wisconsin, Madison CONDOR system [Shi *et al.*, 2011].

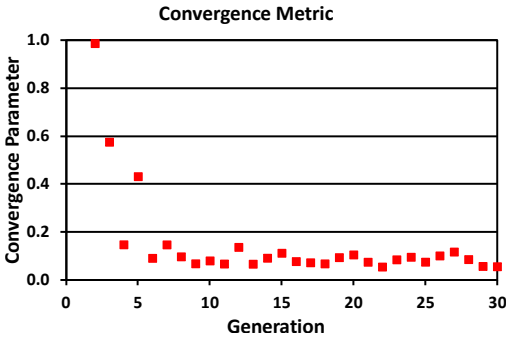

Figure 4.4: Convergence metric showing the Pareto front advancement

Figure 4.5 presents the KIVA results in a 3-D objective space of emissions, PPRR and ISFC. All emission objectives were multiplied together to give a representative 1-D emission comparison. Note that emissions were estimated at EVO timing and ISFC was calculated for the

period from IVC to EVO. This figure confirms that the citizens from the first generation (shown in green) march towards the origin, as shown by the Pareto solutions in red. But it can also be noticed that there are not many Pareto solutions at the center of this chart, which indicates that at high load it is difficult to maintain a low value of both ISFC and PPRR at the same time.

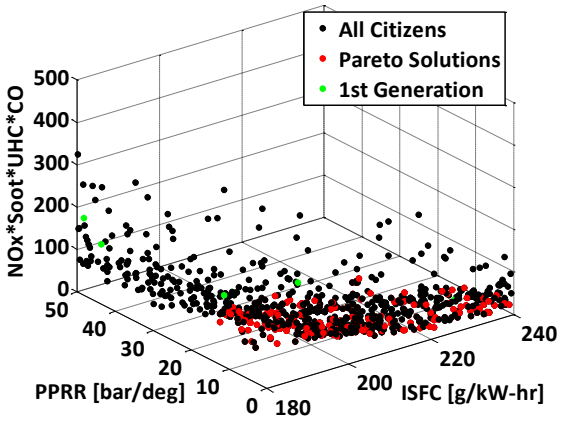

Figure 4.5: KIVA results in 3D objective space

Upon examining ~200 Pareto solutions, two solutions were chosen as possible optimal designs based on the constraints of ISFC < 215 g/kW-hr, NO_x < 0.5g/kW-hr, soot < 0.2 g/kW-hr and PPRR < 20bar/deg. The reason behind choosing the loose constraints for ISFC and PPRR was due to the unavailability of enough solutions with a low value of both of them, as mentioned before. The chosen designs are mentioned together with the baseline case in Table 4.4. Two distinct operating conditions are observed. Design-1 indicates a triple pulse injection strategy with a high EGR while Design-2 indicates a double pulse strategy, where the third pulse is injected within the second pulse's duration, with a comparatively low EGR. It is interesting to note that Design-1 is very similar to the baseline case, indicating that the baseline represents one of the best operating conditions.

Table 4.4: Optimal designs at high load

	Baseline	**Design-1**	**Design-2**
Generation	-	7	14
Citizen	-	0	12
IVC Pressure [bar]	3.25	3.25	3.29
Premixed Fuel %	60.0	60.0	40.8
Fuel % in 2nd Pulse	10	9.6	48.8
Fuel % in 3rd Pulse	30	30.4	10.6
Start of 2nd Pulse [deg ATDC]	-18.60	-76.09	6.31
Start of 3rd Pulse [deg ATDC]	-4.6	-4.6	10.0
%EGR	47.0	47.0	30.8
Performance Analysis			
ISFC [g/kW-hr]	204.55	198.83	213.91
NO_x [g/kW-hr]	0.017	0.019	0.437
Soot [g/kW-hr]	0.045	0.027	0.065
CO [g/kW-hr]	37.09	29.55	14.50
UHC [g/kW-hr]	10.82	8.97	9.04
PPRR [bar/deg]	15.84	18.18	7.03
Ringing Intensity [MW/m^2]	28.51	35.78	6.79
IVC to EVO Thermal Efficiency [%]	40.57	41.94	39.00

Figure 4.6 shows the pressure and HRR profiles of the chosen optimal designs. Design-1 at high EGR ratio (47%), and Design-2 at a comparatively low EGR ratio (30.8%), lead to two different combustion characteristics. The second pulse timing of Design-1 was early enough (-76.09 deg ATDC) to provide a premixed condition with an effective premixed amount of 69.6% (1st pulse+2nd pulse), resulting in a high PPRR. On the contrary, Design-2 displays a two-stage combustion behavior, as can be clearly seen from the distinct heat release rate peaks at around TDC and 10 deg ATDC. The first stage of combustion for Design-2 was solely due to the premixed fuel amount as the second pulse was not introduced before 6 deg ATDC. When the 2nd pulse fuel is injected into the burned gases of the premixed charge, the high temperature of the charge tends to shorten the ignition delay times. At the same time, however, the increased local burned gas amounts or decreased locally available oxygen tend to lengthen the ignition delay times. If the local available oxygen is more than an optimal amount, most of the fuel injected in the 2nd pulse

burns in the mixing controlled combustion mode, and thus NO_x formation is increased substantially due to the high burned gas temperatures. Therefore, appropriate amounts of EGR and premixed fuel are necessary to control NO_x formation during the 2nd stage of combustion by the 2nd pulse. It is notable that the low PPRR of Design-2 allows more premixed fuel amount to increase the effective engine-out work.

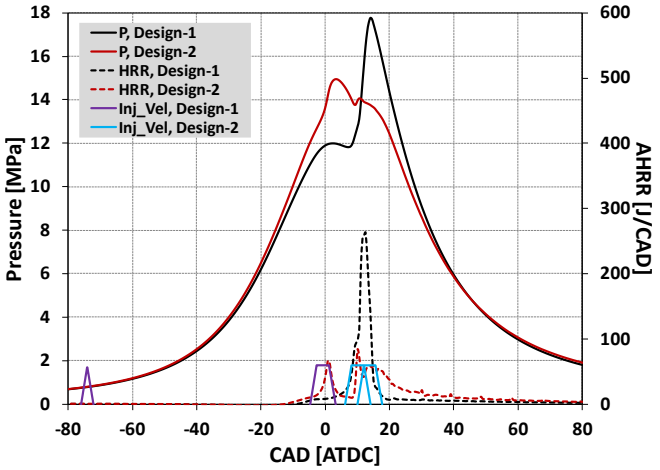

Figure 4.6: Pressure and heat release rates of two optimal designs

Design-1

In order to determine the role of the 2nd pulse injection, a 2-pulse injection case (2-Pulse) was simulated that was modified from Design-1. Omitting the 2nd pulse of Design-1, the 3rd pulse was injected at the same timing with the fuel amount increased to 40% (i.e., 9.6+30.4=40%, see Table 4) in the 2-Pulse case. In Figure 4.7, profiles of in-cylinder pressure, HRR and injection rate are shown. Without the 2nd pulse in Design-1, the ignition timing is significantly retarded and the PPRR is reduced at the expense of increased ISFC, CO and UHC emissions (see Table 4.5). This controlling effect of the 2nd pulse in Design-1 is revealed well in the in-cylinder distributions of equivalence ratio and gas temperatures shown in Figure 4.8. At -16 deg ATDC, it is seen that fuel/air stratification occurs due to the introduction of the 2nd pulse injection, resulting in a near stoichiometric region formed close to the injector. This region drives the ignition process with the

help of the 3rd pulse injection (see 12 deg ATDC temperature distribution). On the contrary, with the rest of the fuel injected at -4.6 deg ATDC for the 2-Pulse case, more than half of the fuel is injected during the expansion stroke and the bulk gas temperatures are further decreased by the evaporation cooling, which results in more retarded ignition, and thus significant decrease of peak pressure and PPRR.

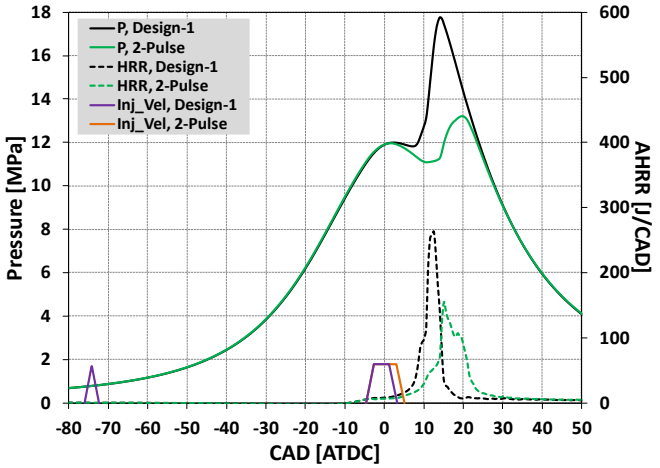

Figure 4.7: Pressure and heat release for Design-1 [Table 4.4] and equivalent double injection case [2-pulse]

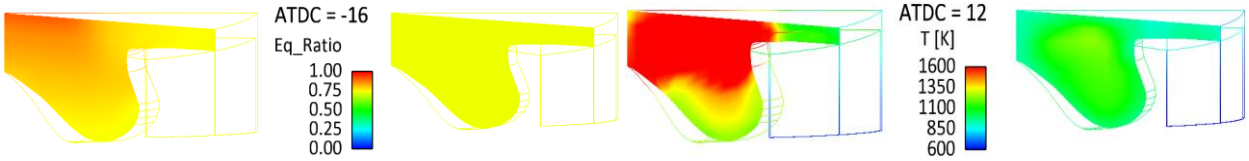

(a) (b)

Figure 4.8: Equivalence ratio and temperature contours for (a) Design-1 and (b) 2-Pulse case

Table 4.5: Performance comparison for Design-1, 2-Pulse and Case-A[1]

	Design-1	**2-Pulse**	**Case-A**
IVC Pressure [bar]	3.25	3.25	3.25
Premixed Fuel %	60.0	60.0	60.0
Fuel % in 2nd Pulse	9.6	-	9.6
Fuel % in 3rd Pulse	30.4	40	30.4
Start of 2nd Pulse [deg ATDC]	-76.09	-	-10
Start of 3rd Pulse [deg ATDC]	-4.6	-4.6	-4.6
%EGR	47.0	47.0	47

[1] Case-A is explained below Table 4.5

Performance Analysis			
	Design-1	**2-Pulse**	**Case-A**
ISFC [g/kW-hr]	198.83	214.28	209.96
NO_x [g/kW-hr]	0.019	0.008	0.011
Soot [g/kW-hr]	0.027	0.045	0.042
CO [g/kW-hr]	29.55	40.20	39.42
UHC [g/kW-hr]	8.97	13.08	12.17
PPRR [bar/deg]	18.18	7.77	11.14
Ringing Intensity [MW/m^2]	35.78	8.62	16.07
Thermal Efficiency [%]	41.94	38.90	39.72

It is interesting to note that retardation of the 2^{nd} pulse timing (SOI2) until -30 deg ATDC had little effect on the ignition timings and PPRR, while further retardation starts delaying the ignition and reducing PPRR, as shown in Figure 4.9. This indicates that the level of mixture stratification is governed by the existence of an appropriate amount of 2^{nd} pulse fuel, and not by its timing, until the interaction of the 2^{nd} and 3^{rd} pulses becomes significantly influential, as in the case of -10 deg ATDC injection timing in Figure 4.9. The in-cylinder fuel and temperature distributions reveal this behavior clearly, as shown in Figure 4.10. In this figure, equivalence ratio and temperature distributions with SOI2 of -10 deg (Case-A), -30 deg (Case-C) and -50 deg (Case-D) are compared at various crank angles. At -10 deg ATDC, right before SOI2 for Case-A, almost the same degree of mixture stratification is observed for Case-C and Case-D, which results in similar ignition delay times and ignition locations in these two cases (see figures at 10 deg ATDC). On the contrary, in Case-A, development of ignition-driving fuel/air mixtures is much delayed due to the late SOI2 and short time for the oxidation reactions to proceed.

Similar behavior is seen for the combustion/thermal efficiencies and NO_x emissions, as shown in Figure 4.11. With retarded SOI2, the combustion/thermal efficiencies are decreased gradually for a wide range of SOI2, then drop rapidly for SOI2 later than -30 deg ATDC. NO_x emissions show similar behavior with respect to SOI2 variation, although their level remains very low over the entire range of SOI2 considered in the study. The performance of engine operation

with SOI2 of -10 deg ATDC is compared with those of Design-1 in Table 4.5. It can be seen from the results that instead of -76 deg ATDC, 2nd pulse injection timings later than -30 deg ATDC are likely to be preferred if a more stringent PPRR (and/or peak pressure) constraint is employed in the optimization simulations. Note that reducing PPRR and peak pressure are obtained at the expense of increased CO and UHC emissions (and thus combustion efficiency).

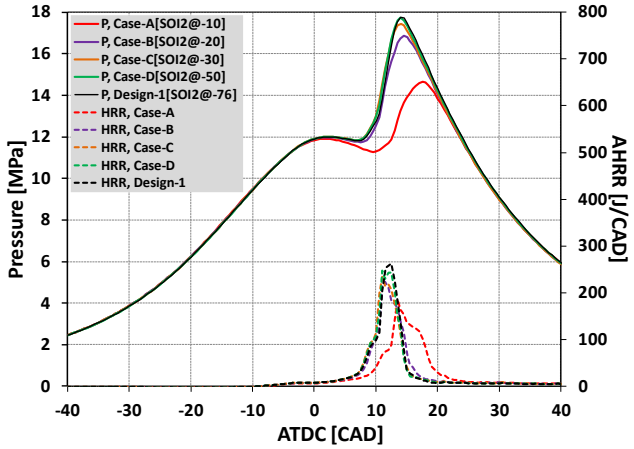

Figure 4.9: Pressure and AHRR plots for Design-1 second injection timing sweep

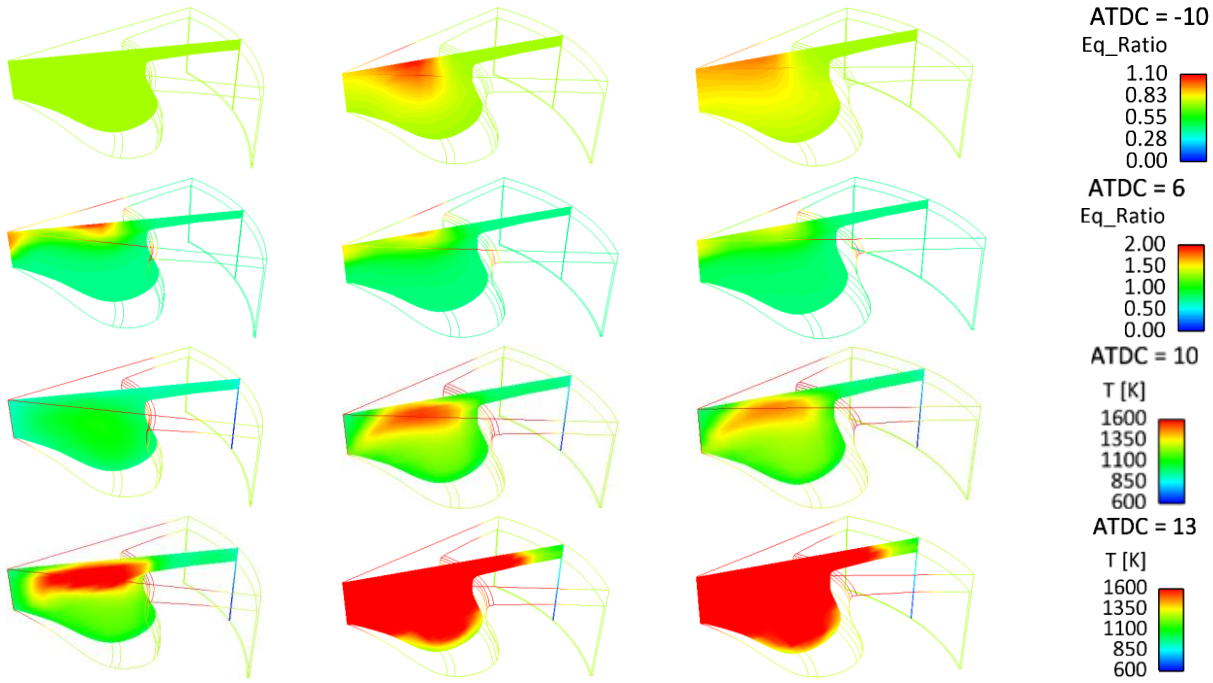

(a) (b) (c)

Figure 4.10: Equivalence ratio and temperature contours for (a) Case-A (b) Case-C and (c) Case-D [see Figure 4.9]

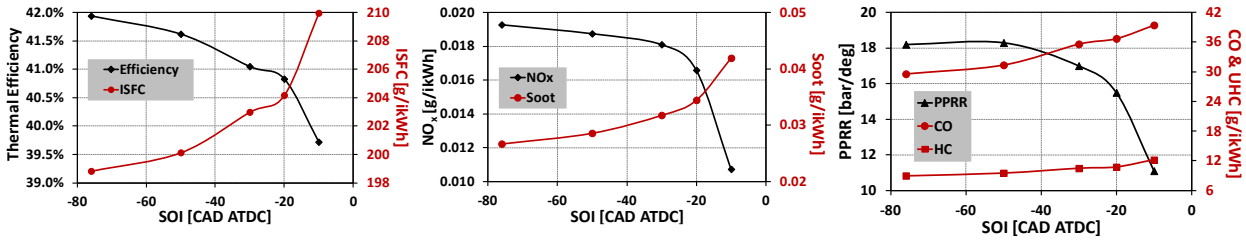

Figure 4.11: Performance plots for Design-1 second injection sweep

Design-2

As described above, the 3rd pulse in Design-2 is injected during the 2nd pulse injection, which practically corresponds to a double pulse injection, i.e., 1st pulse injection during the valve-overlap period (assumed as the pre-mixture) and the 2nd pulse injection at 6.31 deg ATDC with an increased injection pressure to increase the injection amount. This two-stage combustion behavior is similar to that observed in diesel combustion in a light-duty engine [Kokjohn *et al.*, 2008] and in gasoline combustion in a heavy-duty engine [Dempsey *et al.*, 2011].

Table 4.6: Performance comparison for Design-2 related simulations

	Design-2	**Case-A**	**Case-B**
IVC Pressure [bar]	3.29	3.29	3.29
Injection Pressure [bar]	1160	1500	1500
Premixed Fuel %	40.8	40.8	**50.0**
Fuel % in 2nd Pulse	48.8	59.2	**50.0**
Fuel % in 3rd Pulse	10.6	-	-
Start of 2nd Pulse [deg ATDC]	6.31	6.31	6.31
Start of 3rd Pulse [deg ATDC]	10.0	-	-
%EGR	30.8	**36.0**	36.0
Performance Analysis			
ISFC [g/kW-hr]	213.91	230.47	200.92
NO_x [g/kW-hr]	0.44	0.15	0.19
Soot [g/kW-hr]	0.07	0.11	0.08
CO [g/kW-hr]	14.50	27.69	9.69
UHC [g/kW-hr]	9.04	14.16	5.75
PPRR [bar/deg]	7.03	5.00	10.50
Ringing Intensity [MW/m^2]	6.79	3.52	12.80
IVC to EVO Thermal Efficiency [%]	39.00	36.14	41.46

As shown in Table 4.4, the NO_x emission of Design-2 is higher than the emissions target (~0.23 g/kW-hr), which necessitates further reduction. To achieve this, an EGR ratio sweep was

simulated by increasing it up to 42%. The results show that using 36% EGR ratio, the NO_x emission threshold could be met. However, soot, CO and UHC emissions are increased and thermal efficiency is significantly reduced, which is the reason Case-A was not selected as an optimal condition in the optimization simulations. Its operating conditions (called Case-A) and performance data are compared with Design-2 in Table 4.6. (Note that Case-A and Case-B mentioned in Table 4.6, now correspond to Design-2.) The pressure and HRR profiles of Case-A are compared with those of Design-2 in Figure 4.12. With increased EGR ratio, ignition timing is slightly retarded, and thus peak pressure and PPRR are further reduced. Subsequent reduction of burned gas temperatures contributes to the reduction of NO_x emissions.

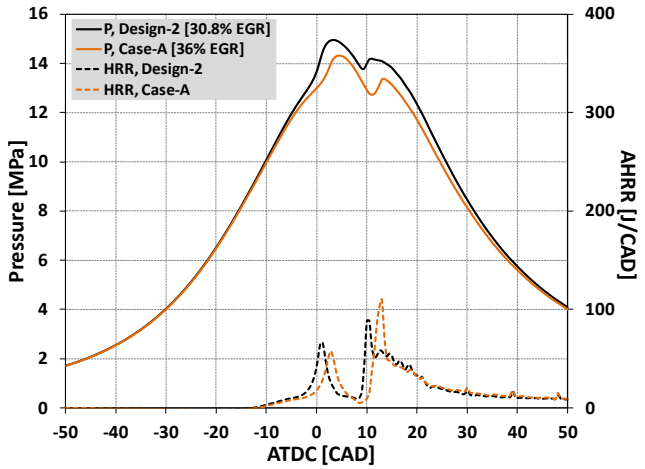

Figure 4.12: Pressure and heat release traces for Design-2 and Case-A

Figure 4.13 describes the effect of EGR on PPRR and emissions at EVO. Note that the soot emission increases with increasing EGR until 40% EGR is reached and decreases with further increase in EGR. This phenomenon has been observed before for diesel combustion [Eng, 2002], which can be explained by the soot formation mechanism. Soot emission is the result of the competing effects of the soot formation and oxidation processes, which are dependent on the equivalence ratio and the burnt gas temperature. As equivalence ratio increases, soot formation increases in fuel-rich regions, whereas, the soot oxidation process reduces. On the other hand,

reduction in temperature lowers both the soot formation and oxidation processes. With an increase in EGR, the air/fuel ratio and the temperature both decrease, dictating the soot generation process. Soot formation prevails until a certain amount of EGR is reached, maintaining a temperature range where soot formation occurs. Soot oxidation is already low at that point due to the lower burnt gas temperature and the unavailability of enough oxygen. This is the reason for the increasing soot trend in Figure 4.13, until 40% EGR is reached. Further increase in EGR reduces the temperature even more, which results in negligible soot formation. Thus, a lowering trend at 42% EGR is seen, as shown in Figure 4.13. An increased amount of CO and UHC can also be observed with the increase in EGR, where the charge temperature was high enough to start the fuel burning, but incomplete combustion resulted in more CO than UHC. All cases presented here have soot emissions below the target of 1 g/kg-f.

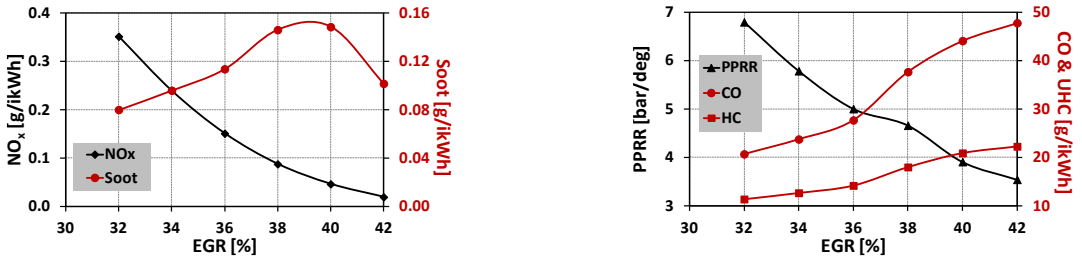

Figure 4.13: Engine performance plot for EGR sweep

In order to investigate possible improvements of thermal efficiency at the expense of increased PPRR from Design-2, double-injections with increased 1st pulse amounts were simulated. Two cases with the 1st pulse split ratio of 45% and 50% (called Case-B in Table 4.6) were simulated with all other conditions maintained the same as in Case-A. Figure 4.14 shows the comparison of pressure and HRR profiles among the three cases.

With increased 1st pulse amount, the heat release rates rise rapidly, which results in increased PPRR. Since more fuel burns in the 1st stage of combustion, the burned gas temperature becomes higher when the 2nd pulse fuel is injected. Thus, the ignition delay of the fuel/air mixture

by the 2nd pulse becomes shorter because of the increase in 1st pulse amount. Due to the prevailing effects of the increased residence time of the 2nd pulse-oriented burned gases in the high temperature condition, NO_x emissions are slightly increased with increasing 1st pulse ratio, although the amount of 2nd pulse fuel is reduced, as compared in Table 4.6. On the contrary, the thermal efficiency is significantly improved to ~41.5%.

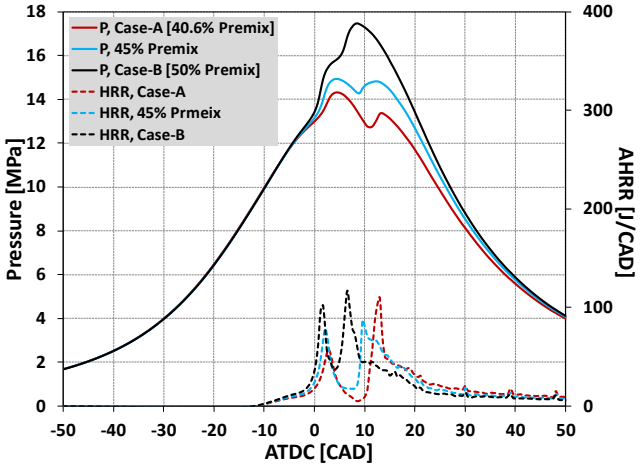

Figure 4.14: Pressure and heat release for different levels of premixing for Design-2

Engine Operation Map Generation

Figure 4.15 demonstrates the engine operating map at two different EGR conditions; the high EGR regime with 47% EGR and the comparatively low EGR regime with 36% EGR, as discussed in Table 4.4. The high EGR regime has been summarized in Figure 4.15a, for both double pulse and triple pulse operation. The premixed versus second pulse injection timing in this figure explored an operating regime for the triple pulse case, where the PPRR is controlled by the premixed fuel amount and the second pulse timing as observed in Figure 4.9. The double-pulse regime in Figure 4.15b shows a ~12 degree window for SOI2 at 60% premixed fuel amount, where the PPRR is restricted by the second pulse fuel interaction with the premixed amount and the combustion instability created by a delayed second pulse injection timing. For lower premixed amount, the PPRR and the combustion stability are found to be very sensitive to the second pulse

timing, showing a narrower operating regime. Figure 4.15b presents the comparatively low EGR operation map. Compared to the triple pulse map in Figure 4.15a, Figure 4.15b is restrained by less premixed fuel amount due to the lower EGR usage. The SOI2 operation window becomes narrower as the premixed amount is reduced, similar to the observation in Figure 4.15a. Interestingly the operating window at 50% 1st pulse amount is very wide, extending to a very late SOI2 (~30 deg ATDC).The reason for this behavior can be explained by comparing the cases in that window. Pressure and heat release traces at three different SOI2 timings, i.e., 8 deg, 18 deg and 28 deg ATDC are shown in Figure 4.16, where the premixed fuel amount is maintained at 50%. This figure clearly indicates that the peak pressure and PPRR are solely controlled by the pre-mixture amount, whereas, the 2nd pulse contributes towards an increase in load. It is observed that with 2nd pulse injection, the HRR is also raised maintaining a long tail in the HRR profile, which indicates that the 2nd pulse fuel is burning mainly in the mixing-controlled combustion mode. Accordingly expansion pressures start deviating at late SOI2 timings from the corresponding pressure profile of the 50% pre-mixture. Until a certain SOI2 (~30 deg ATDC), the burned gas temperatures of the pre-mixture is high enough to combust the 2nd pulse fuel, and thus meet the combustion efficiency threshold. However, further retardation in SOI2 eventually results in excessive unburned fuel amounts, which is excluded from the operation range. On the other hand, the increase in premixed fuel amount is restrained by the PPRR threshold.

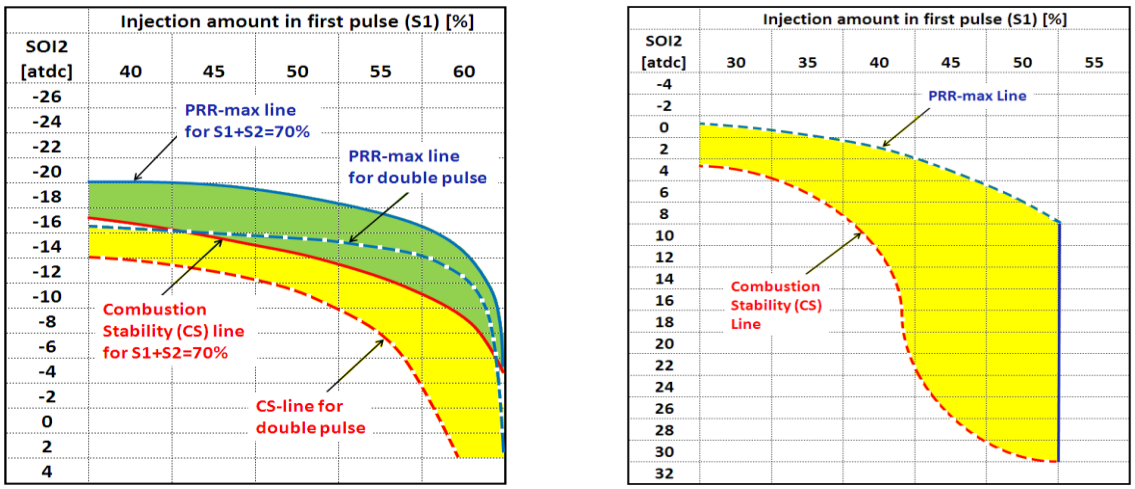

(a) (b)

Figure 4.15: Operation map for (a) high EGR regime (b) low EGR regime

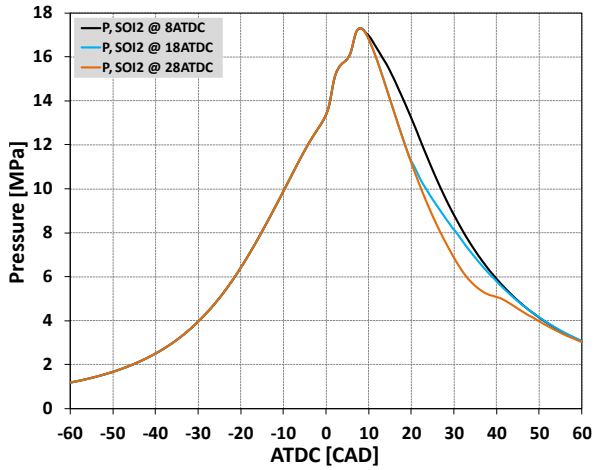

Figure 4.16: Comparison of pressure and heat release traces to observe the effect of second pulse in Design-2

4.4 Discussion

A numerical optimization study was carried out in a high-speed, light-duty gasoline direct-injection, compression-ignition (GDICI) engine at a full load condition. After examining the results, the following conclusions can be drawn.

a. Two different high load operating regimes were revealed from the GA optimization analysis. A high EGR regime was mainly constrained by the PPRR, whereas, a comparatively low EGR regime was constrained by NO_x emissions.

b. The high EGR regime was operated with triple-pulse injections and it was characterized by single-stage combustion mainly after TDC. On the contrary, the low EGR regime showed a preference towards double pulse operation with very retarded 2nd pulse injection timings, and featured two-stage combustion characteristics.
c. In triple-pulse injection operation with high EGR, combustion stability and PPRR were mainly controlled by the second pulse injection timing and amount. On the other hand, using the double pulse strategy along with low EGR, PPRR and emissions were mainly governed by the 1st pulse fuel amount and the 2nd pulse timing was less influential.
d. Using triple pulse injections, the operable range of second pulse injection timings could be extended significantly without affecting the in-cylinder combustion characteristics.
e. In the two-stage combustion strategy, a very wide operating injection timing window was observed over a wide range of 1st pulse fuel amounts.

With the above insights, the research focus was shifted towards low load operation using gasoline fuels, as discussed next.

Chapter 5 Low Load Operation in a Multi-Cylinder Light-Duty CI Engine Using Various Octane Gasoline

This chapter explores the effect of single and multiple injection strategies on low load operation using different octane number gasoline fuels.

5.1 Load Minimization using Triple-Injection Strategy

As a triple injection strategy was found to be successful for high load operation in Chapter 4, low load operation was explored also using the triple-pulse strategy to further understand the effect of each pulse on controlling the in-cylinder combustion behavior. The objective of this section is to also examine the effect of different RON gasoline fuel on the injection strategies. Experiments were conducted at 2 bar and 5 bar BMEP load points using 75 and 93 RON gasoline fuels. The numerical results were validated with the experimental results and provided insights about the engine combustion characteristics at different speeds and low load conditions using the different fuels. Some of the engine operating conditions and fuel properties are mentioned in Table 5.1. The 2 bar BMEP experiments at 1500 rev/min were conducted using only the 75 RON fuel and both the fuels were used to perform the 5 bar BMEP experiments at 2000 rev/min. The different auto-ignition characteristics of these fuels did not allow the 93 RON fuel to run below 5 bar BMEP load using a triple injection strategy.

Table 5.1: Coarse and refined grid comparison

Operating Conditions	
Fuel Used [RON]	75, 93
Engine Load - BMEP [bar]	2, 5
Engine Speed [rev/min]	1500, 2000
Fuel Injection Pressure [bar]	500, 600
Swirl Ratio	2.2
Fuel Specifications	
RON	74.7 / 92.6
MON	73.2 / 81
[RON+MON]/2	74 / 86.8
Specific Gravity	0.659 /0.702
Initial Boiling Point [IBP] [C]	81.7 / 93.2

The simulations considered a $1/7^{th}$ sector mesh [~51.43 degree] with the assumption of sector symmetry. As explained in Chapter 4, in order to save computational time a relatively coarse grid was used with ~12000cells, where the average cell size was ~1.6mm. The computational grid is shown again in Figure 5.1.

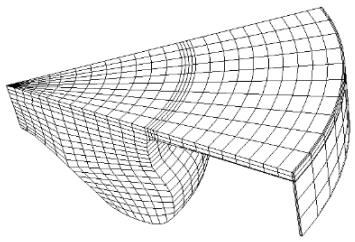

Figure 5.1: Computational grid at TDC

5.1.1 Cylinder-to-Cylinder Variation in a Multi-Cylinder Engine

A feature of a multi-cylinder engine is cylinder-to-cylinder variation along with cycle-to-cycle variability. Figure 5.2 shows motored pressure traces for all four cylinders at 2000 rev/min. It is clear from the figure that all four cylinders have different effective compression ratios. The experimental pressure traces revealed that cylinder 1 had the maximum CR of 17.83. This can be attributed to higher charge mass intake in the other cylinders, which elevates the specific heat ratio

resulting in a reduced CR. It also indicates that the breathing of each cylinder is different. The derived compression ratios for all the cylinders are presented in Table 5.2.

Table 5.2: Effective compression ratios for all four cylinders

	Effective CR
Cylinder1	17.83
Cylinder2	17.18
Cylinder3	17.65
Cylinder4	16.45

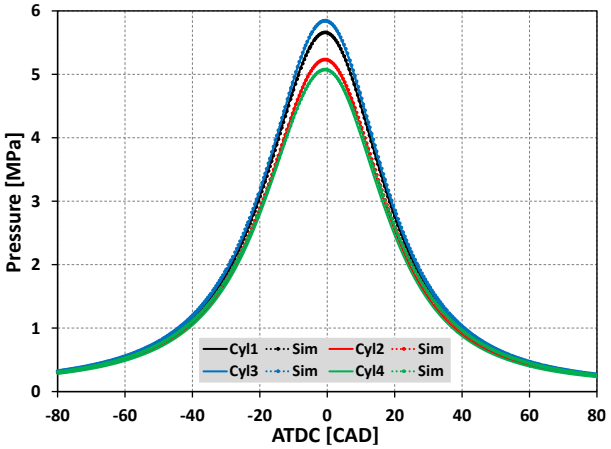

Figure 5.2: Experimental and predicted motored pressure trace comparisons at 2000 rev/min for all four cylinders

Simulations were performed to validate the experimental motored traces for all 4 cylinders. The results indicate that the simulations were able to capture the experimental motored traces reasonably well for all cylinders, except cylinder 4. The numerical results for cylinder 4 showed somewhat higher pressure in the compression and expansion strokes compared to the experiment, which might be due to a cylinder-leakage problem. The above motored-trace comparisons demonstrate the difficulties in modeling a multi-cylinder engine.

5.1.2 Cycle-to-Cycle Variation in Cylinder 1

Along with cylinder-to-cylinder variations, it should also be kept in mind that the experimental pressure traces are the average of 100 cycles. Thus, when considering one specific cycle in a simulation instead of the average, it is not possible to account for the pressure and CA50 variation

from cycle-to-cycle. Some representative cycles from cylinder 1 are shown in Figure 5.3 to support the above statement. The simulation was able to represent the combustion phasing of one of the cycles perfectly, whereas, an over-prediction of the expansion pressure can be observed.

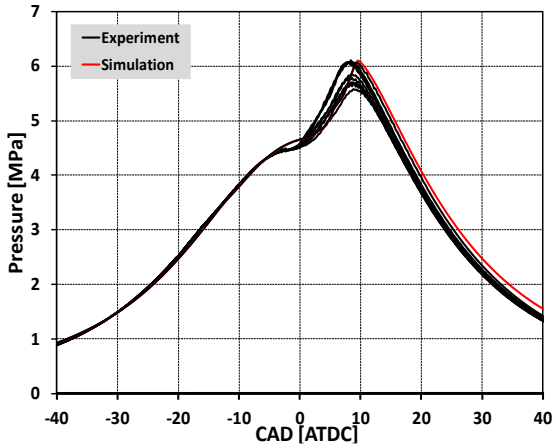

Figure 5.3: Cycle-to-cycle variation in cylinder 1 of the multi-cylinder engine

When cycle-to-cycle variation is compounded with cylinder-to-cylinder variation, simulation work appears to be even more difficult. This inevitably leads to some uncertainties in the present study.

5.1.3 2 bar BMEP Load Condition Study using 75 RON/74 PRF Gasoline

This load condition was studied using only 74 PRF fuel as it was very difficult to ignite 87 AKI gasoline at the light load condition while maintaining controllability of the engine.

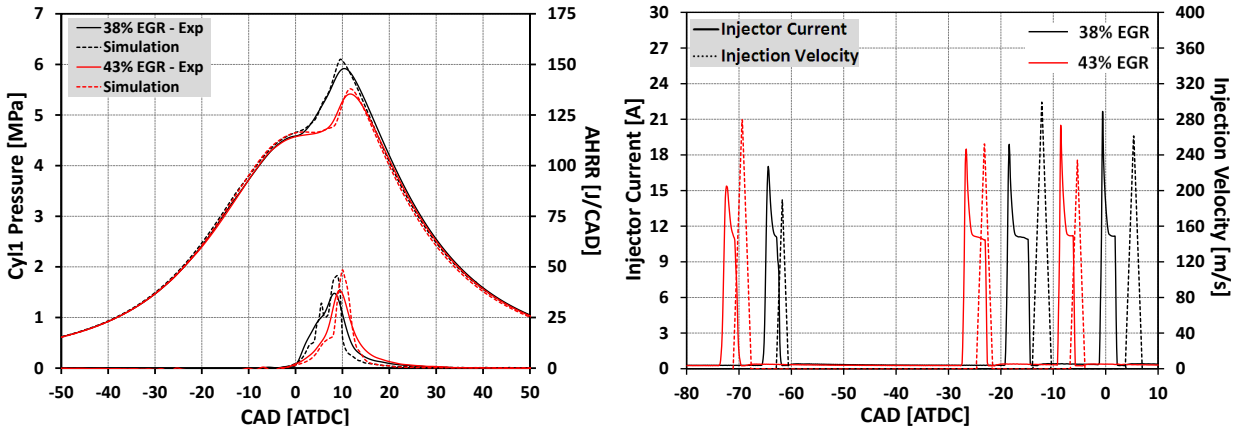

(a) (b)

Figure 5.4: (a) Experimental and predicted pressure and heat release comparisons and (b) experimental injector current and predicted injection velocity plots for 74 PRF fuel at 2 bar BMEP

The experiments were performed at two different EGR conditions, i.e., 38% and 43%, in order to minimize NO_x emissions, and ~8.78 mg/cyc of fuel was used to maintain the 2 bar BMEP load. Figure 5.4a illustrates a comparison between the predicted and experimental pressure and heat release traces. It is seen that the numerical model does an excellent job in capturing the combustion phasing, but the peak pressure is slightly over-predicted. This could be because a simplified trapezoidal rate shape profile was used initially in the simulation, which influences the peak pressure.

Figure 5.4b shows the injection velocity and injector current plots with time. Bosch bench measurements were conducted to estimate the actual injection split amounts to be used in the simulations. As can be observed, the injector opening delay is larger for some of the injection events compared to others, and for the 38% EGR case, the second and third injections started after the injector current command.

A comparison is shown in Figure 5.5, where the fuel splits were altered based on the command splits and Bosch bench measurements, while keeping the start of injection timings same. The command split is based on the area under the injector current command signals.

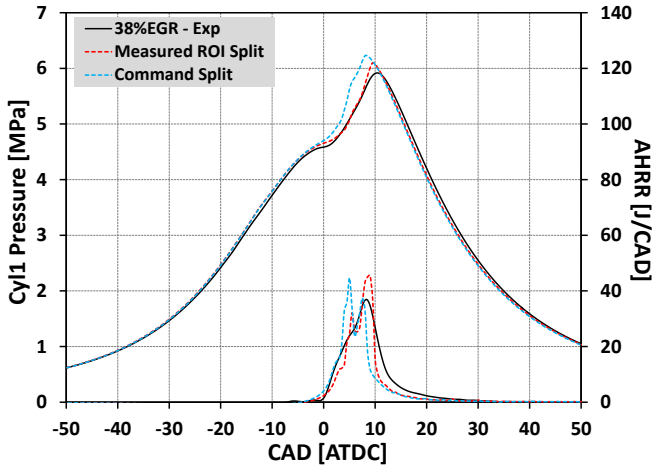

Figure 5.5: Comparisons of pressure and heat release traces due to the fuel split differences obtained from the Bosch bench measurement and the injector current command

Table 5.3 shows the fuel split differences between the Bosch bench measurement and injector current commands for the 38% EGR case. The command splits indicate that with more than 70% of the fuel was injected before the third injection, the pressure rise rate was elevated, whereas when 65% of the fuel was injected in the first two injections as obtained from Bosch bench measurements, it provided a better comparison with the experimental pressure trace. This indicates that the measured fuel splits provide a better indication of the actual experimental fuel fractions. This is not surprising due to the complex wave interactions in the fuel injection lines.

Table 5.3: Fuel splits obtained from Bosh bench measurement and injector current command

	% EGR	**Injected Fuel Frac 1st/2nd/3rd**	**Injection Timing [ATDC] 1st/2nd/3rd**
Measured ROI Split	38	0.184 / 0.458 / 0.358	-62.88 / -14 / 3.748
Command Split	38	0.293 / 0.413 / 0.294	-62.88 / -14 / 3.748
Measured ROI Split	43	0.400 / 0.326 / 0.274	-71.116 / -24.7 / -6.824

The experimental and predicted performances for the two different EGR ratios are compared in Table 5.4. With a global equivalence ratio of ~0.4 the soot was extremely low at these low load conditions. Carbon-monoxide [CO], unburned hydro-carbon [UHC] and indicated specific fuel consumption [ISFC] were over-predicted in the simulations. The experimental ISFC was calculated from the pressure traces from IVC to EVO. The discrepancies in emissions could be due to cylinder-to-cylinder variability, and cylinder 1 was observed to be more efficient compared to the other cylinders. With increased EGR the burn-rate decreases with a corresponding rise in cycle-to-cycle combustion variation, which resulted in roughly double the UHC and CO seen in the experiments. Under-predicted combustion efficiency could also be due to variations in the injection parameters, which could also have a cylinder dependency. The behavior of the predicted NO_x emissions is confusing since it is over-predicted for the 38% EGR case, whereas it is under-

predicted for the 43% EGR case. But overall, the numerical prediction shows less NO_x and more CO, UHC and ISFC with an increase in EGR, which is consistent with the experiments.

Table 5.4: Performance comparison between experiments and simulations at 2 bar BMEP load points

	P_Intake [bar]	P_IVC [bar]	T_Intake [C]	T_IVC [C]	Specific NOx [g/kW-hr]	Specific HC [g/kW-hr]	Specific CO [g/kW-hr]	η_Comb	ISFC [g/kW-hr]
Exp - 38% EGR	1.05	-	81.40	-	0.23	5.70	6.22	0.98	193.093
Sim	-	1.07	-	117.00	1.53	11.83	11.90	0.94	203.175
Exp - 43% EGR	1.04	-	74.17	-	0.09	10.30	11.39	0.96	210.420
Sim	-	1.06	-	102.00	0.08	36.92	27.50	0.83	224.5

The predicted in-cylinder fuel and temperature distributions are shown in Figure 5.6 for the two different EGR cases. To understand the in-cylinder behavior one should note the fuel splits in the two different EGR cases, as listed in Table 5.3. The plots explain how the EGR distribution changes the global equivalence ratio and the burn rate, resulting in a delayed heat release and reduced NO_x. Note the variation in the distribution range listed in the legend column of Figure 5.6. Even though more than 70% of the fuel was injected by -15 deg ATDC for case-b, the temperature contours indicate lower in-cylinder temperatures in comparison to case-a, where only 18% of the fuel was injected. This is likely due to the fuel vaporization cooling, as well as the EGR cooling effect. At 4 deg ATDC, when almost 64% of the fuel was injected for case-a, a locally rich region can be observed in the cylinder bowl which, with the help of the third injection, initiated the combustion process. On the other hand, a locally rich near-wall region at 4 deg ATDC for case-b indicates that there might be higher wall heat transfer losses, and when the mixture preparation was rich enough in the cylinder bowl, it helped elevate the heat release. The late combustion and lower in-cylinder temperature distribution helped to lower the NO_x formation for case-b, as can be observed in the NO_x distribution contours at 10 deg ATDC and 25 deg ATDC in Figure 5.6, compared to case-a. The UHC can be seen mostly in the cylinder crevice region, which indicates

the necessity of using a realistic crevice flow model. The CO images indicate that it is found in the near-nozzle and squish regions. More CO is observed in case-b mainly due to the lower in-cylinder temperatures.

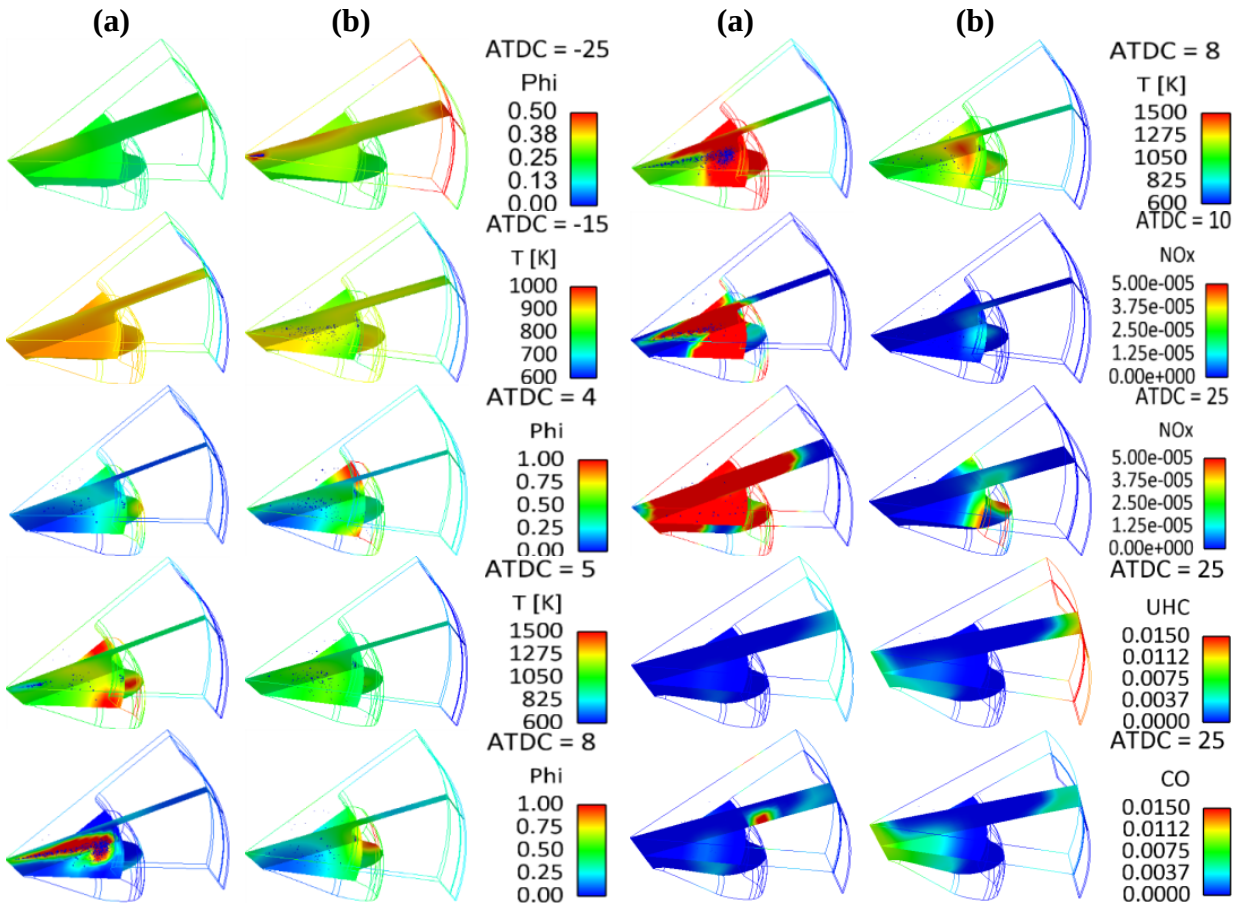

Figure 5.6: Equivalence ratio [Phi], Temperature, NO_x, CO and UHC contours for 2 bar BMEP (a) 38% EGR and (b) 43% EGR

5.1.3.1 Cylinder-to-Cylinder Variability Effect for a Combusting Case

Figure 5.7 illustrates the cylinder-to-cylinder variations for the combusting case. The 38% EGR experimental data is considered for this study. The parameters that needed to be altered to capture the experimental cylinder-to-cylinder variation were the temperatures and pressures at IVC, the fuel splits and start of injection timings, which are summarized in Table 5.5. The

difference in CR, charge mass and fuel intake of the cylinders could possibly be the reasons behind the required changes in operating conditions.

Table 5.5: Operating conditions for 2 bar BMEP 38%EGR case used in model predictions to account for cylinder-to-cylinder variation

Cylinder No	P_IVC [bar]	T_IVC [K]	Injected Fuel Frac 1st/2nd/3rd	Injection Timing [ATDC] 1st/2nd/3rd
1	1.07	390	0.184 / 0.458 / 0.358	-62.88 / -14 / 3.748
2	1.04	390	0.184 / 0.475 / 0.341	-62.88 / -20 / 0.000
3	1.07	390	0.184 / 0.458 / 0.358	-62.88 / -14 / 0.000
4	1.08	410	0.184 / 0.458 / 0.358	-62.88 / -14 / 3.748

It can be observed from Figure 5.7 that the combustion phasings were well-captured by the simulations for cylinders 1, 3 and 4. However, the computational results for cylinder 2 had a longer ignition delay and an over-predicted peak pressure, even after the advancement of the second pulse timing and amount compared to the other cylinders. The IVC pressure needed to be lowered for cylinder 2 because of the lower CR compared to cylinders 1 and 3. However, the IVC pressure and temperature were both increased for cylinder 4 to capture the experimental pressure trace while it had the lowest CR. The injection characteristics for cylinder 4 were kept the same as in cylinder 1.

While conducting the experiments in the test-lab it was observed that combustion instabilities were mostly caused by cylinder 4, which was very difficult to ignite. Its lower CR, combined with a possible leakage problem, made this cylinder's combustion behavior extremely unstable. To maintain the load, cylinder 4 always needed more fuel compared to the other cylinders. As the simulations considered the same amount of fuel for all the cylinders, enough oxygen and in-cylinder temperature were required to produce comparable engine-out work as in the experiment. This is the reason behind the increased boost and temperature in the simulations. Instead of changing the temperature, similar combustion could also be achieved by lowering the EGR, which is depicted in Figure 5.8.

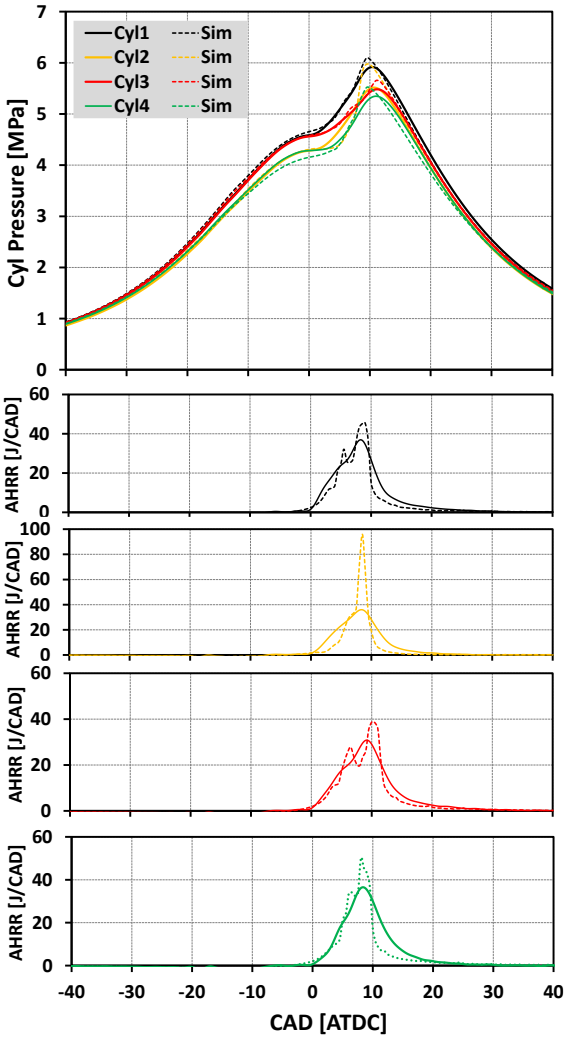

Figure 5.7: Cylinder to cylinder variation of pressure and heat release traces for 2 bar BMEP 38% EGR case

5.1.3.2 Effect of Boundary Conditions on Combustion

Three simulated cases for cylinder 4 are shown in Figure 5.8. The IVC conditions for these cases are given in Table 5.6, while keeping the injection variables the same as indicated in Table 5.5. Case-A shows that maintaining the IVC pressure and temperature conditions the same as in cylinders 1 and 3 results in misfire, which is due to the low CR and the leakage effects mentioned earlier. In Case-B the IVC pressure and temperature were increased to achieve reasonable in-cylinder combustion. Similar behavior could also be attained by reducing the EGR ratio without changing the IVC pressure and temperature, as represented in Case-C. Table 5.6 illustrates that

increasing the IVC pressure raised the oxygen [O_2] concentration, which compensates for the increased temperature. Thus, there is not much difference in the O_2 concentrations between Case-A and Case-B. Using the same EGR ratio did not change the carbon dioxide [CO_2] concentration and the global equivalence ratio much either for these two cases. This suggests that the reason behind the misfire of Case-A was the cold in-cylinder temperature. On the other hand, considering Case-B as the base case, reduced EGR ratio increased the O_2 concentration by ~13% and lowered the CO_2 concentration by ~54%, both of which helped in combustion in Case-C. As the global equivalence ratio depends on the CO_2 concentration, which again depends on EGR ratio, a lower global equivalence ratio is observed in Case-C.

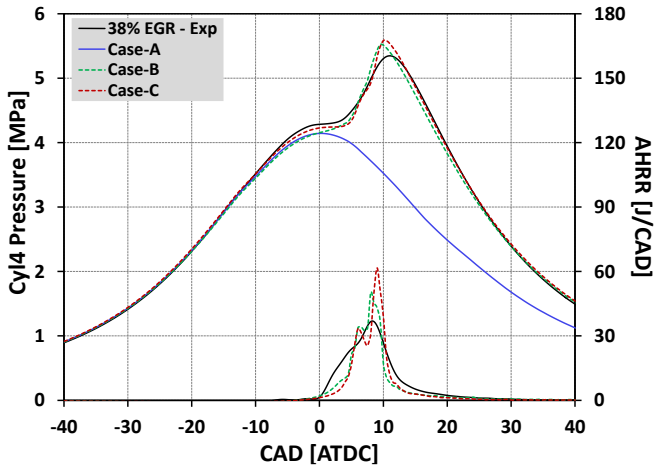

Figure 5.8: Pressure and heat-release comparisons for cylinder 4 (A) by increasing the IVC temperature and (B) by lowering the EGR amount, as listed in Table 5.6

Table 5.6: IVC conditions for three simulated cases for cylinder 4 in Figure 5.8

Cases	EGR %	P_IVC	T_IVC	O2 molefrac	CO2 molefrac	Global Eq. Ratio
A	38	1.07	390	0.17	0.0237	0.467
B	38	1.08	410	0.168	0.0247	0.487
C	22	1.07	390	0.192	0.0109	0.368

5.1.3.3 Fuel Effects on In-Cylinder Combustion

While the above results indicate that there is already enough complexity in a multi-cylinder engine, accounting for fuel effects to it makes the engine operation even more challenging. As

mentioned earlier, the gasoline fuels considered in this study were approximated as PRF fuels, where the PRF numbers are equivalent to the Pump Octane Numbers [PON], and the simulations were conducted by changing the PRF number to examine its effect.

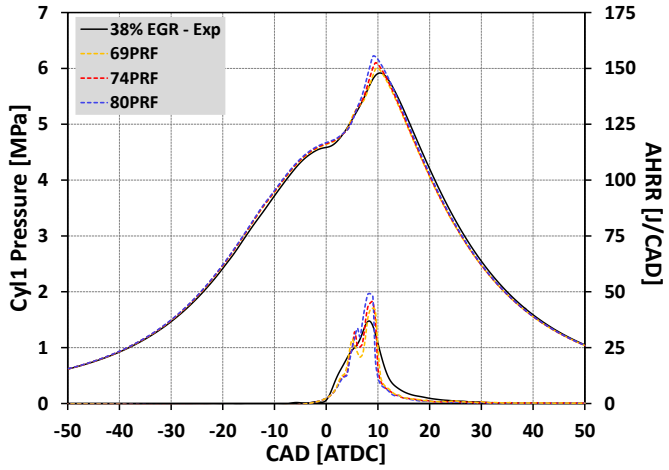

Figure 5.9: Effect of different PRF number fuels on in-cylinder pressure and heat release traces

The effect of PRF number on cylinder pressure and heat release traces is demonstrated in Figure 5.9. Three different PRF fuels considered were 69, 74 and 80 PRF. The operating conditions for 74 PRF fuel in cylinder 1 are the same as mentioned in Table 5.5, whereas, 69 PRF fuel required more EGR and 80 PRF fuel required less EGR to capture the combustion phasing of the experimental pressure trace, as summarized in Table 5.7.

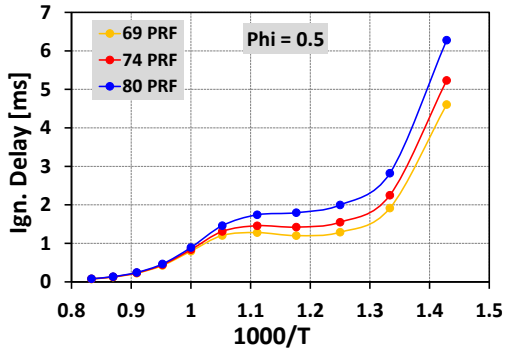

Figure 5.10: Effect of PRF on constant volume ignition delay at 40 bar pressure and phi=0.5

To help understand the results a constant volume ignition delay study was performed using the zero dimensional Chemkin chemistry solver to study the effect of PRF number on ignition

delay, as shown in Figure 5.10. Considering that ignition occurred close to 40 bar pressure at a global phi of ~0.5 for the 38% EGR case in the 2 bar BMEP experiment, the constant volume calculations were performed with these conditions. Figure 5.10 indicates that at a constant pressure, the higher PRF fuel delays the ignition significantly in the low temperature regime, whereas, the difference is almost negligible at high temperatures, beyond ~1000K. To compensate for this ignition delay difference, the EGR ratio needed to be increased for the most reactive 69 PRF fuel and had to be reduced for the least reactive 80 PRF fuel. The 38% EGR case with 74 PRF fuel was considered to be the baseline case here. With an increase in EGR from 38% to 43% the O_2 concentration decreased by ~5% and the CO_2 concentration increased by 20%, both of which helped in maintaining the combustion phasing the same as the 74 PRF fuel. On the other hand, a 7% increase in O_2 concentration from the baseline case along with a reduction of CO_2 by ~29% helped to improve the ignition delay for the 80 PRF fuel, resulting in similar combustion phasing as the baseline case.

The performance comparison in Table 5.7 illustrates that 80 PRF fuel provided somewhat better ISFC compared to the 74 PRF fuel at the expense of more NO_x due to the lower EGR usage. On the other hand, more EGR produced less NO_x for the 69 PRF fuel with a small expense of increased CO and UHC. Soot remained very low for all the cases.

Table 5.7: Boundary conditions and performance comparisons among engine simulations using three different PRF fuels

	69PRF	**74PRF**	**80PRF**
EGR %	43	38	30
O2 Molefrac	0.161	0.17	0.182
CO2 Molefrac	0.029	0.024	0.017
Global Eq. Ratio	0.513	0.467	0.413
Soot @ EVO [g/kW-hr]	0.004	0.003	0.002
NOx @ EVO [g/kW-hr]	0.945	1.533	2.698
CO @ EVO [g/kW-hr]	12.305	11.864	11.424
UHC @ EVO [g/kW-hr]	11.943	11.828	11.218
ISFC [g/kW-hr]	203.713	203.175	201.772
Combustion Effi. [%]	93.515	93.617	93.855

The present 2 bar load study with 74 PRF fuel reveals the complexity of the combustion process in a multi-cylinder engine. The effect of cycle-to-cycle variation, cylinder-to-cylinder variation and the importance of the injection timings and amounts, and the fuel chemistry were addressed. Two different EGR strategies were examined in order to control emissions. Even though the simulations were able to capture the experimental emission trends, the over-prediction of CO and UHC also suggests that the details of the piston-liner crevice model are important.

5.1.4 5 bar BMEP Load Condition Study using 75 RON/74 PRF Gasoline

Using 74 PRF fuel, three different 5 bar BMEP cases were explored with variations of EGR in order to control emissions. ~14.9 mg/cyc of the fuel was introduced to maintain the load. The experiments showed that with the increase in EGR, both NO_x and hydrocarbon emissions could be controlled with small changes in the injection strategy, but at the expense of increased soot. Table 5.8 indicates the IVC conditions, fuel splits and start of injection timings for the three different EGR ratios – 3%, 11% and 27%, respectively.

Table 5.8: IVC conditions and injection strategies for 74 PRF 5 bar BMEP load

% EGR	P_IVC [bar]	T_IVC [K]	Injected Fuel Frac 1st/2nd/3rd	Injection Timing [ATDC] 1st/2nd/3rd
3	1.3	370	0.129 / 0.250 / 0.621	-82 / -22 / 8
11	1.3	370	0.195 / 0.250 / 0.555	-84.44 / -25 / 6
27	1.3	390	0.168 / 0.270 / 0.562	-86.87 / -28/ 3

Figure 5.11 shows the experimental pressure and heat release comparisons with the predictions. Interestingly, a slight ignition advancement can be observed in the experiments with the increase in EGR, which is due to the small advancement of the injection timings, as well as from changes in the injected fuel fractions. These low load conditions were observed to be extremely sensitive to small changes in fuel fraction, which will be discussed later in this section.

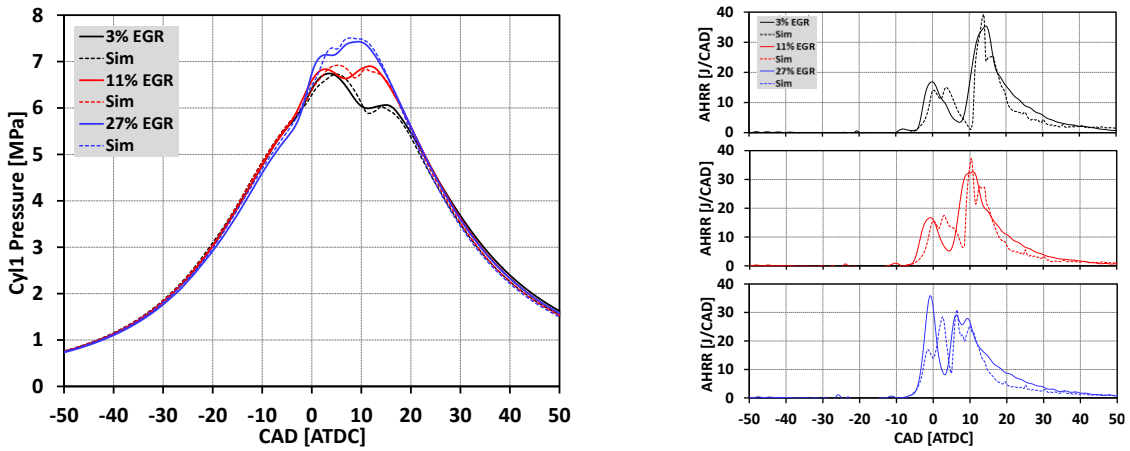

(a) (b)

Figure 5.11: Experimental and predicted (a) pressure and (b) heat release comparisons for 74 PRF fuel at 5 bar BMEP load

To better visualize the injection strategies, the injector current and the injection velocity plots against timings are shown in Figure 5.12. It is observed that the injection timings were somewhat advanced with increased EGR in order to achieve better premixing for efficient combustion.

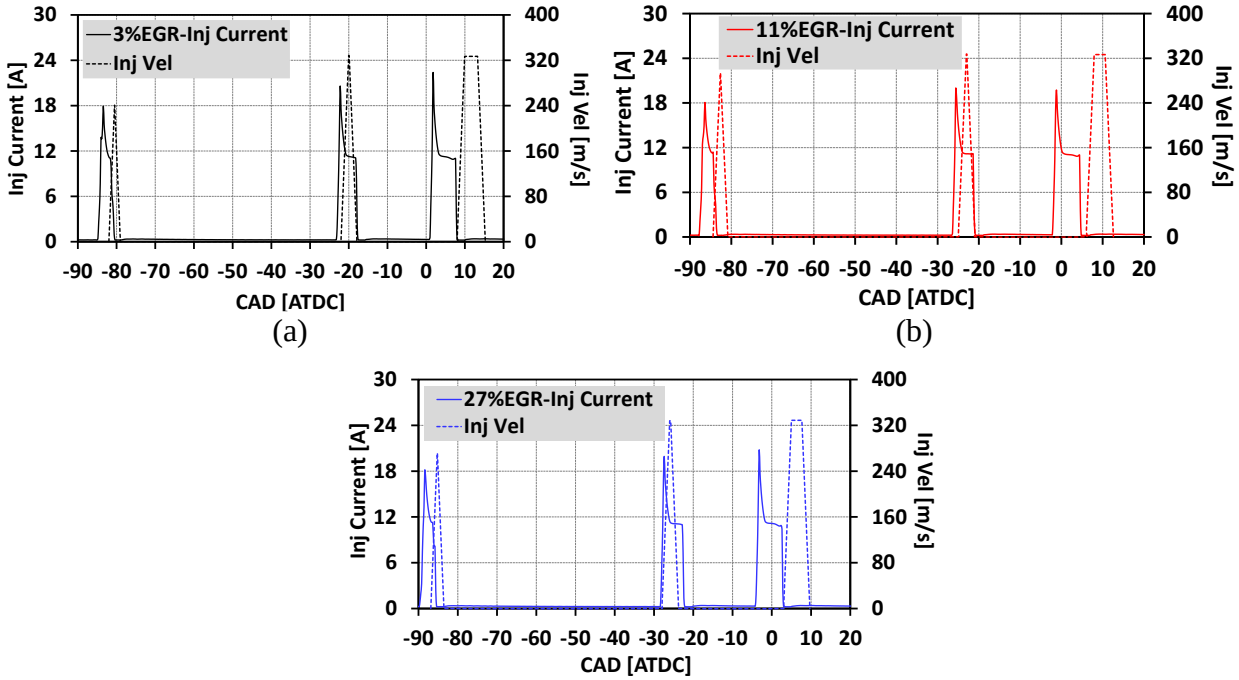

(a) (b) (c)

Figure 5.12: Experimental injector current and simulated injection velocity plots for 74 PRF fuel at 5 bar BMEP

Table 5.9 shows performance comparisons between the experiments and simulations for all three EGR cases. A decrease in NO_x can be observed with an increased EGR, as expected. However, NO_x is over-predicted in the simulations and so are UHC and CO. Even though the soot emission was small in both the experiments and simulations, both soot and NO_x were higher than the emission targets.

Table 5.9: Performance comparison between experiments and simulations for 74PRF fuel at 5 bar BMEP load

	P_Intake [bar]	T_Intake [K]	Specific NOx [g/kW-hr]	Specific UHC [g/kW-hr]	Specific CO [g/kW-hr]	FSN	Soot [g/kW-hr]	η_Comb	ISFC [g/kW-hr]
Exp - 3% EGR	1.196	34.004	0.858	1.646	1.957	0.310	-	0.991	193.419
Simulation	-	-	3.782	10.978	17.822	-	0.033	0.937	211.525
Exp - 11% EGR	1.204	43.006	0.723	1.453	1.447	0.550	-	0.992	190.863
Simulation	-	-	3.303	10.783	13.805	-	0.022	0.938	201.457
Exp - 27% EGR	1.201	76.824	0.402	1.273	0.962	2.640	-	0.993	180.651
Simulation	-	-	1.829	7.445	10.627	-	0.038	0.953	200.482

Figure 5.13 indicates the in-cylinder combustion behavior of the 5 bar BMEP load points. With ~44% fuel injected in the first two injections, case-c [27% EGR] shows a locally rich region in the cylinder bowl, which with the help of the comparatively early third injection initiated combustion. The third injection occurred at 3 deg ATDC and initiated the heat release, as can be observed from the temperature contours at 3 deg ATDC. On the other hand, with almost the same amount of fuel injected before the third injection event, case-b [11% EGR] shows a comparatively small locally high-temperature region, as indicated by the temperature contours at 0 deg ATDC. Because of the use of uncooled EGR, to increase the intake temperature in an effort to maintain the combustion phasing, the fuel burning was helped in case-c, as opposed to case-a and case-b. With ~38% fuel injection before the third pulse, case-a [3% EGR] has a comparatively low temperature at 0 deg ATDC. At 10 deg ATDC, when the injection event was almost complete for case-c, a locally hot region inside the cylinder generated the NO_x, as indicated by the NO_x contour plot at 10 deg ATDC. However, the higher EGR did not allow the temperature to increase further

in the expansion stroke and maintained the NO_x level. On the other hand, the late third pulses for case-a and case-b generated high-temperature regions, mostly in the bowl and close to the wall, generating more NO_x. Thus, more NO_x, along with more CO and UHC, can be observed for case-a and case-b compared to case-c because of the delayed third pulse and the lower intake temperature. CO is mainly observed in the cylinder bowl, which is again caused by the late third injection. UHC is observed in both the cylinder bowl and the liner regions, which indicates that the late third injection might have caused UHC generation in the cylinder bowl, whereas the cylinder crevice might contribute as well. With almost the same amount of third pulse fuel and a lower EGR, higher NO_x, CO and UHC for case-b seems unlikely. But, the difference in fuel splits and SOI timings are important, as discussed next.

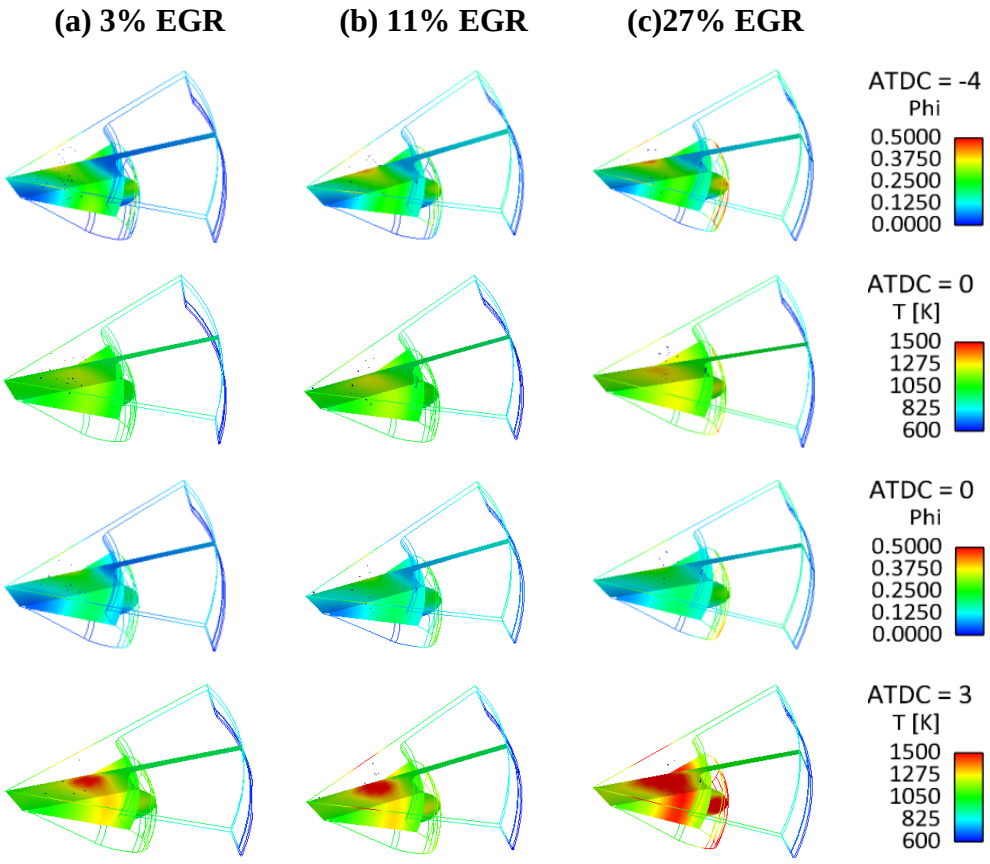

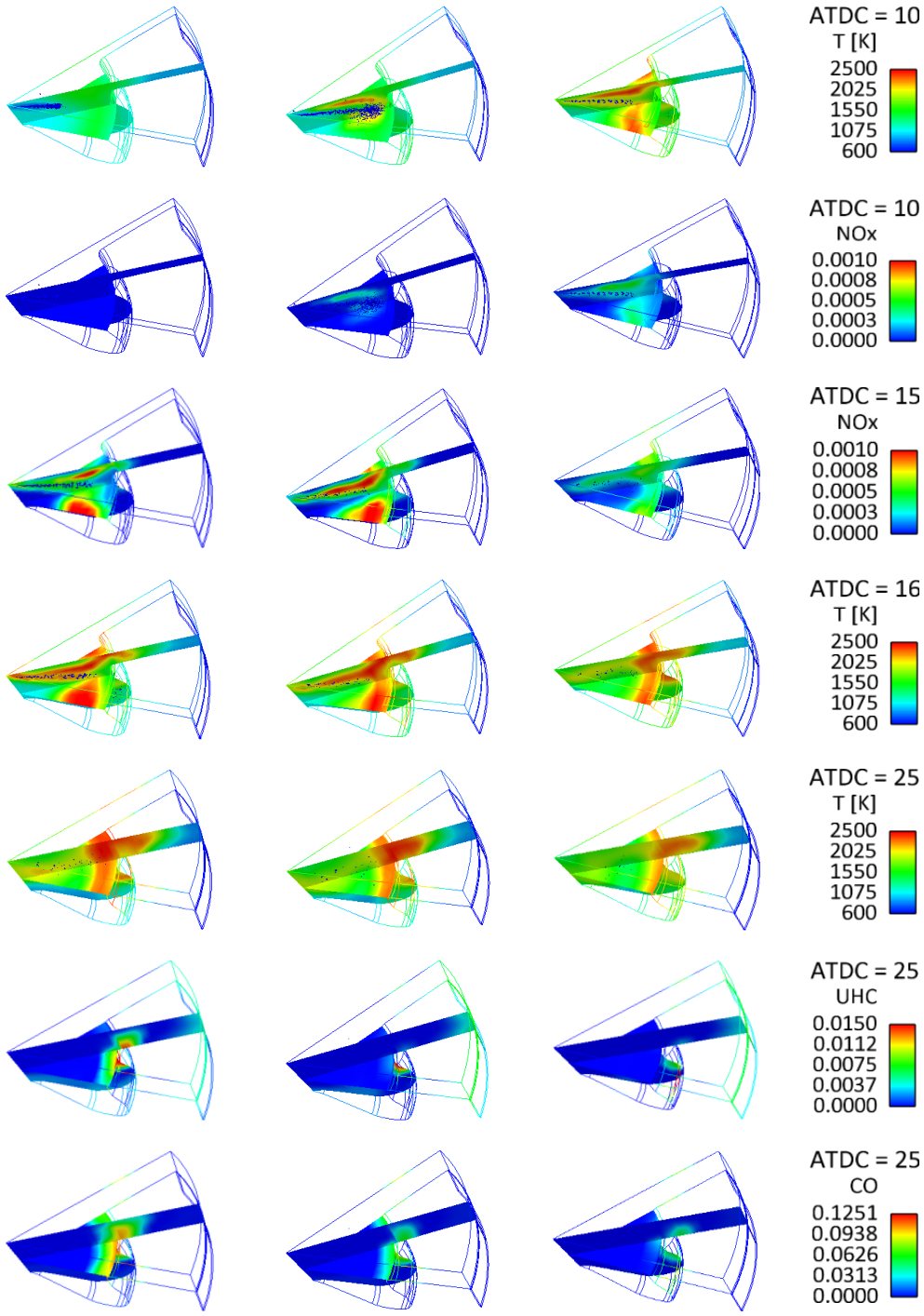

Figure 5.13: Equivalence ratio [Phi], temperature, NO_x, CO and UHC contours for 74 PRF fuel at 5 bar BMEP (a) 3% EGR (b) 11% EGR and (c) 27% EGR

5.1.4.1 Sensitivity to Injection Parameters

Three different 3% EGR cases were considered with different injection amounts and timings to assess the sensitivity of the results. When using the fuel splits measured by the Bosch bench, if the first fuel split was changed, the second and third fuel split ratio was kept the same as the measured one, and a similar procedure was followed for the second and the third fuel split changes. Following the fuel split sweep, a timing sweep was also computed to investigate combustion behavior.

The SOI timings and fuel splits for the three cases chosen in this study are mentioned in Table 5.10. Note that cases of Table 5.10 are different from those of Table 5.6. Figure 5.14 illustrates pressure, heat release and injection velocity traces for all three cases. Two important conclusions were noted. First, between Case-B and Case-C, even though almost ~45% of the fuel was injected in the first two pulses, the second pulse played a very important role to change the combustion behavior. Note that the injection timings are same between the two cases. A similar phenomenon was observed by Adhikary *et al.* [2012] for the triple-injection case in a light-duty single-cylinder engine operated at ~16 bar load. In the present case ~2.5mg of fuel difference is used in the second pulse, which is a small amount when compared to the total fuel injection of ~15mg. Second, between Case-A and Case-B, the sum of the fuel in the first two pulses is ~38% versus ~45%. As pointed out before, a small change in the second pulse fueling makes a significant difference in combustion behavior. But here the combustion characteristics are somewhat similar between the two cases before the start of the third pulse. This can be attributed to the change of second pulse timing in Case-A. As can be seen, only a difference of 2 deg in the second pulse timing had a significant impact on ignition. The ensight images in Figure 5.15 are helpful to understand this phenomenon better.

Table 5.10: Fuel fractions and SOI timings for 5 bar 3% EGR simulations using 74 PRF fuel

Cases	Injected Fuel Frac 1st/2nd/3rd	Injection Timing [ATDC] 1st/2nd/3rd
A	0.129 / 0.250 / 0.621	-82 / -22 / 8
B	0.260 / 0.184 / 0.556	-82 / -19.6 / 3.88
C	0.107 / 0.350 / 0.543	-82 / -19.6/ 3.88

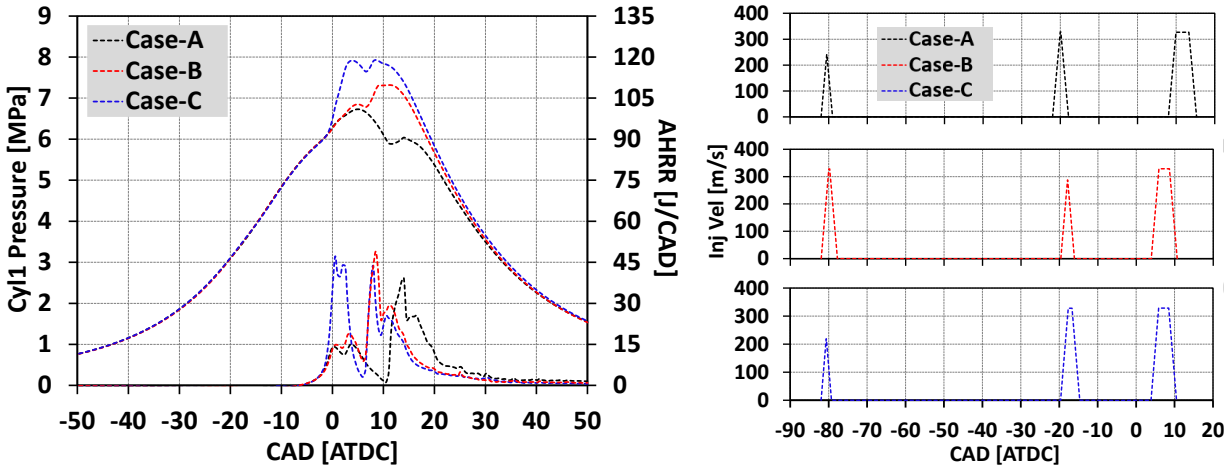

(a) (b)

Figure 5.14: Pressure, heat release and injection velocity traces for 5 bar 3% EGR simulations using 74 PRF fuel

In-cylinder temperature and equivalence ratio images shown in Figure 5.15 indicate that the ~35% of fuel injected in the second pulse of Case-C created a locally rich region in the bowl, which, with the help of the ~54% third injection elevated the heat release. On the other hand, a higher first pulse in Case-B created a locally rich mixing in the squish region, resulting in higher UHC emission. Comparison between Case-A and Case-B is interesting because the larger second pulse compared to the first pulse in Case-A is expected to show a similar phi distribution as in Case-C, even though the fuel splits are different. However, the equivalence ratio distributions at -1 deg ATDC are different. The advanced second pulse in Case-A controlled the fuel distribution in such a way that the phi distribution was similar to that of Case-B before the third injection. The UHC and CO in Case-A resulted from the very late third injection, at 8 deg ATDC. However, the

higher NO_x emissions in Case-B and Case-C are from the interaction of the combined first two pulses with the third one.

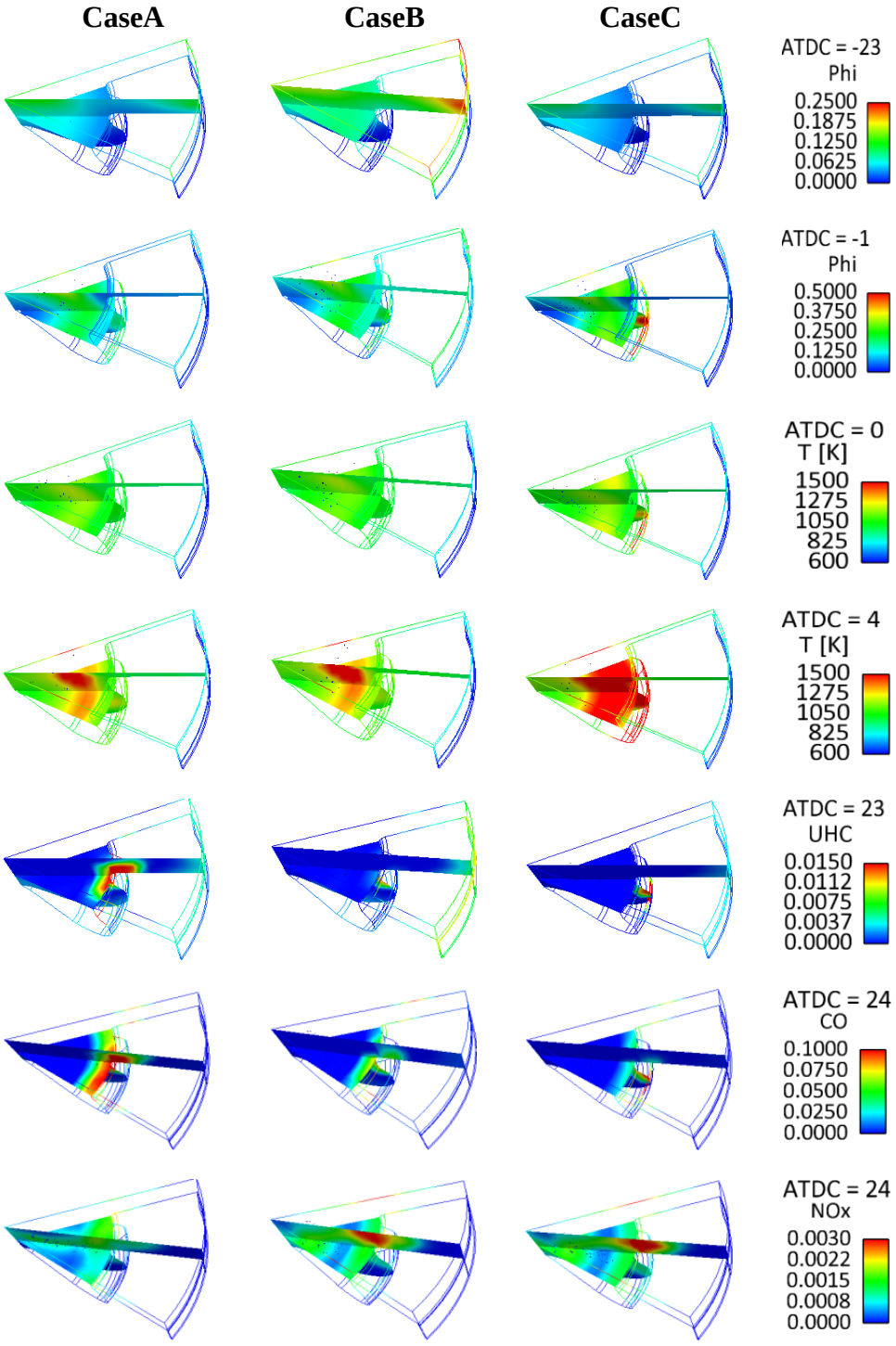

Figure 5.15: In-cylinder temperature, phi and UHC images for 5 bar 3% EGR simulations using 74PRF fuel

5.1.4.2 Effect of Third Pulse Timing on Soot

The 27% EGR case was considered to study the effect of third pulse timing on soot evolution. Even though one of the primary intentions of the experiments was to study this phenomenon, due to multi-cylinder engine controllability issues, it was not possible to conduct those experiments.

Figure 5.16 shows in-cylinder pressure, heat-release and the injection velocity plots for three different cases. Case-1 represents the numerical simulation for 27% EGR, also shown earlier in Figure 5.11. The injection splits and the timings for this case are listed in Table 5.8. Maintaining all other operating conditions the same as in Case-1, the only difference among the three cases is the third pulse timing, which is 3 deg ATDC for Case-1, -5 deg ATDC for Case-2 and -10 deg ATDC for Case-3. Quite predictably, the PPRR increased with the advancement of the third pulse timing, as seen in Figure 5.16.

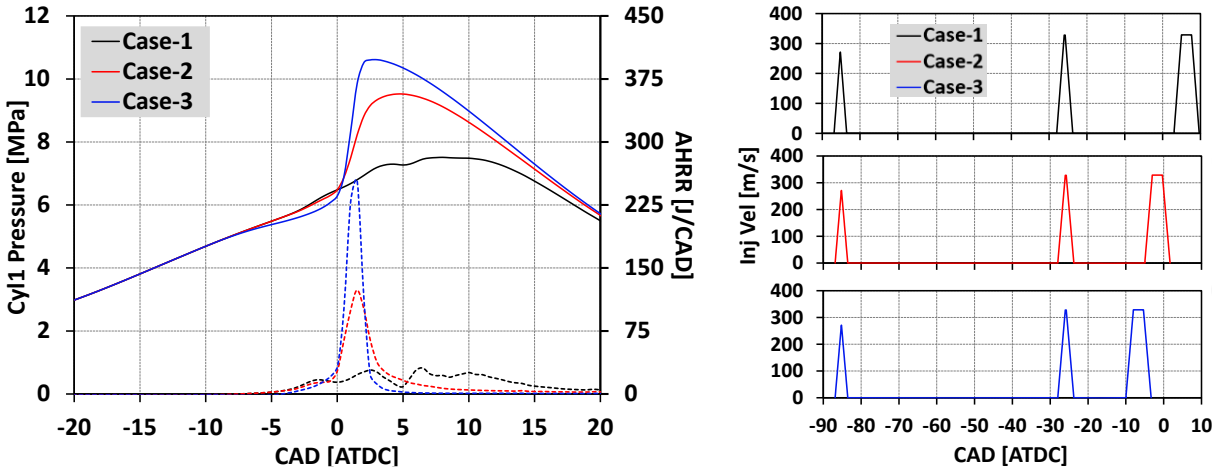

(a) (b)

Figure 5.16: In-cylinder (a) pressure, heat release and (b) injection velocity traces for 5 bar 27% EGR simulations using 74 PRF fuel with third pulse timings of 3, -5 and -10 deg ATDC for cases 1, 2 and 3, respectively

Table 5.11 presents performance comparisons for the three cases. Lower soot is predicted with the advancement of third pulse timings, but at the expense of increased NO_x. Reduction of CO and UHC were caused by the advanced third injection timings, as expected. The plots in Figure 5.18 explain the reasons behind the emission trends.

Table 5.11: Performance comparisons among Case-1, Case-2 and Case-3

	Case-1	**Case-2**	**Case-3**
3rd Injection Timing [deg ATDC]	3	-5	-10
Soot @ EVO [g/kW-hr]	0.0380	0.0061	0.0003
NOx @ EVO [g/kW-hr]	1.829	4.568	8.147
CO @ EVO [g/kW-hr]	10.627	7.756	5.652
UHC @ EVO [g/kW-hr]	7.445	5.876	4.298
ISFC [g/kW-hr]	200.482	193.294	192.076
Combustion Effi.	0.953	0.962	0.972

As indicated in Figure 5.16, the heat release started early for Case-1 compared to the other two cases. This is due to the earlier third injection in Case-2 and Case-3, which provided a vaporization cooling effect and delayed the ignition. This can also be observed from the temperature contour plots in Figure 5.17 at -1 deg ATDC. Soot precursor, acetylene [C_2H_2] contour plots are shown at 3 deg ATDC and 9 deg ATDC. According to the two-step soot model, insufficient C_2H_2 oxidation is the primary cause of soot formation. Introducing the third pulse at -10 deg ATDC ended the injection event almost at the onset of heat release, providing the necessary temperature and oxygen conditions for C_2H_2 oxidation to take place in Case-3, resulting in negligible soot at EVO. Third pulse injection at -5 deg ATDC for Case-2 allowed some of the fuel to be injected during the heat release, into a hotter environment. But, part of the oxygen was already used by that time, as indicated by the O_2 contour plot at 3 deg ATDC. For this reason, even though the soot amount is very low in Case-2, it is slightly higher when compared to Case-3. On the other hand, the third pulse occurred almost after the first stage of heat release in Case-1. The scarcity of oxygen and a comparatively lower in-cylinder temperature caused the maximum soot for this case. Higher in-cylinder temperatures caused the NO_x to be the maximum for Case-3, along with the lowest soot, as shown in the temperature and NO_x contours at 10 deg ATDC. UHC in crevice region is mainly caused by the very early first injection for all the cases. However, the late third injection caused more CO and UHC in the bowl region of Case-1.

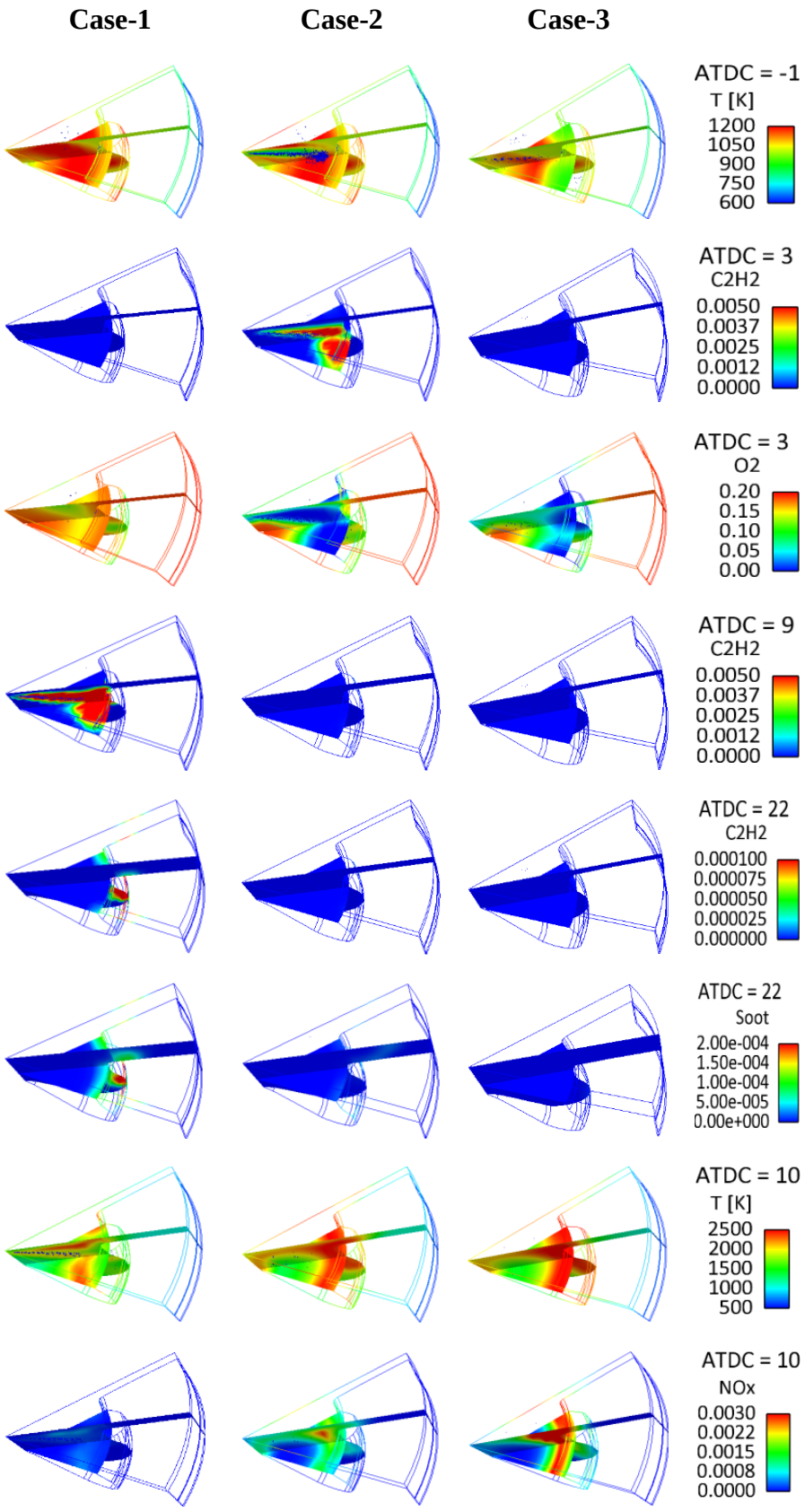
Case-1
Case-2
Case-3
ATDC = -1
T [K]
1200
1050
900
750
600
ATDC = 3
C2H2
0.0050
0.0037
0.0025
0.0012
0.0000
ATDC = 3
O2
0.20
0.15
0.10
0.05
0.00
ATDC = 9
C2H2
0.0050
0.0037
0.0025
0.0012
0.0000
ATDC = 22
C2H2
0.000100
0.000075
0.000050
0.000025
0.000000
ATDC = 22
Soot
2.00e-004
1.50e-004
1.00e-004
5.00e-005
0.00e+000
ATDC = 10
T [K]
2500
2000
1500
1000
500
ATDC = 10
NOx
0.0030
0.0022
0.0015
0.0008
0.0000

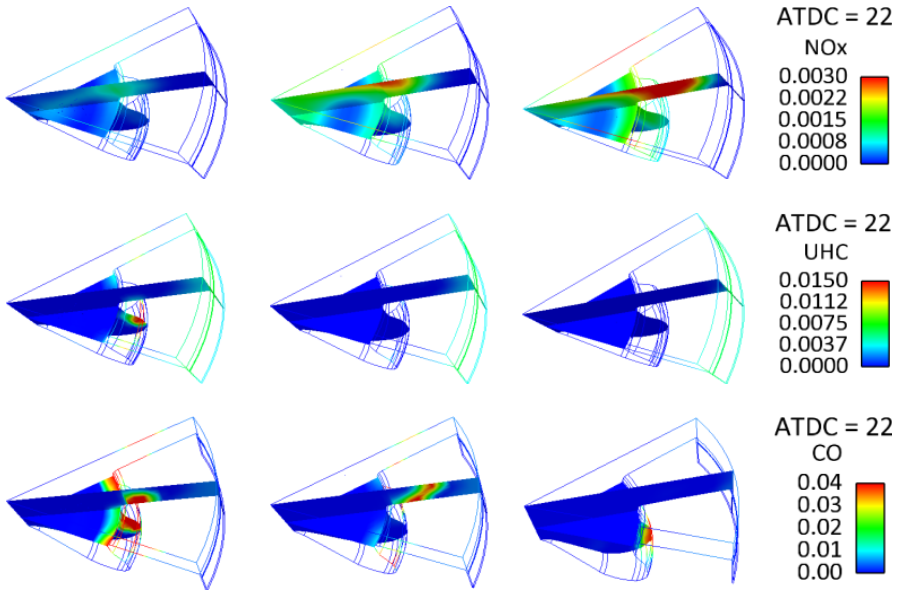

Figure 5.17: In-cylinder temperature, C_2H_2, O_2, NO_x, CO and UHC images for 5 bar 27% EGR simulations using 74PRF fuel

5.1.5 5 bar BMEP Load Condition Study Using 93 RON/87 PRF Gasoline

This section discusses the multi-cylinder engine's performance when fueled with 87 PRF gasoline at 5 bar BMEP, and the effect of injection pressure and EGR ratio were studied. The IVC pressure and temperature conditions, along with the fuel splits and SOI timings are listed in Table 5.12. Table 5.13 shows the performance results for all the cases. The 500 bar injection pressure cases will be discussed first, followed by the 600 bar injection pressures and a comparison.

Table 5.12: IVC conditions and injection strategies for 87 PRF fuel at 5 bar BMEP load

% EGR	P_IVC [bar]	T_IVC [K]	Injection Pressure [bar]	Injected Fuel Frac 1st/2nd/3rd	Injection Timing [ATDC] 1st/2nd/3rd
6	1.58	370	500	0.038 / 0.550 / 0.412	-87.00 / -62.21 / 5.00
23	1.45	380	500	0.034 / 0.550 / 0.416	-86.86 / -61.77 / 5.00
23	1.24	380	600	0.270 / 0.420/ 0.310	-86.86 / -25.02/ -1.01
29	1.23	390	600	0.352 / 0.448 / 0.200	-91.00 / -26.00/ 5.00

Table 5.13: Performance comparison between experiments and simulations for 87 PRF fuel at 5 bar BMEP load

	Injection Pressure [bar]	P_Intake [bar]	T_Intake [C]	Specific NOx [g/kW-hr]	Specific UHC [g/kW-hr]	Specific CO [g/kW-hr]	FSN	Soot [g/kW-hr]	η_ Comb	ISFC [g/kW-hr]
Exp - 6% EGR	500	1.49	61.0	1.315	9.207	4.767	0.080	-	0.961	182.138
Simulation	500	-	-	4.191	5.709	7.462	-	0.006	0.965	182.772
Exp - 23% EGR	500	1.38	71.5	0.363	7.096	3.219	0.950	-	0.971	180.700
Simulation	500	-	-	1.996	5.437	5.696	-	0.011	0.968	185.751
Exp - 23% EGR	600	1.19	68.0	0.568	1.726	1.429	0.980	-	0.990	183.580
Simulation	600	-	-	2.401	12.996	8.034	-	0.000	0.930	194.232
Exp - 29% EGR	600	1.19	90.0	0.204	1.363	1.272	0.460	-	0.990	201.618
Simulation	600	-	-	1.250	13.174	9.898	-	0.001	0.928	195.659

5.1.5.1 Validations at 500 bar Injection Pressure

Experimental and predicted pressure and heat release comparisons at 500 bar injection pressure are illustrated in Figure 5.18a at two different EGR ratios. ~17.7 mg/cyc of fuel was used to maintain the load using 87 PRF fuel. Note that the fuel amount is higher compared to the 5 bar BMEP experiments using 74 PRF fuel, which can be attributed to the auto-ignition characteristics of these fuels. Also, compared to the 74 PRF fuel injection strategy at 5 bar BMEP, a significantly early second injection timing can be observed for the 87 PRF cases in order to achieve more premixing. The injector current plots in Figure 5.18b indicate similar injection strategies for both 87 PRF cases considered here. Delayed combustion can be observed with an increase in EGR, as expected. However, the added EGR required the intake temperature to be raised by a few degrees, as mentioned in Table 5.13. To control the load at an increased temperature, the intake pressure needed to be adjusted as well. Figure 5.18a shows that the simulations were able to capture the experimental traces reasonably well.

Table 5.13 shows that with the increase in EGR, NO_x, CO and UHC reduce with improved combustion efficiency, which was observed in the 74 PRF 5 bar load cases as well. But, for the 74 PRF cases, this was due to the small change in injection strategy, whereas in this case it is the smaller intake pressure, as shown in Table 5.12. The emission trends were captured well by the

simulations, whereas the NO_x and CO were over-predicted as before. UHC was under-predicted opposite to the 74 PRF 5 bar cases.

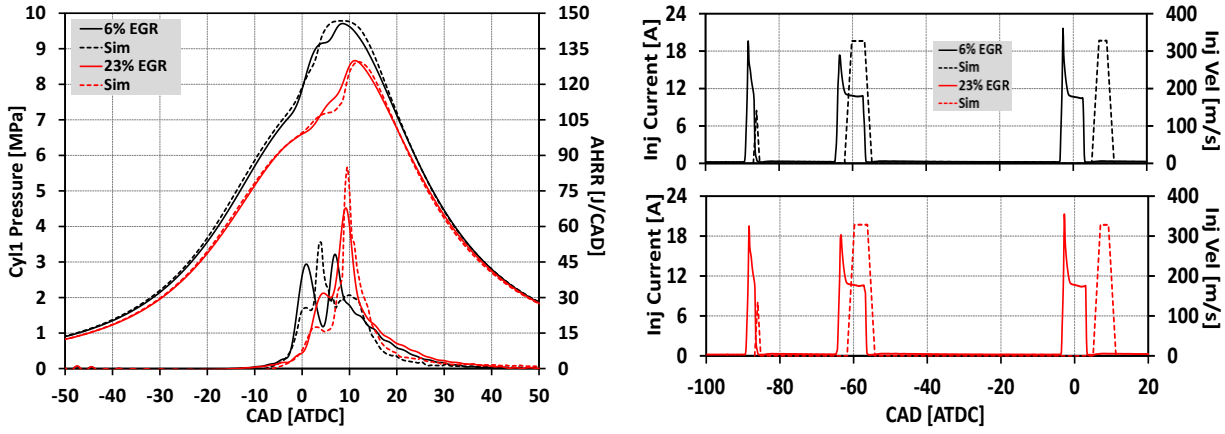

(a) (b)

Figure 5.18: (a) Experimental and predicted pressure and heat release comparisons, (b) experimental injector current and injection velocity traces at 5 bar load using 87 PRF fuel and 500 bar injection pressure

5.1.5.2 Validations at 600 bar Injection Pressure

Figure 5.19a shows the experimental and predicted pressure and heat release comparisons at 600 bar injection pressure. ~15.65 mg/cyc of injected fuel was required to maintain the load at this condition, which indicates that a lower fuel usage accompanies the use of higher injection pressures. However, the ISFC might increase when compared to the 500 bar injection pressure, depending on other operating parameters. Experimental injector current and numerical injection velocity plots are shown in Figure 5.19b. With an increase in EGR the intake temperature needed to be raised, which caused the experimental pressure and heat release traces to be the same. However, the injection splits and SOI timings were also somewhat different for these cases. The numerical pressure traces indicate delayed combustion phasing for both cases, whereas, the compression and expansion pressures are captured well. Adjusting the third pulse SOI timings could have provided better agreement, but the discrepancy in peak pressure would have increased.

The experimental performance results in Table 5.13 show that with an increase in EGR all emissions decrease including the soot, whereas there is an increase in ISFC. The simulations indicate lower NO_x with increased EGR, as expected. CO, UHC and ISFC increased with higher EGR, mainly due to the late third pulse in the high EGR case. Soot was predicted to be extremely low at the higher injection pressure, which reflects faster break-up and better premixing. Interestingly, both EGR cases indicate the same combustion phasing in the simulations, even though the third injection event ends at 3.5 deg ATDC for the 23% EGR case and for the 29% EGR case it ends at 9 deg ATDC.

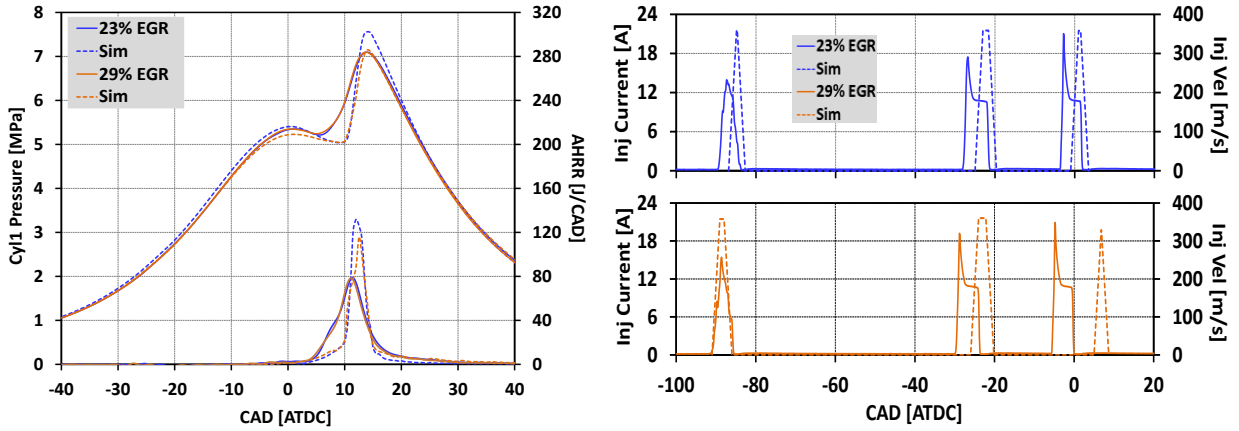

(a) (b)

Figure 5.19: (a) Experimental and predicted pressure and heat release comparisons, (b) experimental injector current and injection velocity traces at 5 bar load using 87 PRF fuel and 600 bar injection pressure

The in-cylinder temperature and fuel distribution plots in Figure 5.20 explain the reason behind achieving the same combustion phasing with different fuel splits and SOI timings, as mentioned in Table 5.12.

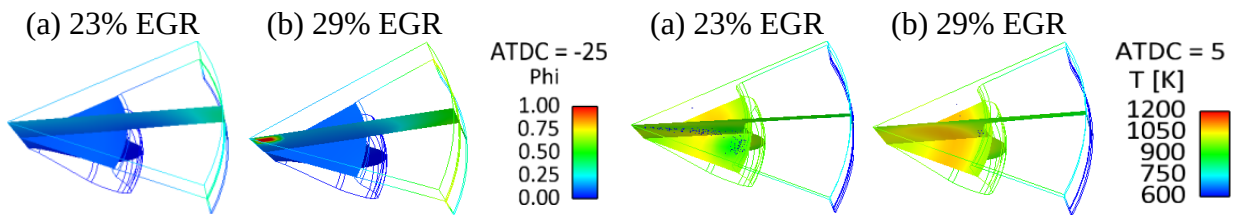

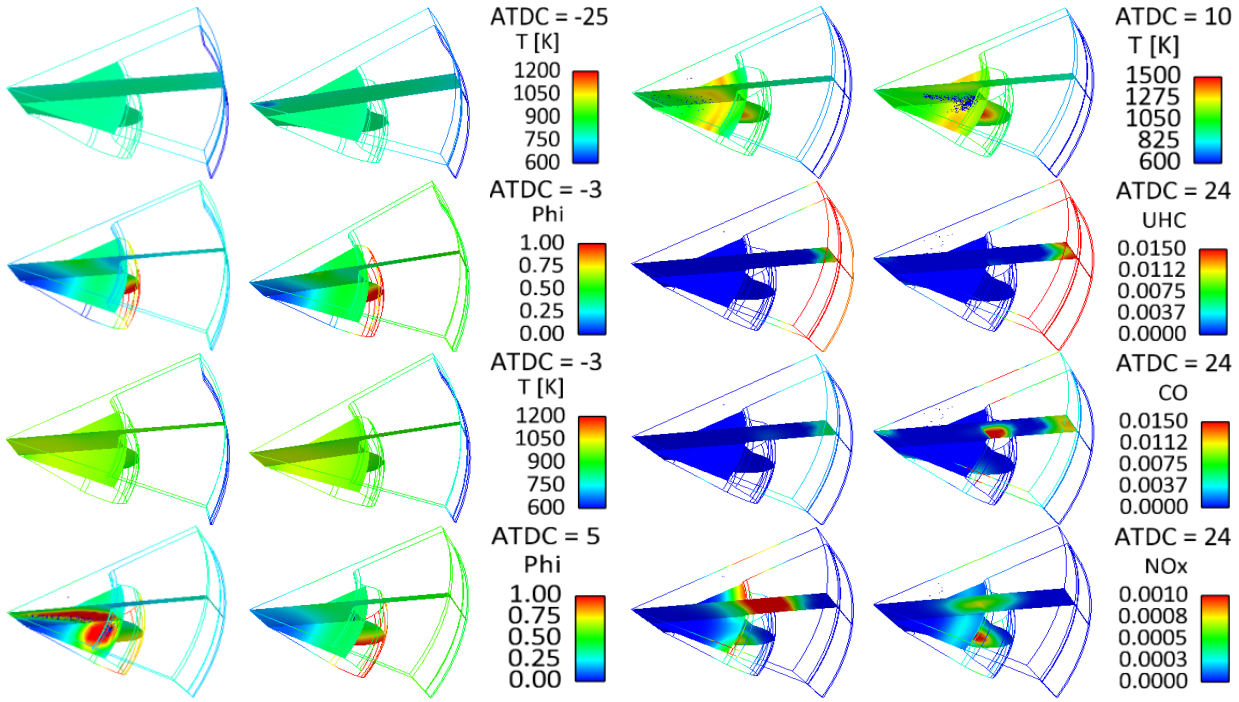

Figure 5.20: In-cylinder temperature, phi, CO, UHC and NO_x images for 87 PRF fuel at 600 bar injection pressure

With ~35% of the fuel injected in the first pulse, case-b shows a comparatively rich squish region at -25 deg ATDC, while only ~27% of the fuel was injected in case-a. The second pulse amounts and timings were somewhat similar for these two cases, which played an important role in establishing the same level of fuel stratification at -3 deg ATDC. Earlier in this chapter it was indicated that the second pulse amount and timing have a significant impact in controlling the combustion. An earlier third pulse [at -1 deg ATDC] in case-a helped to start the combustion, as shown in the temperature contours at 5 deg ATDC. But with ~31% of the fuel in the third pulse, the vaporization cooling effect along with a lower in-cylinder temperature delayed the combustion in case-a. On the other hand, with only~20% of the fuel injected at 5 deg ATDC, the higher in-cylinder temperature and lower vaporization cooling effect caused the combustion phasing of case-b to be the same as in case-a. The larger first pulse of case-b resulted in higher UHC in the crevice and the squish regions, which is observed from the UHC contours at 24 deg ATDC. CO was mainly

generated in the squish region, mostly from the delayed third pulse in case-b. NO_x in the bowl region indicates that the comparatively higher EGR helped alleviate the emissions in case-b.

5.1.5.3 Experimental Comparison between Two 5 bar BMEP Load Points Using 75 RON and 93 RON Gasoline Fuels

This section explores the required differences in intake conditions and injection strategies in the experiments when the multi-cylinder CI engine was operated at 5 bar BMEP load, using two different gasoline fuels. The experimental boundary conditions and the emission results are shown in Table 5.14.

Table 5.14: Difference in boundary conditions and engine performance between two different PRF fuels

RON	%EGR	P_Intake [bar]	T_Intake [C]	Specific NOx [g/kW-hr]	Specific HC [g/kW-hr]	Specific CO [g/kW-hr]	FSN	η_comb	ISFC [g/kW-hr]
75	3	1.196	34	0.858	1.646	1.957	0.3	0.991	193.419
93	6	1.49	61	1.315	9.207	4.767	0.1	0.961	182.138

As the experiments considered a very low level of EGR for these two cases, an effort was made to compare the difference in combustion behavior with two different gasoline fuels. Figure 5.21 illustrates the experimental pressure and heat release traces and the injector current plots for the two cases. As indicated in Table 5.1, with a lower specific gravity and a lower boiling point 75 RON gasoline ignites more easily than 93 RON fuel. Thus, to maintain the CA50, the higher RON fuel needed elevated intake pressure and temperature to have enough available oxygen and temperature for the fuel to ignite. Also the level of premixing was increased by advancing all three injections, where the second pulse advancement is the most significant one. The importance of second pulse injection timing has been stated several times in this study, since it has a significant impact in controlling the in-cylinder combustion. The performance comparison in Table 5.14 shows an increase in NO_x, CO and UHC at the experimented operating condition using 93 RON fuel, whereas soot plummets due to the increased premixing. An exact comparison between the

two fuels was not possible due to the variation of boundary conditions, and EGR ratio. However, this study shows how much impact fuel property variation can have on multi-cylinder engine operation strategy.

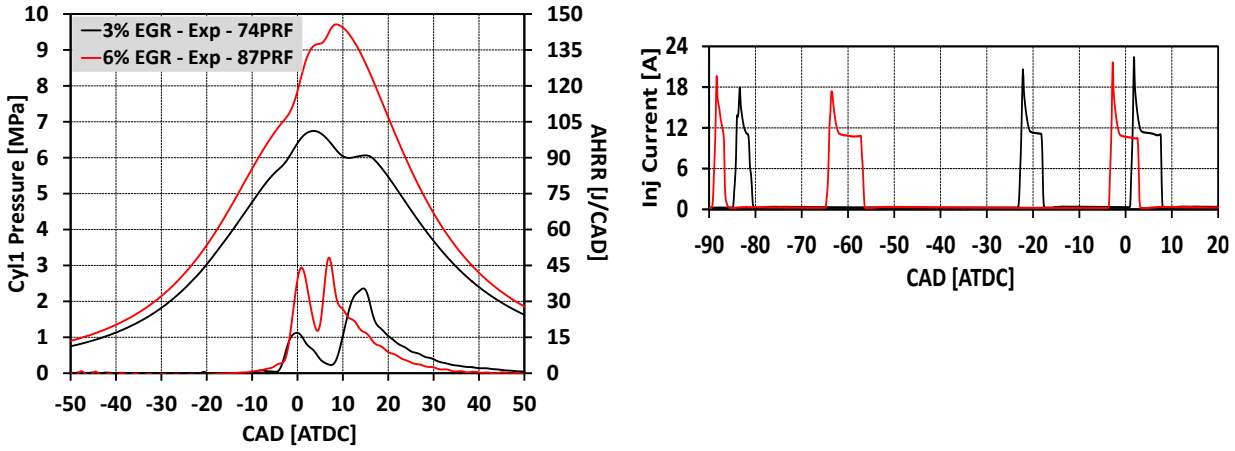

(a) (b)

Figure 5.21: (a) Experimental pressure, heat release and (b) injector current comparisons using two different PRF fuels at 5 bar BMEP load using low EGR conditions

5.1.6 Discussion

A numerical investigation was performed to understand multi-cylinder engine GDICI operation. Emphasis was provided on 2 bar and 5 bar BMEP load conditions. The following conclusions can be drawn.

a. The four cylinders of the multi-cylinder engine were found to have different effective compressive ratios, which caused a significant cylinder-to-cylinder combustion variability.

b. With the lowest compression ratio and possible leakage, cylinder 4 was the most difficult one to control.

c. Along with cylinder-to-cylinder variations, considerable cycle-to-cycle variability caused the numerical study to be even more challenging.

d. Simulations were conducted by modeling the PON of the fuel with a PRF fuel. The predictions indicated sensitivity of the results to the PRF composition. Thus, it is important to model all components of the fuel to represent the actual fuel properties. This is discussed in the next chapter.
e. UHC was predicted to be mostly from the crevice region, which was not resolved well in the simulations.
f. The emission trends were captured in the simulations. However, considering the complexity of multi-cylinder engine operation, quantitative discrepancies were noted.
g. Increased temperature and lowered EGR ratio were found to have similar effects on in-cylinder combustion.
h. Low load operation in the multi-cylinder engine was found to be very sensitive to the fuel splits and SOI timings.
i. For triple-pulse operation, an advanced third injection is effective in lowering the soot.
j. Faster fuel break-up caused by higher injection pressures required the injection strategy to be changed.
k. To maintain the combustion phasing, a higher RON fuel required a different injection strategy to introduce more premixing.

The above study indicated that it is difficult to achieve 2 bar BMEP load using 93 RON fuel. Therefore, single injection studies were conducted using the same fuel to obtain lower load. In the next section, load minimization using a single injection strategy is discussed to isolate injection effects instead of the fuel interaction effects, as seen in the multiple injection strategy study.

5.2 Load Minimization using a Single-Injection Strategy

This part of the study assesses the reactivity of 93 RON [87AKI] gasoline in the GM 1.9L 4-cylinder diesel engine to extend the low load limit via a single injection strategy. The experiments were conducted at 1500 rev/min, and the injection timing was varied from -42 to -9 deg ATDC, with a step-size of 3 deg. The minimum fueling level was defined in the experiments such that the coefficient of variance [COV] of indicated mean effective pressure [IMEP] was less than 3%. The study revealed that injection at -27 deg ATDC allowed a minimum load of 2 bar BMEP to be achieved. Also, advancement in the start-of-injection [SOI] timing in the experiments caused an earlier CA50, which became retarded with further advancement in SOI timing. To help explain these behaviors, simulations were carried out at six different SOI timings, -15, -21, -24, -27, -33 and -36 deg ATDC, respectively, to explain the CA50 trend.

5.2.1 Validation of Experimental Data

From the single injection experiments at various SOI command timings it was observed that, with the advancement of injection timing, CA50 advanced first and then retarded with further advancement. Note that with different fuel amounts the load also varied with the change in SOI command timing. To explain this behavior, six SOI data points were chosen to perform the computational analysis, which are shown in Figure 5.22. These cases are also tabulated in Table 5.15 along with the IVC temperatures, the injected fuel mass/cycle/cylinder data and the actual injection duration data, which were considered in the simulations. ‘SOI Command Timing’ in Table 5.15 indicates the time the injector current started rising in the experiments, whereas ‘Actual SOI Timing’ indicates the actual start of injection after considering the nozzle opening delay period. ‘SOI command timing’ will be indicated as ‘SOI timing’ for the present validation study.

Table 5.15: Data points considered for simulation

	IVC Temperature [K]	Injected Fuel Mass/Cycle/Cylinder [mg]	SOI Command Timing [ATDC]	Actual SOI Timing [ATDC]	Actual Inj. Duration [CAD]
Case A	376	12.0	-15	-12	10.22
Case B	366	10.2	-21	-18	9.1
Case C	368	10.2	-24	-21	9.1
Case D	362	9.8	-27	-24	8.76
Case E	356	10.2	-33	-30	9.1
Case F	362	10.4	-36	-33	9.46

The experimental pressure traces at the various SOI command timings can be observed in Figure 5.22a, whereas the heat release rates are shown in Figure 5.22b. Both the pressure and the heat release traces indicate an advanced combustion phasing with the advancement in SOI timings from -15 to -24 deg ATDC. Delayed combustion phasing can be observed from -24 to -33 deg ATDC SOI timings, which advances again at -36 deg ATDC SOI timing. In order to explain this phenomenon, simulations were performed for all the cases mentioned in Table 5.15.

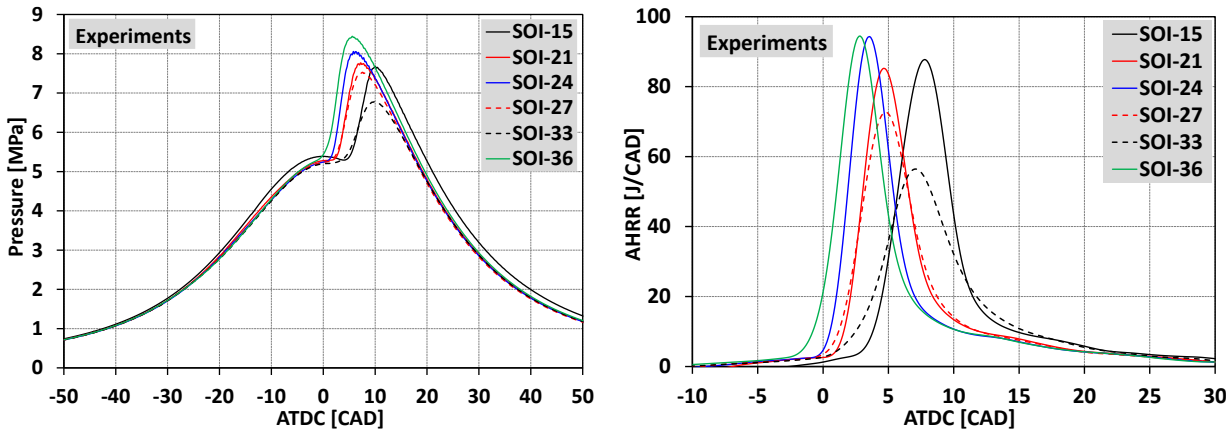

(a) (b)

Figure 5.22: Experimental (a) pressure and (b) apparent heat release traces at various injection timings

The IVC temperatures shown in Table 5.15 were obtained by trial-and-error to match the experimental pressure trace data. It is interesting to note that they are correlated with the predicted in-cylinder temperatures at EVO, as shown in Figure 5.23. Higher EVO temperature implies hotter internal residual gas in the cylinder at IVC, justifying the increase in IVC temperature as shown (the intake runner temperature was held fixed in the experiments).

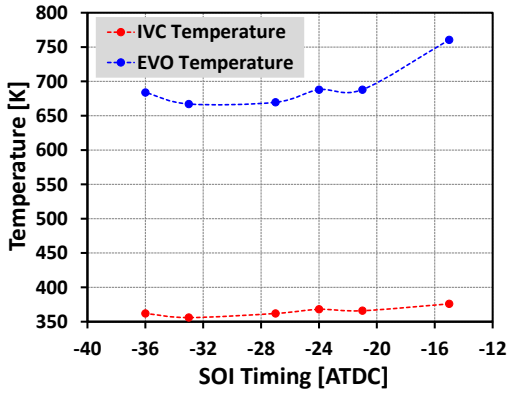

Figure 5.23: Temperatures at IVC and EVO for all the simulated data points

Figure 5.24 shows comparisons between the experimental and computational pressure and heat release traces for all the cases mentioned in Table 5.15. The injection velocity plots in Figure 5.24 indicate the actual injection timing and the injection rate shape. ~15% EGR was estimated for all the validation cases presented here. The results show reasonably good agreement between the experiments and the simulations, however, the pressure at the end of the compression stroke was slightly over-predicted and the heat release duration was under-predicted for all the cases. Over-predicted compression pressure can be partly attributed to the cool flame heat release, as shown in Figure 5.25. Though the cool flame amount in Figure 5.25 is quite low, a reduced cool flame peak and an increase in cool flame heat release duration can be observed with advancement in SOI timing, which is due to the larger mixing time available before combustion.

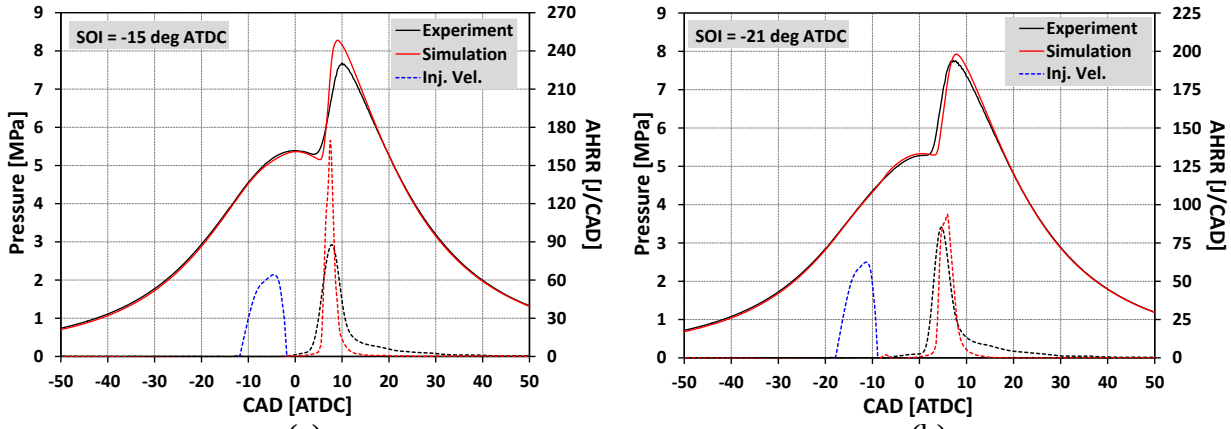

(a) (b)

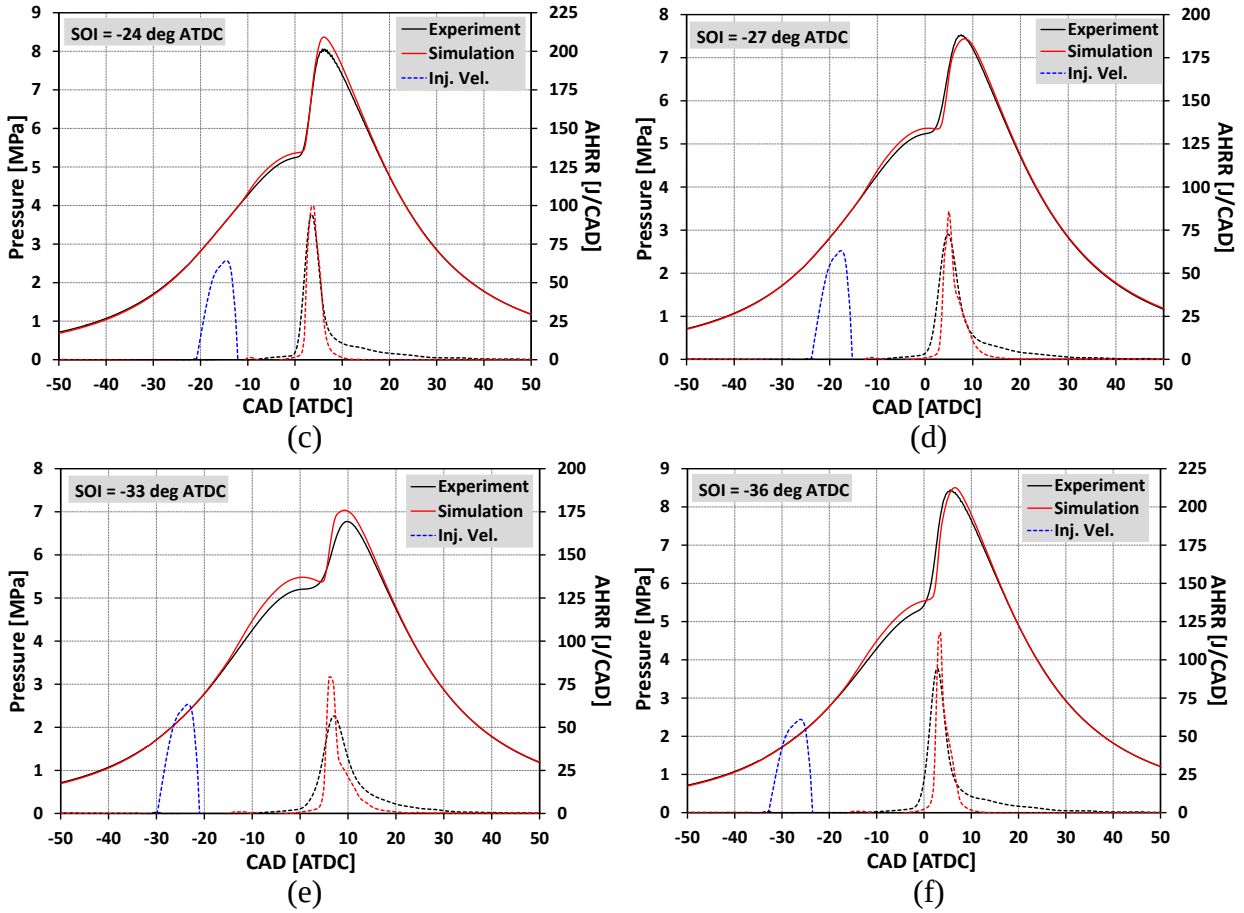

Figure 5.24: Experimental and predicted pressure and heat release comparison at SOI timings of (a) -15 deg (b) -21 deg (c) -24 deg (d) -27 deg (e) -33 deg and (f) -36 deg ATDC

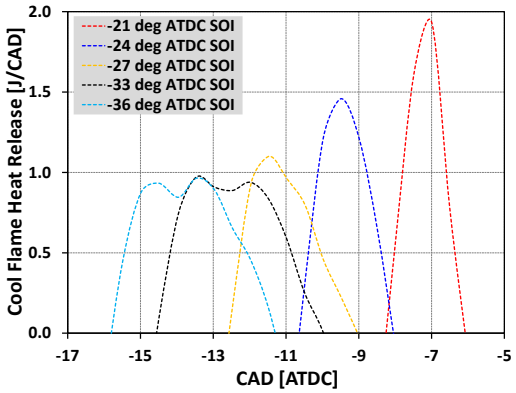

Figure 5.25: Cool flame heat release in the simulations for various SOI command timings

Performance comparisons between the experiments and simulations at the various SOI timings are shown in Figure 5.26. The CA10 and CA50 predictions agree reasonably well with the experiments, as can be observed in Figures 5.26a and 5.26b, respectively. Combustion efficiency

is under-predicted for the -33 and -27 deg ATDC SOI timings, which will be explained later in this section with the help of in-cylinder contour images. Figure 5.26d indicates an over-predicted BMEP trend at the various SOI command timings. To predict the BMEP, engine frictional loss was calculated based on the Chen-Flynn friction model using GT-Power [Gamma Technologies, 2009] simulations. NO_x, carbon-monoxide [CO] and unburned hydrocarbon [UHC] trends were well-captured in simulations, although the magnitudes were mostly over-predicted, as can be observed in Figures 5.26e, 5.26f and 5.26g, respectively. The discrepancy in emission results can be attributed to the complexity of multi-cylinder engine operation, where cylinder-to-cylinder variation along with the cyclic variability dictates the overall combustion behavior of the engine [Adhikary *et al.*, 2013].

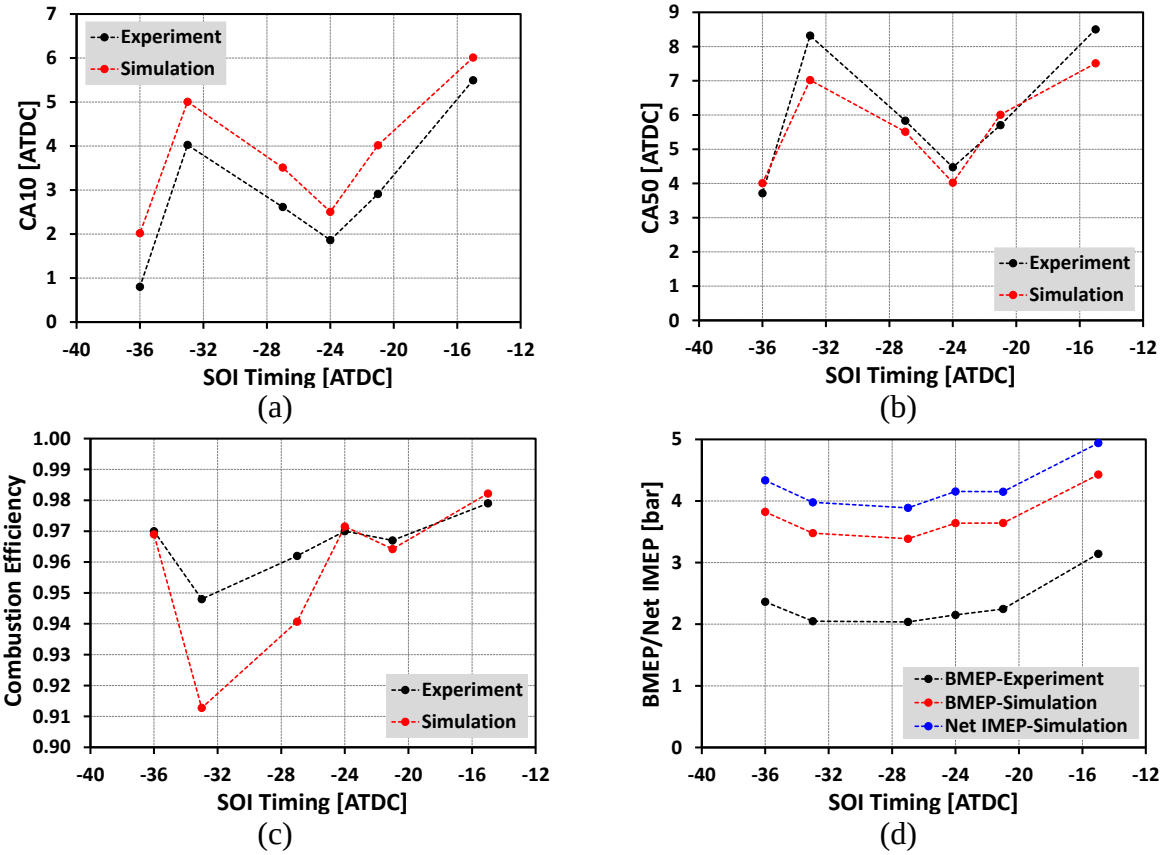

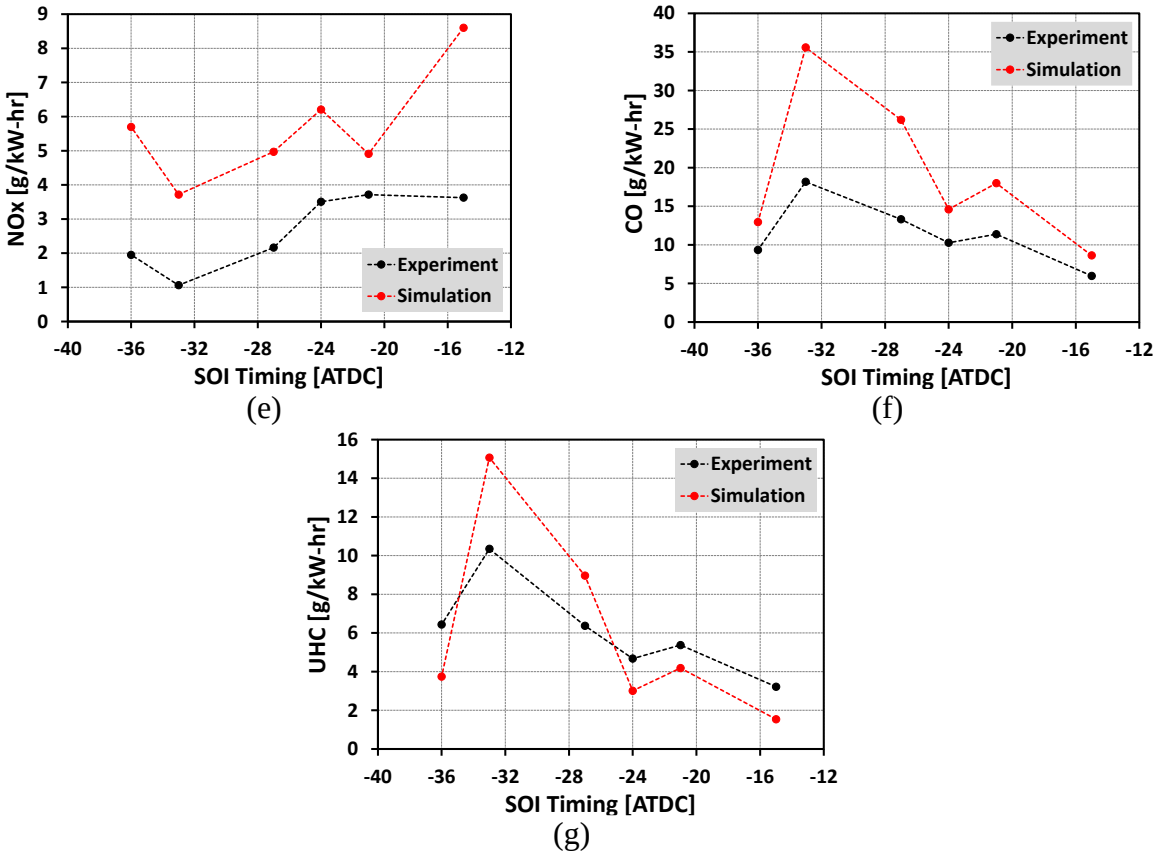

Figure 5.26: Comparisons between experimental and simulated (a) CA10 (b) CA50 (c) Combustion Efficiency (d) BMEP (e) NO_x emission (f) CO emission and (g) UHC emission

At -15 deg ATDC SOI timing [Case-A], injection ends at -1.78 deg ATDC, as can be observed in Figure 5.24a. Thus, the in-cylinder pressure and temperature was high enough to start the combustion once a sufficiently locally rich region is formed, as shown in the equivalence ratio and temperature contours in Figure 5.27. Due to the high in-cylinder temperatures, the NO_x emission is also high in this case.

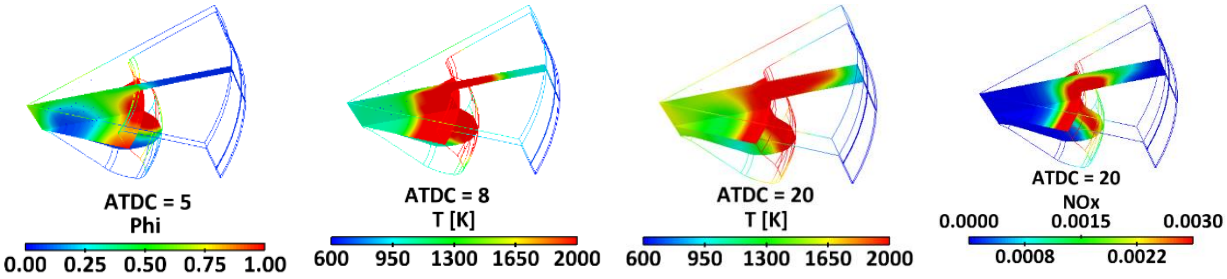

Figure 5.27: Equivalence ratio, temperature and NO_x contour plots for -15 deg ATDC SOI command timing case [Case-A]

Comparing Case-B [-21 deg ATDC SOI timing] and Case-C [-24 deg ATDC SOI timing], an advanced CA50 can be observed in Case-C, which can be attributed to the 2 degree higher IVC temperature. Figure 5.28 indicates that with the presence of a locally rich region in the bowl for both Case-B and Case-C, Case-C experienced earlier combustion, as can be observed from the temperature contours at 3 deg ATDC.

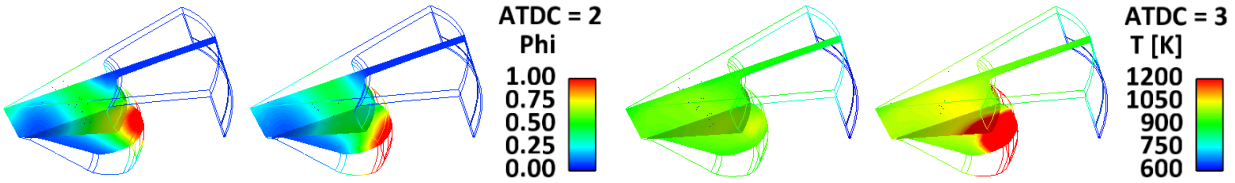

Figure 5.28: Equivalence ratio and temperature contour images for -21 [Case-B] and -24 [Case-C] deg ATDC SOI command timing

Comparing Case-C [-24 deg ATDC SOI timing] and Case-D [-27 deg ATDC SOI timing], a retarded CA50 is observed with advanced injection timing, which is due to the difference in fuel amounts and IVC temperatures. With 0.4mg more fuel and a 6 degree higher IVC temperature, Case-C shows earlier combustion compared to Case-D. Equivalence ratio contours in Figure 5.29 demonstrate that a locally rich region in the bowl is formed for both Case-C and Case-D at 2 deg ATDC, which with the help of the higher IVC temperature shows earlier combustion for Case-C. This causes higher NO_x emission in Case-C, along with lower CO emission, as indicated by the CO contour images at 20 deg ATDC.

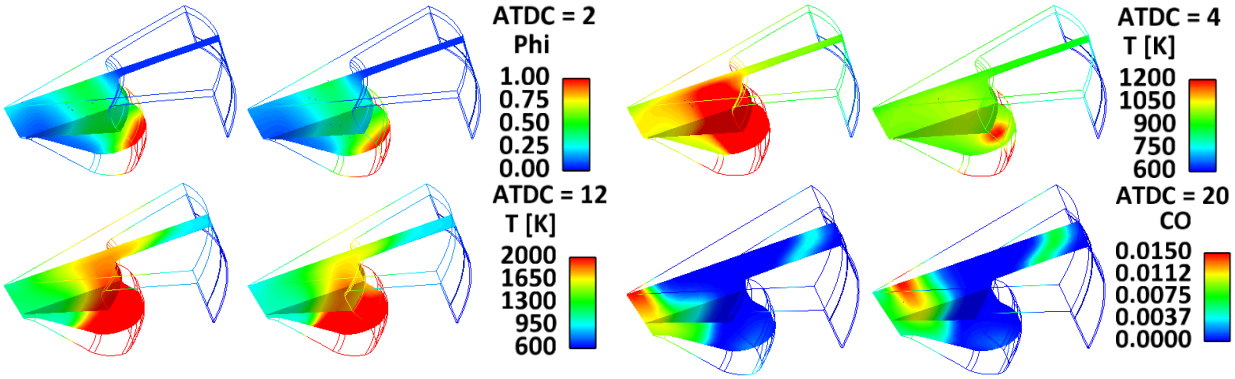

Figure 5.29: Equivalence ratio, temperature and CO contour images for -24 [Case-C] and -27 [Case-D] deg ATDC SOI command timing

CA50 comparison between Case-D [-27 deg ATDC SOI iming] and Case-E [-33 deg ATDC SOI timing] indicates late combustion in Case-E due to the 6 degree lower IVC temperature compared to Case-D. With a 0.4 mg higher fuel amount, the late combustion phasing in Case-D highlights that low load operation is very sensitive to the IVC temperature. With an almost similar equivalence ratio distribution at 2 deg ATDC, the combustion starts earlier for Case-D, as demonstrated in Figure 5.30. The wider high temperature region in Case-D at 10 deg ATDC resulted in higher NO_x and lower UHC and CO emissions, as seen in the CO contour at 20 deg ATDC.

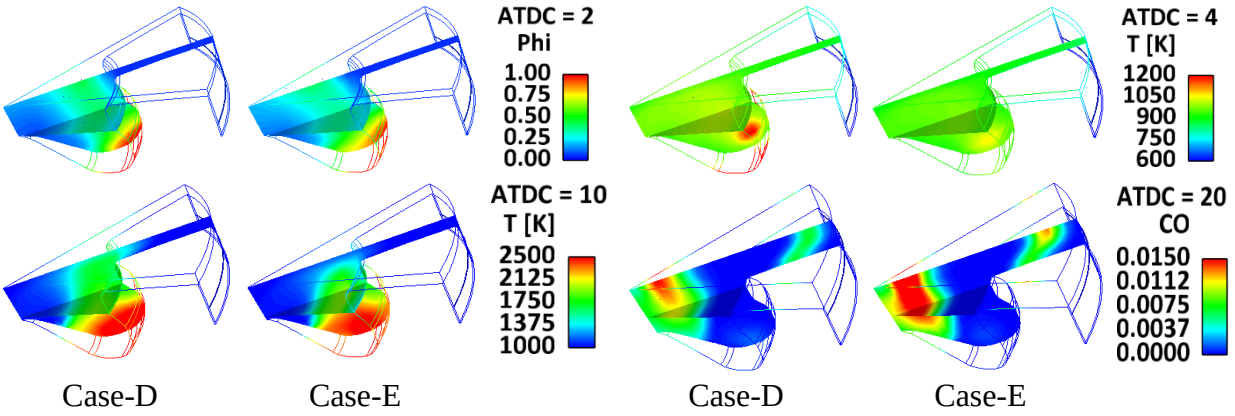

Figure 5.30: Equivalence ratio, temperature and CO contour images for -27 [Case-D] and -33 [Case-E] deg ATDC SOI command timing

With the change in injection timing from -33 deg ATDC [Case-E] to -36 deg ATDC [Case-F] the CA50 advances due to the 6 degree higher IVC temperature. Case-F also used 0.2 mg higher

fuel amount than Case-E, as mentioned in Table 5.15. Figure 5.31 indicates similar equivalence ratio distributions for both Case-E and Case-F, which with the help of the higher IVC temperature, starts earlier combustion in Case-F. This results in higher NO_x and lower UHC emission, as can be observed from the NO_x and UHC contour plots at 20 degree ATDC in Figure 5.31.

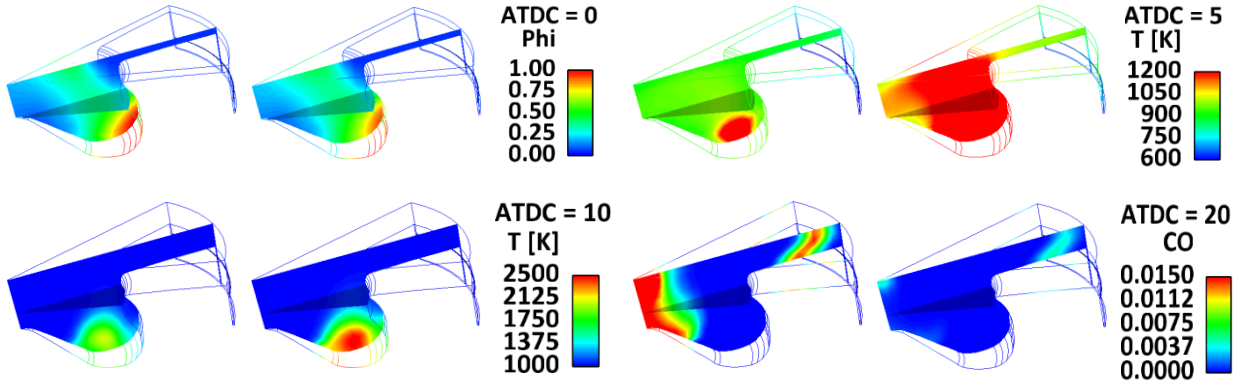

Figure 5.31: Equivalence ratio, temperature and CO contour images for -33 [Case-E] and -36 [Case-F] deg ATDC SOI command timing

The above validations using the experimental pressure data indicated that low load operation is very sensitive to the IVC temperature. This finding could also be partially influenced by the modeling constraints, which include using a sector mesh instead of the actual charge distribution at IVC, neglect of the effect of spray-to-spray variations and the absence of the consideration of valve cutouts, which cause uncertainties in the simulation results. However, Figure 5.26d shows that with the initial and boundary conditions obtained by matching the experiments, the minimum achievable net IMEP attained by the simulations was ~4 bar. Therefore, additional investigations were performed to observe the effect of various parameters, including injection parameters, swirl, and nozzle hole diameter, in an attempt to provide guidance for methods to extend the minimum load even further.

5.2.2 Load Control Using Single Injection Strategy

In order to achieve a load lower than 4 bar net IMEP, single injection operation was modeled using three different fuel amounts, 6, 7 and 8 mg at 366K IVC temperature. At a constant fueling rate, the SOI timing was varied from -40 to -16 deg ATDC while maintaining the combustion efficiency and PPRR at 85% and at 12 bar/deg, respectively. Figure 5.32 shows the engine performance results at the various SOI timings using the different fueling rates. 'SimOfExpData' in Figure 5.32 indicates the performance of the validation data points discussed in the model validation section at the different SOI timings. It can be observed from Figure 5.32a that changing the fuel amount from 6 to 8 mg alters the equivalence ratio from 0.17 to 0.23. The combustion efficiency plot in Figure 5.32b demonstrates the difficulty to burn 6 mg of fuel at an equivalence ratio of 0.17 while maintaining the combustion efficiency above 85%. At an injection timing of -36 deg ATDC or later, 7 mg fuel provides a combustion efficiency of ~90%, whereas 8 mg fuel burns well over the range of investigated injection timings. The PPRR was well-maintained for all the single injection cases presented in this section. The net IMEP obtained using 7 mg fuel was ~2.5 bar, whereas with 8 mg fuel it was ~3.3 bar, which was lower than the net IMEP observed from the model validation study, as shown in Figure 5.32d.

The simulations indicate a lower level of NO_x formation with both 7 and 8 mg fuel until -20 deg ATDC SOI timing. However, the NO_x emission increased with further retardation of the SOI timing due to the formation of locally rich regions from less mixing, resulting in rapid combustion. Figure 5.32f indicates the CO emissions, which varied from 20 to 30 g/kW-hr for 8 mg fuel, whereas it was ~50 g/kW-hr for 7 mg fuel while maintaining a combustion efficiency ~90%. The CO emission was fairly high for all the cases mentioned in this section and thus further investigations were carried as will be explained later. The UHC emission for the 7 mg fuel cases

varied from ~10 to 20 g/kW-hr, whereas for 8 mg fuel cases it was below 10 g/kW-hr, as shown in Figure 5.32g. The UHC emission increased gradually for the late injection cases because of the higher inhomogeneity in the mixture preparation, which generated more unburned fuel in the chamber. As can be observed in Figure 5.32h, using 7 mg fuel, the CA50 advanced first with the advanced SOI timing, then it remained constant from -22 to -28 deg ATDC SOI timing, and with the further advanced SOI timing the CA50 retarded. Similar CA50 trends were observed for 8 mg fuel, with a slight variation in CA50 from -22 to -24 and -26 deg ATDC.

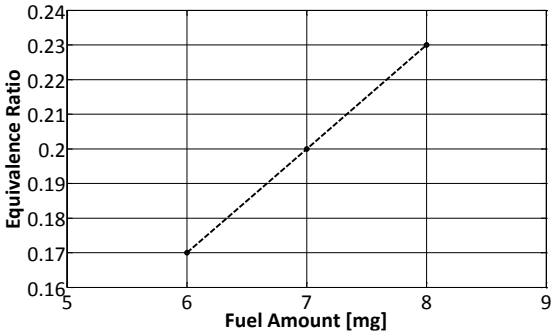

(a)

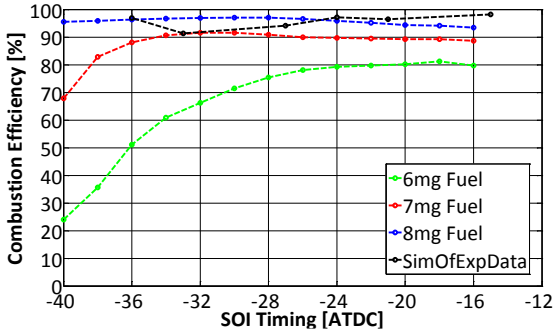

(b)

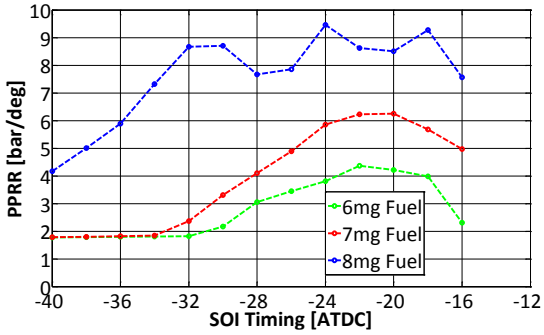

(c)

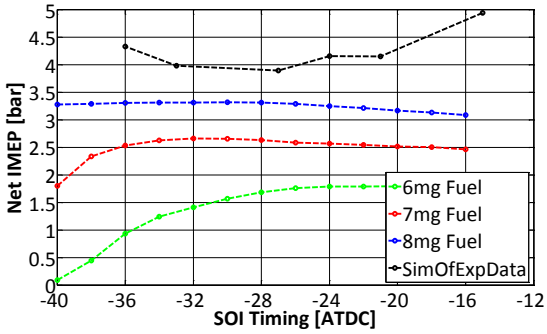

(d)

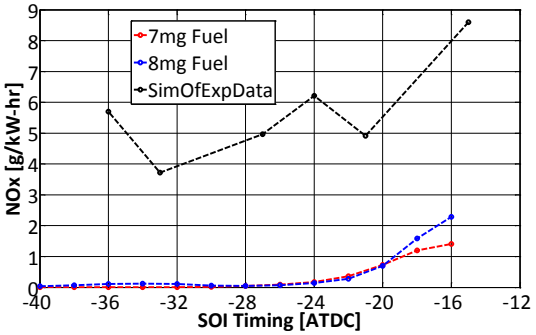

(e)

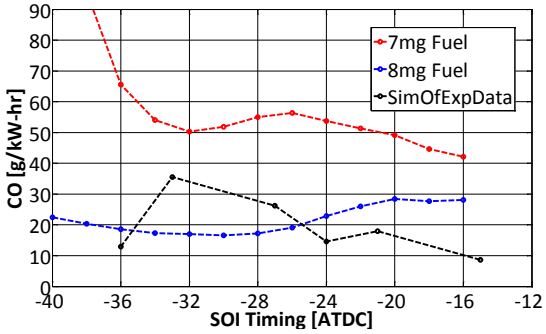

(f)

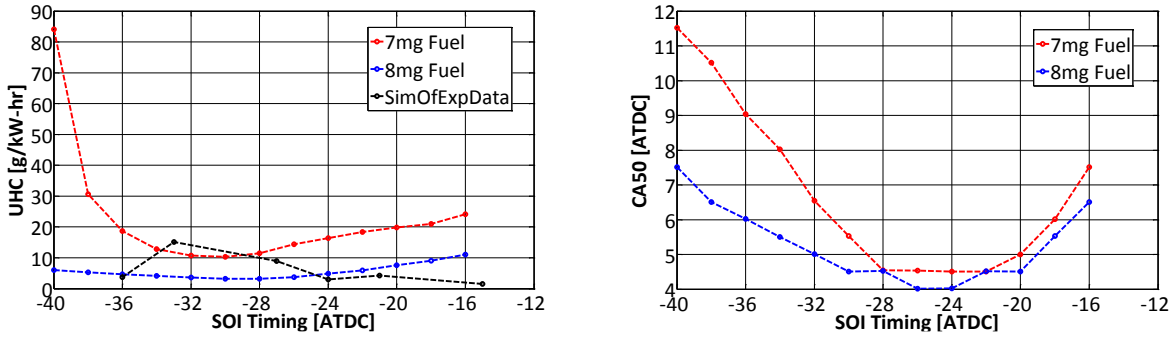

(g) (h)

Figure 5.32: Engine performance comparison at 6, 7 and 8 mg fueling conditions while varying the SOI timing. (a) Equivalence Ratio (b) Combustion Efficiency (c) PPRR (d) Net IMEP (e) NO_x emission (f) CO emission and (g) UHC emission

Figure 5.33 shows the pressure and heat release traces at -28 and -22 deg ATDC SOI timings using 7 and 8 mg fuel, respectively. Similar combustion phasings can be observed at the two different SOI timings in Figure 5.33a using 7 mg fuel and in Figure 5.33b using 8 mg fuel. This is explained in Figure 5.34 with the help of equivalence ratio and the temperature contours.

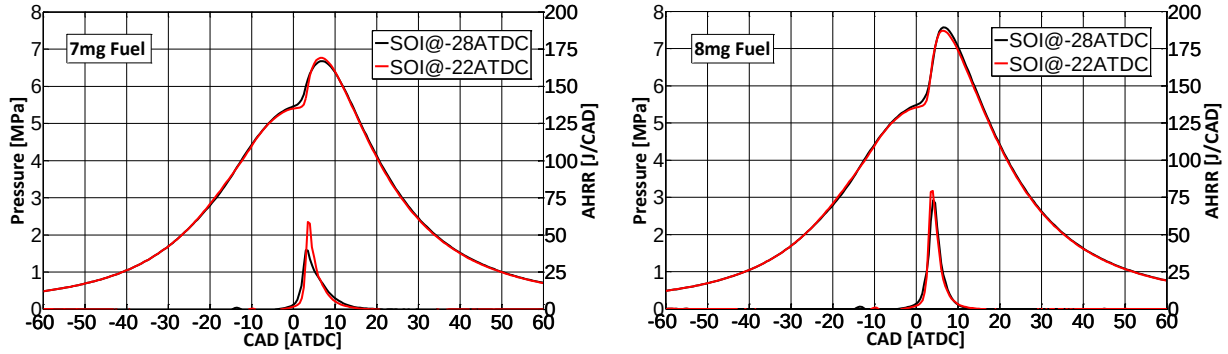

(a) (b)

Figure 5.33: Pressure and heat release traces at -28 and -22 deg ATDC SOI timings for (a) 7 mg fuel and (b) 8 mg fuel

Figure 5.34a shows the equivalence ratio distribution using 7 mg fuel at -28 and -22 deg ATDC SOI timing. Due to less mixing the -22 deg ATDC case shows a larger region of locally rich mixture compared to the -28 deg ATDC case. The presence of the locally rich region for both cases introduces similar combustion phasings. However, the larger locally rich region for the -22 deg ATDC case provided a higher heat release, as can be observed in Figure 5.34c, indicating a higher peak in the heat release in Figure 5.33a. Similar phenomena were observed for the 8 mg

cases, where less premixing from the -22 deg ATDC SOI timing case formed a larger region of locally rich mixture, which produced a higher heat release, as can be observed in Figure 5.34b and 5.34d.

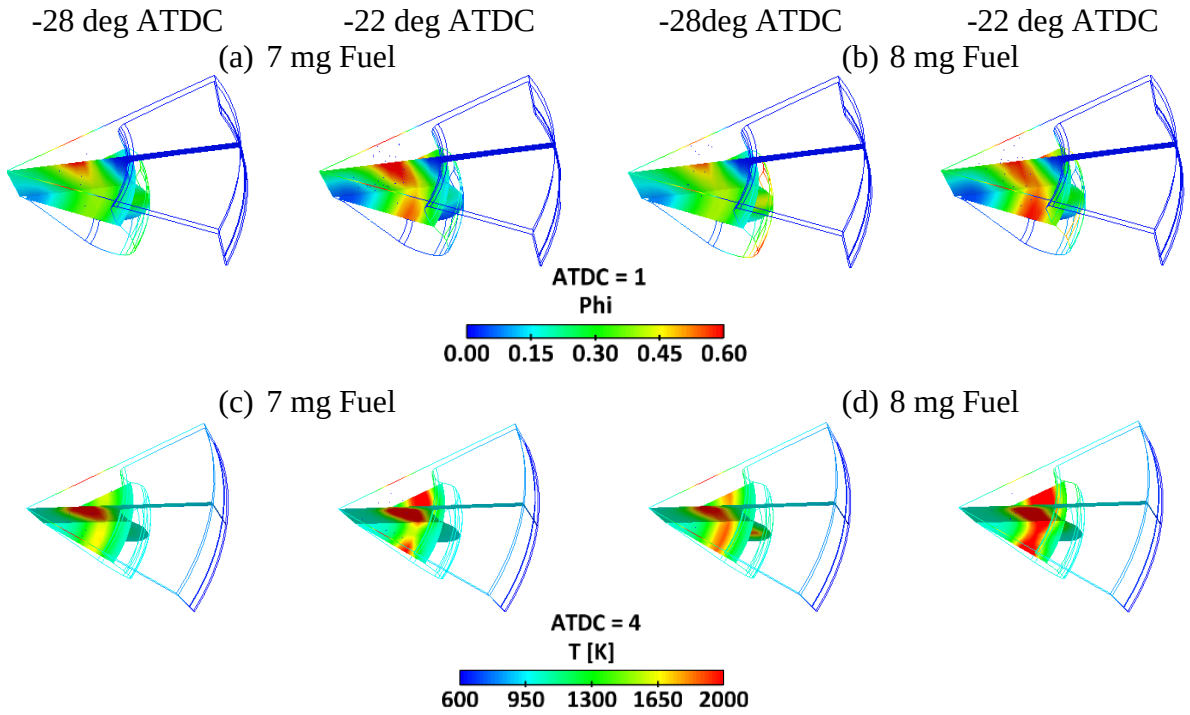

Figure 5.34: (a) Equivalence Ratio and (c) temperature contours for 7 mg fuel at -28 and -22 deg ATDC SOI.
b) Equivalence Ratio and (d) temperature contours for 8 mg fuel at -28 and -22 deg ATDC SOI.

The CA50 plot in Figure 5.32h also demonstrates that similar combustion phasings were obtained at -28 and -22 deg ATDC SOI timings using two different fuel amounts, 7 and 8 mg. The pressure and heat release traces for these cases are shown in Figures 5.35a and 5.35b at -28 and -22 deg ATDC SOI timings, respectively. In both the figures 8 mg fuel displays higher peak pressure and more heat release because of the larger amount of fuel burning in the combustion chamber.

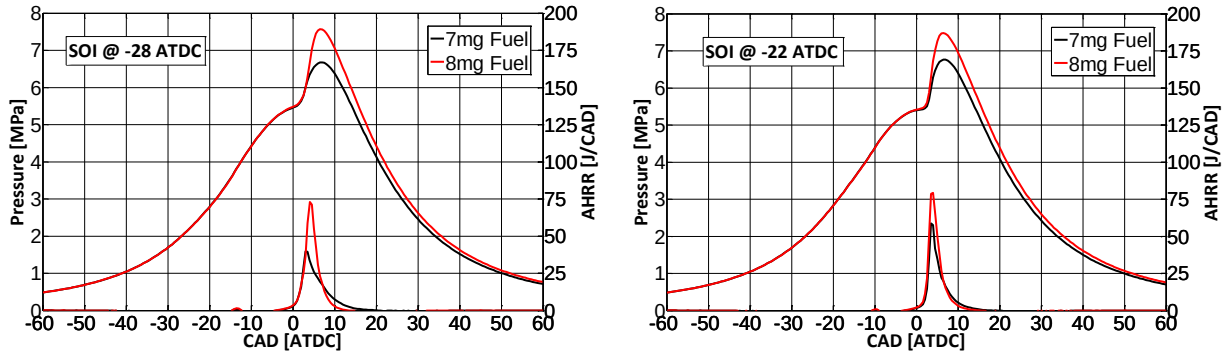

(a) (b)

Figure 5.35: Pressure and heat release traces for 7mg and 8mg fuel at (a) -28 deg and (b) -22 deg ATDC SOI timings

The equivalence ratio distributions in Figure 5.34a and 5.34b corresponding to 7 and 8 mg fuelings, respectively, at -28 deg ATDC SOI timing indicate a locally rich region in the bowl and close to the cylinder head for the 8 mg case. As the injection duration for both the cases were same, the injection pressure was higher for the 8mg case because of the higher fuel amount. This resulted in heat release from a larger region for the 8 mg case, as can be observed from the temperature distribution mentioned in Figures 5.34c and 5.34d at -28 deg ATDC. For the 7 mg case, due to less fuel and lower injection pressure, the locally rich region was close to the cylinder head, which started combustion at the same time as in the 8 mg case.

This section demonstrates that single injection cases are capable of producing lower load than those observed in the experiments with a lower fueling level. However, in the experiments maintaining a fueling rate lower than 9.8 mg/cycle/cylinder was a challenge due to large observed cylinder-to-cylinder variability. Computational investigation using the single injection approach showed the capability of producing ~2.5 bar net IMEP by using 7 mg fuel/cycle/cylinder. However, the larger CO production with 7 mg fuel is a concern. Thus, further investigation was carried out in order to explore methods to reduce CO emissions.

5.2.3 Effect of Swirl on Emissions at Low Load

In order to attempt to reduce CO emissions, the swirl ratio was varied from 0.7 to 2.2 for the 7 mg fuel cases. Previously all the simulations were performed using the stock engine swirl ratio of 2.2. This was altered to 1.5 and 0.7 to observe its impact on emissions while maintaining low load fueling.

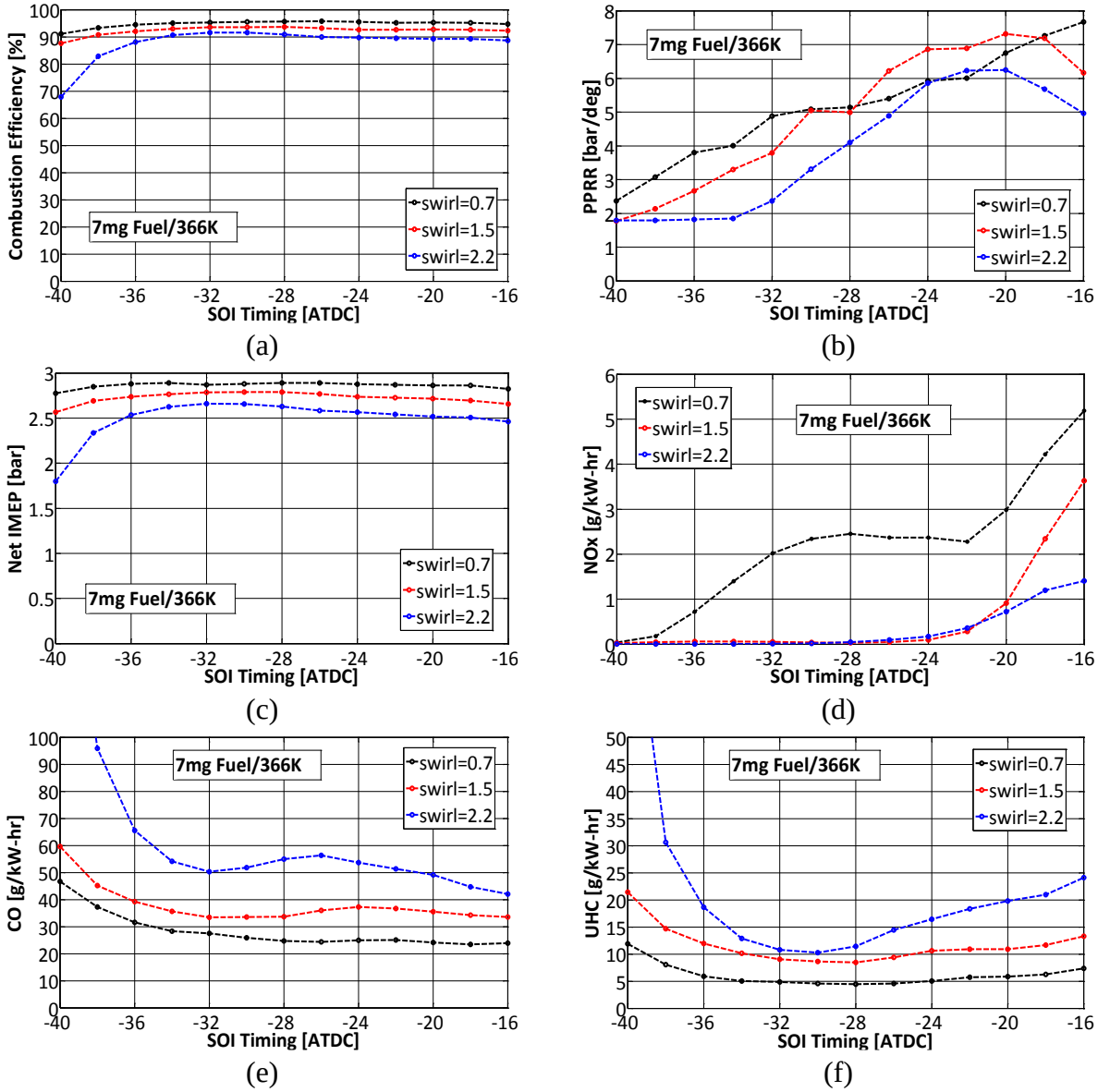

Figure 5.36: Engine performance comparisons at 0.7, 1.5 and 2.2 swirl ratios while varying the SOI timings. (a) Combustion Efficiency (b) PPRR (c) Net IMEP (d) NO_x emission (e) CO emission (f) UHC emission

Performance comparisons at the different swirl ratios are shown in Figure 5.36. Figure 5.36a indicates that with the lower swirl, better combustion efficiency can be achieved without having a significant impact on PPRR, as seen in Figure 5.36b. The net IMEP was raised from ~2.5 bar to ~2.8 bar with the reduction in swirl ratio from 2.2 to 0.7, as can be observed in Figure 5.36c. Figure 5.36d shows higher NO_x emissions with the swirl reduction, which is due to the locally rich region observed at lower swirl due to less mixing, as indicated in the equivalence ratio contour in Figure 5.37. This results in rapid heat release, forming a larger high temperature region, and therefore more NO_x. The CO emissions are reduced to ~25 g/kW-hr from ~50 g/kW-hr by reducing the swirl, whereas the UHC emission is maintained at ~5 g/kW-hr with the lower swirl, as shown in Figures 5.36e and 5.36f, respectively.

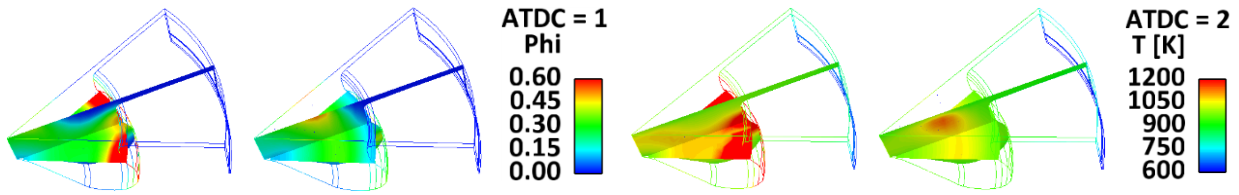

Figure 5.37: Equivalence ratio and temperature contours for 0.7 and 2.2 swirl at -32 deg ATDC SOI

5.2.4 Effect of Nozzle Diameter on Emissions at Low Load

As observed in the previous section, use of a lower swirl ratio can reduce CO emissions significantly, but at the expense of increased NO_x. Therefore, in an attempt to reduce both NO_x and CO at low load, the nozzle diameter effect was investigated.

7 mg fuel was injected at -32 deg ATDC SOI timing. This SOI timing was chosen based on the previous results, which showed that at this timing 7 mg fuel can provide combustion efficiency above 90%. Simulations were conducted at 2.2 swirl ratio and at two different IVC temperatures, 366K and 385K, respectively. The nozzle diameter was varied from 80 to 200

microns with a step-size of 20 microns. The injection duration was kept constant while changing the nozzle hole diameter, which resulted in a higher injection velocity with a smaller hole size, as shown in Figure 5.38a.

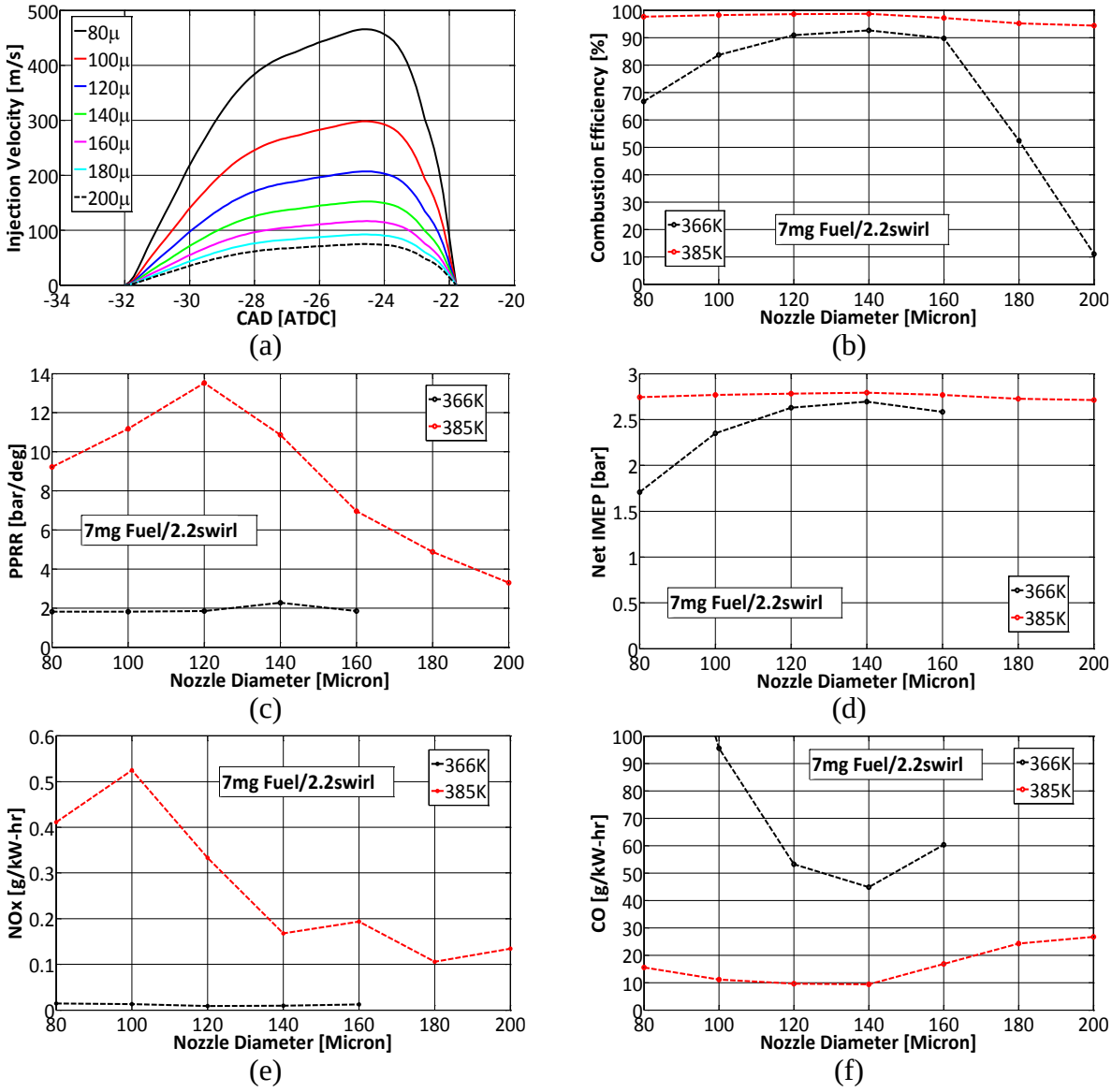

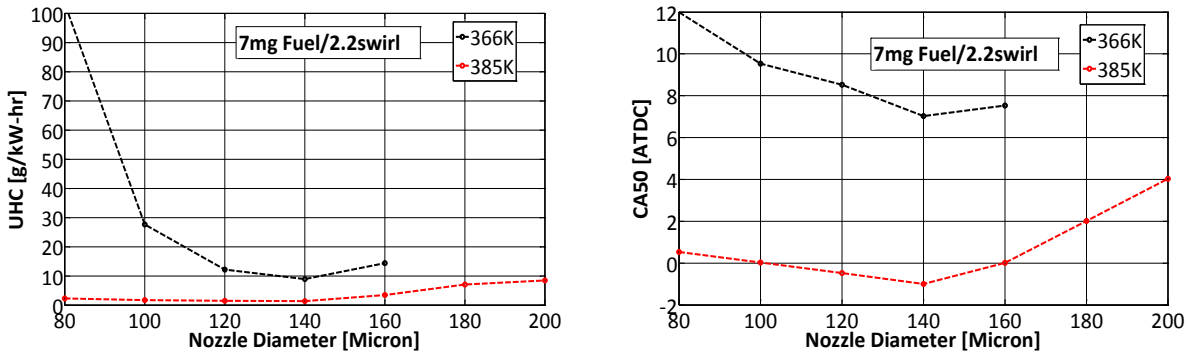

(g) (h)

Figure 5.38: Engine performance comparisons at 366K and 385K IVC temperatures while varying nozzle hole diameter. (a) Injection velocity (b) Combustion Efficiency (c) PPRR (d) Net IMEP (e) NO_x emission (f) CO emission (g) UHC emission (h) CA50

The combustion efficiency plot in Figure 5.38b indicates more than 90% efficiency for the 385K cases, whereas the 366K cases burn effectively within the nozzle diameter range of 120 to 160 microns. Peak pressure was slightly higher than 12 bar/degree for a nozzle diameter of 120 micron at 385K. Overall, at both IVC temperatures less than 3 bar net IMEP was achieved, as indicated in Figure 5.38d. The NO_x was higher than the emission regulation target for the 385K cases, but was maintained at a value lower than 0.5 g/kW-hr. The CO emission was ~50 g/kW-hr for the 366K cases, whereas it was ~15 g/kW-hr for the 385K IVC temperature cases. The UHC emission was less than 10 g/kW-hr for the 385K cases, whereas it was ~10 g/kW-hr for the combusting cases at 366K. The CA50 plot in Figure 5.38h indicates that at 385K, with an increase in nozzle diameter from 80 to 140 microns, CA50 advances, whereas with further increase in hole diameter it retards. Similar behavior can be observed for the 366K cases.

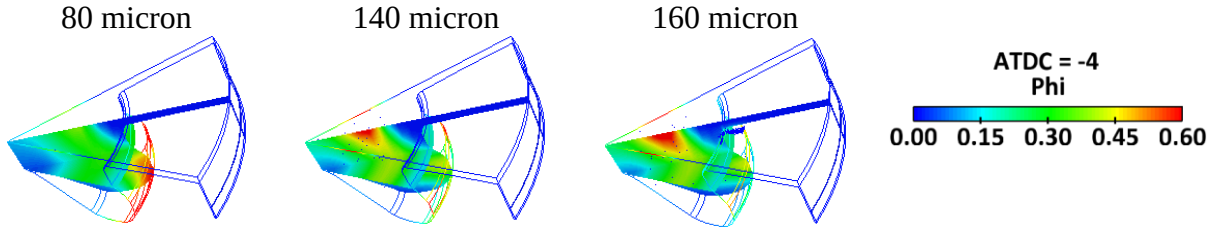

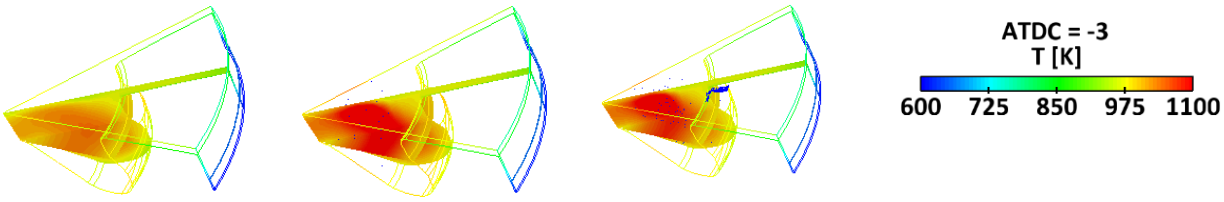

Figure 5.39: Equivalence ratio and temperature contours for 80, 140 and 160 micron nozzle hole diameter at -32 deg ATDC SOI

The equivalence ratio and temperature contours in Figure 5.39 illustrate that the 80 micron hole diameter causes faster break-up, creating a locally rich region only in the bowl, whereas fuel break-up from the 140 micron diameter nozzle creates a locally rich region both in the bowl and close to the cylinder head. On the contrary, the hole diameter of 160 micron creates a locally rich region only close to the cylinder head due to the slower fuel breakup. The different equivalence ratio distributions provide almost similar start-of-ignition timings with a difference in the amount of heat release. The temperature contour for the 160 micron hole diameter case clearly indicates the presence of some larger droplets in the squish region, introducing a smaller heat release and therefore a retarded CA50. This study shows that the nozzle diameter needs to be optimized in order to achieve effective fuel breakup to produce the required load with reasonable engine-out emissions.

5.2.5 Discussion

This section summarized numerical investigations executed to provide insights to single injection experiments performed while maintaining a minimum fueling rate over a range of injection timings. The following conclusions can be made.

a. An advancement of CA50 with advancement in injection timing was seen at first, which became retarded with further advancement in SOI timing. The simulations captured this CA50 trend reasonably well, and the results indicated that light load conditions are very sensitive to the IVC temperature. Overall experimental engine performance trends were

predicted quite well in the simulations. The numerical results recorded the minimum net IMEP of 4 bar seen in the experimental validation.

b. Single injection simulations using 6, 7 and 8 mg fueling with a sweep of SOI timings indicated that ~3.3 bar IMEP load could be produced by using 8mg fuel, whereas ~2.5 bar IMEP load was produced while using 7mg fuel. In the experiments, a fuel amount as low as 7mg could not be used mainly due to cylinder-to-cylinder variability. This study also showed that at a specific SOI timing it was possible to achieve the same CA50 with different amounts of fuel. Also, while using a constant amount of fuel, the same CA50 was achieved over a range of injection timings.

c. Due to higher CO emissions from the 7mg fuel case seen at the various SOI timings, computations were performed using 0.7, 1.5 and 2.2 swirl ratios. The results indicated that CO and UHC emissions were greatly improved with lower swirl, but at the expense of larger NO_x emissions. A net IMEP lower than 3 bar was achievable at 0.7 swirl ratio.

d. The effect of nozzle hole diameter on NO_x and CO emissions was also investigated. Simulations were performed using 366K and 385K IVC temperatures where 7 mg fuel was injected at -32 deg ATDC SOI. The results showed that at the higher IVC temperature both the NO_x and the CO emissions were lower, compared to the effect observed from reduced swirl. However, the NO_x was still higher than the target value. The simulations also showed that the nozzle hole diameter needs to be optimized to achieve effective fuel breakup, and therefore the desired load with reasonable emissions.

5.3 Effect of Injector Inclusion Angle on Load Minimization

Injector included angle is an important parameter from a spray characterization perspective and it was found to have an impact on load minimization. Single injection experiments were carried

out at the Argonne National Laboratory using 120 deg and 148 deg injector included angles to observe its influence on minimizing engine load [Kolodziej *et al.*, 2014]. At 850 rev/min engine speed, the injector command timing using 93 RON gasoline injection was varied from -33 to -6 deg ATDC with a step-size of 3 deg while maintaining the COV of IMEP less than 3%. Lower than 2 bar BMEP load was attained using both inclusion angles, whereas a minimum load of 1.17 bar was achieved using 120 deg injector included angle. Simulations were performed to validate these experiments and to provide explanations for differences in combustion behavior with the change in injector included angle.

Figure 5.40 indicates a very good agreement between experimental and numerical motored pressure trace at 850 rev/min. The compression ratio used in the simulation was 17 instead of 17.8. It is speculated that the change in compression ratio could have been caused by the alteration of the bearing clearances from using the engine over the years, which led to changes in the crevice volumes.

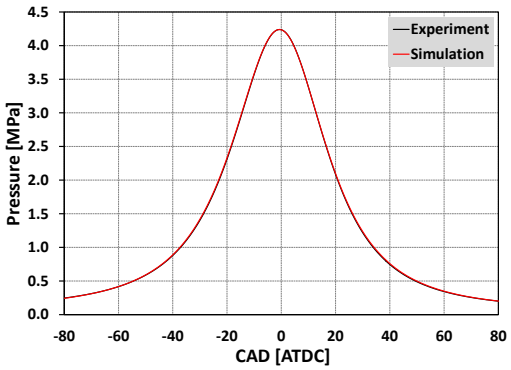

Figure 5.40: Motored pressure comparison between experiment and simulation

In the present study, the injector with 120 deg included angle will be referred as injector-A, whereas the 148 deg included angle injector will be referred to as injector-B.

To observe the effect of injector included angle, simulations were performed using the two different injectors by varying the SOI command timings from -27 to -18 deg ATDC, all of which provided below 2 bar BMEP load points in the experiments. Initially, the PRF2 mechanism was

used for 87 AKI gasoline simulations, which has been extensively validated, as shown in Appendix A for HCCI experiments using PRF fuels. However, due to the influence of fuel aomposition discussed before, the PRF fuel chemistry was replaced by a more realistic 15-component gasoline surrogate chemistry model [Ra *et al.*, 2014]. Figure 5.41 represents the distillation curve comparison between the experiment and simulation for the 93 RON/ 87 AKI gasoline. The mass fractions of the considered fuel components are also mentioned in the figure.

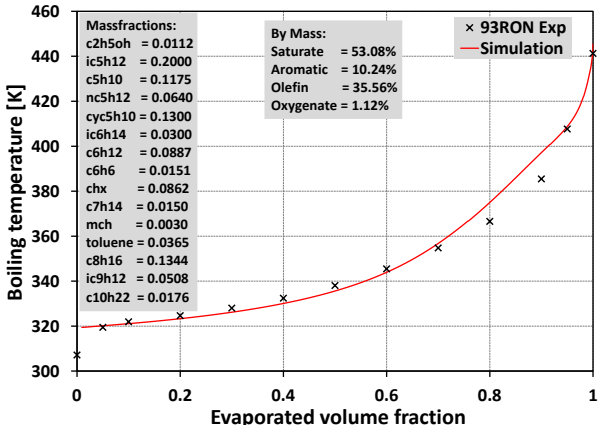

Figure 5.41: 93 RON gasoline distillation curve comparison between experiment and simulation

5.3.1 Difference between PRF and 15-Component Gasoline Fuel Chemistry

To characterize the fuel models, an ignition delay study was performed to compare the auto-ignitability of the PRF and 15-component gasoline fuels. Chemkin simulations were conducted at 40 bar pressure, which is close to the compression pressure for light load cases, and at two different equivalence ratios, 0.5 and 1.0. At 0.5 phi, the 15-component fuel showed noticeably lower ignition delays in the low temperature region, as can be observed in Figure 5.42a. Even though the ignition delay looks very similar for the 87 PRF and 15-component fuels at 1.0 phi, as can be seen in Figure 5.42b, it is slightly lower for the 15-component gasoline in the temperature range from 800K to 1000K, which can cause significant differences in CA10 and CA50 comparisons in engine simulations.

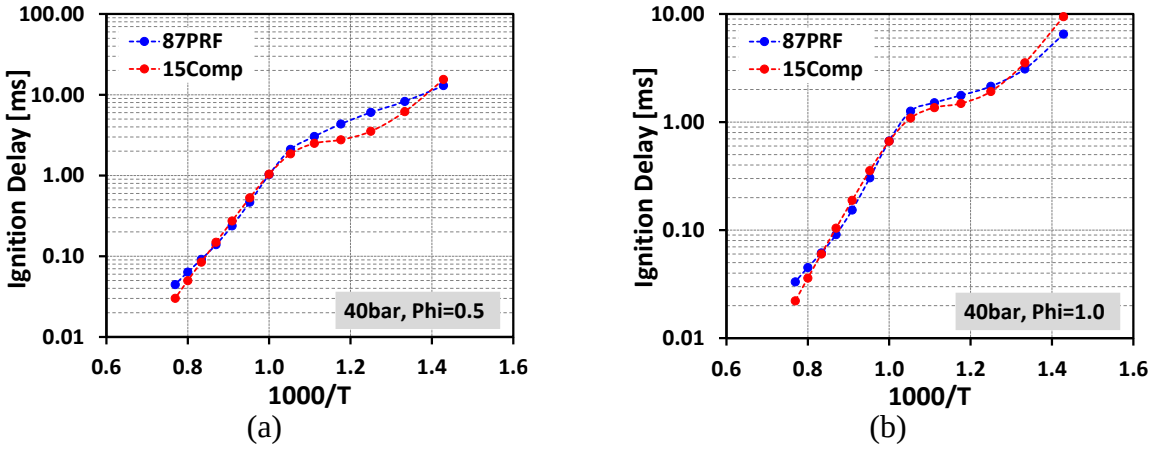

Figure 5.42: Ignition delay comparison between PRF and 15-component fuels at 40bar and at (a) phi=0.5 and (b) phi=1.0

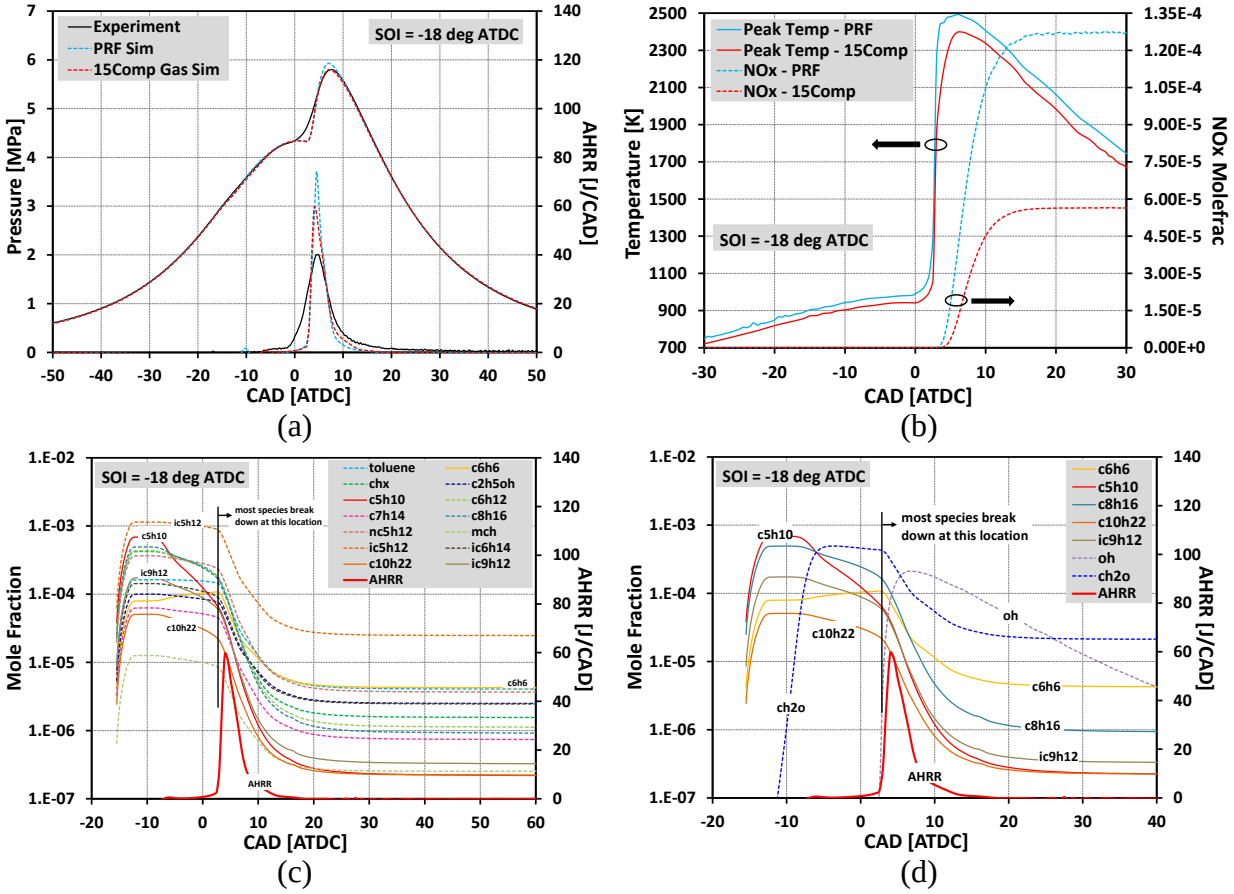

Figure 5.43: (a) Pressure and heat release comparisons and (b) temperature and NO_x mole fraction comparisons between PRF and 15-component gasoline fuel chemistry at -18 deg ATDC SOI command timing point using injector-B.
AHRR and mole fractions of (c) all fuel components and (d) important fuel components in 15-component gasoline simulation.

In order to further demonstrate differences between the PRF and 15-component fuel chemistry in engine simulations, -18 deg ATDC SOI command timing point was picked at the injector-B conditions.

A nozzle opening delay of 1.5 deg was considered in the computations, which indicated -16.5 deg ATDC SOI timing in simulations for a -18 deg ATDC SOI command timing case. To avoid confusion, from now onwards the SOI timings mentioned in this section are referred to as SOI command timings. In order to capture the experimental CA50, 372K IVC temperature was used in the PRF simulation, whereas it was 354K for the 15-component simulation, which can be attributed to the difference in the auto-ignition characteristics of the fuels, as shown in Figure 5.42. Figure 5.43a indicates a slight over-prediction of experimental peak pressure using the 87 PRF fuel chemistry, whereas the 15-component gasoline surrogate model captured the compression, peak and expansion pressures fairly well. However, both the PRF and 15-component fuel chemistry showed a delayed start of combustion compared to the experiment. Figure 5.43b presents the peak temperature and NO_x emission plots using both mechanisms. From the figure it is evident that the ~18K difference in IVC temperature resulted in ~80K difference in peak temperature, which produced a fairly low NO_x while using the 15-component fuel chemistry. The corresponding Phi-T distributions are shown in Figure 5.44 before and after the start of combustion, at 0 deg and 4 deg ATDC, respectively. The figures indicate similar equivalence ratio distributions for the PRF and 15-component simulations, whereas the 15-component chemistry shows a lower peak temperature compared to the PRF simulation. This keeps the 15-component fuel combustion out of the NO_x formation region, as shown in Figure 5.44b. Emission results using two different fuel chemistry models are compared later in this section.

Figure 5.43c illustrates the evolution of all fuel species used in the 15-component gasoline surrogate model, whereas Figure 5.43d shows the important fuel species, which contributed more towards the onset of ignition. The figures indicate that C_5H_{10} was consumed significantly earlier than other fuel components, which coincided with the appearance of formaldehyde [CH_2O]. Other fuel components, like C_8H_{16}, iC_9H_{12} and $C_{10}H_{22}$ also started decomposing almost at the same time as C_5H_{10}. However, their decomposition rate was significantly lower than C_5H_{10}, as shown in Figure 5.43d. With the decomposition of higher-order hydrocarbon species C_6H_6 was formed as an intermediate species, as indicated by the accumulation of C_6H_6 first, followed by decomposition at a later stage. CH_2O consumption and OH accumulation appeared to track the decomposition of most of the other fuel species in the 15-component fuel model, indicating that C_5H_{10} contributed the most to the thermal ignition time, along with the C_8H_{16}, iC_9H_{12} and $C_{10}H_{22}$ fuel species.

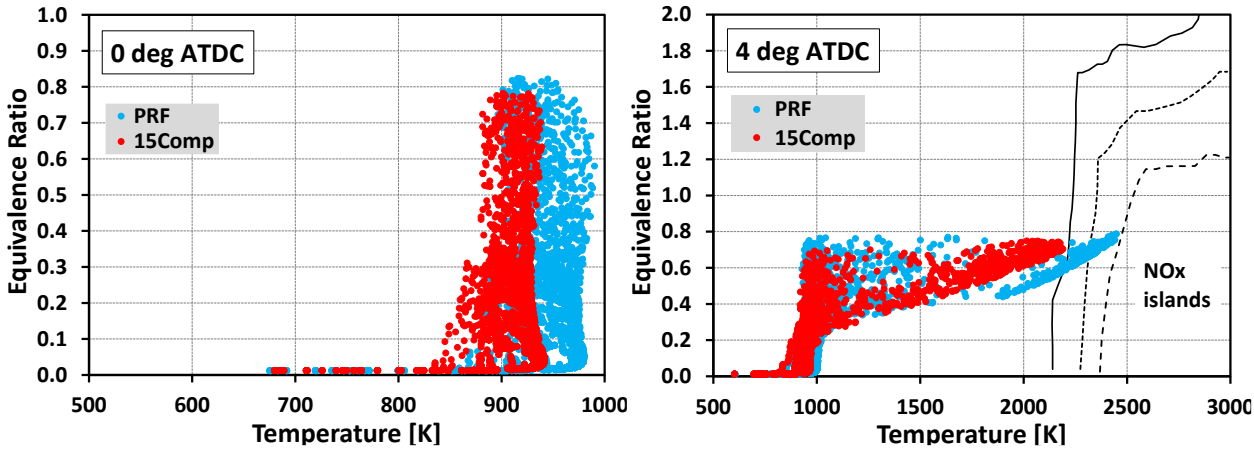

(a) (b)

Figure 5.44: Phi-T distributions from PRF and 15-component fuel simulations at -18 deg ATDC SOI. The distributions are at (a) 0 deg ATDC and (b) 4 deg ATDC

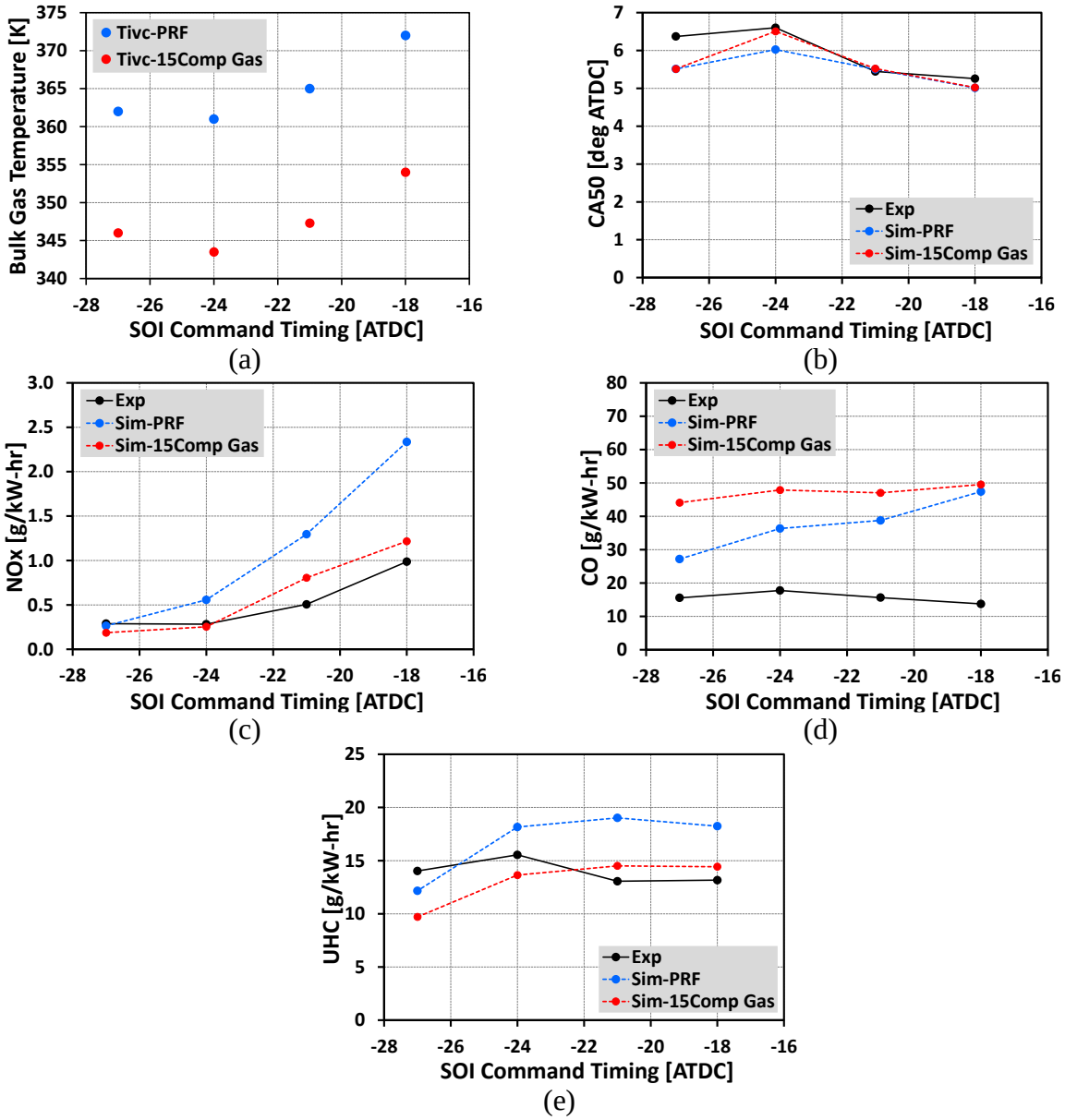

Figure 5.45: Comparisons between (a) IVC temperature using PRF and 15-component fuel chemistry and experimental and simulated (b) CA50 (c) NO_x (d) CO and (e) UHC emissions

Engine performance was compared using both the PRF and 15-component gasoline surrogate mechanisms in Figure 5.45. For the same engine operating condition simulations, Figure 5.45a required lower IVC temperatures while using 15-component fuel chemistry, which resulted in lower NO_x as can be observed in Figure 5.45c. The engine performance comparisons in Figure 5.45 indicate that the 15-component model predicted better the CA50 and NO_x emission compared to the PRF simulation. However, the CO emission was greatly over-predicted by the 15-component

model simulation. Both CO and UHC emissions were mainly from the squish region as was observed earlier in this work. Considering the better performance obtained using the 15-component model, the rest of the simulations in this section were performed using it instead of the PRF mechanism.

5.3.2 Comparison between 120 deg [Injector-A] and 148 deg [Injector-B] Injector Included Angle

With the improved fuel chemistry model simulations were carried out from -27 to -18 deg ATDC SOI command timing as mentioned before. Figure 5.45 demonstrates the comparisons between experiments and simulations at different SOI command timings using the two different injectors.

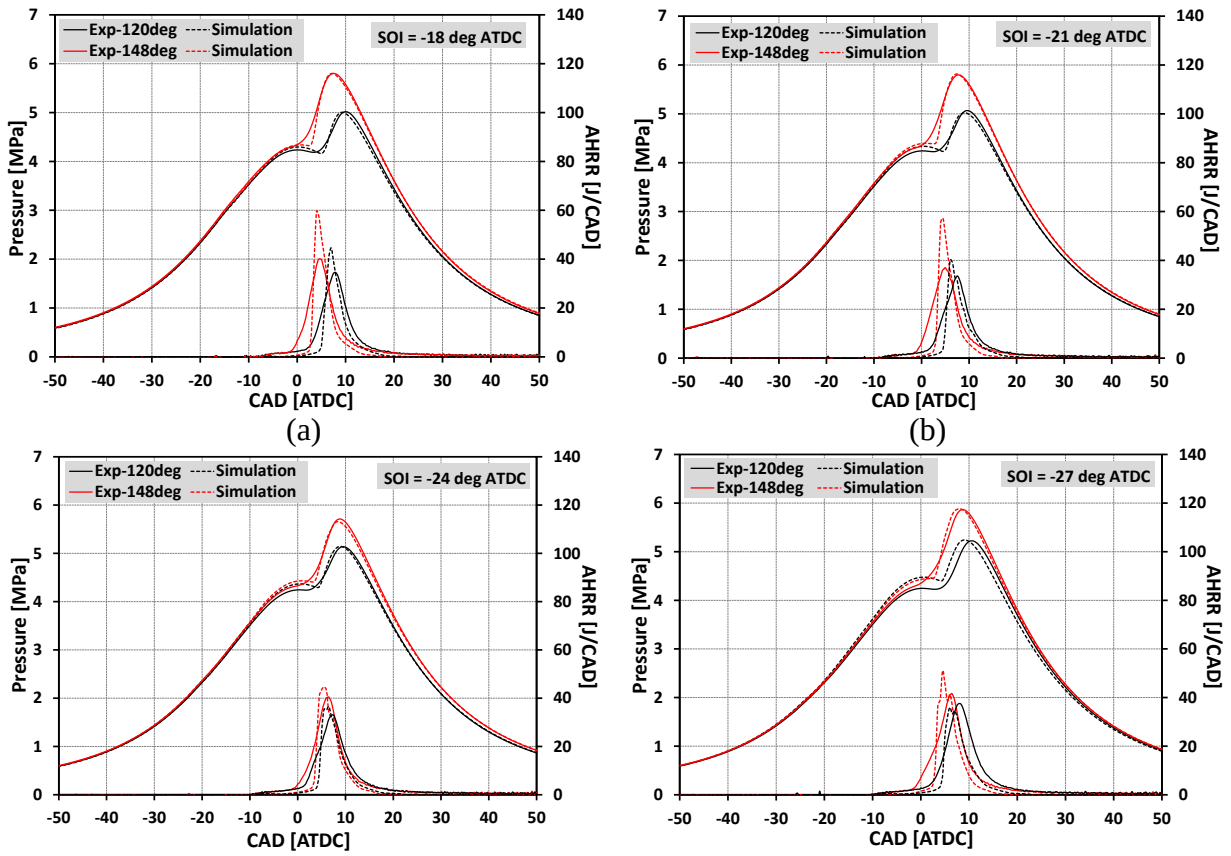

Figure 5.46: Experimental and numerical pressure and heat release comparisons at (a) -18 deg (b) -21 deg (c) -24 deg and (d) -27 deg ATDC SOI timings using injector-A [120 deg included angle] and injector-B [148 deg included angle]

The experiments were conducted at 50°C intake air temperature and zero boost. At each injection point the minimum fueling level was maintained by controlling the COV of IMEP to be less than 3%. In Figure 5.46 all injection points indicated lower pressure using injector-A, which corresponded to a lower fueling amount. Use of a narrower inclusion angle allowed the fuel to target the bowl instead of squish region which helped obtain more efficient combustion at low load conditions. This is discussed in detail later in this section. Figure 5.46 shows a reasonably good agreement between experiments and the simulations. However, at -27 deg ATDC SOI command timing, the injector-A simulation over-predicted the average compression pressure slightly. Using both injectors the peak pressures remained almost the same over the range of considered SOI timings.

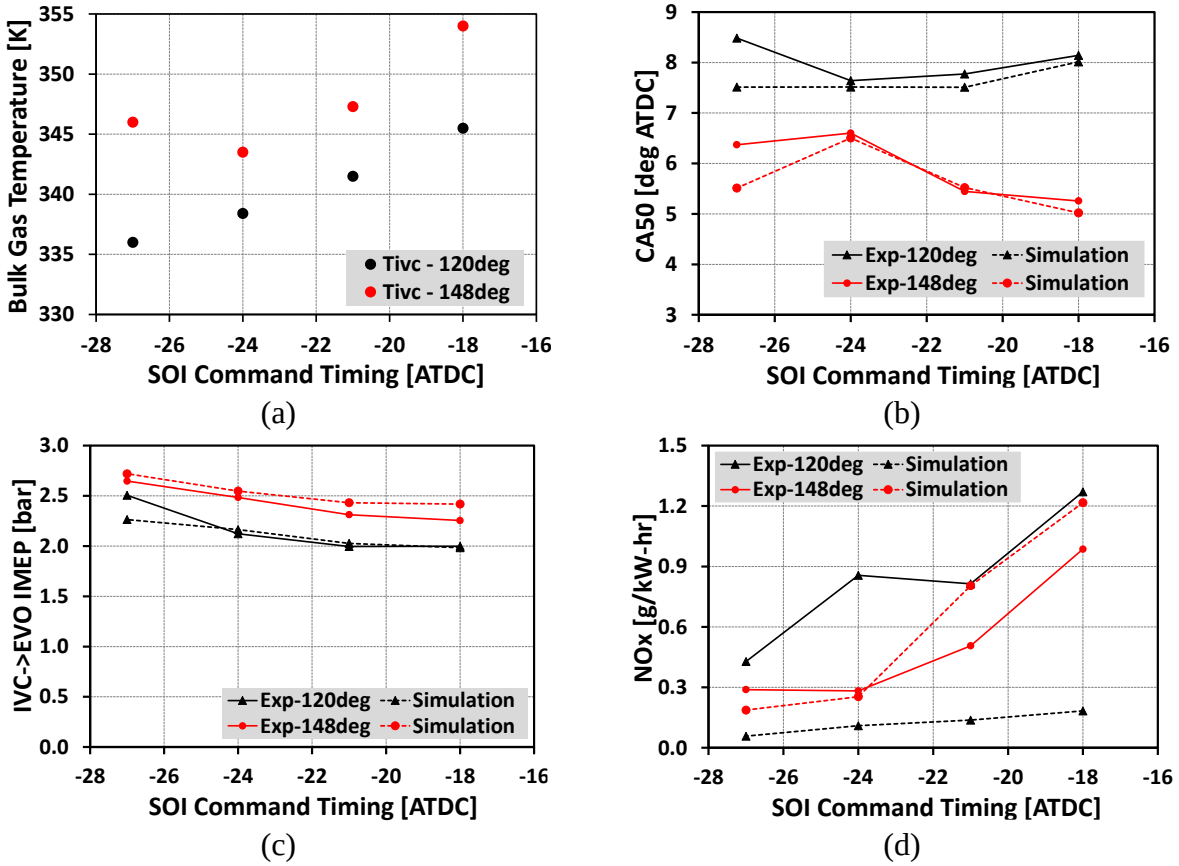

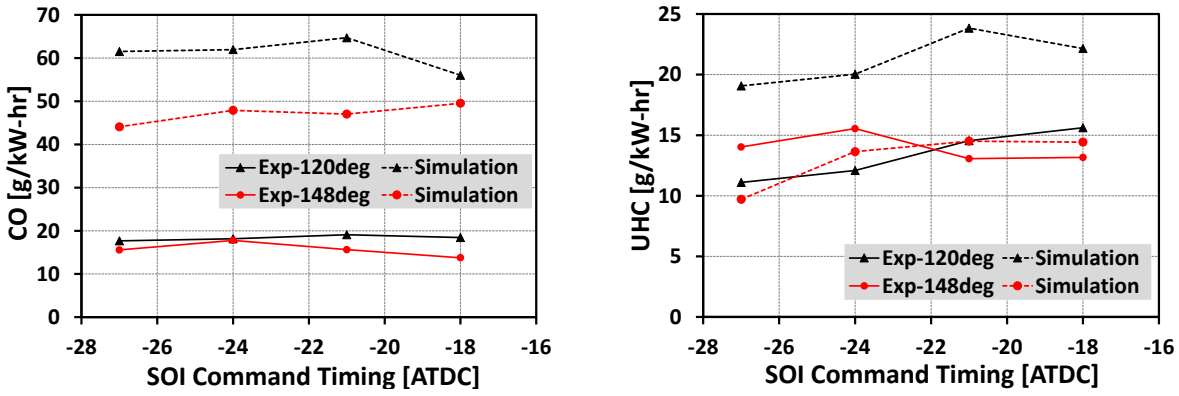

(e) (f)

Figure 5.47: (a) IVC temperature plot and comparisons between experimental and numerical (b) CA50 (c) IMEP (d) NO_x (e) CO and (f) UHC emissions using injector-A [120 deg included angle] and injector-B [148 deg included angle]

Comparisons between the experimental and numerical engine performances are depicted in Figure 5.47 using the two different injectors. As before, the IVC temperatures needed to be altered in the computations to capture the experimental CA50s at the different SOI timings, as can be observed in Figure 5.47a. As discussed in Chapter 5.2, simulating an engine with a sector mesh with a constant IVC temperature does not replicate the actual in-cylinder temperature distribution, and therefore tuning of the IVC temperature was chosen as an option in the simulations to reproduce the experimental combustion characteristics. The IVC temperatures used for the injector-A simulations were somewhat lower than for the injector-B cases, producing delayed CA50s for the entire range of the SOI timing sweep, as shown in Figure 5.47b. Figure 5.47c presents the IMEP comparisons from IVC to EVO demonstrating a lower IMEP using injector-A compared to injector-B, which was well-captured in the simulations. Indirectly, Figure 5.47c also specifies that the minimum fueling rate was maintained at -18 deg ATDC SOI command timing using both injectors. NO_x emissions were largely under-predicted in the injector-A simulations, as shown in Figure 5.47d, whereas the experimental emission trends were captured by both the injector simulations. This suggests the possibility of wall-wetting in the injector-A experiments, which was not modeled very well in the corresponding computations. Because of the under-

predicted NO_x, over-predicted CO and UHC were expected to accompany the incomplete combustion for the injector-A cases, which are shown in Figure 5.47e and 5.47f, respectively. For the injector-B simulations, CO was over-predicted whereas the UHC trend was fairly well captured. To demonstrate the reasons behind the lower fueling rate usage for injector-A, in-cylinder fuel and temperature distributions at -21 deg ATDC SOI timing were studied for both the injectors, as shown in Figure 5.48.

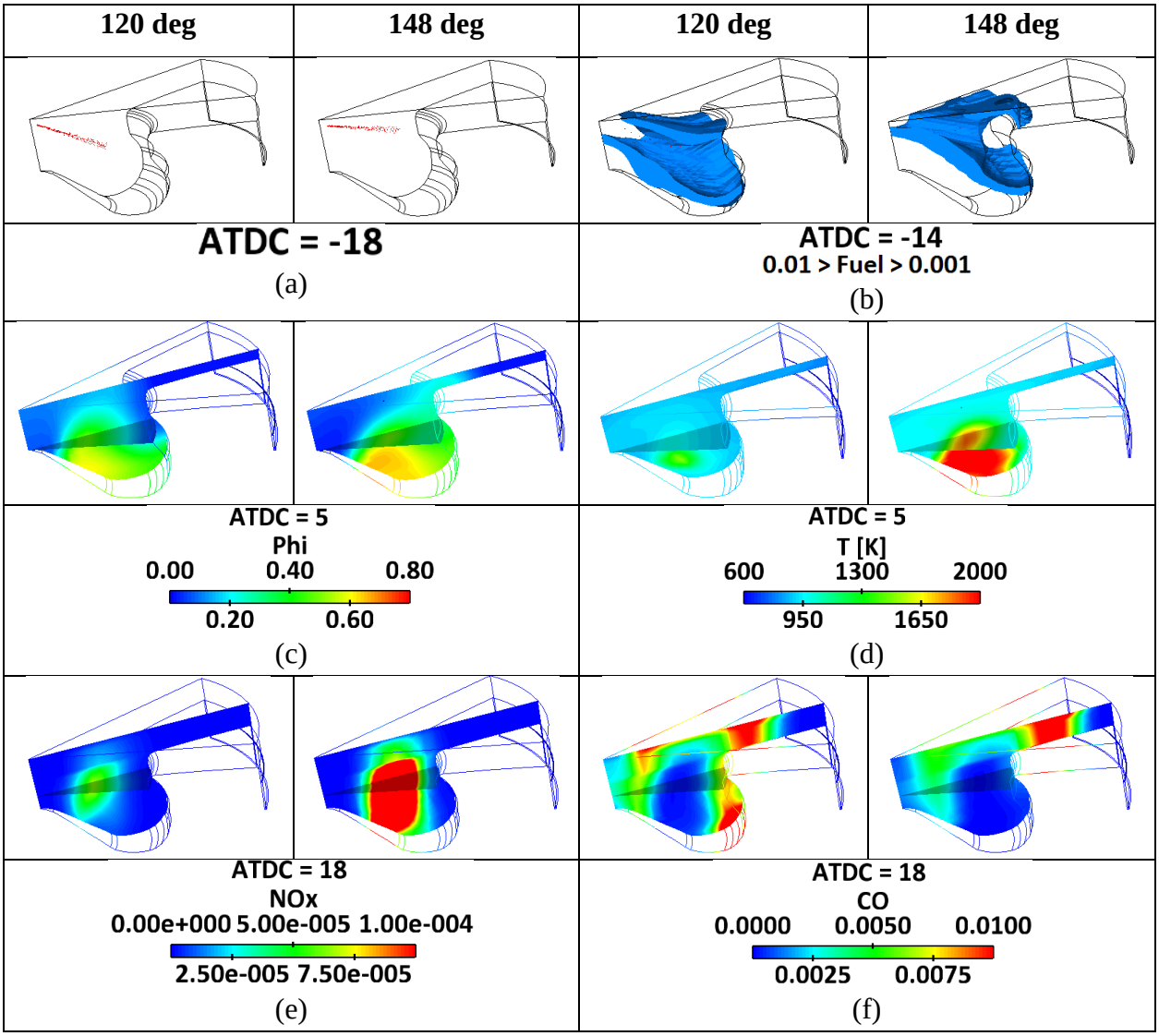

Figure 5.48: Contours for -21 deg ATDC SOI command timing cases using injector-A [120 deg included angle] and injector-B [148 deg included angle]

The fuel spray using injector-A targets the bowl region and therefore most of the fuel resides in the bowl, as can be observed in Figures 5.48a and 5.48b. On the other hand, the spray targets the bowl re-entrainment region in the injector-B case, allowing some of the fuel to enter in the squish region, as shown in the fuel iso-volume plot in Figure 5.48b. Figure 5.48c indicates a locally rich region in the bowl for the injector-B case, resulting in earlier heat release, as can be observed in Figure 5.48d. The IVC temperature and the fuel amount for the injector-A case were 342K and 6.34 mg respectively, whereas it was 347K and 7.16 mg, respectively, for the injector-B case. Both the higher fuel amount and IVC temperature helped establish earlier combustion using injector-B. But, all the fuel targeted the bowl region while using injector-A helped in the combustion, generating lower NO_x and slightly higher amount of CO in the bowl, even though the fuel amount was ~12% lower compared to the injector-B case. As the operating conditions for the different injector cases were not the same, a fair comparison of the injector included angle effects is made in the next section.

5.3.3 Effect of SOI on Combustion Phasings using Injector-A [120 deg included angle] and Injector-B [148 deg included angle]

This section reports the numerical investigation of the effect of SOI timings on combustion phasings while using two different injectors – injector-A and injector-B. However, unlike in the experiments, all engine operating parameters, including engine speed, IVC conditions and injection parameters were kept constant in order to isolate the effects of injection timing on combustion phasing only, which has implications on combustion stability. Performing such experiments was difficult due to the possibility of violent combustion. The operating conditions for these simulations were obtained from the simulated conditions at -18 deg ATDC SOI timing using injector-B, which are mentioned in Table 5.16.

Table 5.16: Engine operating conditions

RPM	850
P_{IVC} [bar]	1.13
T_{IVC} [K]	354
Internal EGR [%]	5
Fuel Amount [mg/cyc/cyl]	7.14
Injection Duration [deg]	3.926

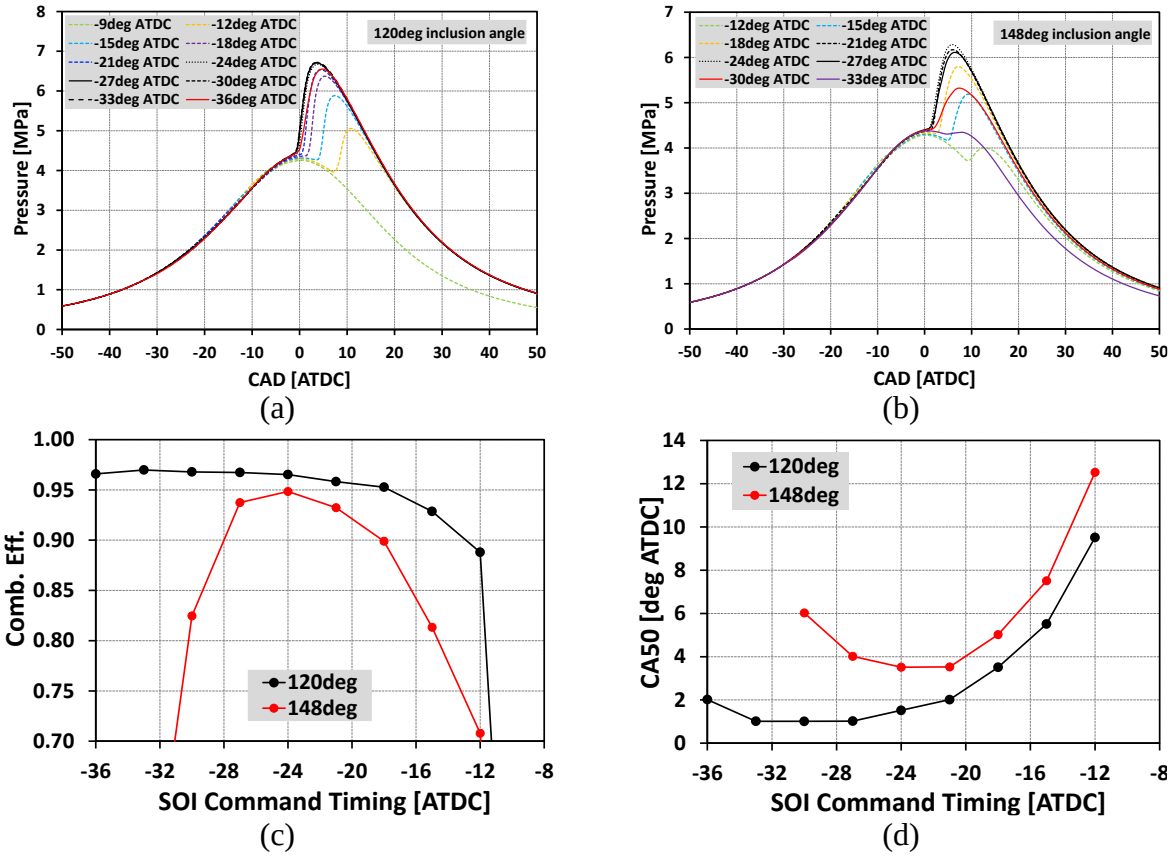

Figure 5.49: Simulated in-cylinder pressure traces at various SOI timings for (a) injector-A [120 deg included angle] and (b) injector-B [148 deg included angle].
(c) Combustion efficiency and (d) CA50 variation with SOI timing sweep using injector-A and injector-B.

Some representative cases at various SOI timings are shown in Figure 5.49 using both injectors. Both injector cases indicate an advancement of CA50 with advanced SOI timings. However, once the stable combustion point was reached, CA50 remained constant for a range of SOI timings and then started retarding further, showing unstable combustion, as can be observed in Figure 5.49d. It can be noted from Figure 5.49c that the SOI timing range for stable combustion is larger for the injector-A simulations. To illustrate the difference in combustion characteristics

with the two different included angles, an earlier SOI timing at -30 deg ATDC and a late SOI timing at -12 deg ATDC were considered for further analysis.

5.3.3.1 Combustion Behavior Using Injector-A and Injector-B at -12 deg and -30 deg ATDC SOI Timings

Figure 5.50 illustrates the difference in combustion behavior at -12 deg and -30 deg ATDC SOI timings using injector-A and injector-B. The difference in pressure and heat release behavior at -12 deg ATDC SOI timing are shown in Figure 5.50a, whereas the results at -30 deg ATDC SOI timing are indicated in Figure 5.50b. Both figures confirm the earlier combustion using injector-A. Earlier combustion phasings using injector-A also verifies the experimentally observed lower fueling amount when compared to injector-B. At -12 deg ATDC SOI timing the heat release started after 5 deg ATDC using both injectors. The equivalence ratio-temperature [phi-T] distribution at Figure 5.50c depicts that the combustion occurs when the equivalence ratio is greater than 0.2. Phi-T distributions at both 10 and 16 deg ATDC are shown in Figure 5.50c and 5.50e, respectively. Both figures show a significant amount of fuel residing in the temperature region less than 1000K while using injector-B, indicating lower combustion efficiency. Similar phenomena were observed for the -30 deg ATDC SOI timing cases. The heat release started near to TDC using both injectors, as shown in Figure 5.50b. The Phi-T distribution at 5 deg and 16 deg ATDC indicate a significant amount of fuel resides in cold regions [less than 1000K] while using injector-B, as can be observed in Figure 5.50d and 5.50f, respectively. Overall, larger mixing times for the -30 deg ATDC SOI case provide better combustion compared to the -12 deg ATDC SOI case using both injectors.

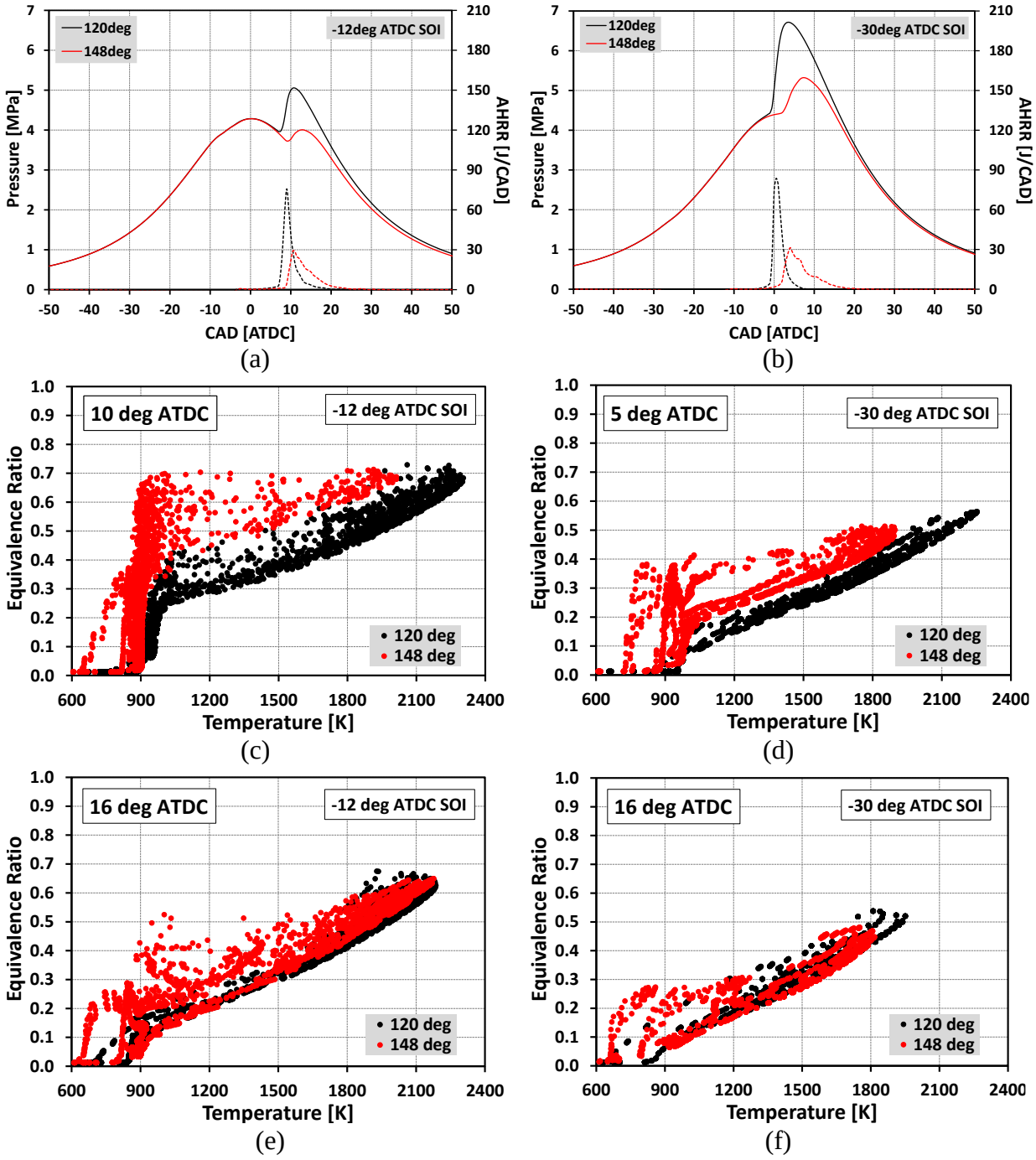

Figure 5.50: Pressure and heat release comparisons using two different injectors at (a) -12 deg and (b) -30 deg ATDC SOI.
Phi-T distribution at -12 deg ATDC SOI timing at (c) 10 deg and (e) 16 deg ATDC.
Phi-T distribution at -30 deg ATDC SOI timing at (d) 5 deg and (f) 16 deg ATDC.

Figure 5.51 compares the equivalence ratio, fuel and temperature distributions at -12 and -30 deg ATDC SOI. At -12 deg ATDC SOI, a locally rich region can be observed at -1 deg ATDC

using injector-A, which helped establish the earlier heat release at 9 deg ATDC. Even though most of the fuel targeted the bowl region using injector-A, due to the effect of swirl and tumble motion some of the fuel was pushed into the squish region, as shown at 16 deg ATDC, resulting in lower combustion efficiency, as explained before. The fuel and temperature distributions at 16 deg ATDC indicate a higher squish flow and lower squish temperature for the injector-B case, supporting the claim of the larger low-temperature region mentioned before using Figure 5.50e. Similar phenomena were observed for the -30 deg ATDC SOI timing case, except the fact that there was hardly any squish fuel for the injector-A case, as most of the fuel had enough residence time to be ignited in the bowl region due to the earlier injection, as can be observed in Figure 5.51.

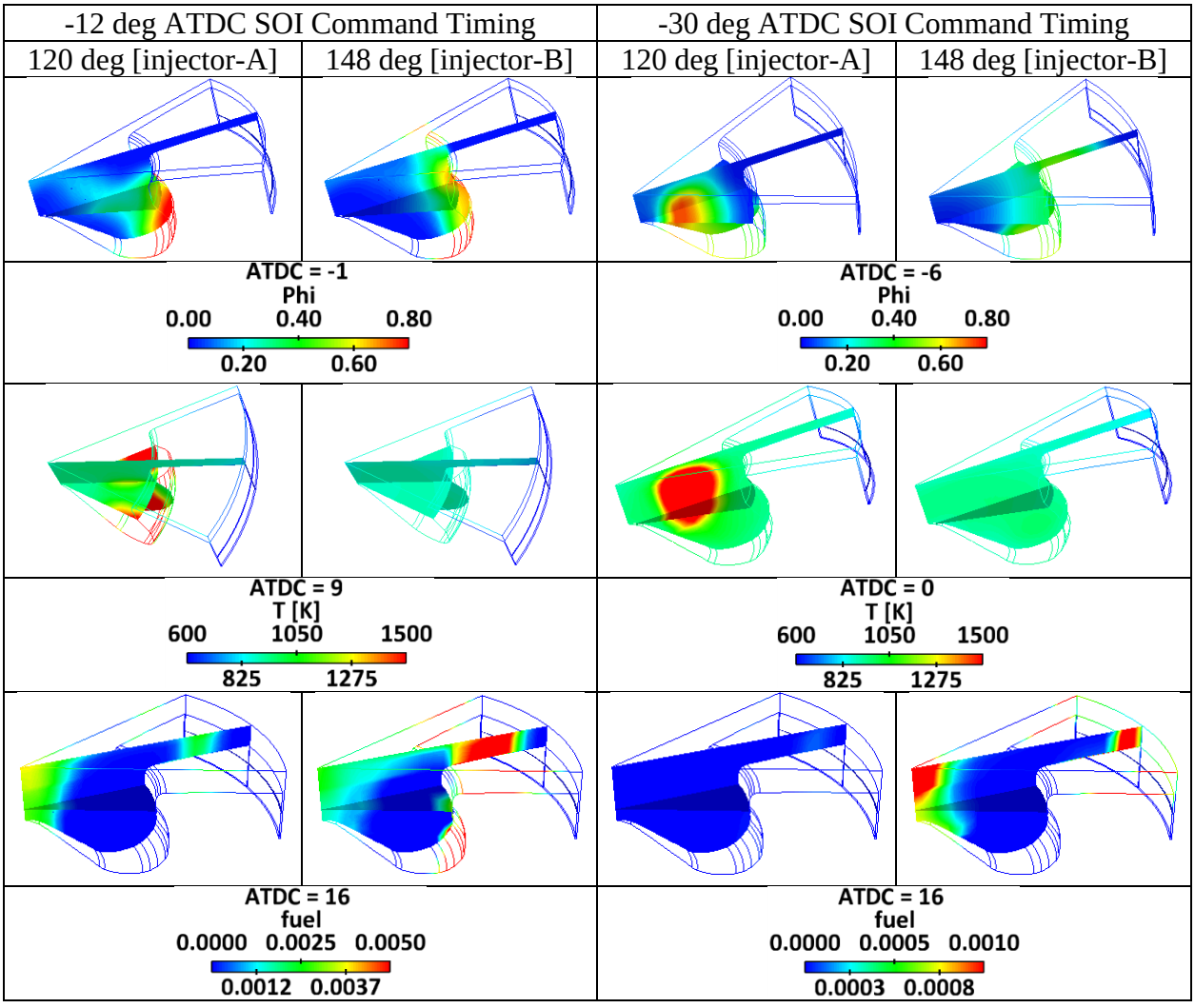

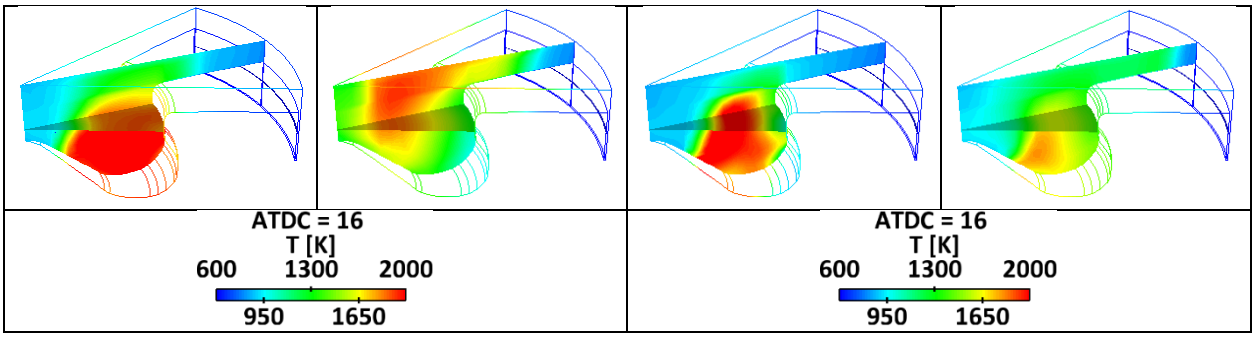

Figure 5.51: Fuel, equivalence ratio and temperature distribution at -12 deg and -30 deg ATDC SOI command timings using injector-A and injector-B

To quantify the amount of fuel residing in the squish region using both injectors, non-reacting simulations were performed. Fuel mass percentages trapped in the squish region were quantified at TDC over a range of SOI timings using both the injectors, as illustrated in Figure 5.52. The SOI timing was varied from -48 deg to -9 deg ATDC with a step-size of 3 deg. Both injector simulations indicated a reduction in trapped fuel-mass when the SOI timing was delayed from -48 deg ATDC, which increased further at very late timings. The figure clearly specifies more trapped fuel with the usage of injector-B for the entire range of SOI timings, satisfying the conclusions provided for the combusting case. For very late injection timings the trapped fuel amount was higher due to the significant squish flow near TDC. For injector-A a significantly high amount of trapped fuel [more than 15%] at an SOI timing of -42 deg ATDC or earlier made it appear to be extremely hard to ignite, whereas for injector-B the timing was -33 deg ATDC or earlier. This result is very similar to that reported by Opat *et al.* [2007], where they observed a significant amount of squish fuel at SOI timings earlier than -30 deg ATDC on similar engine hardware.

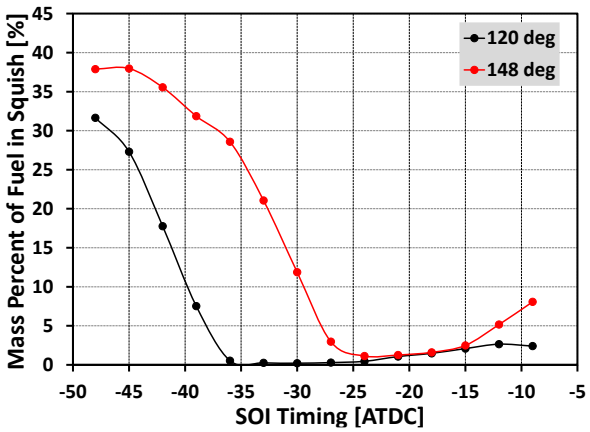

Figure 5.52: Quantification of squish fuel at TDC for non-reacting simulations

5.3.3.2 Combustion Behavior at Different SOI Timings

Figures 5.53a and 5.53b illustrate similar combustion behavior for injector-A from -33 to -24 deg ATDC SOI timings, whereas Figure 5.53b shows the similar behavior for injector-B from -27 to -21 deg ATDC SOI timings. This phenomenon was observed before for the high load cases, as mentioned in Chapter 4, and for the low load cases, as specified in Chapter 5.2. Interestingly, even though the combustion behavior was mostly the same over the range of injection timings, the NO_x emission was lower at earlier timings, whereas the CO emission remained nearly same, as mentioned in Figure 5.53c and 5.53d respectively. However, for injector-B, the CO emission was altered because the spray targeted the re-entrainment part of the bowl, which slightly changed the combustion behavior as well, as can be observed from the pressure trace in Figure 5.53b. CO emission was the lowest for the highest peak pressure point, as expected.

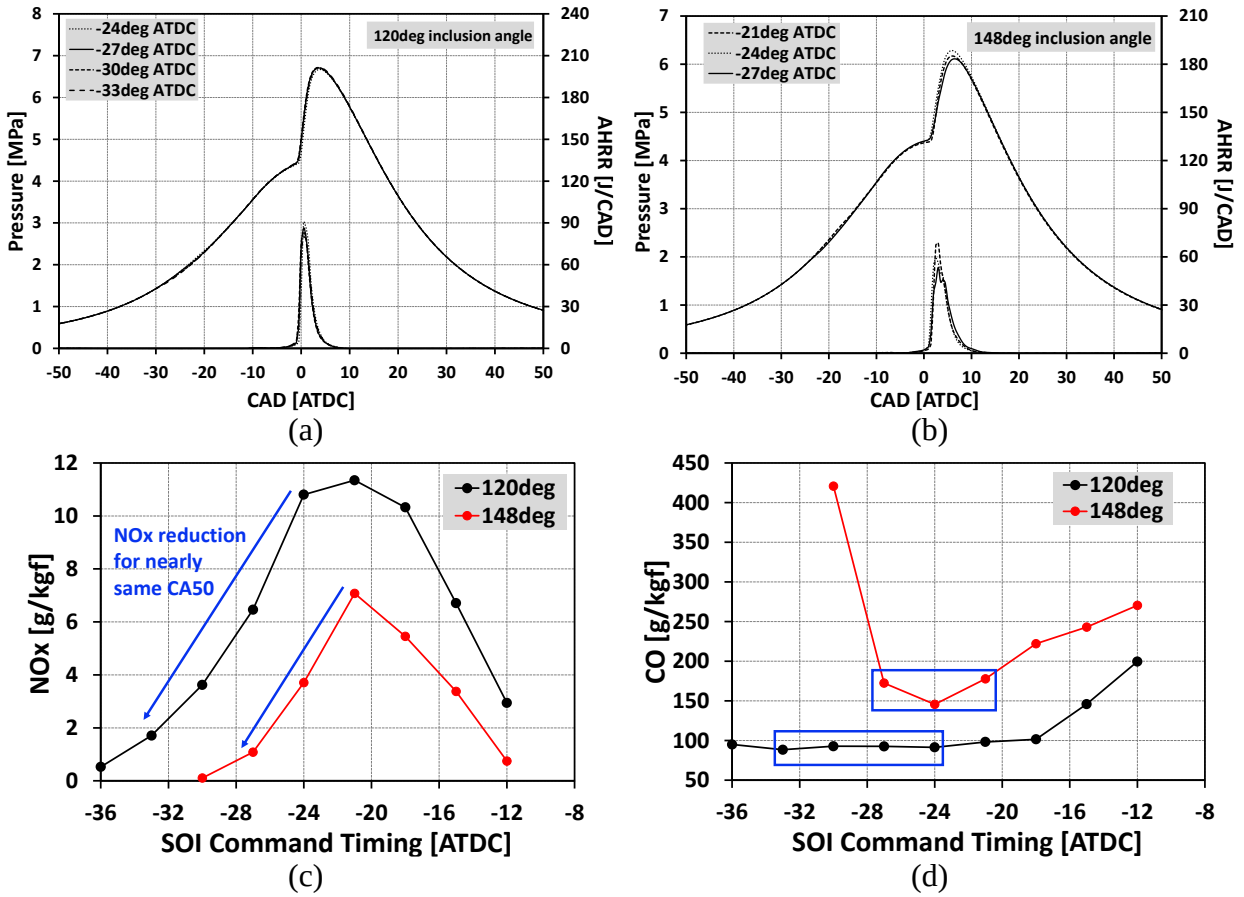

Figure 5.53: Similar pressure and heat release traces for (a) injector-A [120 deg] and (b) injector-B [148 deg].
(c) NO_x and (d) CO emissions over the range of injection timings using injector-A and injector-B.

To explain the NO_x reduction with the advancement in SOI timing, injector-A cases were analyzed using phi-T distribution diagrams. Figure 5.54a represents the phi-T distribution plot before combustion, at -5 deg ATDC, for all four cases, which are shown in Figure 5.53a, whereas Figure 5.54b indicates the phi-T distribution after combustion, at 5 deg ATDC. The distributions were observed to be very similar for all four cases before combustion, where the peak equivalence ratio was lower with the advanced SOI timing because of the more homogeneous fuel distribution, as shown in Figure 5.54a. Therefore, as combustion started from the fuel-rich region, the temperature of the peak equivalence ratio region increased in such a fashion that the higher the peak equivalence ratio, the higher the peak combustion temperature, as can be noticed in Figure

5.54b. With higher peak temperature the phi-T distribution started penetrating the NO_x island and therefore generated more NO_x.

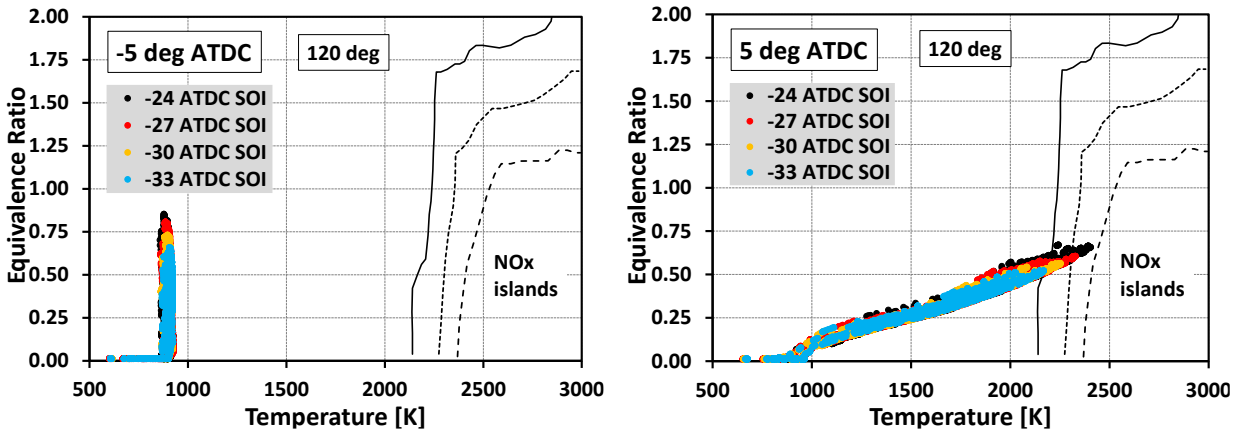

(a) (b)

Figure 5.54: Phi-T distribution at (a) -5 deg ATDC and (b) 5 deg ATDC for injector-A cases at -24, -27, -30 and -33 deg ATDC SOI timings

5.3.4 Discussion

To study the effect of injector included angle, a more accurate 15-component gasoline surrogate chemistry model was used to properly represent the 87 AKI gasoline used in the experiments. Under engine-like conditions the 15-component fuel chemistry predicted lower ignition delays in the low temperature region, resulting in lower IVC temperature required to obtain the same CA50 as with the simpler PRF fuel chemistry. Two different injectors were explored in this study, injector-A with 120 deg included angle and injector-B with 148 deg included angle. The following conclusions can be drawn from the injector included angle study.

a. Compared to the PRF chemistry model, the15-component gasoline fuel chemistry predicted the experimental NO_x emissions using injector-B quite well over the range of SOI timings, whereas the CO was over-predicted, which is thought to be mainly due to the absence of a reliable piston-liner crevice model.

b. Comparison between injector-A [120 deg included angle] and injector-B [148 deg included angle] was made at four different SOI timings, -18, -21, -24 and -27 deg ATDC. All cases indicated earlier combustion using injector-B due to the lower fueling rate used in the injector-A cases. Even though the experimental NOx emission trends were captured well using both injectors, NOx was largely under-predicted in the simulations while using injector-A. This suggests the possibility of wall-wetting in the experiments, which was not captured well in the simulations.

c. Unfortunately, the injector included angle experiments were performed at different load conditions (while maintaining minimum fueling rate at each injection timing). Thus, to make a fair comparison between the two injectors, simulations were carried out from -36 to -6 deg ATDC SOI timings with a step-size of 3 deg, while keeping the initial and boundary conditions the same for all the cases. The results indicated a larger range of stable combustion (-12 to -36 deg ATDC SOI timings) for injector-A, compared to (-15 to -30 deg ATDC SOI timings) the injector-B simulations. This is due to the more effective fuel combustion because the spray targets the bowl region in the combustion chamber using Injector-A. Earlier CA50 and stable combustion using injector-A explains the need for lower fueling rates observed in the experiments when compared to injector-B.

d. Non-reacting simulation results indicated that a significant amount of fuel resided in the squish region while using injector-B over the range of injection timings. The squish fuel was higher for very early injection timings due to the fuel targeting the squish region, whereas at very late injection timings significant squish flow occurred near TDC, also increasing the squish fuel. The span of reasonable injection timings causing a lower amount of squish fuel was found to be a function of the injector included angle.

e. Both injector-A and injector-B displayed a range of SOI timings showing the same CA50 while the NO_x emission was reduced at earlier timings. This was due to the more homogeneous fuel distribution at earlier injection timings, causing lower equivalence ratios and therefore lower peak combustion temperatures.

To further reduce the load while using gasoline, EHN additive experiments were conducted at ANL, which was offered as another solution for the cold-startability issue in GDICI operation. In order to investigate those experiments computationally, an EHN mechanism was developed and validated first, and was later used to explain the ANL data obtained with EHN and 93 RON gasoline, as elaborated next in Chapter 6.

Chapter 6 Effect of EthylHexyl Nitrate [EHN] Additive on Low Load Operation

6.1 EHN Mechanism Development

Alkyl nitrates are a class of chemicals that have been identified as effective fuel additives, which can be used in small amounts to improve the fuel's ignition quality. The weak chemical bonds of these fuels decompose rapidly at modest temperatures, affecting the fuel ignition delay. A common cetane improving additive is EHN, whose chemical formula is $C_8H_{17}NO_3$. EHN is stable at room temperature and its decomposition is even slower in a fuel solution at high pressure [Oxley *et al.*, 2001; Bornemann *et al.*, 2002], which ensures the stability of EHN decomposition within the fuel injection system. EHN decomposition starts once it is injected inside the cylinder. However, once ignition occurs, the details of the combustion process are dictated by the bulk fuel properties [Higgins *et al.*, 1998]. Studies on EHN chemistry [Pritchard, 1989; Al-Rubaie *et al.*, 1991; Clothier *et al.*, 1993; Bornemann *et al.*, 2002] indicate the formation of the heptyl radical, formaldehyde and nitrogen-dioxide [NO_2] in a two-step reaction.

$C_8H_{17}NO_3$ [EHN] → $C_8H_{17}O$ [EHO] + NO_2 [Rxn 1]

$C_8H_{17}O$ → C_7H_{15} + CH_2O [Rxn 2]

This two-step reaction mechanism will be referred to as the Westbrook [WB-EHN] Mechanism. Clothier *et al.* [1993] studied iso-octyl nitrate whose chemical formula is same as EHN, but it has a different chemical structure. They speculated that there might be an HNO_2 [HONO] production step from the interaction between CH_2O and the NO_2 radical. HNO_2 can then be decomposed to NO and OH radicals, where the OH radical can participate in the ignition process and the NO can be recycled to NO_2. Rxn3, Rxn4 and Rxn5 indicate these reaction steps:

NO_2 + CH_2O → HNO_2 + HCO [Rxn 3]

$NO_2 + HCO \rightarrow HNO_2 + CO$ [Rxn 4]

$HNO_2 \rightarrow NO+OH$ [Rxn 5]

Stein *et al.* [1999] used a low-dilution flow reactor [LDFR] to study the initial decomposition temperature of EHN and its corresponding products in the absence of oxygen. This study revealed that the entire decomposition of EHN had occurred by 550K. At 12.5 atm pressure as the temperature was raised, EHN decomposition in a mixture of nC_7H_{16} and 10% EHN (by mole) increased the concentration of formaldehyde [CH_2O] and NO in the mixture. They also showed the importance of considering NO chemistry in determining the auto-ignition temperature of the fuel. They mixed 50 ppm of NO with three different PRF fuels, 0, 87 and 92 PRF respectively, and studied the CO mole fraction evolution with and without NO, and observed a difference. They speculated that, in the temperature range of 780K to 1100K, NO reacts with available HO_2 radicals forming a highly reactive OH radical, as shown in Rxn6 and Rxn7:

$NO + HO_2 \rightarrow OH + NO_2$ [Rxn 6]

$NO_2 + H \rightarrow NO + OH$ [Rxn 7]

This ensures rapid reaction in regions where the H radical branching reaction is not that important.

EHN's molecular structure indicates the weakest bond occurs between the nitrogen [N] and oxygen [O] atoms in the molecule. Therefore, in the newly developed EHN mechanism of the present study the chain initiation step was modeled in such a way that the N-O bond of the nitrate, that connects to the hydrocarbon molecule, breaks to produce a large hydrocarbon species and corresponding small species. EHN decomposition produces alkoxy radicals [EHO] or aldehydes [ECHO] and small nitric species. Following the study of Arenas *et al.* [2008], the nitric products of the uni-molecular decomposition were modeled to be NO_2 and nitrous acid [HONO]. Based on the study of Ra and Reitz [2014] reactions with active radicals were modeled as generic-type

reactions to produce 7 alkyl oxides including the two species produced from the uni-molecular decomposition [Reaction 1-17 in Appendix C]. The alkyl oxides considered in the present study are shown in Table 6.1. The reactions were modeled to include some major characteristics of the oxidation process, including initiation of oxidation process by hydrogen abstraction, formation of fuel radicals by hydrogen abstraction or thermal decomposition, regeneration of active radials such as O, OH and HO_2, formation of carbonyl (aldehydes) and decomposition to smaller radicals and intermediate species.

Table 6.1: Alkyl oxides considered in newly developed EHN mechanism

Name	Structure	Name	Structure
EHN	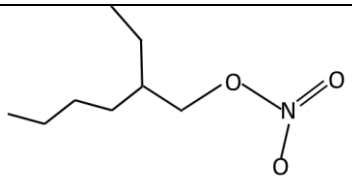	ECHO	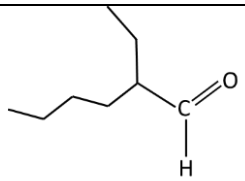
EHOH	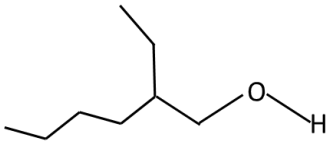	EHOO	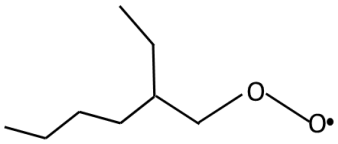
ECOOH	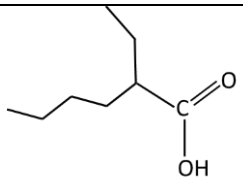	EHO_2	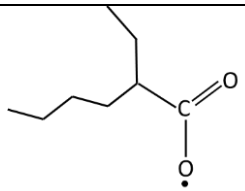
EHO	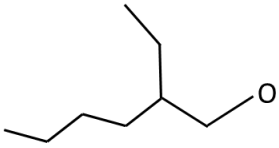	EHOOH	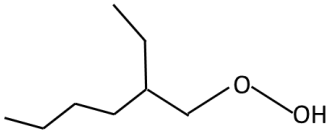

The present study considered five different major abstractors, which include H, OH, O, HO_2, and O_2. Although the formation of conjugate fuel radicals [e.g., the EHN radical from the EHN molecule] was expected, those were not considered for the current mechanism due to their expected negligible effect on the ignition delay and NOx formation. For each active radical reaction with EHN, two reactions were formulated to produce NO_2 [e.g., Reaction 3 in Appendix

C] and HONO [e.g., Reaction 4 in Appendix C], whereas the third reaction was modeled to generate one of the hydrogen abstraction products, such as H_2, OH, HO_2 and H_2O_2. Reaction with molecular oxygen produces OH and HO_2 as active radicals [Reaction 8, 16-18 in Appendix C], which are used in other initiation reactions.

In the mechanism the decomposition of the 7 alkyl oxides are modeled such that the oxygen-containing carbon branch breaks from the rest of the molecule to produce a heptyl radical (C_7H_{15}) and corresponding small species [Reaction 18-24 in Appendix C]. In order to simplify the reaction pathways in the present skeletal reaction mechanism, this process is modeled as uni-molecular decomposition reactions. The products of this decomposition step include highly reactive species such as CH_2OH, HCO and OH, as well as relatively stable species, such as CH_2O, CO and CO_2. The heptyl radicals generated from the decomposition of the alkyl oxides further reacts with the oxygen molecule to enter the degenerate branching process, which accelerates the oxidation reactions. It is notable that, since a significant amount of NO_2 is generated from the EHN reaction kinetics, initiation reactions by NO_2 are considered when the EHN reaction mechanism is coupled with the oxidation mechanism of the main fuels [e.g., $nC_7H_{16}+NO_2=C_7H_{15}+HONO$].

The kinetic parameters of the modeled EHN reactions were first obtained from similar elementary reactions in detailed mechanisms for the same carbon-number n-alkane, i.e., n-octane [Westbrook *et al.*, 2009]. After considering the reported high reactivity of EHN at low temperatures, the reaction rate constants were adjusted based on an ignition delay sensitivity analysis [Ra *et al.*, 2011] under various temperature and pressure conditions, so that the predicted ignition delay curves captured the reported reactivity of EHN available in the literature. It is well known that the energy barrier to produce the intermediates can vary depending upon the molecule's structure. However, in the present study, the reactions involving one specific reactant radical were

modeled to have the same energy barrier, since the generic reactions combine several reaction classes into a one-step reaction.

To complement the NO_x formation reactions, additional reactions involving HONO and its isomer, HNO_2, were considered in the present study. Rasmussen *et al.* [2008] studied the effect of NO_x on methane [CH_4] oxidation in a laboratory-scale high pressure laminar flow reactor. Their results revealed a significant decrease in the chain-initiation reaction temperature upon addition of nitrogen oxides. The reaction of nitrogen oxides with the O/H radical pool produced chain-initiating OH radicals and also contributed to the chain-propagating cycle, where the reaction of NO/NO_2 with hydrocarbon radicals produced NO_2/NO. Rxn8 and Rxn9 below are an example.

$NO_2 + CH_3 \rightarrow NO + CH_3O$ [Rxn 8]

$NO + CH_3O_2 \rightarrow NO_2 + CH_3O$ [Rxn 9]

Based on the above study and the research of Hori *et al.* [1998], NO_x and hydrocarbon interaction reactions were considered in the newly developed EHN mechanism along with some additional NO_x formation reactions. This new mechanism will be referred to as the ERC-EHN mechanism from now onwards in this work and the mechanism is detailed in Appendix C.

6.2 EHN Mechanism Validation Using Shock-Tube Data

The newly developed EHN mechanism was added to the 15-component gasoline surrogate model [Ra *et al.*, 2014] to simulate HCCI experiments of Dempsey *et al.* [2013] using gasoline and EHN additive, where the EHN amount was varied from ~0-10% by mass. For brevity the 15-component fuel chemistry mechanism will be referred as the 15-Comp mechanism from now onwards. Chemical reactions of many higher order hydrocarbon species chemistry are included in this mechanism, which has been extensively validated by Ra *et al.* [2014]. Figure 6.1 compares the experimental and simulated ignition delays of nC_7H_{16} and iC_8H_{18} at 40 bar pressure and at

stoichiometric conditions. The nC_7H_{16} experimental data was obtained from Hartmann *et al.* [2009], whereas iC_8H_{18} data is from Fieweger *et al.* [1997].

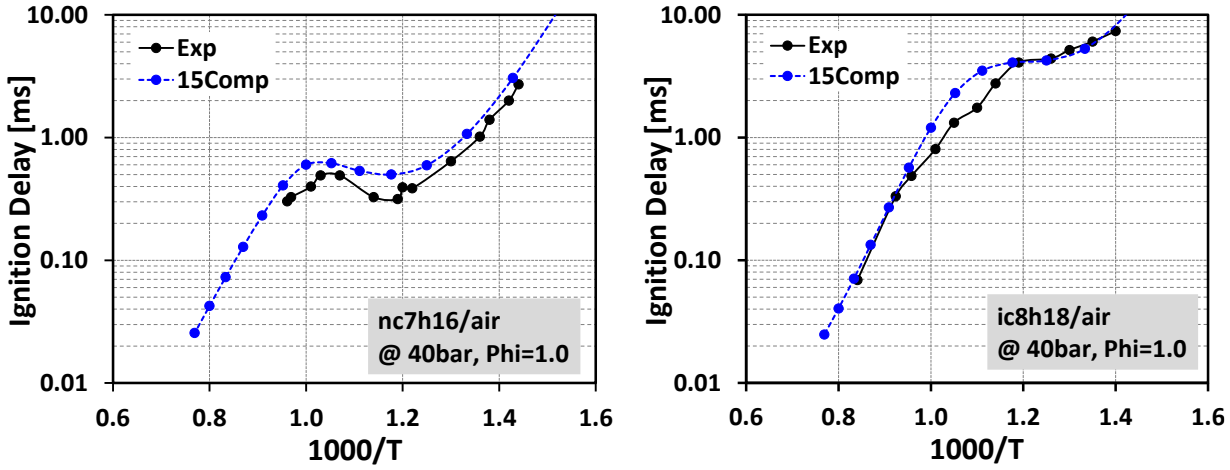

Figure 6.1: Constant volume stoichiometric ignition delay of (a) nC_7H_{16}/air and (b) iC_8H_{18}/air at 40 bar pressure

Figure 6.1 indicates that the 15-Comp mechanism slightly over-predicts the experimental ignition delay of nC_7H_{16} over the entire range of temperatures. On the other hand, the iC_8H_{18} ignition delay in the range of 850K to 1000K is slightly over-predicted in simulations. However, considering the complexity of large mechanism validation, this small discrepancy was ignored and the 15-Comp mechanism was used as the base fuel mechanism for the rest of the simulations reported in this Chapter.

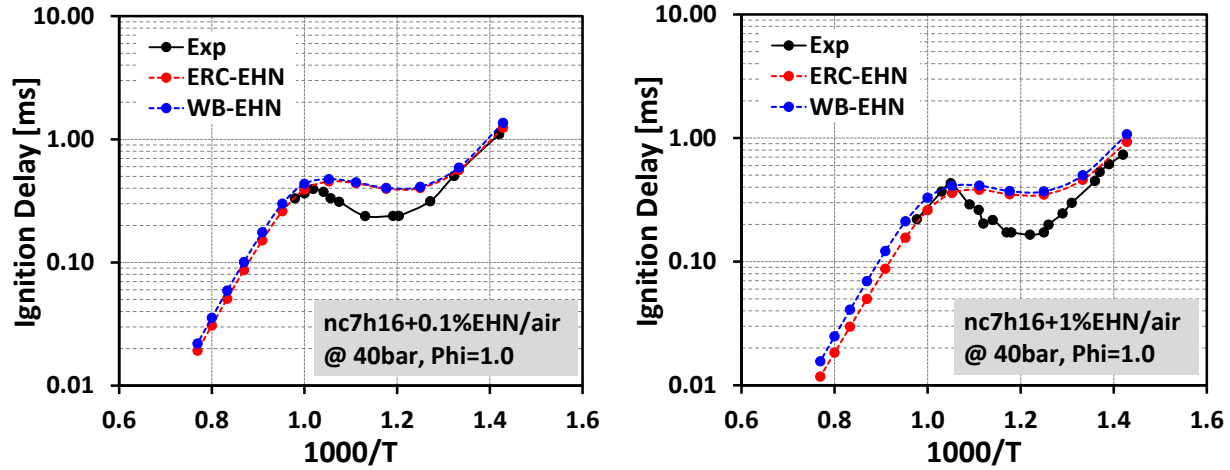

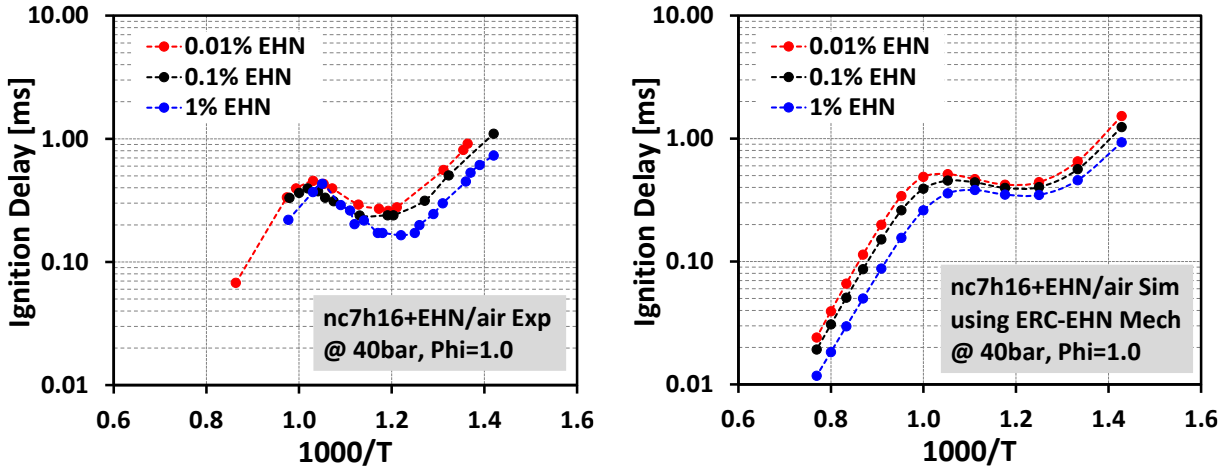

Figure 6.2: Constant volume ignition delay (a) comparisons of nC_7H_{16}/0.1%EHN/air experiments and simulations, (b) comparisons of nC_7H_{16}/1%EHN/air experiments and simulations, (c) experiments of nC_7H_{16}/air with various EHN amount, (d) simulations of nC_7H_{16}/air with various EHN amount at 40 bar pressure and stoichiometric condition

Figures 6.2a and 6.2b compare the performance of the WB-EHN and ERC-EHN mechanisms with the only available experimental shock-tube data from Hartmann *et al.* [2009]. 0.1% and 1% by mass of EHN were used in the mixture of nC_7H_{16} and EHN at stoichiometric conditions and 40 bar pressure. The figures indicate an over-prediction of the ignition delay in the simulations using both mechanisms, which can be partly attributed to the over-prediction of the nC_7H_{16} and iC_8H_{18} mechanism, which was observed in Figure 6.1. Both EHN mechanisms are in close agreement with each other, whereas the ERC-EHN mechanism appears to be slightly more reactive. Interestingly, the discrepancy between the two mechanisms increases for a higher percentage of EHN. Figure 6.2c indicates the change in ignition delay with the gradual change of EHN mass-percent from 0.01% to 1% in nC_7H_{16}/EHN shock-tube experiments. The trend indicates that the reactivity increases with EHN addition, which is captured well in the simulations, as shown in Figure 6.2d. However, early ignition of nC_7H_{16} and the very small percentage of EHN usage makes validation difficult as the ignition delay time differences are small.

The literature also includes RCM experiments using the EHN additive. However, the heat transfer and blow-by effects seen using an RCM complicates comparisons with simulations. Therefore, RCM data was not used, but details of RCM simulation attempts are provided in Appendix B.

The present results indicated that the presence of NO_x chemistry in the ERC-EHN mechanism did not have any significant impact on the ignition delay. However, the investigated EHN percentage was very small and also it was found to have an impact on NO_x emission predictions.

6.3 Validation of HCCI Experiments Using Gasoline and EHN

To explore the effect of the ERC-EHN mechanism on NO_x emission predictions, simulations were performed to validate the HCCI experiments conducted by Dempsey *et al.* [2013]. The experiments were carried out using the single-cylinder version of the 4-cylinder GM engine, as mentioned in Chapter 3.1, at global equivalence ratios of 0.26 and 0.3. The intake temperature was varied from 30 to 90C with a step-size of 15C. The EHN mass-percent in 96 RON gasoline was changed from ~0.47% to 9.5% over the range of intake temperatures. Details of the experiments can be obtained from Dempsey *et al.* [2013].

Simulations were executed at three different intake temperature conditions, 60, 75 and 90C, at an equivalence ratio of 0.26. The conditions were chosen in such a way that the EHN effect could be investigated in a reasonable intake temperature window. As 2-D and 3-D HCCI simulations gave very similar results, as shown in Appendix A, all HCCI simulations mentioned in this section were carried out using 2-D grid for computational efficiency.

It is well accepted that HCCI combustion is mainly fuel chemistry-driven, and the fuel physical properties do not have much impact on combustion. However, it is important for spray

experiments and also HCCI simulations, that the fuel properties are properly defined. Due to the unavailability of physical property data for EHN, it was modeled using n-Heptyl Benzene [$C_{13}H_{20}$] properties, which are reported to be similar to the additive [2EHN Industry Work Group, 2004]. Some of the physical properties are compared in Table 6.2, which shows that the molecular weight, the vapor pressure and the latent heat of vaporization of EHN and $C_{13}H_{20}$ are quite in agreement. However, EHN has a higher density and lower viscosity.

Table 6.2: Physical properties of EHN and $C_{13}H_{20}$

	MW [g/mol]	Density [mg/cc]	Viscosity [cSt]	Boiling Temperature [K]	Vapor Pressure @ 20C [Pa]	Latent Heat of Vaporization [kJ/kg]
EHN	175.23	0.960	1.80	> 373	27.0	368.0
$C_{13}H_{20}$	176.30	0.857	2.15	518.63	28.4	371.5

The 93 RON fuel composition from Chapter 5.3 was used for the gasoline modeling. Figure 6.3 shows the change in distillation curve when EHN is added to the 15-component gasoline surrogate model. To consider the polarity effect of the EHN molecule, simulations were performed with and without UNIFAC [Jiao, 2010]. The figure indicates that the distillation curve is not influenced significantly by non-ideal vaporization and polar molecule effects. As EHN is a heavy fuel component, the distillation curve clearly shows an increase in boiling temperature with EHN addition, as expected.

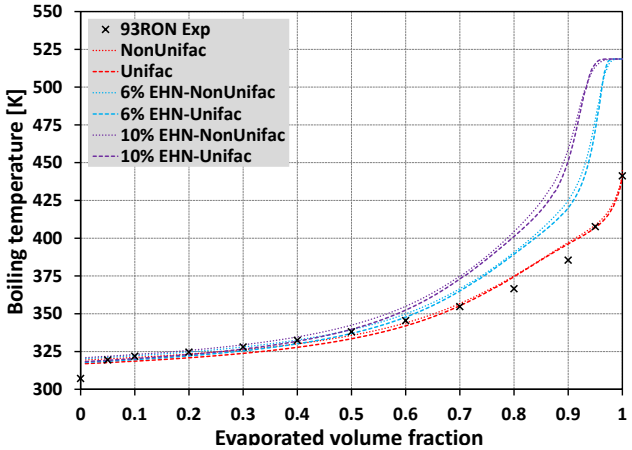

Figure 6.3: Change in distillation curve with the addition of EHN

6.3.1 Comparison between WB-EHN and ERC-EHN Mechanisms at 60C HCCI Conditions

60C intake manifold temperature HCCI experiments were performed by varying the EHN mass-percent from ~1% to ~9.5%. Figure 6.4a shows the bulk gas temperature at IVC used in the simulations with the two different EHN mechanisms. The simulations required an increase in bulk gas temperature at IVC to capture the experimental CA50 for higher levels of EHN doping. Considering the IVC temperature distribution from the full cycle simulation presented in Figure A-5 of Appendix A, an increase in the computational IVC gas temperature can be accepted, as also discussed in Chapter 5. It is interesting to note that the IVC temperatures are well correlated to the experimental exhaust gas temperatures, as well as with the EVO temperatures from the simulations, as shown in Figure 6.4a. This implies that hotter internal residual gas exists in the cylinder at IVC for the higher EVO temperature cases, justifying the increase in IVC temperature. Similar correlations between IVC and EVO temperatures was observed in Chapter 5.2. However, the IVC gas temperature needed to be raised even more while using WB-EHN mechanism. The difference in IVC temperature using the two different EHN mechanisms also increased at higher levels of EHN doping, which supports the observation of higher discrepancies in ignition delay for larger EHN percentages, as shown in Figure 6.2a and 6.2b.

Figure 6.4b shows the CA50 comparison between the experiments and the simulations using the two different EHN mechanisms. The predicted CA50s using the ERC-EHN mechanism are slightly longer than the experiments for higher amounts of EHN doping, whereas the WB-EHN mechanism shows an excellent agreement. Previously it was observed that the WB-EHN mechanism was slightly less reactive compared to the ERC-EHN mechanism, and for higher EHN percentages the reactivity difference becomes prominent. Thus, the agreement in CA50 can be

attributed to the reactivity increase due to the elevated IVC temperature while using the WB-EHN mechanism.

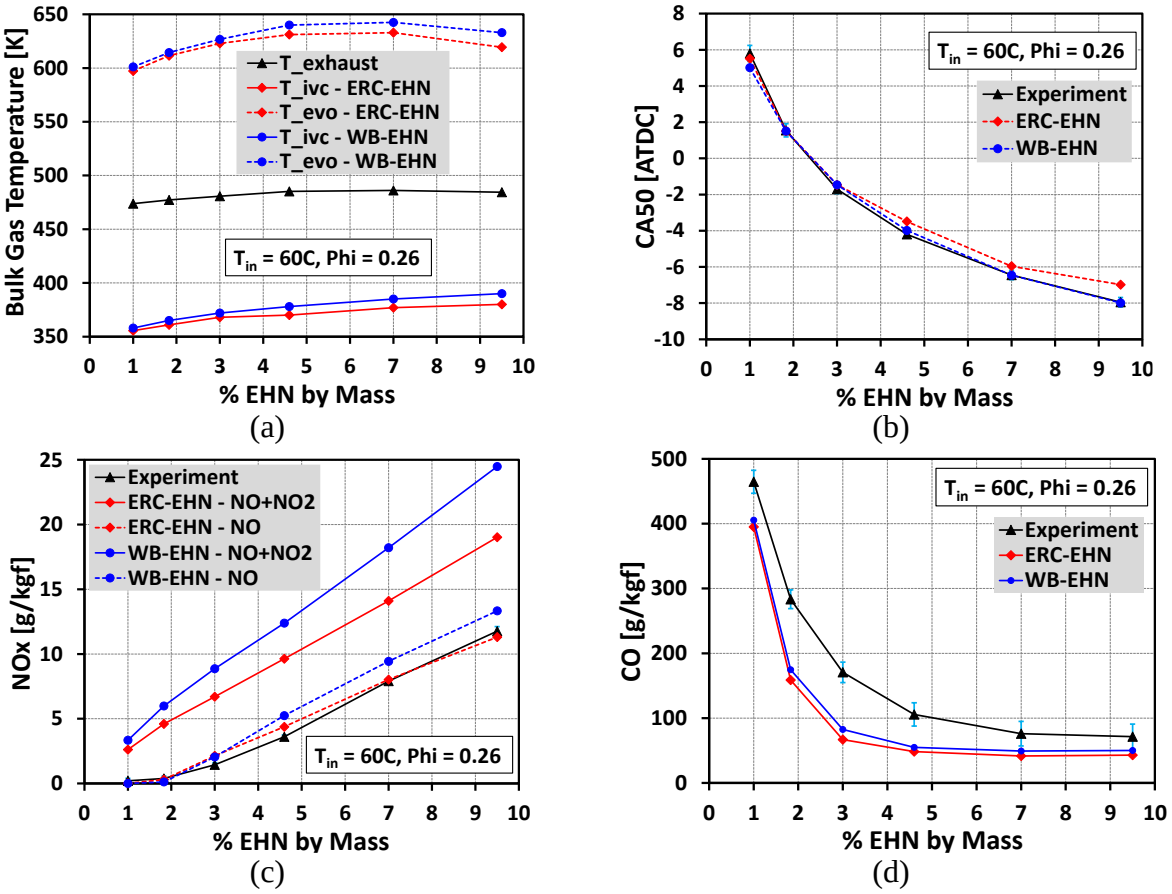

Figure 6.4: (a) Change in bulk gas temperature, (b) CA50, (c) NO_x and (d) CO emission comparisons between experiments and simulations with the change in EHN doping level for 0.26 equivalence ratio and 60C intake temperature conditions

Figures 6.4c and 6.4d compare the NO_x and CO emissions, respectively. In both experiments and simulations NO_x emission indicate the sum of NO and NO_2 amounts. Therefore 'NO+NO2' in the legend is referred as NO_x from now onwards. As can be observed in Figure 6.4c both EHN mechanisms captured the experimental NO_x emission trend, however, it was largely over-predicted. On the other hand, considering only NO emission came closer to the experimental NO_x emission. This indicates the possibility of a NO_x measurement issue while conducting the experiments. In the experiments, the total NO_x is measured with a chemiluminescence analyzer.

Chemiluminescence is the process of photon emission during a chemical reaction. When nitric oxide (NO) reacts with ozone (O_3), chemiluminescence detects the intermediate product, NO_2, during the reaction [Heywood, 1988]. Therefore the exhaust gas sample is first passed through a catalyst, which converts the NO_2 to NO prior to being sent to the analyzer. However, if there is catalyst poisoning, the NO_x emission from the experiment only indicates NO [Dempsey *et al.*, 2015].

The CO predictions from both mechanisms are in agreement, as can be observed in Figure 6.4d. The experimental CO emission trend is captured well, however, it is mostly under-predicted in the simulations. The CO emission is mostly from the crevice and squish regions, as portrayed in Figure 6.5. Under-prediction of CO could be attributed to the unreliability of the crevice model used in the simulations, along with uncertainties in the experimental data. All the simulation results presented in the following are with ERC-EHN mechanism, unless otherwise mentioned.

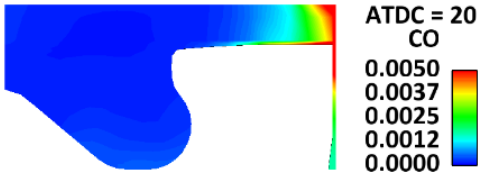

Figure 6.5: CO emission for 3% EHN case at 60C and 0.26 phi

To understand the thermal effect of EHN addition, constant volume ignition delay simulations were performed at 900K initial temperature, 40 bar pressure and 0.3 equivalence ratio using 15-component gasoline and EHN additive. Figure 6.6a shows an earlier temperature evolution with EHN addition. However, this does not indicate any temperature increase at the initial stage due to the addition of EHN, as observed with DTBP cetane improver [Wang *et al.*, 2014], which confirms that the chemical effect of EHN prevails over the thermal effect.

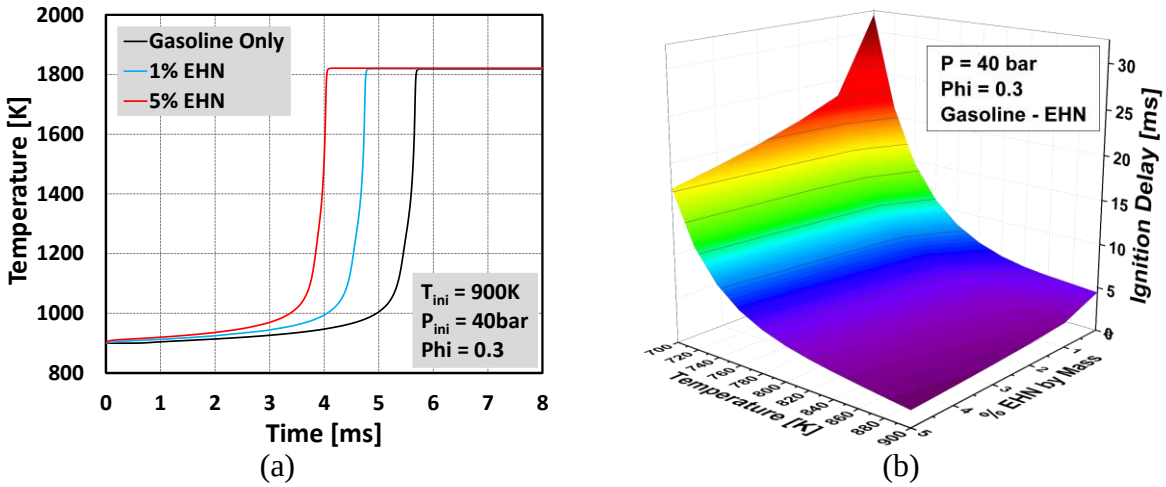

(a) (b)

Figure 6.6: (a) Temperature profile for 15-component gasoline and EHN mixture [by mass] at 900K temperature, 40 bar pressure and 0.3 phi (b) Effect of initial temperature and EHN addition on gasoline ignition delay

Constant volume simulations were further extended to evaluate the reactivity of EHN on gasoline over a range of temperatures and EHN mass fractions. Figure 6.6b indicates that the reactivity of gasoline can be increased by either increasing the initial temperature or the EHN addition. EHN additive is found to be more effective under low temperature conditions. Also, it is evident from the figure that the initial temperature has stronger effect at lower EHN amount. Overall, similar ignition delays can be obtained with a different combination of initial temperature and EHN content. This justifies performing the HCCI experiments using a range of intake temperatures and EHN amounts.

6.3.2 Engine performance Validations at 60, 75 and 90C Intake Temperature Conditions

As mentioned earlier, three different experimental intake temperature conditions were chosen for the validations (60, 75 and 90C). Figure 6.7 represents the pressure profile comparisons at 60C, where the EHN doping level was varied from 1% to 9.5%.

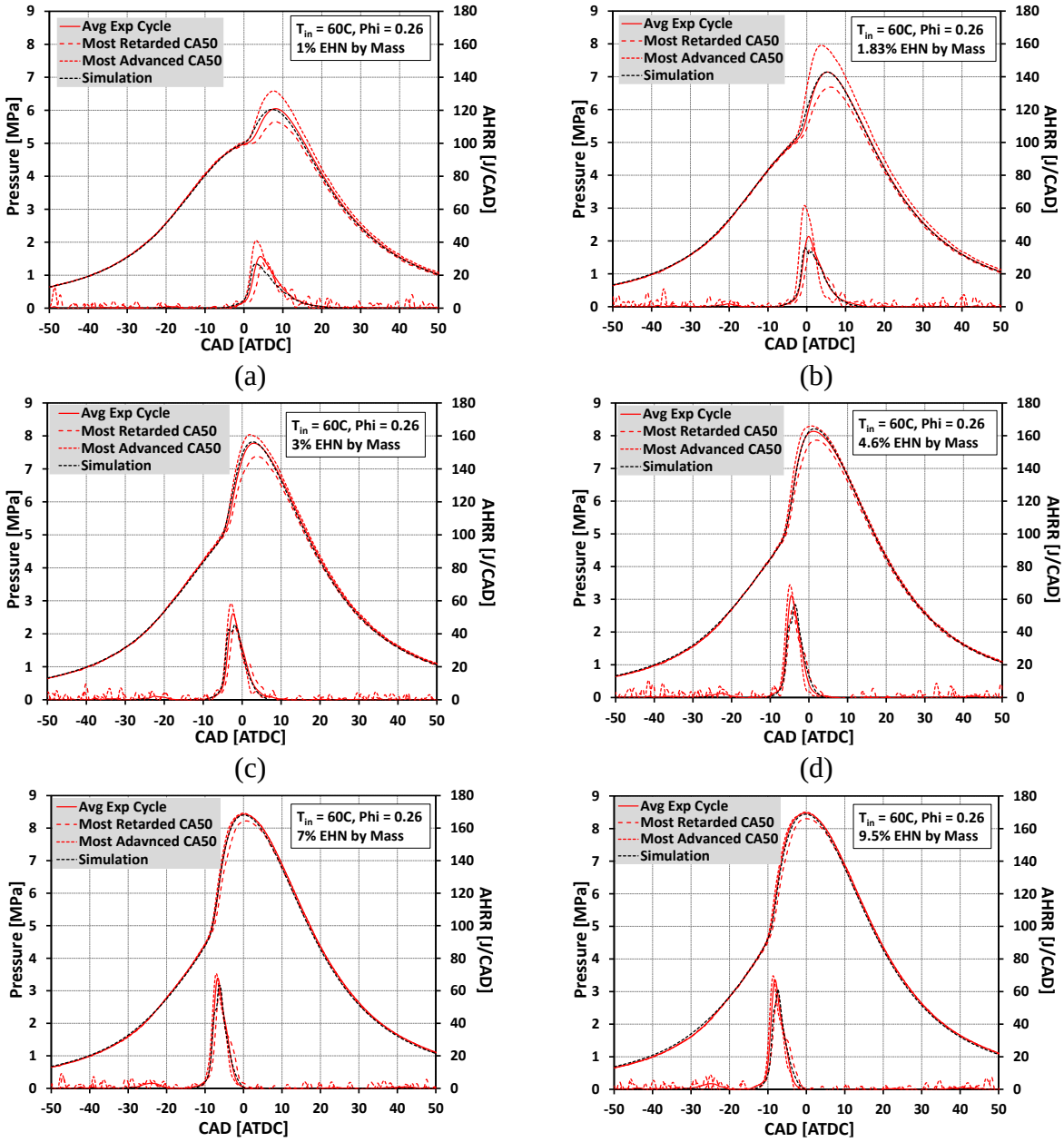

Figure 6.7: Experimental and simulated pressure and heat release comparisons at 60C intake temperature and 0.26 phi

Each figure in Figure 6.7 shows the pressure and heat release data from the average experimental cycle [Avg Exp Cycle] (which is the average of 300 cycles), a cycle representing the most retarded CA50 in the experiments, a cycle representing the most advanced CA50 in the experiments, and the simulations. The most retarded and most advanced cycles describe the bounds

of CA50 and peak pressures for a specific set of experiments. It also shows that simulating the average cycle data is not always representative as there is a possibility of CA50 uncertainties in experiments. Therefore, it is not expected that the simulated result captures the average experimental cycle. However, all figures indicate very good agreement between the average experimental data and the simulated results. The heat release traces and durations are captured quite well in simulation. It can be noted that the cycle-to-cycle variation of CA50 and peak pressure in experiments reduce with higher amounts of EHN, which can be due to the difficulty of controlling very small amounts of EHN in the fuel flow-rate measurements.

Figures 6.8 and 6.9 show similar validation of the pressure and heat release traces for 75 and 90C, respectively. The EHN amount was varied from 0.66 to 6.6% for 75C and 0.47 to 2.79% for 90C cases. With higher intake temperatures the amount of EHN doping had to be reduced to avoid violent combustion. As observed for the 60C cases, the 75 and 90C cases also indicate larger CA50 and peak pressure bounds for lower EHN amounts, whereas the variation is reduced significantly with an increase in EHN doping.

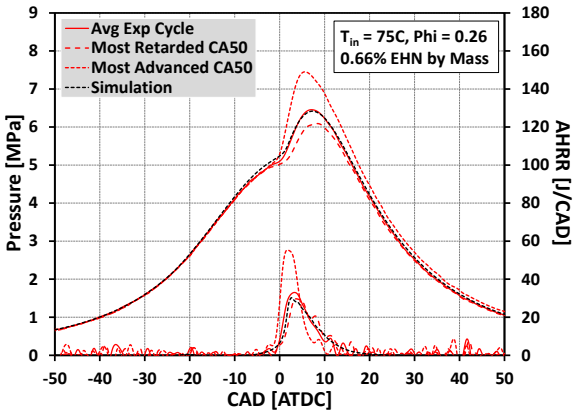

(a)

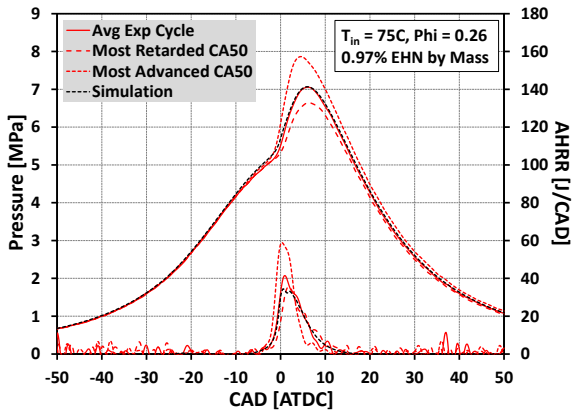

(b)

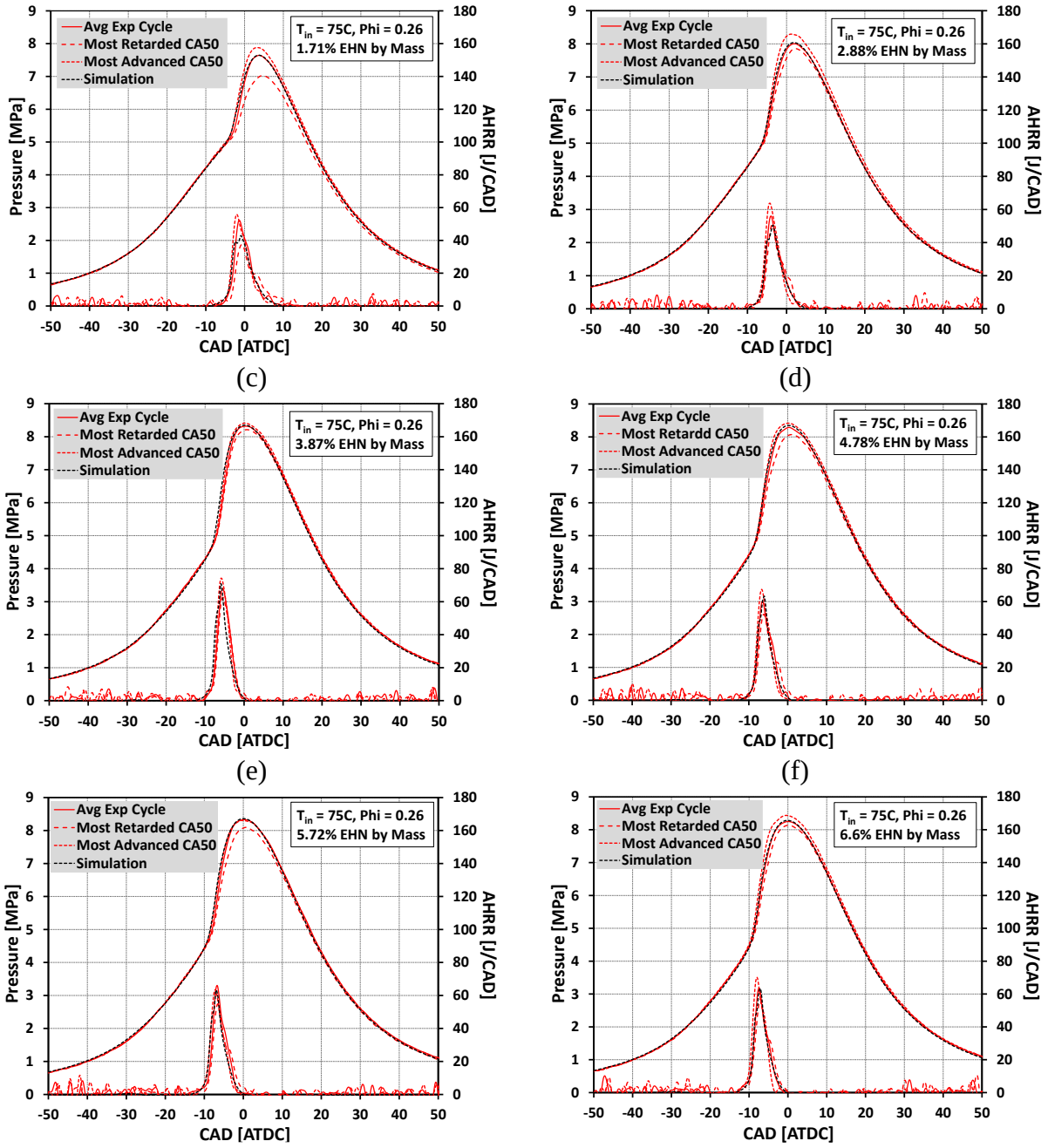

Figure 6.8: Experimental and simulated pressure and heat release comparisons at 75C intake temperature and 0.26 phi

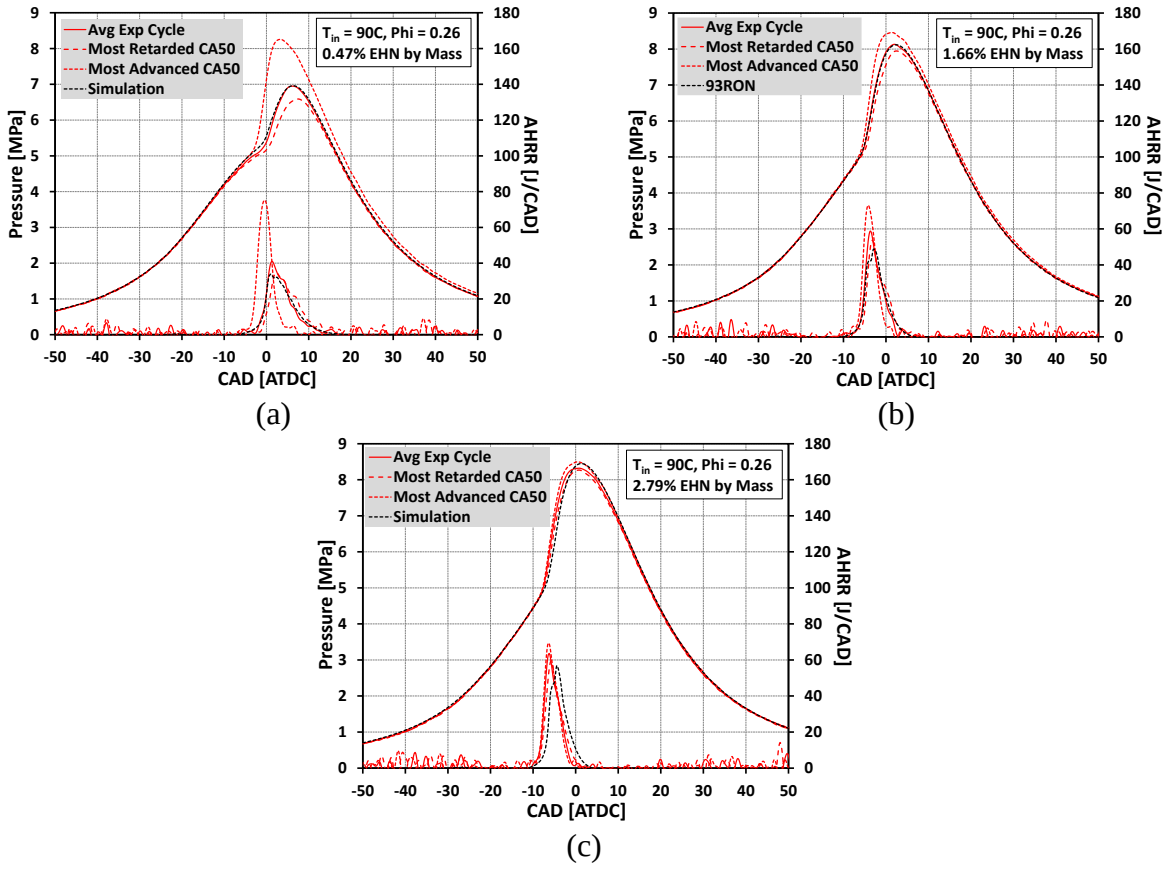

Figure 6.9: Experimental and simulated pressure and heat release comparisons at 90C intake temperature and 0.26 phi

Figure 6.10a presents the exhaust gas temperature from the experiments and the IVC and EVO temperatures from the simulation over a range of EHN doping levels at 60, 75 and 90C intake temperatures. As explained before, the figures demonstrate a correlation among the IVC, EVO and exhaust gas temperatures, justifying an increase in IVC temperature with higher EHN percentage due to the presence of hotter residual gas at IVC.

The simulated CA50 matches the experimental CA50 quite well over the range of intake temperatures, as illustrated in Figure 6.10b. However, a noticeable discrepancy is observed for the 2.79% EHN case at 90C intake temperature, but it is within the CA50 bound, as can be observed in Figure 6.9c. Figure 6.10b also indicates that in order to obtain the CA50 at TDC, ~2.5% EHN

is required at 60C intake temperature, whereas ~1.5% and ~1.1% EHN are needed at 75 and 90C intake temperatures respectively, which complements the ignition delay map shown in Figure 6.6b.

As mentioned before, it is likely that the present HCCI experiments only measured NO emission instead of both NO and NO_2 [Dempsey *et al.*, 2015]. Therefore, both NO_x and NO emissions are plotted from the simulations in Figure 6.10c. Both the emission trends capture the experimental NO_x trends. However, at all three intake temperature conditions, the predicted NO is found to be in closer agreement with the experimental NOx. Experiments performed by Ickes *et al.* [2009], Kaddatz *et al.* [2012] and Dempsey *et al.* [2013] indicated the result that the NO_x emission is equivalent to $1/3^{rd}$ of the fuel-bound NO_2 when EHN is used as a fuel. Therefore, the $1/3^{rd}$ line was also plotted in the NO_x emission graphs at the three intake temperature conditions. At the 60C intake temperature, $1/3^{rd}$ of fuel-bound NO_2 slightly over-predicts the experimental NO_x emission for less than 4.5% EHN, whereas it under-predicts for EHN percentages higher than 4.5%. At the 75 and 90C intake temperature conditions, $1/3^{rd}$ of fuel-bound NO_2 over-predicts the experimental NO_x emissions over the entire range of EHN percentage. However, assuming that the experiments measured only NO and not NO_2, $1/3^{rd}$ of the fuel-bound NO_2 exhibits a significant discrepancy compared to the actual NO_x measurements.

CO emission comparisons are indicated by Figure 6.10d at all three intake temperature conditions. For the entire range of EHN and intake temperature variations, CO is under-predicted in the simulations, which can again be attributed to the unreliability of the piston-liner crevice model and experimental uncertainties. However, overall experimental HCCI engine performance using the EHN additive was reasonably well-predicted by the newly developed ERC-EHN mechanism.

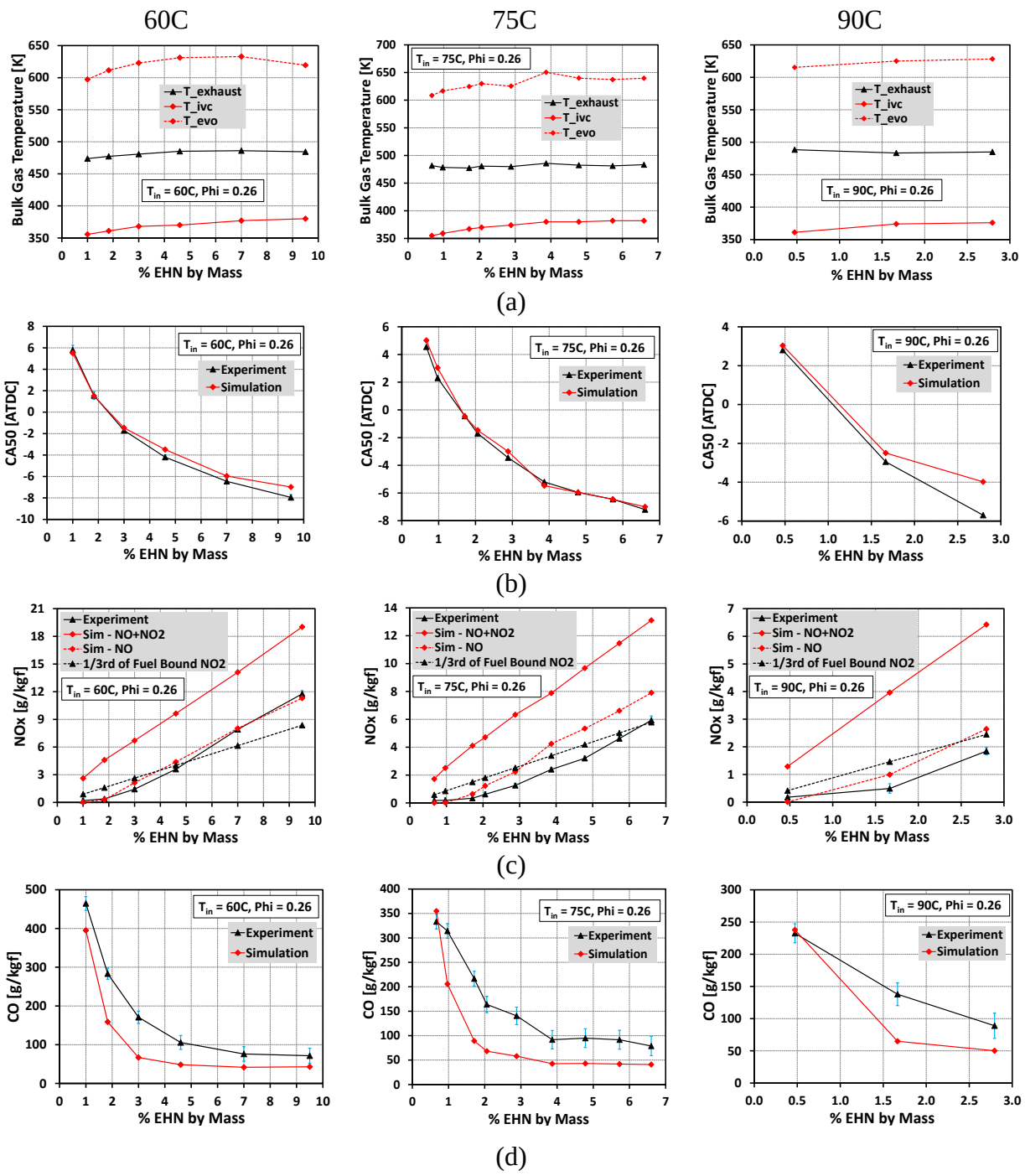

Figure 6.10: (a) Change in bulk gas temperature plot. Comparison between experimental and simulated (b) CA50 (c) NO_x emission and (d) CO emission at 60, 75 and 90C intake temperatures and 0.26 phi

6.4 PRF Map Generation Using Gasoline and EHN Mixture

From the simulation perspective an effort was made to generate a PRF map, which indicates the equivalent change in fuel PRF number with the addition of EHN with gasoline and 96 PRF fuel. 96 PRF was chosen considering the fact that 96 RON gasoline fuel can be modeled as 96 PRF. The fuel energy was kept almost constant at ~418 J for all the simulation results mentioned in this section. Therefore, the fuel amount needed to be adjusted slightly with varying percentages of EHN. As the PRF2 mechanism was previously well-validated by Wang et al. [2013], the mechanism was used for all the present PRF fuel maps, whereas the 15-component fuel chemistry was used to represent gasoline. 93 RON gasoline fuel components were used for the 87 AKI gasoline simulations. The initial conditions for the 96 PRF simulation with EHN were obtained from the 60C intake temperature simulation at 3% EHN, and the corresponding pressure and heat release traces are shown in Figure 6.7c. To determine the IVC temperature for the 15-component simulations with EHN, the CA50 at 1% EHN was compared using both the 15-component and 96 PRF base fuels.

Figure 6.11 shows a comparison between the 96 PRF and 15-component base fuels using 1% EHN additive, keeping the fuel energy constant. The results indicate almost similar pressure and heat release distributions, however, the PPRR and the peak heat release were slightly higher in the 96 PRF case. At 1.35 bar IVC pressure, the IVC temperature for 96 PRF simulation was 390K, whereas it was 360K for the 15-component simulation, which showed almost similar CA50 as the 96 PRF case. Therefore, the rest of the 96 PRF base fuel simulations were performed using 1.35 bar IVC pressure and 390K IVC temperature, whereas the 15-component simulations were performed using the same IVC pressure but 360K IVC temperature.

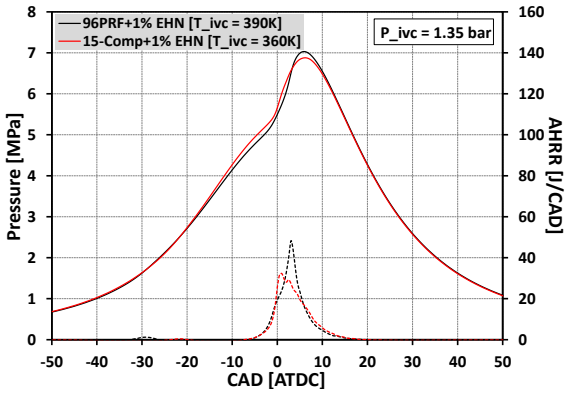

Figure 6.11: Pressure and heat release comparison at 1% EHN condition using 96 PRF and 15-component fuel

The fuel and EHN simulation results shown in Figure 6.12 correspond to the primary horizontal axis, which indicate the variation of EHN percentage, whereas the PRF simulation results correspond to the secondary horizontal axis, which specifies the PRF number variation. The EHN amount was varied from 1 to 20% by mass in the additive simulations, whereas the PRF number was varied from 40 to 100 in the PRF-only simulations. '87AKI Gasoline' in the legends of all the figures indicates the 15-component fuel chemistry representing 93 RON gasoline. As mentioned earlier, the fuel energy was held constant at ~418J for all the simulation, as specified in Figure 6.11a. However, for 96 PRF simulations with EHN additive, the energy changed by less than 0.5% with the increase in additive amount, which is negligible. With constant fuel energy, the global equivalence ratio changed slightly around 0.28 for the EHN cases, whereas it was close to 0.26 for the PRF cases, as can be observed in Figure 6.12b. Figure 6.12c shows the pressure rise rate which is less than 12 bar/deg for all cases. However, higher than 80 PRF number showed a very low pressure rise rate in the 'PRF-only' computations, which is due to poor combustion because of the lower auto-ignitability characteristics, as can be observed from the combustion efficiency plot in Figure 6.12d. Except for less than 2% EHN, all other cases revealed ~90% combustion efficiency, as portrayed in Figure 6.12d.

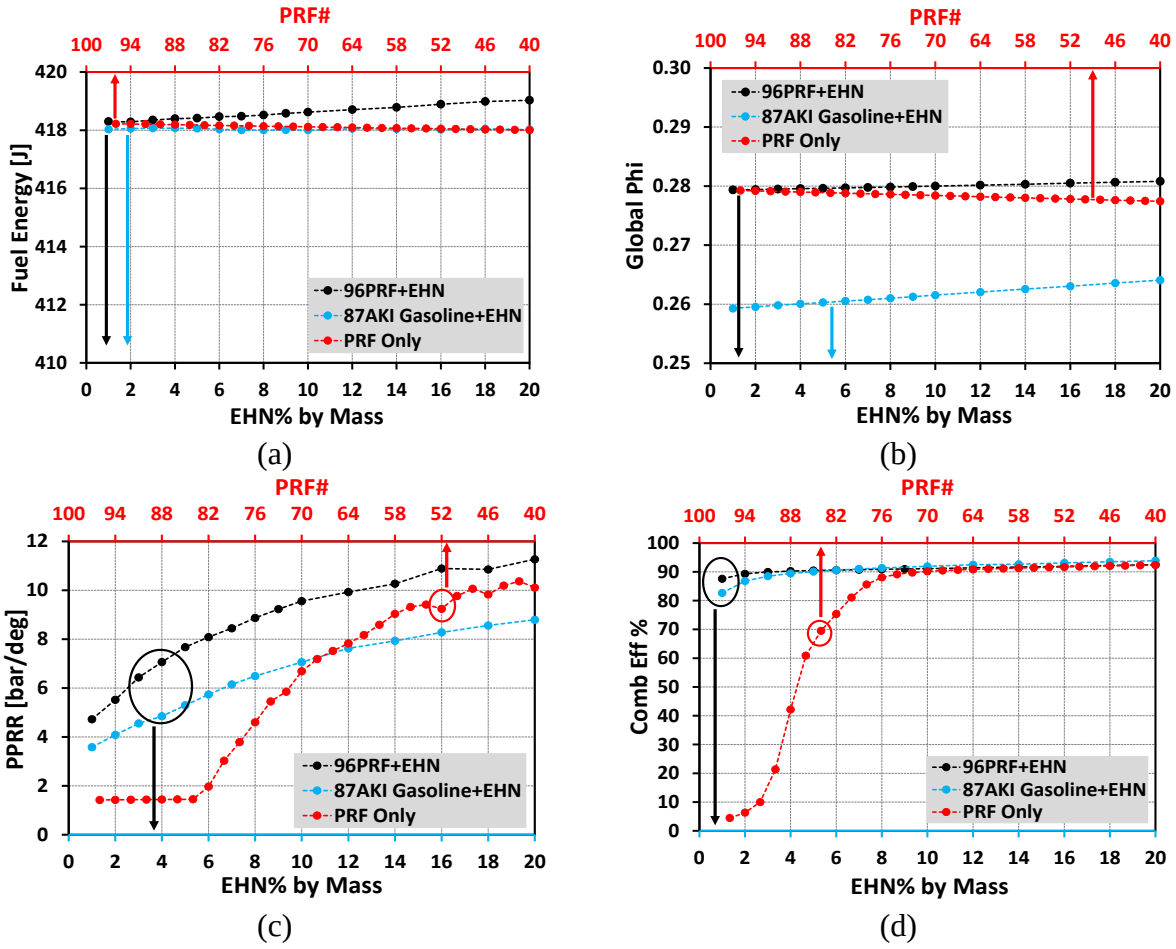

Figure 6.12: (a) Fuel energy, (b) global phi, (c) PPRR and (d) combustion efficiency comparisons among PRF fuel only, 96 PRF and 15-component fuel with EHN additive

Similar to Figure 6.12, Figure 6.13 also presents a primary horizontal axis for EHN related simulations, and a secondary horizontal axis for PRF-only simulations. The computed IMEP from IVC to EVO is ~ 3 bar for all the cases, as depicted in Figure 6.13a, which confirms the constant fuel energy.

At the chosen initial and boundary conditions, Figure 6.13b portrays the CA10 over the range of EHN and the PRF considered. The results show that 96 PRF and 15-component base fuel simulations with varying amount of EHN provide CA10 values which could be mapped against the PRF-only simulations. Interestingly, for less than 10% EHN amounts, CA10 identifies the ignition delay to be very close to just one specified PRF number. As an example, when 8% EHN

is used with both 96 PRF and 15-component fuels, the CA10 value indicates the corresponding PRF number to be 59 on the secondary horizontal axis, as shown in Figure 6.13b. This indicates that with EHN addition in a base fuel, the computed PRF number of the fuel mixture can be increased and can be mapped using actual PRF number simulations.

The CA50 shown in Figure 6.13c illustrates almost exact mapping of CA50 over the entire range of EHN amount and the PRF numbers used. As an example, at 12% EHN usage, the computed CA50s using the 96 PRF and 15-component base fuels indicate similar combustion phasing as in a 50 PRF fuel simulation, even though their CA10 slightly differs, as per Figure 6.13b. It is important to note that with the addition of EHN with a base fuel, similar combustion phasing can be achieved as for the original PRF number fuel while maintaining the IMEP. Therefore, depending on the chosen operating condition, the EHN amount added to a base fuel can always be mapped against an equivalent PRF number, which is an important conclusion from the present EHN study.

In Figure 6.13d the NO_x numbers for the PRF-only simulations are shown by the red-colored y-axis, whereas for the EHN related simulations, the numbers are indicated by the black-colored y-axis. The NO_x emission was found to be very small for the PRF simulations, whereas it was quite high for the EHN simulations, as expected. As the IVC temperature for the 15-component cases was lower [360K] compared to the 96 PRF simulations [390K], the NO_x emission was also found to be lower for the 15-component base fuel cases over the range of EHN percentage. The maximum temperature plot in Figure 6.13e indicates the highest in-cylinder temperatures for all the cases. The PRF-only and 96 PRF with EHN cases appeared to show similar maximum temperatures even though the NO_x emission is lower for the PRF simulations due to the absence of EHN.

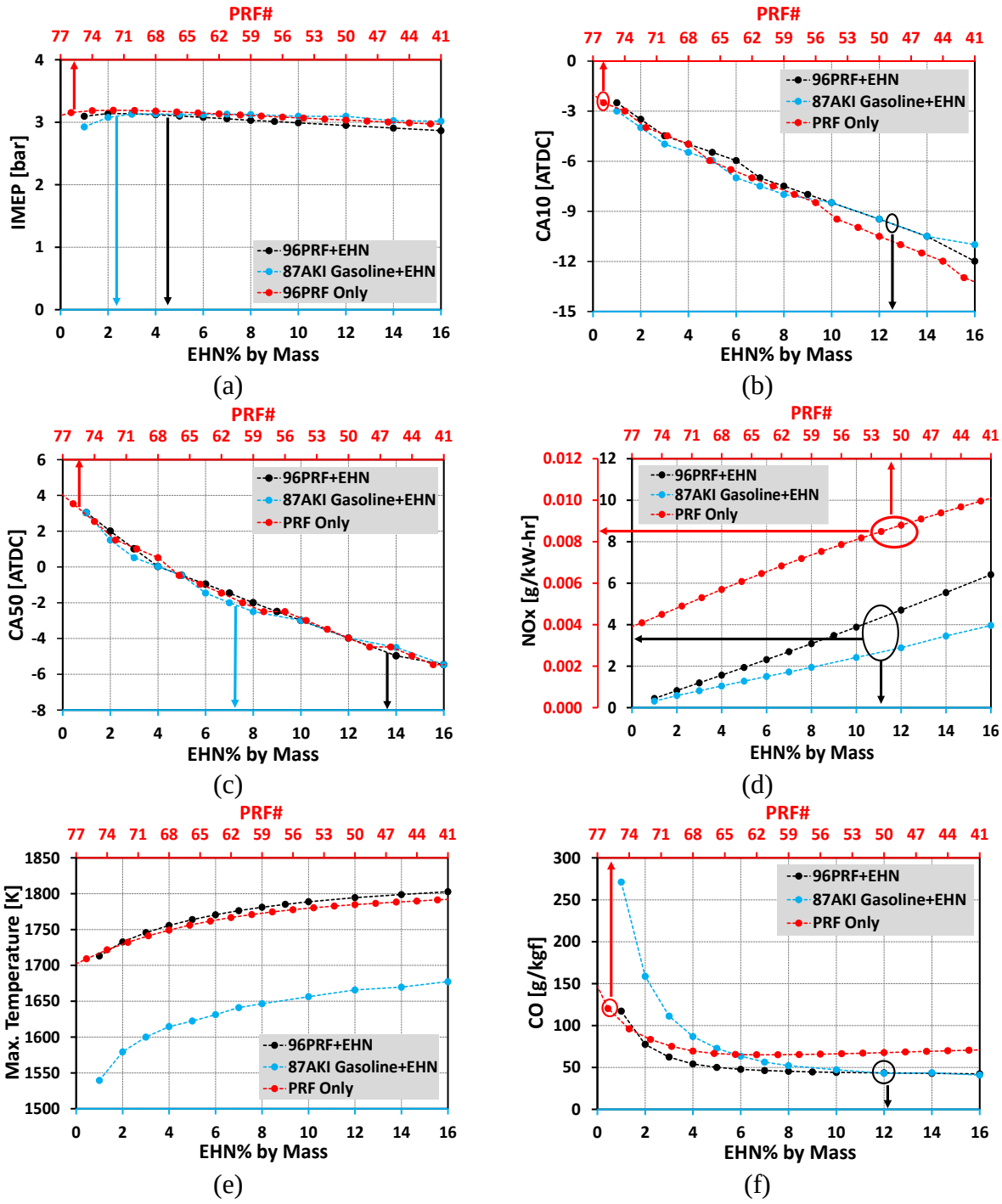

Figure 6.13: (a) IMEP, (b) CA10, (c) CA50, (d) NO_x, (e) Maximum Temperature and (f) CO emission comparisons among PRF-only fuel and 96 PRF and 15-component base fuel with EHN additive

With lower IVC temperature the 15-component base fuel cases display higher CO emission compared to the 96 PRF base fuel cases. Over the range of EHN doping, the maximum temperature

for the 15-component base fuel cases changes from ~1535K at 1% EHN to ~1675K at 16% EHN, showing a ~140K maximum temperature difference, whereas the difference is only ~90K for the 96 PRF base fuel cases. This explains the wide variation of CO for 15-component simulations with increased level of EHN doping compared to the 96 PRF base fuel simulations. At 8% EHN the CO emissions from both 96 PRF and the 15-component base fuel simulations were found to be almost the same, and remained almost constant with further increase in EHN amount. This is due to the early start of combustion, which provided enough residence time to burn most of the fuel with some left in the crevice and squish regions. To support this statement, CO emission comparisons are shown in Figure 6.14 for the 15-component fuel simulations using 3% and 10% EHN amounts.

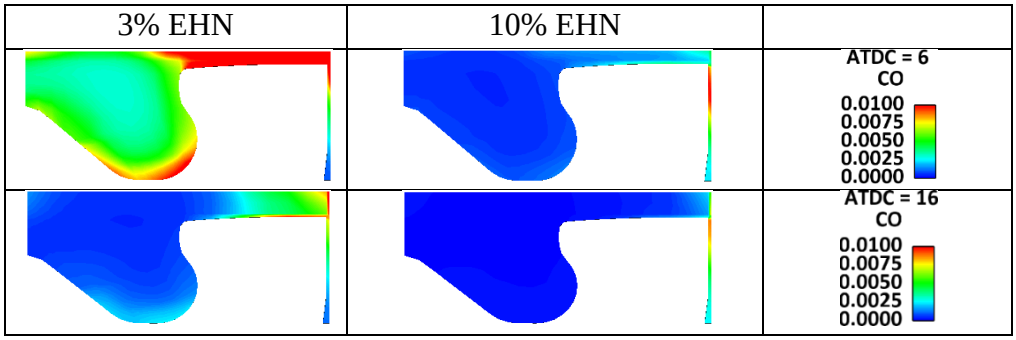

Figure 6.14: CO emission comparisons for 3% and 10% EHN cases using 15-component base fuel

6.5 Validation with GDICI Engine Experiments using 93 RON Gasoline and 0.4% EHN by Volume

Experiments were conducted at the Argonne National Laboratory using 93 RON gasoline as the base fuel with 0.4% EHN (by volume) added. The intake temperature was 50^{o}C and the injection timing was varied from -42 to -6 deg ATDC at 1500 rev/min, while maintaining a minimum fueling rate at each injection point. The details of the experiments are given by Kolodziej *et al.* [2014].

As mentioned before, the physical properties of EHN were modeled using n-Heptyl Benzene [$C_{13}H_{20}$] properties. Figure 6.15 shows the comparison between the experiments and simulations for SOI timings varying from -30 to -18 deg ATDC with a step-size of 3 deg. These simulations considered a nozzle opening delay of ~0.32 ms or 3 deg. As before, the SOI timing in this section refers to the SOI command timing used in the experiments. The legend, named 'EHN – Sim' in each figure, indicates the simulation of the experiment conducted with 0.4% EHN, whereas 'No EHN – Sim' indicates the simulation result where EHN was replaced by gasoline while maintaining all initial and boundary conditions the same as the 'EHN – Sim' case. All figures show good agreement between the experiments and simulations, but with slight over-prediction of peak heat release. Compared to the experiments, the onset of heat release was slightly delayed in all the EHN simulations, which could also reflect experimental cycle-to-cycle variations. Very interestingly, when the EHN was replaced by gasoline over the entire range of SOI timings, the combustion was significantly retarded, proving that even a very small amount of EHN serves as an effective auto-ignition improver. (The fuel energy was increased by only ~0.8J with the replacement of EHN by gasoline fuel.) The figures also indicate that while using EHN, to achieve a CA50 similar to the 'No EHN' cases, the fuel amount can be reduced significantly, validating the approach of requiring a minimum fueling rate by using EHN, as mentioned by Kolodziej et al. [2014].

Since the experiments maintained a different fueling level with and without EHN, it was difficult to make unconfounded comparisons of the effect of EHN. Therefore, the simulations were helpful in understanding how much impact the EHN had on CA50.

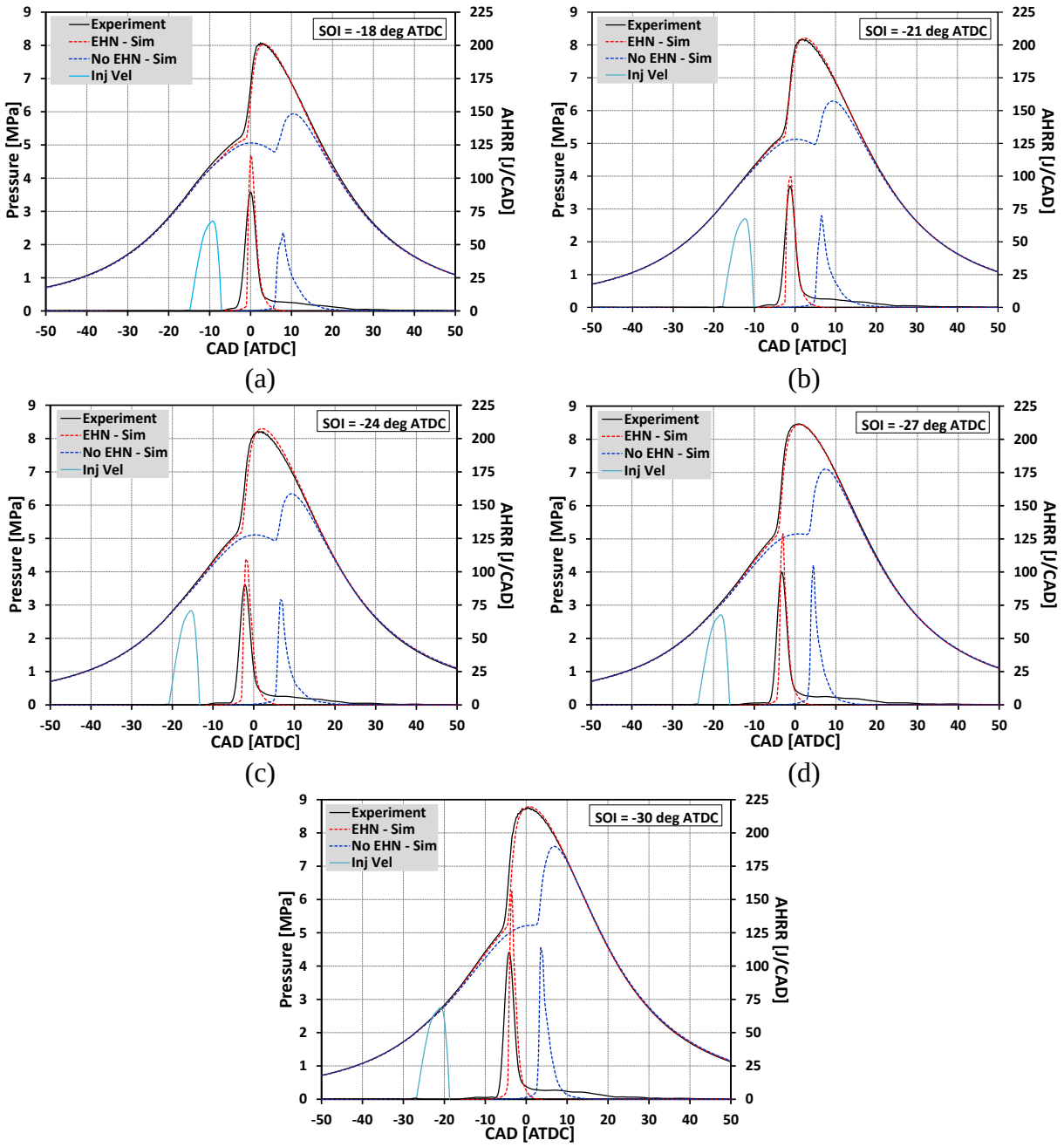

Figure 6.15: Comparison between experiments and simulations at different SOI timings using 87 AKI gasoline and 0.4% EHN by volume

Figure 6.16 compares the CA50 and the NO_x emission trends between the experiments and simulations. As shown in the figure, the trends are captured quite well in the simulations. However, a noticeable difference in NO_x emission can be seen between the EHN and No-EHN simulations, which is due to the combined effect of the late combustion phasing and the EHN usage. NO_x

emission increased with the late injection timing because of the fuel injection into a hot in-cylinder environment.

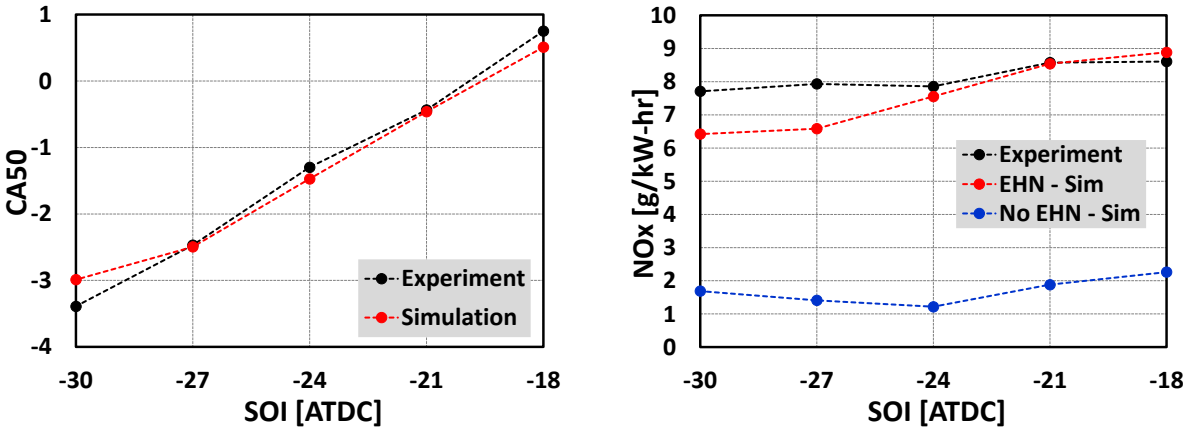

(a) (b)

Figure 6.16: (a) CA50 and (b) NO_x emission comparison between experiments and simulations over the range of SOI timings

Figure 6.17a illustrates the evolution of C_5H_{10} (which contributed the most towards the thermal ignition time, as explained in Chapter 5.3), CH_2O, OH and EHN for both with and without EHN simulations at -27 deg ATDC injection timing. The EHN mole fraction history indicates very early consumption of EHN, within ~10 deg from the start of injection. As the EHN gets consumed, accumulation of CH_2O and CH_3O_2 takes place. CH_2O is a direct-decomposition product of EHN, whereas CH_3O_2 is a by-product, which is generated by following the reaction pathways shown in Figure 6.17b. Earlier CH_3O_2 species generation helps in the prior decomposition of the C_5H_{10} species, which contributes to the earlier ignition for the EHN case, as revealed in Figure 6.17a. Eventually, CH_2O consumption and OH accumulation control the heat release.

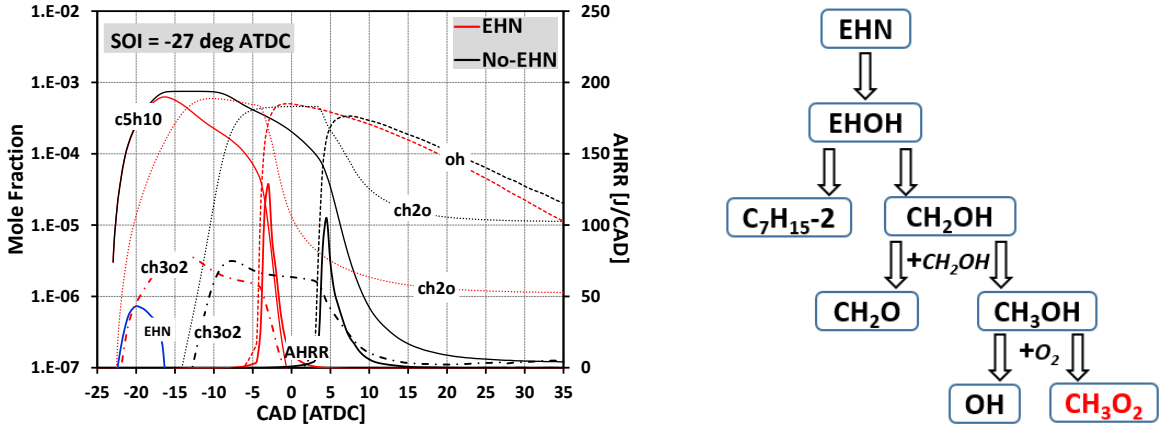

(a) (b)

Figure 6.17: (a) AHRR and Species evolution and (b) CH_3O_2 species evolution pathway for -27 deg ATDC SOI timing case using with and without EHN

As there was no gasoline/EHN experimental data available at 850 rev/min, in order to observe the effectiveness of EHN to lower the load at lower engine speed simulations were carried out using 0.4% EHN added to the gasoline at -18, -21, -24 and -27 deg ATDC SOI timings. The computational conditions and fueling rates were obtained from the gasoline simulations using 148 deg injector included angle over a range of SOI timings, as mentioned in Chapter 5.3.2.

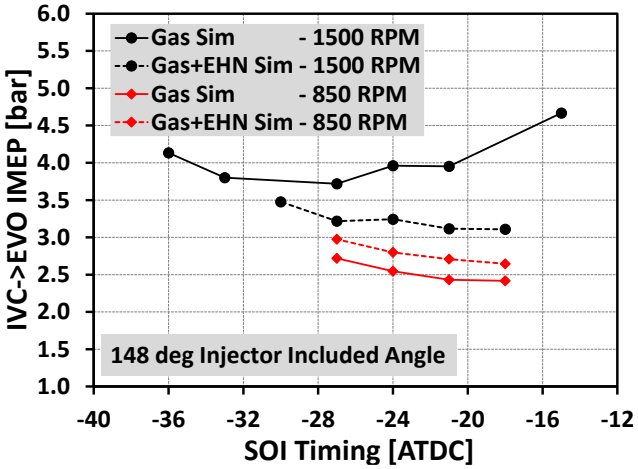

Figure 6.18: IMEP comparisons with and without EHN at 850 and 1500 rev/min engine speed

At 850 rev/min same fueling rate at a specific injection timing produced more IMEP using EHN, as can be observed in Figure 6.18. The figure also demonstrated that at 1500 rev/min numerical validations of the minimum fueling rate experiments showed a lower fueling rate using

EHN. Therefore it can be assumed that the EHN experiments at 850 rev/min would also have shown a lower fueling rate than the one used in the simulation, creating the possibility of lowering the load even further. But even with the current fueling rate, simulations at 850 rev/min using EHN showed lower load compared to the 1500 rev/min simulations. The above results indicated the prospect of reducing the load below 2.5 bar IMEP, using EHN and 148 deg injector included angle, at a lower speed.

6.6 Discussion

A new EHN mechanism [ERC-EHN] was developed in this work to study the effect of addition of a cetane improver on the fuel PRF number. A 15-component gasoline mechanism was combined with the EHN mechanism and used to validate shock-tube, HCCI and engine spray data. The following conclusions can be made from this study.

a. Shock-tube experiments performed by Hartmann et al. using 0.01, 0.1 and 1% EHN by mass with nC_7H_{16} were modeled. The simulations were conducted using both the ERC-EHN and WB-EHN mechanisms added to the 15-component gasoline fuel mechanism. Both EHN mechanisms indicated a slight over-prediction of the ignition delay in the low temperature region. For the 15-component mechanism the difference was found to be due to the over-predicted nC_7H_{16} ignition delay. However, the ignition delay trends were captured well in the simulations while varying the EHN percentage from 0.01 to 1%.
b. Shock-tube data validation also indicated a noticeable difference in the predicted ignition delay between the ERC-EHN and WB-EHN mechanisms with higher amounts of EHN.
c. As the ERC-EHN and WB-EHN mechanisms did not demonstrate any significant differences in predicted ignition delays, simulations were performed using HCCI experimental data using gasoline and 1-9.5% EHN by volume at 60C intake temperature

and 0.26 phi. 93 RON gasoline fuel components were used for the gasoline simulation. However, the WB-EHN and ERC-EHN mechanisms showed significant differences in NO_x emission, justifying the new EHN mechanism development. But, as discussed earlier, recent studies suggest that only NO may have been measured in the experiments. Therefore, NO emission from the simulation was compared with the presented NO_x data from the experiments.

d. HCCI simulations at 60, 75 and 90C intake temperatures and 0.26 phi captured the experimental pressure and heat release traces quite well along with all the emission trends. In the experiments, at higher intake temperatures the EHN amount needed to be reduced in order to avoid violent combustion. This trend was seen in the simulations too.

e. Constant volume ignition delay study indicates that the chemical effect of EHN prevails over the thermal effect to shorten the ignition delay, as opposed to DTBP.

f. A PRF-EHN map was generated using both gasoline and 96 PRF fuels as the base fuels and EHN was added to alter the PRF number. PRF-only simulations were also performed to capture the effective fuel PRF number while using the EHN additive. The initial and boundary conditions for all the PRF-related simulations were taken from the 3% EHN data validation at 60C. The IVC temperature for 15-component simulations was decided by maintaining the same CA50 as with 1% EHN using the 96 PRF base fuel. The fuel energy was kept constant for all the data points included in the map, and therefore the fuel amount was changed slightly at various EHN conditions. The map was made at ~0.28 global phi for the entire range of PRF-only and 96 PRF base fuel simulations, whereas for the 15-component base fuel simulations the phi was ~0.26.

g. At the given initial and boundary conditions, the PRF-only simulations indicated stable combustion only at PRF numbers of 77 or lower. CA10 and CA50 showed a nearly perfect mapping for the presented PRF [77 – 41 PRF] and EHN [0 – 16% by mass] ranges added to the base fuel. For example, 4% EHN by mass added to either the 96 PRF or 15-component base fuel provided the same CA50 as for a 68 PRF fuel. It should be noted that the IVC temperature using the 96 PRF base fuel was higher [390K] than for the 15-component base fuel [360K], indicating the requirement of higher intake temperatures for 96 PRF base fuel experiments.

h. NO_x emissions with the 15-component base fuel simulations were lower than for the 96 PRF base fuel simulations due to lower the IVC temperature. However, the NO_x emission was much lower in the PRF-only simulations compared to the EHN related cases because of the absence of EHN.

i. For the EHN related computations, lower EHN amounts caused higher CO emission due to the lower combustion temperatures. Once the EHN amount was high enough (i.e., ~8% or higher), the CO emission did not alter much as the in-cylinder temperature was high enough to burn most of the fuel in the bowl region within a few crank angle degrees from the start of combustion.

j. Experiments performed at ANL with 93 RON gasoline and 0.4% EHN by volume were modeled. The experimental results were well-captured using the simulations over the range of injection timings considered. Computational analysis was performed to separate the effect of EHN using the 15-component gasoline chemistry at same initial and boundary conditions. This changed the fuel amount by ~0.8J, which was negligible. The results

showed a significant retardation in CA50 without EHN addition, explaining the lower fuel amount observed while using EHN in the experiments.

k. Detailed analysis of the EHN and No-EHN cases at -27 deg ATDC SOI timings showed the generation of CH_2O and CH_3O_2 species from EHN decomposition. The CH_3O_2 species helped in the early decomposition of C_5H_{10}, which was found to be the main species in the 15-component fuel surrogate model contributing towards the thermal ignition delay. The early decomposition of C_5H_{10} explains the earlier ignition with the use of EHN.

Chapter 7 Conclusions

This chapter provides a summary of the work done in the present study toward fulfilling the objective of running a GDICI engine at light load conditions and discusses directions for future work.

In the study the GM 1.9L engine was used as the base engine. Multi-cylinder engine experiments and modeling were used to investigate GDICI spray combustion characteristics, while modeling of a single-cylinder version of the same engine was used to probe HCCI operation using gasoline and additives. As an engine should be able to operate over a wide range of speed and load conditions, the initial studies were conducted at high load conditions, whereas later the focus shifted towards low load operation.

High Load Operation:

A numerical optimization study was conducted at high load operating conditions to investigate the effect of several design parameters on stable and clean operation of the engine. The parameters considered for the optimization study were the IVC pressure, premixed fuel fraction, which was referred to as the first pulse amount, the ratio of the fuel fractions in the second and third pulses (i.e., for maximum of three injections), the start of second and third pulse injection timings and the EGR percentage. The study revealed a high EGR regime [~47%] which was mainly constrained by the PPRR, and a relatively low EGR regime [~36%] which was restricted by the NO_x emission. The high EGR regime was characterized by triple-pulse injections and single-stage combustion, whereas the low EGR operation was inclined towards double-pulse injections and two-stage combustion. The second pulse timing and amount were found to be the main controlling parameters in triple-pulse operation, whereas the combustion stability and emissions were mainly governed by the first pulse in the double-pulse strategy. Triple pulse operation allowed a wide

range of second pulse timings to be used without affecting the in-cylinder combustion behavior. On the other hand, the two-stage combustion strategy provided a very wide second-pulse timing window over a wide range of premixed fuel amounts.

Low Load Operation using Multiple Injection Strategies:

The purpose of each injection in a triple-pulse or double-pulse injection strategy was well-studied for high load operation. This motivated exploring the use of the triple-pulse injection strategy for light-load operation. The experiments were conducted at the Argonne National Laboratory using the 4-cylinder GM 1.9L engine. 75 RON and 93 RON gasoline fuels were used to produce 2 bar and 5 bar BMEP load points for study. Computations were performed to provide insights into the importance of triple-pulse operation at low load and revealed the following.

The experiments showed that using 93 RON fuel, it was impossible to achieve 2 bar BMEP load. Contributing to this was the fact the simulations indicated that the engine had different effective compression ratios in all four cylinders, which caused significant cylinder-to-cylinder combustion variability. Along with that, cycle-to-cycle variability issues caused the computations to be even more challenging. The simulations were conducted using a PRF fuel model. The PRF number was assumed to be the same as the PON number of the fuel. Emission trends were captured well in the simulations, even though same quantitative discrepancies were present, which were attributed to the complexity of the multi-cylinder engine operation. Low load operation in the multi-cylinder engine was found to be very sensitive to the fuel splits and injection timings. Controlling the small amount of fuel injected in each pulse caused combustion controllability issues during the experiments, mainly due to the very different combustion behavior of cylinder number 4, which had the lowest CR of 16.45 compared to the highest 17.8 CR cylinder. With changes in fuel PON number, the injection strategy also needed to be altered due to the difference in fuel auto-ignitability.

Low Load Operation using a Single Injection Strategy:

The triple-pulse experiments experienced difficulty in achieving 2 bar BMEP load using 93 RON gasoline. Accordingly, single-pulse experiments were conducted using the same fuel. The injection timing was varied from -42 to -6 deg ATDC with a step-size of 3 deg while maintaining the minimum fueling rate with acceptable COV of IMEP [< 3%] at each injection point. The minimum fueling rate was maintained in order to avoid either violent combustion or misfire. The experiments indicated that ~2 bar BMEP load could be achieved at 1500 rev/min.

The experiments first indicated an advancement of CA50 with advancement in the injection timing, but CA50 retarded with further advancement in the SOI timing. The simulations explained the reason to be due to the temperature distribution, which changed the ignition location in the cylinder with the change in injection timing. The computations assumed uniform in-cylinder temperature distributions at IVC, but the IVC temperature needed to be altered slightly in order to match the experimental CA50 to account for changes in the temperature of the residual gas in the combustion chamber from the previous cycle. Validation of the experimental data indicated a minimum IMEP of 4 bar (calculated from IVC to EVO). However, the computations illustrated the possibility of using even lower fuel amounts to achieve low load operation while obtaining stable combustion. Use of a lower swirl ratio [0.7] allowed less than 3 bar IMEP in the computations, but at the expense of increased NO_x emission. The simulations also suggested the benefit of injector hole diameter optimization in order to achieve effective spray break-up and to attain lighter load operation with reasonable emissions.

Effect of Injector Included Angle:

In order to explore the effect of the injector included angle, two different injectors were used in the experiments at 850 rev/min; injector-A with 120 deg included angle and injector-B with 148 deg included angle. The simulations were performed using a more accurate 15-component gasoline

fuel chemistry mechanism, which also provided better NO_x emission trends than a simpler PRF fuel mechanism. With both mechanisms, the over-prediction of CO was argued to be due to the absence of a reliable crevice model.

The injector-A and injector-B simulations were compared with the experiments for a range of injection timings varied from -27 to -18 deg ATDC, with a step-size of 3 deg. The results featured a significant under-prediction of NO_x emission using injector-B, which indicates the possibility of spray wall-wetting in the experiments, which was not well-modeled in the simulations.

To make a better comparison between injector-A and injector-B, additional simulations were carried out from -36 to -6 deg ATDC SOI timings with a step-size of 3 deg, while keeping the initial and boundary conditions constant for all cases. Injector-A showed a wider range of stable combustion and advanced CA50s compared to injector-B, indicating more effective fuel burning due to the spray targeting the bowl, instead of the squish region. This explains the lower fueling rates observed using injector-A in the multi-cylinder engine experiments. Over the range of injection timings for the non-reacting cases, the amount of squish fuel was found to be much higher for injector-B cases.

Both the injectors gave the same CA50 over a range of SOI timings, and NO_x reduced with advanced timings. This was due to the more homogeneous fuel distribution seen at earlier injection timings, which lowered the peak equivalence ratio and therefore the peak combustion temperature.

EHN Study:

The above studies indicated that low load points using 93 RON gasoline could be achieved by using a single injection and a narrower injector included angle. However, experiments at ANL demonstrated the possibility of lowering the load even further by using a fuel additive, which is also helpful for the cold-start condition. EHN was selected the additive to be explored. Therefore, an EHN additive chemistry mechanism was developed and validated against available shock-tube,

HCCI and engine spray data. Simulations were also used to generate a PRF-EHN map which indicates the change in fuel PRF number that corresponds to varying EHN amounts in gasoline and in 96 PRF base fuel.

The newly developed ERC-EHN mechanism captured shock-tube ignition delay trends fairly well when the EHN amount was varied from 0.01 to 1%. However, the simulations over-predicted ignition delays in the low-temperature regime, which was caused by inaccuracies in the nC_7H_{16} related reactions in the 15-component base mechanism.

Validation of HCCI experimental data at 60, 75 and 90C intake temperatures and 0.26 equivalence ratio predicted NO emission trends well while using the ERC-EHN mechanism. NO was monitored in the simulations since it was discovered that the experiments may have featured faulty operation of the NO_2 catalytic convertor, making the NO_x data suspect.

The PRF-EHN map shows the effective PRF number when EHN is added to either gasoline or the 96 PRF base fuels. All initial and boundary conditions were kept the same for the simulations, other than the IVC temperature used in the 15-component surrogate cases, which was 360K versus 390K for PRF related simulations. This IVC temperature was calibrated based on the CA50 agreement with use of 1% EHN. The map showed much lower NO_x emission for the PRF-only simulations, compared to the EHN due to the presence of nitrogen in the fuel.

Finally, engine experiments with 93 RON gasoline and 0.4% EHN (by volume) over a range of SOI timings were used to validate the models. The results showed very good agreements of pressure traces and CA50 between the experiments and simulations, and confirmed that a significant advance of CA50 can be obtained with the use of EHN, in agreement with the lower fueling rates observed in the ANL experiments with EHN.

Future Work

Even though this work contributes significantly to understand low load operation in a GDICI engine, more investigation is desirable as follows.

1. A light load GA optimization study should be conducted by varying the injection strategy, speed, EGR level, injection pressure, swirl ratio and nozzle hole diameter to investigate the importance of all these parameters on achieving cleaner operation at light loads.
2. Initially a low load operation map could be generated using gasoline with a single-injection strategy at various speed, injection pressures and injector included angles. Next, the operation map should be extended to include important parameters suggested in the low load optimization study.
3. More shock-tube data should be obtained with the EHN cetane improver additive. This will be useful to further validate the ERC-EHN mechanism. It is noted that simulating RCM data could also be helpful, but the modeling is more complicated.
4. The EHN reactivity should be compared with that of other additives, such as DTBP, at engine-like conditions. PRF maps, like the one generated in this study, should be produced with alternative additives. This will provide important practical information on CA50 and emissions with varying amounts of additive.

References

2EHN Industry Work Group (2004). Best Practices Manual, *ATC document 76, pp. 14*

Abani, N., Munnannur, A., and Reitz, R.D. (2008). Reduction of numerical parameter dependencies in diesel spray models, *J. Eng. Gas Turbines and Power, Vol. 130 (3), 032809*

Abraham, J. (1997). What is adequate resolution in the numerical computations of transient jets?, *SAE Technical Paper 970051*

Adhikary, B.D., Ra, Y., Reitz, R.D., Ciatti, S. (2012). Numerical Optimization of a Light-Duty Compresion Ignition Engine Fuelled With Low-Octane Gasoline, *SAE Technical Paper 2012-01-1336*

Adhikary, B.D., Reitz, R.D., Ciatti, S. (2013). Study of In-cylinder Combustion and Multi-Cylinder Light Duty Compression Ignition Engine Performance Using Different RON Fuels at Light Load Conditions, *SAE Technical Paper 2013-01-0900*

Affleck, W.S., and Thomas, A. (1968). An opposed piston Rapid Compression Machine for preflame reaction studies, *Proc. Inst. Mech. Eng., Vol. 183, pp. 365-387*

Al-Rubaie, M.A.R., Griffiths, J.F., and Sheppard, C.G.W. (1991). Some Observation on the Effectiveness of Additives for Reducing the Ignition Delay Period of Diesel Fuels, *SAE Technical Paper 912333*

Amsden, A.A. (1997). KIVA-3V: A block structured KIVA program for engines with vertical and canted valves, *Los Alamos National Laboratory Report LA-13313-MS*

Amsden, A.A. (1999). KIVA-3V, Release 2, Improvements to KIVA-3V, *Los Alamos National Laboratory Report LA-UR-99-915*

Aradi, A., and Ryan, T. (1995). Cetane effect on diesel ignition delay times measured in a constant volume combustion apparatus, *SAE Technical Paper 952352*

Beale, J.C., and Reitz, R.D. (1999). Modeling spray atomization with the Kelvin Helmholtz/ Rayleigh Taylor hybrid model, *Atomization and Sprays, Vol. 9, pp. 623-650*

Borgqvist, P., Tunestal, P., and Johansson, B. (2012). Gasoline partially premixed combustion in a light-duty engine at low load and idle operating conditions, *SAE Technical Paper 2012-01-0687*

Bornemann, H., Scheidt, F. and Sander, W. (2002). Thermal decomposition of 2 EthylHexyl Nitrate, *Int. J. of Chemical Kinetics, Vol. 34(1), pp. 34-38*

Boyer, R.L. (1949). Status of dual-fuel engine development, *SAE Technical Paper 490018*

Brakora, J. (2012). A comprehensive combustion model for biodiesel-fueled engine simulations, *PhD Thesis in Mechanical Engineering, University of Wisconsin-Madison*

Ciatti, S., and Subramanian, S. (2011). An experimental investigation of low octane gasoline in diesel engines, *J. Eng. Gas Turbines Power, Vol. 133(9), 092802*

CONVERGE: A three-dimensional computational fluid dynamics program for transient or steady-state flows with complex geometries, *Version 1.3*

Clothier, P.Q.E., and Pritchard, H.O. (1993). Brief Communication, *Combustion & Flame, Vol. 95, pp. 427-429*

Deb, K., Pratap, A., Agarwal, S., and Meyarivan, T. (2002). A fast and elitist multi objective genetic algorithm: NSGA-II, *IEEE Transactions on Evolutionary Computation, Vol. 6(2), pp. 182-197*

Dec, J.E., and Canaan, R.E. (1998). PLIF imaging of NO formation in a DI diesel engine, *SAE Technical Paper 980147*

Dec, J.E., Yang, Y. (2010). Boosted HCCI for high power without engine knock and with ultra-low NO_x emissions - using conventional gasoline, *SAE Int. J. Engines, Vol. 3(1), pp. 750-767*

Dempsey, A.B., and Reitz, R.D. (2011). Computational optimization of a heavy-duty compression ignition engine fueled with conventional gasoline, *SAE Int. J. Engines, Vol. 4(1), pp. 338-359*

Dempsey, A.B., Walker, N.R., and Reitz, R.D. (2013). Effect of cetane improvers on gasoline, ethanol and methanol reactivity and the implications for RCCI combustion, *SAE Int. J. Fuels Lubr. Vol. 6(1), pp. 170-187*

Dempsey, A.B., Curran, S., Reitz, R.D. (2015). Characterization of Reactivity Controlled Compression Ignition (RCCI) using Premixed Gasoline and Direct-Injected Gasoline with a Cetane Improver on a Multi-Cylinder Engine, *SAE World Congress 2015*

Eng, J. (2002). Characterization of Pressure Waves in HCCI Combustion, *SAE Technical Paper 2002-01-2859*

Eng, J.A., Leppard, W.A., and Sloane, T.M. (2003). The effect of di-tertiary butyl peroxide (DTBP) addition to gasoline on HCCI combustion, *SAE Technical Paper 2003-01-3170*

Fieweger, K., Blumenthal, R., and Adomeit, G. (1997). Self-ignition of SI engine model fuels: A shock tube investigation at high pressure, *Combustion & Flame, Vol. 109(4), pp. 599-619*

Gas Research Institute. "GRI-Mech, v3.0" Available: *www.me.berkeley.edu/gri-mech/*

Gamma Technologies (2009). www.gtisoft.com, *GT Suite v7.00*

Goldsborough, S.S. (2013). Personal Communication, *Argonne National Laboratory*

Han, Z., and Reitz, R.D. (1995). Turbulence modeling of internal combustion engines using RNG k-ε models, *Combustion Science and Technology, Vol. 106, pp. 267-295*

Hanson, R.M., Kokjohn, S.L., Splitter, D.A., and Reitz, R.D. (2011). Fuel effects on reactivity controlled compression ignition (RCCI) combustion at low load, *SAE Int. J. Engines, Vol. 4(1), pp. 394-411*

Hara, H., Itoh, Y., Henein, N.A., and Bryzik, W. (1999). Effect of cetane number with and without additive on cold startability and white smoke emissions in a diesel engine, *SAE Technical Paper 1999-01-1476*

Hartmann, M., Tian, K., Hofrath, C., Fikri, M., Schubert, A, Schiel, R., Starke, R., Atakan, B., Schulz, C., Maas, U., Jager, F. K., and Kuhling, K. (2009). Experiments and modeling of ignition delay times, flame structure and intermediate species of EHN-doped stoichiometric n-heptane/air combustion, *Proc. Combust. Inst., Vol. 32, pp. 197-204*

Hasegawa, R., and Yanagihara, H. (2003). HCCI combustion in DI diesel engine, *SAE Technical Paper 2003-01-0745*

Heywood, J.B. (1988). *Internal Combustion Engine Fundamentals*, McGraw-Hill, New York

Higgins, B.S., Siebers, D.L., and Aradi, A.A. (2001). Comparison of 2-ethylhexyl nitrate and fuel composition induced changes in the diesel spray ignition process, *Int. J. Engine Research, Vol. 2(1), pp. 47-67*

Higgins, B., Siebers, D., Mueller, C., and Aradi, A. (1998). Effects of an ignition-enhancing, diesel-fuel additive on diesel-spray evaporation, mixing, ignition, and combustion, *Twenty-Seventh Symposium (International) on Combustion, Vol. 27 (2), pp. 1873-1880*

Hiroyasu, H., and Kadota, T. (1976). Models for combustion and formation of nitric oxide and soot in DI diesel engines, *SAE Technical Paper 760129*

Hori, M., Matsunaga, N., Marinov, N., Pitz, W., and Westbrook, C.K. (1998). An experimental and kinetic calculation of the promotion effect of hydrocarbons on the NO- NO_2 conversion in a flow reactor, *Proc. Combust. Inst., Vol. 27, pp. 389-396*

Ickes, A.M., Bohac, S.V., and Assanis, D.N. (2009). Effect of 2-ethylhexyl nitrate cetane improver on NO_x emissions from premixed low temperature diesel combustion, *Energy & Fuels, Vol. 23, pp. 4943-4948*

Inagaki, K., Fuyuto, T., Nishikawa, K., Nakakita, K., and Sakata, I. (2006). Dual-fuel PCI combustion controlled by in-cylinder stratification of ignitability, *SAE Technical Paper 2006-01-0028*

Jiao, Q. (2010). Modeling the influence of molecular interactions on the vaporization of multi-component fuel sprays, *MS Thesis in Mechanical Engineering, University of Wisconsin-Madison*

Johnson, T.V. (2011). Diesel emissions in review, *SAE Technical Paper 2011-01-0304*

Kaddatz, J., Andrie, M., Reitz, R.D., and Kokjohn, S.L. (2012). Light-duty reactivity controlled compression ignition combustion using a cetane improver, *SAE Technical Paper 2012-01-1110*

Kalghatgi, G. (2005). Auto-ignition quality of practical fuels and implications for fuel requirements of future SI and HCCI engines, *SAE Technical Paper 2005-01-0239*

Kalghatgi, G., Risberg, P., and Angstrom, H. (2006). Advantages of fuels with high resistance to auto-ignition in late-injection, low-temperature, compression ignition combustion, *SAE Technical Paper 2006-01-3385*

Kalghatgi, G., Risberg, P., and Angstrom, H. (2007). Partially pre-mixed auto-ignition of gasoline to attain low smoke and low NO_x at high load in a compression ignition engine and comparison with a diesel fuel, *SAE Technical Paper 2007-01-0006*

Kalghatki, G., Hildingsson, L., and Johansson, B. (2010). Low NO_x and low smoke operation of a diesel engine using gasoline like fuels, *J. Eng. Gas Turbines Power, Vol. 132(9), 092803*

Kee, R.J., Rupley, F.M., and Miller, J.A. (1989). CHEMKIN-II: A FORTRAN chemical kinetics package for the analysis of gas phase chemical kinetics, *Sandia National Laboratory Report*

Kimura, S., Aoki, O., Ogawa, H., Muranaka, S., and Enomoto, Y. (1999). New combustion concept for ultra-clean and high-efficiency small DI diesel engines, *SAE Technical Paper 1999-01-3681*

Kimura, S., Aoki, O., Kitahara, Y., and Aiyoshizawa, E. (2001). Ultra-clean combustion technology combining a low-temperature and premixed combustion concept for meeting future emission standards, *SAE Technical Paper 2001-01-0200*

Kodama, K., Hiranuma, S., Doumeki, R., Takeda, Y., and Ikeda, Y. (2005). Development of DPF system for commercial vehicles [Second Report] – active regenerating function in various driving condition, *SAE Technical Paper 2005-01-3694*

Kokjohn, S.L., and Reitz, R.D. (2008). A computational investigation of two-stage combustion in a light-duty engine, *SAE Int. J. Engines, Vol. 1(1), pp. 1083-1104*

Kokjohn, S.L., Hanson, R.M., Splitter, D.A., and Reitz, R.D. (2011). Fuel Reactivity Controlled Compression Ignition (RCCI): A pathway to controlled high-efficiency clean combustion, *Int. J. Engine Research, Vol. 12(3), pp. 209-226*

Kolodziej, C.P., Ciatti, S., Vuilleumier, D., Adhikary, B.D., and Reitz, R.D. (2014). Extension of the lower load limit of gasoline compression ignition with 87 AKI gasoline by injection timing and pressure, *SAE Technical Paper 2014-01-1302*

Kolodziej, C.P., and Ciatti, S. (2014). Effects of injector nozzle inclusion angle on extending the lower load limit of gasoline compression ignition using 87 AKI gasoline, *Proceedings of ASME Fall Technical Conference, ICEF2014-5632*

Kong, S. C., Sun, Y. and Reitz, R. D. (2007). Modeling diesel spray flame liftoff, sooting tendency, and NO_x emissions using detailed chemistry with phenomenological soot model, *J. Eng. Gas Turbines and Power, Vol. 129, pp. 245-251*

Lange, W., Cooke, J., Gadd, P., Zurner, H., Schlogi, H., and Richter, K (1997). Influence of fuel properties on exhaust emissions from advanced heavy-duty engines considering the effect of natural and additive enhanced cetane number, *SAE Technical Paper 972894*

Lim, J.H., and Reitz, R.D. (2014). High load (21bar IMEP) dual fuel RCCI combustion using dual direct injection, *J. Eng. Gas Turbines and Power, Vol. 136(10), 101514*

Liotta, F. (1993). A peroxide based cetane improvement additive with favorable fuel blending properties, *SAE Technical Paper 932767*

Liu, A.B., Mather, D., and Reitz, R.D. (1999). Effects of drop drag and breakup on fuel sprays, *SAE Technical Paper 930072*

Liu, Y., Tao, F., Foster, D. E., and Reitz, R. D. (2005). Application of a multiple-step phenomenological soot model to HSDI diesel multiple injection modeling, *SAE Technical Paper 2005-01-0924*

LLNL: www-pls.llnl.gov/science_and_technology-chemistry-combustion-gasoline-surrogate

Loeper, P. (2013). Experimental investigation of gasoline compression ignition combustion in a light-duty diesel engine, *PhD Thesis in Mechanical Engineering, University of Wisconsin-Madison*

Manente, V., Sonder, M., Johansson, B., and Tunestal, P. (2009). Effects of different type of gasoline fuels on heavy duty partially premixed combustion, *SAE Int. J. Engines, Vol. 2(2), pp. 71-88*

Manente, V., Sonder, M., Johansson, B., and Tunestal, P. (2012). Gasoline partially premixed combustion: high efficiency, low NO_x and low soot by using an advanced combustion strategy and a compression ignition engine, *Int. J. Vehicle Design, Vol. 59 (2-3), pp. 108-128*

Mueller, C.J., and Upatnieks, A. (2005). Dilute clean diesel combustion achieves low emissions and high efficiency while avoiding control problems of HCCI, *11^{th} Annual Diesel Engine Emissions Reduction (DEER) Conference*

Munnannur, A. (2007). Droplet collision modeling in multi-dimensional engine spray computations, *PhD Thesis in Mechanical Engineering, University of Wisconsin-Madison*

Nagle, J., and Strickland-Constable, R.F. (1962). Oxidation of carbon between 1000-2000 C, *Proc. of the Fifth Carbon Conf., Vol.1*

Najt, P., and Foster, D. (2002). Compression-ignited homogeneous charge combustion, *SAE Technical Paper 830264*

Nandi, M., Jacobs, D., Liotta, F., and Kesling, H. (1994). The performance of a peroxide-based cetane improvement additive in different diesel fuels, *SAE Technical Paper 942019*

Neely, G.D., Sasaki, S., Huang, Y., Leet, J.A., and Stewart, D.W. (2005). New diesel emission control strategy to meet US Tier 2 emissions regulations, *SAE Technical Paper 2005-01-1091*

Neely, G.D., Sasaki, S., and Sono, H. (2007). Investigation of alternative combustion crossing stoichiometric air fuel ratio for clean diesels, *SAE Technical Paper 2007-01-1840*

Nieman, D.E., Dempsey, A.B., and Reitz, R.D. (2012). Heavy-duty RCCI operation using natural gas and diesel, *SAE Int. J. Engines, Vol. 5(1), pp. 270-285*

Odaka, M., Koike, N., and Suzuki, H. (1998). Deterioration effect of three-way catalyst on nitrous oxide emissions, *SAE Technical Paper 980676*

Okude, K., Mori, K., Shiino, S., and Moriya, T. (2004). Premixed compression ignition (PCI) combustion for simultaneous reduction of NO_x and soot in diesel engine, *SAE Technical Paper 2004-01-1907*

Onishi, S., Jo, S., Shoda, K., Jo, P., and Kato, S. (1979). Active thermo-atmosphere combustion (ATAC) – A new combustion process for internal combustion engines, *SAE Technical Paper 790501*

Opat, R., Ra, Y., Gonzalez, M.A., Krieger, R., Reitz, R.D., Foster, D.E., Durrett, R.P., and Siewert, R.M. (2007). Investigation of mixing and temperature effects on HC/CO emissions for highly dilute low temperature combustion in a light-duty diesel engine, *SAE Technical Paper 2007-01-0193*

Oxley, J., Smith, J., Rogers, E., Ye, W., Aradi, A., and Henly, T. (2001). Heat-Release Behavior of Fuel Combustion Additives, *Energy & Fuels, Vol. 15(5), pp. 1194-1199*

O'Rourke, P.J., and Amsden, A.A. (2000). A spray/wall interaction submodel for the kiva-3 wall film model, *SAE Technical Paper 2000-01-0271*

Perini, F., Galligani, E., and Reitz, R. D. (2012). An analytical jacobian approach to sparse reaction kinetics for computationally efficient combustion modeling with large reaction mechanisms, *Energy Fuels, 26(8), pp. 4804–4822*

Perini, F. (2013). Personal Communication, *University of Wisconsin – Madison*

Pritchard, H.O. (1989). Brief Communications, *Combustion & Flame, Vol. 75, pp. 415-416*

Ra, Y., and Reitz, R.D. (2008). A reduced chemical kinetic model for IC engine combustion simulations with primary reference fuels, *Combustion & Flame, Vol. 155, pp. 713-738*

Ra, Y., Yun, J.E., and Reitz, R.D. (2009). Numerical simulation of diesel and gasoline-fueled compression ignition combustion with high pressure late direct injection, *Int. J. Vehicle Design, Vol. 50(1/2/3/4), pp. 3-34*

Ra, Y., Yun, J.E., and Reitz, R.D. (2009). Numerical parametric study of diesel engine operation with gasoline, *Combustion Science and Technology, Vol. 181(2), pp. 350-378*

Ra, Y., and Reitz, R.D. (2009). A vaporization model for discrete multi-component fuel sprays, *Int. J. Multiphase Flow, Vol. 35, pp. 101-117*

Ra, Y., and Reitz, R.D. (2011). A combustion model for IC engine combustion simulations with multi-component fuels, *Combustion & Flame, Vol. 158(1), pp. 69-90*

Ra, Y., Loeper, P., and Reitz, R.D. (2011). Study of high speed gasoline direct injection compression ignition (GDICI) engine operation in the LTC regime, *SAE Int. J. Engines, Vol. 4(1), pp. 1412-1430*

Ra, Y., Loeper, P., Andrie, M., Krieger, R., Foster, D., Reitz, R.D., and Durrett, R. (2012). Gasoline DICI engine operation in the LTC regime using triple-pulse injection, *SAE Int. J. Engines Vol. 5(3), pp. 1109-1132*

Ra, Y., and Reitz, R.D. (2014). A combustion model for multi-component fuels using physical surrogate group chemistry representation (PSGCR), *In Preparation*

Rasmussen, C. L., Rasmussen, A.E., and Glarborg, P. (2008). Sensitizing effects of NO_x on CH4 oxidation at high pressure, *Combustion & Flame, Vol. 154, pp. 529-545*

Risberg, P., Kalghatgi, G., Angstrom, H., and Wayhlin, F. (2005). Auto-ignition quality of diesel-like fuels in HCCI engines, *SAE Technical Paper 2005-01-2127*

Saito, S., Shinozaki, R., Suzuli, A., Jyoutaki, H., and Takeda, Y. (2003). Development of urea-SCR system for commercial vehicle – basic characteristics and improvement of NO_x conversion at low load operation, *SAE Technical Paper 2003-01-3248*

Schwab, S.D., Guinther, G.H., Henly, T.J., and Miller, K.T. (1999). The effects of 2-ethylhexyl nitrate and di-tertiary-butyl peroxide on the exhaust emissions from a heavy-duty diesel engine, *SAE Technical Paper 1999-01-1478*

Sellnau, M., Sinnamon, J., Hoyer, K., and Husted, H. (2011). Gasoline direct injection compression ignition (GDCI) – Diesel-like efficiency with low CO_2 emissions, *SAE Int. J. Engines, Vol. 4(1), pp. 2010-2022*

Sellnau, M., Sinnamon, J., Hoyer, K., and Husted, H. (2012). Full-time gasoline direct-injection compression ignition (GDCI) for high efficiency and low NO_x and PM, *SAE Technical Paper 2012-01-0384*

Senecal, P. K., and Reitz, R. D. (2000). Simultaneous reduction of engine emissions and fuel consumption using genetic algorithms and multi-dimensional spray and combustion modeling, *SAE Technical Paper 2000-01-1890*

Shi, Y., and Reitz, R.D. (2008). Assessment of optimization methodologies to study the effects of bowl geometry, spray targeting and swirl ratio for a heavy-duty diesel engine operated at high-load, *SAE Int. J. Engines, Vol. 1(1), pp. 537-557*

Shi, Y., Ge, H.W., and Reitz, R.D. (2011). Computational Optimization of Internal Combustion Engines, *Springer, ISBN 978-0-85729-618-4*

Shimazaki, N., Tsurushima, T., and Nishimura, T. (2003). Dual mode combustion concept with premixed diesel combustion by direct injection near top dead center, *SAE Technical Paper 2003-01-0742*

Splitter, D., Hanson, R., Kokjohn, S.L., and Reitz, R.D. (2011). Reactivity controlled compression ignition (RCCI) heavy-duty engine operation at mid- and high-loads with conventional and alternative fuels, *SAE Technical Paper 2011-01-0363*

Stein, Y., Yetter, R.A., Dryer, F.L., and Aradi, A. (1999). The Autoignition Behavior of Surrogate Diesel Fuel Mixtures and the Chemical Effects of 2-Ethylhexyl Nitrate (2-EHN) Cetane Improver, *SAE Technical Paper 1999-01-1504*

Sun, Y. (2007). Diesel combustion optimization and emissions reduction using adaptive injection strategies (AIS) with improved numerical models, *PhD Thesis in Mechanical Engineering, University of Wisconsin-Madison*

Sung, C.J., Curran, H.J. (2014). Using rapid compression machines for chemical kinetics studies, *Progress in Energy and Comb. Sc., Vol. 44, pp. 1-18*

Takeda, Y., Keiichi. N., and Keiichi. N. (1996). Emission characteristics of premixed lean diesel combustion with extremely early staged fuel injection, *SAE Technical Paper 961163*

Tanaka, S., Ayala, F., Keck, J.C., and Heywood, J.B. (2003). Two-stage ignition in HCCI combustion and HCCI control by fuels and additives, *Combustion & Flame, Vol. 132, pp. 219-239*

Theis. J.R., Ura, J.A., Li, J.J., Surnilla, G.G., Roth, J.M., and Goralski Jr., C.T. (2003). NO_x release characteristics of Lean NO_x Traps during rich purges, *SAE Technical Paper 2003-01-1159*

Tomita, E., Kawahara, N., Piao, Z., and Yamaguchi, R. (2002). Effects of EGR and early injection of diesel fuel on combustion characteristics and exhaust emissions in a methane dual fuel engine, *SAE Technical Paper 2002-01-2723*

Tsurushima, T., Kunishima, E., Asaumi, Y., Aoyagi, Y., and Enomoto, Y. (2002). The effect of knock on heat loss in homogeneous charge compression ignition engines, *SAE Technical Paper 2002-01-0108*

United States Environmental Protection Agency [EPA] (2007). http://www.dieselnet.com/standards/us/hd.php

Wang, H., Yao, M., and Reitz, R.D. (2013). Development of a reduced primary reference fuel mechanism for internal combustion engine combustion simulations, *Energy Fuels, Vol. 27(12), pp. 7843-7853*

Wang, H., Dempsey, A.B., Yao, M., Jia, M., and Reitz, R.D. (2014). Kinetic and numerical study on the effects of Di-Tert-Butyl Peroxide additive on the reactivity of methanol and ethanol, *Energy Fuels, Vol. 28(8), pp. 5480-5488*

Weall, A., and Collins, N. (2009). Gasoline fuelled partially premixed compression ignition in a light duty multi cylinder engine: A study of low load and low speed operation, *SAE Technical Paper 2009-01-1791*

Westbrook, C.K., Pitz, W.J., Herbinet, O., Curran, H.J., and Silke, E.J. (2009). A comprehensive detailed chemical kinetic reaction mechanism for combustion of n-alkane hydrocarbons from n-octane to n-hexadecane, *Combustion & Flame, Vol. 156(1), pp. 181-199*

Wurmel, J., Silke, E.J., Curran, H.J., Ó Conaire, M.S., and Simmie, J.M. (2007). The effect of diluent gases on ignition delay times in the shock tube and in the rapid compression machine, *Combustion & Flame, Vol. 151, pp. 289-302*

Appendix A Low Load Operation Using PRF Fuels

The PRF experiments were conducted by Dempsey *et al.* [2013] over a wide range of intake temperatures, varying from 30 to 90C in steps of 15C and at two different equivalence ratios, 0.26 and 0.3. In order to validate the PRF2 mechanism [Wang *et al.*, 2013] for engine simulation, computations were performed at three different intake temperatures, 30, 60 and 90C, at an equivalence ratio of 0.3. The PRF2 mechanism consists of 73 species and 296 reactions. The mechanism reduction process was summarized in detail by Brakora [2012]. Figure A-1 shows constant volume stoichiometric nC_7H_{16} and iC_8H_{18} ignition delay comparisons at 40 bar pressure. The iC_8H_{18} shock-tube experimental data was obtained from Fieweger *et al.* [1997], whereas the nC_7H_{16} data was from Hartmann *et al.* [2009]. These simulations were performed using the PRF2 mechanism implemented in the Chemkin 0-D code.

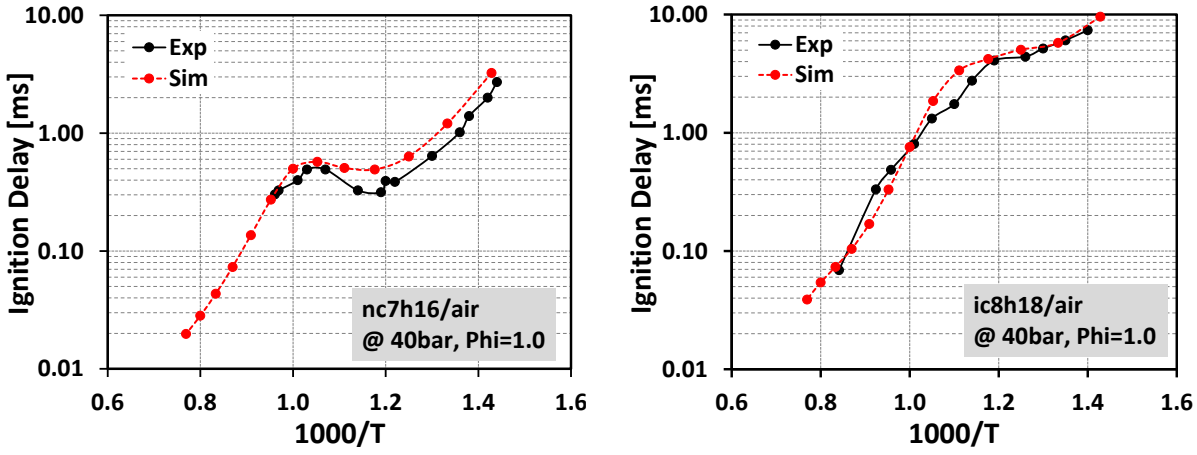

Figure A-1: Constant volume stoichiometric ignition delay of (a) nC_7H_{16}/air and (b) iC_8H_{18}/air at 40 bar pressure

Figure A-1 indicates that the PRF2 mechanism captures the experimental ignition delay of nC_7H_{16} fairly well. However, the nC_7H_{16} ignition delay in the low temperature range is slightly over-predicted in the simulations. Considering the reasonably good agreement with nC_7H_{16} and

iC_8H_{18} shock-tube ignition delay experiments PRF2 mechanism was used to conduct the HCCI simulations.

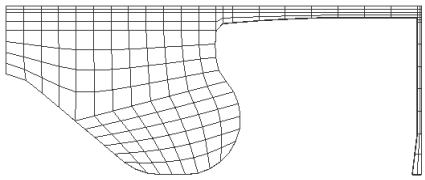

Figure A-2: Computational grid at TDC for HCCI simulations

All the simulations were performed from IVC to EVO using the 2-D relatively coarse grid to reduce the computational time. The grid shown in Figure A-2 has an effective compression ratio of 16.7 and a minimum grid size of 1.7 mm. Figure A-3 presents the pressure and heat release comparisons between using 2-D and 3-D geometries along with the emission results, which are seen to be in very good agreement with each other.

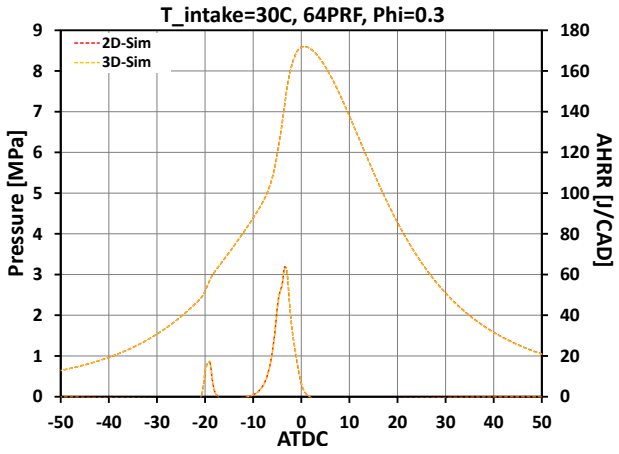

	2D-Sim	**3D-Sim**
CA50 (deg. ATDC)	-3.982	-3.499
NOx [g/kw-hr]	0.012	0.013
CO [g/kw-hr]	19.839	20.228
HC [g/kw-hr]	30.998	31.412
Soot [g/kW-hr]	0.005	0.005
Combustion Eff (%)	91.133	91.105

Figure A-3: Pressure, heat release and emission comparisons between 2-D and 3-D simulations

Thus, the rest of the HCCI simulations were performed with the 2-D computational grid.

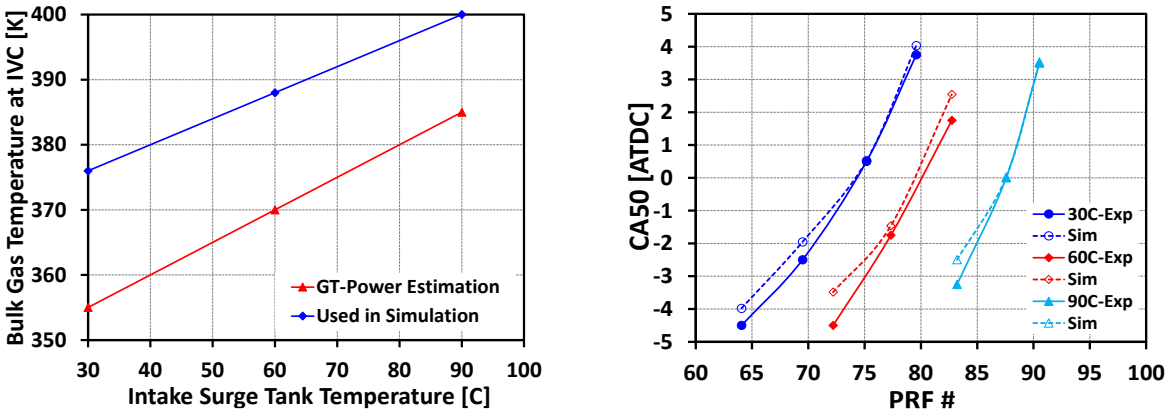

(a) (b)

Figure A-4: (a) Comparison between GT-Power estimated bulk gas temperature at IVC and the one used in simulations, (b) CA50 comparisons between experiments and simulations for different PRF fuels at various intake temperatures

Figure A-4(a) shows estimated IVC temperatures using the GT-Power cycle simulation code and the temperatures used in the KIVA computations. The injected port fuel amounts, experimental intake surge-tank temperatures, intake runner wall temperatures and in-cylinder wall temperatures were used as boundary conditions for the cycle simulations. It was observed that the GT-Power estimated IVC temperature did not provide enough reactivity to capture the experimental CA50 when used in the CFD model, and thus the IVC temperature needed to be raised in simulations. This indicates that even though a mechanism can capture shock-tube ignition delay data fairly well, it does not guarantee good performance in capturing the ignition delay of engine experiments. Reasons for this might include interactions between the extremely complex physical and chemical processes inside the combustion chamber, including turbulence created by the swirl and tumble motions, heat transfer, fuel evaporation and gas phase chemistry effects. Full engine cycle simulations of Perini [2013] that considered the intake and exhaust port flows of an engine with a very similar configuration as the engine used for the HCCI experiments are summarized in Figure A-5. Figure A-5a shows the initial and boundary conditions for the full cycle simulation. The engine was operated at 1500 rev/min and a swirl ratio of 2.2.

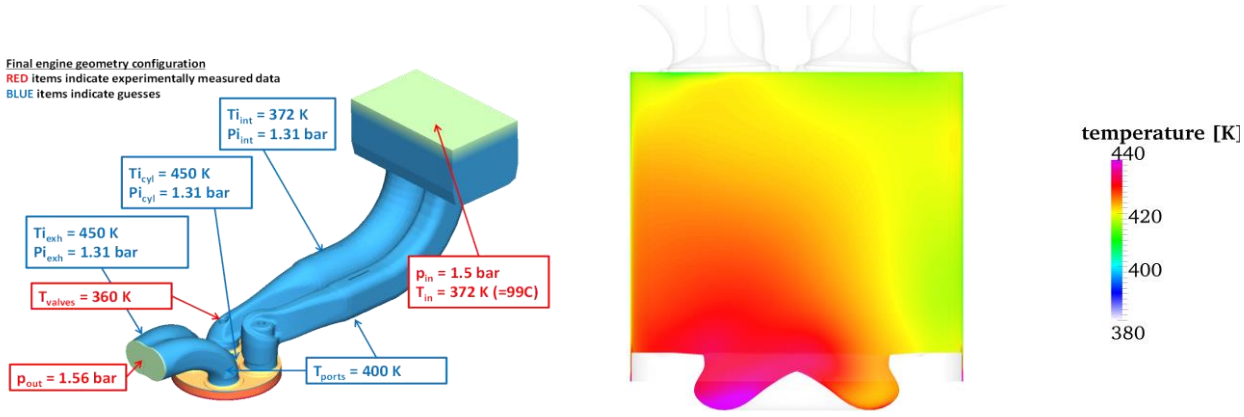

(a) (b)

Figure A-5: (a) Initial and boundary conditions for full cycle simulations and (b) cross-sectional temperature distribution at IVC

Figure A-5b shows the in-cylinder temperature distribution at IVC from the simulations, and inhomogeneity of the in-cylinder temperature distribution can be clearly observed. The maximum in-cylinder temperature [463K] is observed in the bowl region, whereas the near-wall region shows a minimum temperature of 381K. Thus, performing a 2-D sector simulation with the average constant in-cylinder temperature of 422K may not provide a proper representation of the chamber conditions, since the combustion is expected to start from hot locations. This suggests the necessity of increasing IVC temperatures somewhat in sector simulations in order to compensate for the absence of locally hot regions, which can intensify the combustion process.

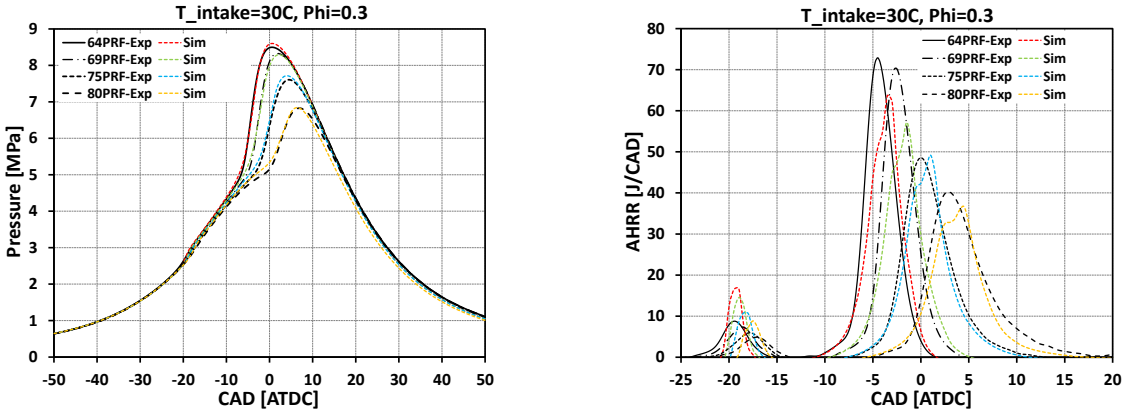

(a) (b)

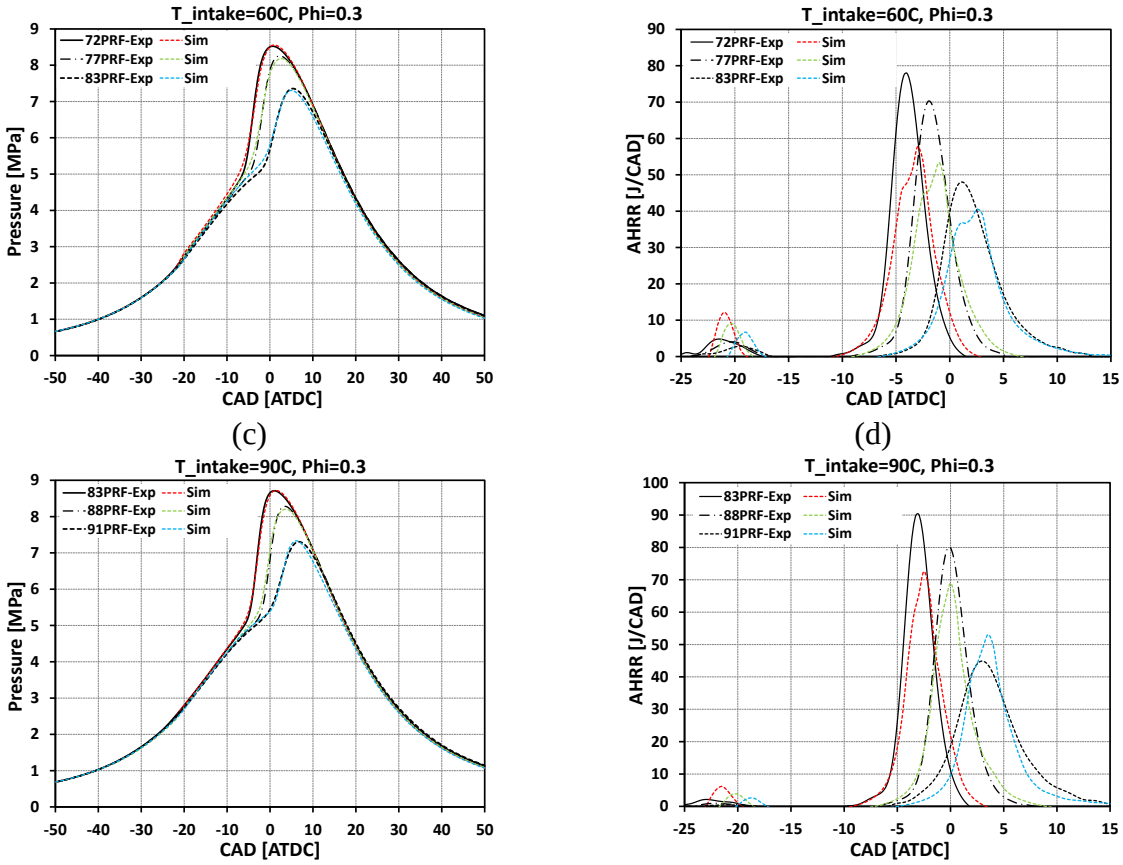

Figure A.6: Pressure and heat release comparisons at (a) 30C (c) 60C and (e) 90C intake temperatures and magnified heat release comparisons at (b) 30C (d) 60C and (f) 90C intake temperatures

Figure A-6 shows comparisons between experimental and computational pressure and heat release traces at an equivalence ratio of 0.3 for the three different intake temperatures, i.e., 30, 60 and 90C. The results show reasonably good agreement between the experiments and the simulations, however, the pressure during the expansion stroke is slightly lower in the computations for all cases. The cool flame heat release peak is higher in the simulation and the duration is shorter compared to the experiments, which can be clearly observed in Figure A-6b, Figure A-6d and Figure A-6f. The higher cool flame peak in the simulations increases the compression stroke pressure before main ignition. On the other hand, the main heat release peak is mostly lower in the simulations, whereas the duration is in quite good agreement with the

experiments. However, at a fixed intake temperature the main heat release duration increases with an increase in the PRF number, as shown in Figure A-7a. This is due to the fact that at a fixed temperature, a higher PRF number indicates the presence of more iC_8H_{18} in the fuel, which takes a longer time for ignition. For the same reason CA50 also retards with use of a higher PRF number fuel, as shown in Figure A-4b.

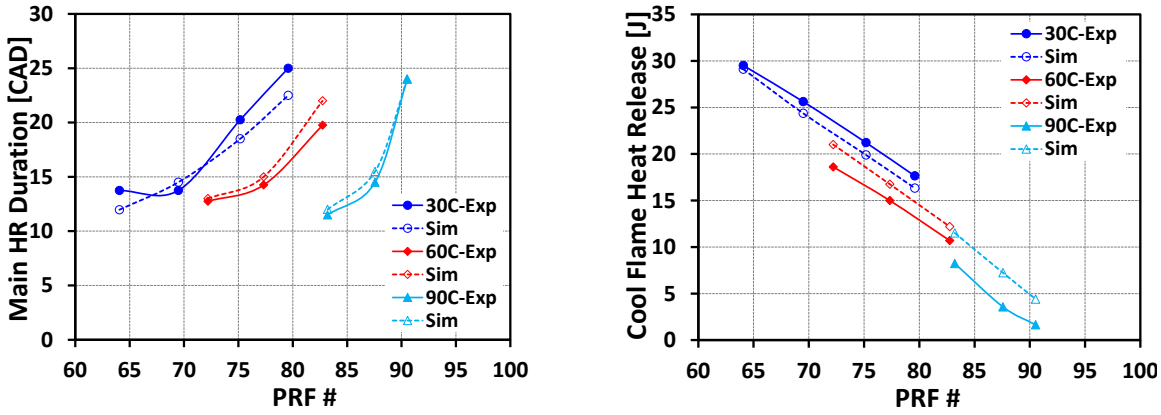

(a) (b)

Figure A-7: (a) Main heat release duration comparisons and (b) cool flame amount comparisons between experiments and simulations for different PRF fuels at various intake temperatures

Figure A-7b compares the cool flame heat release amounts in the experiments and the simulations at different intake temperatures. The results indicate that at a lower intake temperature the cool flame amount is slightly under-predicted in the simulations, whereas with an increase in intake temperature, the simulations over-predict the cool flame and the difference gets bigger with higher intake temperatures. This can be attributed to the amount of formaldehyde formed, which changes with the variation of intake temperature and fuel composition.

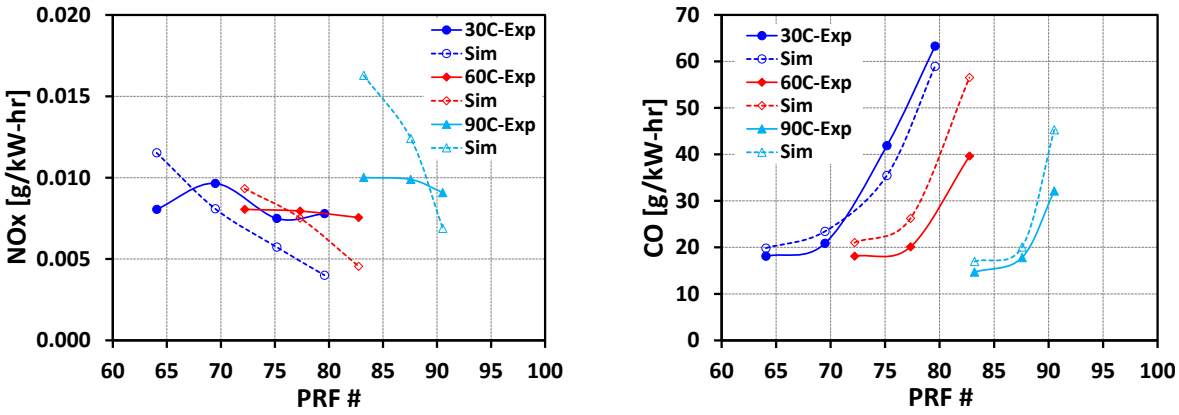

(a) (b)

Figure A-8: (a) NO_x emission and (b) CO emission comparisons between experiments and simulations for different PRF fuels at various intake temperatures

The light-load HCCI experiments were conducted at a very lean condition, so the soot emission was negligible, which was also confirmed by the simulations. Figure A-8 compares the NO_x and CO emissions between the simulations and experiments. Figure A-8a indicates that at a fixed intake temperature, an increase in the PRF number reduced the NO_x emissions, both in the experiments and the simulations. However, at 30C intake temperature the experimental NO_x emissions increased in moving from the 64 PRF to the 69 PRF fuel. Uncertainties in the emission data might be the reason. Incomplete fuel burning, and therefore lower in-cylinder temperatures instigated by the higher PRF number fuel, reduces NO_x emissions. Also, higher intake temperatures produced higher NO_x, as expected, but overall, the NO_x levels were low in both the experiments and the simulations. The CO emission trends were captured fairly well in the simulations for the various intake temperatures. However, CO was over-predicted at the 60 and 90C intake temperature conditions, as can be observed in Figure A-8b. This can mainly be attributed to trapped CO in the piston-liner crevice region. The CO contour for the 91 PRF case at 90C intake temperature is shown in Figure A-9 as an example.

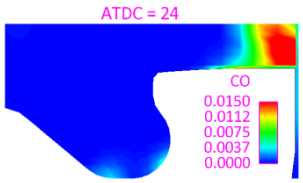

Figure A-9: CO contour plot at 24 deg ATDC for the 91 PRF case at 90C intake temperature

Appendix B Ignition Delay Study in a Rapid Compression Machine [RCM]

A key to improve IC engine efficiency is to understand the fuel chemistry. Complete qualitative and quantitative characterization of the fuel decomposition reactions would be helpful to predict the fuel oxidation over wide ranges of pressure and temperature, leading to improved predictions of engine performance and reduced emission. Rapid Compression Machine [RCM] experiments are valuable to characterize chemical kinetics at low-to-intermediate temperatures and elevated pressures.

An RCM simulates a single stroke of an IC engine where the compression ratio, initial temperature and charge composition can be easily controlled [Sung *et al.*, 2014]. Once the favorable condition is reached at the end of the compression stroke, the fuel autoignites after a characteristic delay time depending upon the fuel chemistry. Typical post-compression pressure and temperature conditions in an RCM are in the range of 1-6 MPa and 700-1200 K, respectively, whereas the test times are in the range of 1-200 ms [Wurmel *et al.*, 2007]. However, due to the longer test times heat losses in the RCM are significant, which complicates the analysis of the results. To minimize heat losses the compression process needs to be rapid, which necessitates over-robust engineering and can cause aerodynamic heating [Affleck *et al.*, 1968].

Wurmel *et al.* [2007] reported that simulating the RCM data is quite challenging since blow-by and heat loss calculation are needed. However, some effort was invested in modeling Rapid Compression Machine [RCM] ignition delay data obtained from the Argonne National Laboratory [Goldsborough, 2013] , as elaborated in this section.

B.1 RCM Experiments

EHN was added to 91 PRF base fuel at 40, 70 and 100C intake temperatures to conduct the RCM experiments, the geometrical information of which is mentioned in Table B-1.

Table B-1: RCM geometry specification

CR	10.2
Bore [cm]	5.08
Stroke [cm]	15.6

91 PRF fuel was doped with 0.1, 1 and 3% EHN by volume at stoichiometric conditions to measure the RCM ignition delay. Lower compression temperature experiments were conducted using nitrogen [N2] as dilution gas, whereas both nitrogen and argon were used for the higher compression temperature experiments in the ratio of 25:75 by volume. This is because the proportion of diluent gases alters the overall heat capacity of the mixture, and therefore extends the range of compressed gas temperatures. Instead of 21% oxygen by mole in the oxidizer gas, only 11% oxygen was used in the experiments to avoid violent combustion at higher compression pressures and temperatures. For the experiments mentioned in this section the compression pressure was maintained at ~21 bar.

B.2 0-D RCM Simulation

0-D Chemkin simulations were performed initially to validate the experimental ignition delay data using 91 PRF fuel and 0-3% EHN by volume at stoichiometric conditions. Figure B-1 shows the comparison between the experiments and simulations. It is seen that the ignition delay is largely under-predicted in the simulations. The smaller the EHN amount, the higher is the discrepancy. Higher ignition delays in the experiments can also be attributed to higher blow-by and heat losses, as mentioned in the literature [Mittal *et al.*, 2006; Sung *et al.*, 2014]. Argon was not used as a diluent for the 3% EHN experiments due to the possibility of reaching high compression

temperatures, where sudden unexpected combustion can happen due to the higher amount of additive usage, as can be observed in Figure B-1d.

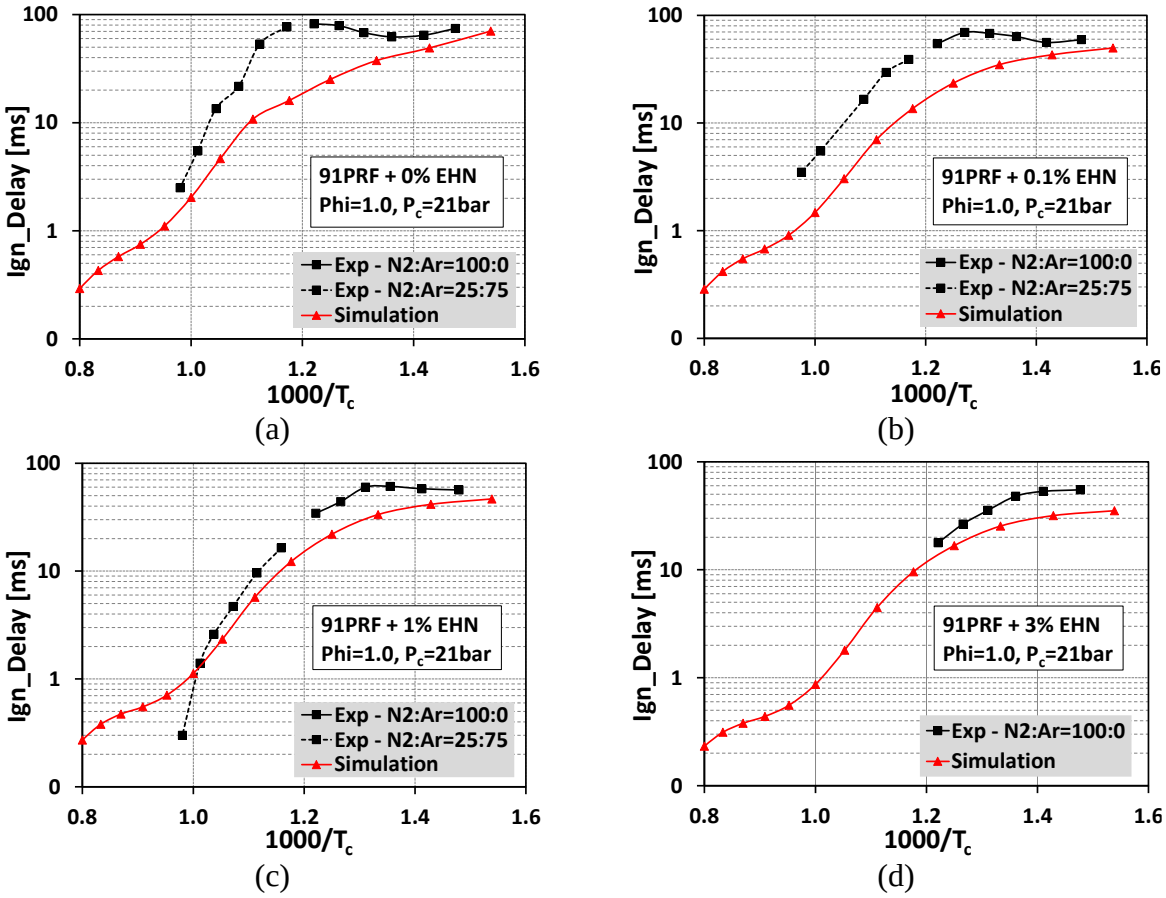

Figure B-1: Ignition delay comparisons between experiments and 0-D simulations

The above results indicate that a 0-D Chemkin simulation does not account for the complex motions of the gas mixture, along with the heat losses, which are possible reasons for the disagreements between experiments and simulations. Therefore 3-D RCM computations were attempted using the KIVA3V-SpeedChem code.

B.3 3-D RCM Simulation

Figure B-2a represents the RCM geometry used in the 3-D simulation having a compression ratio of 10.2. The volume history calculated from the experiments was used to specify the piston motion in the simulation. Figure B-2b represents the RCM volume history over time.

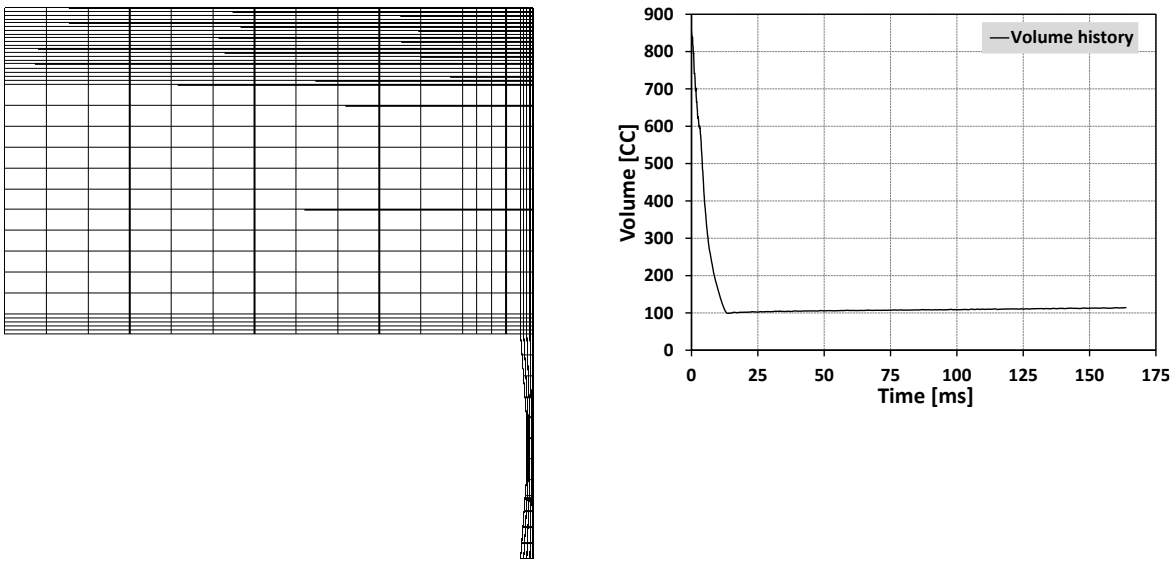

(a) (b)

Figure B-2: (a) RCM geometry used in 3-D simulation, and (b) volume history of RCM

The heat transfer in the multi-dimensional code was calculated based on the Woschni correlation, where the average cylinder gas velocity was approximated by the piston velocity. To validate the code, non-reacting pressure traces were compared between the experiments and simulations at three different intake temperatures, 40, 70 and 100C. Figure B-3a specifies two different regions - the compression stroke cycle, and the point when the compression pressure is achieved, the pressure drop due to the heat loss from the constant volume reaction chamber. These two regions are noticeable in all the figures included in Figure B-3. Each of the figures shows two different non-reacting pressures using the diluents nitrogen and argon in ratios of 25:75 and 100:0. The maximum compression pressure is ~2 MPa, whereas the compression temperature changes depending upon the diluent ratio and intake temperatures. The figures also indicate that fuel oxidation did not take place during the compression process. All three figures display very good agreements between the experiments and simulations, which shows the validity of the numerical models used in simulations. Therefore, an effort was made to simulate one of the reacting cases

using 91 PRF fuel at 100C intake temperature using a nitrogen and argon diluent ratio of 25:75 at stoichiometric condition.

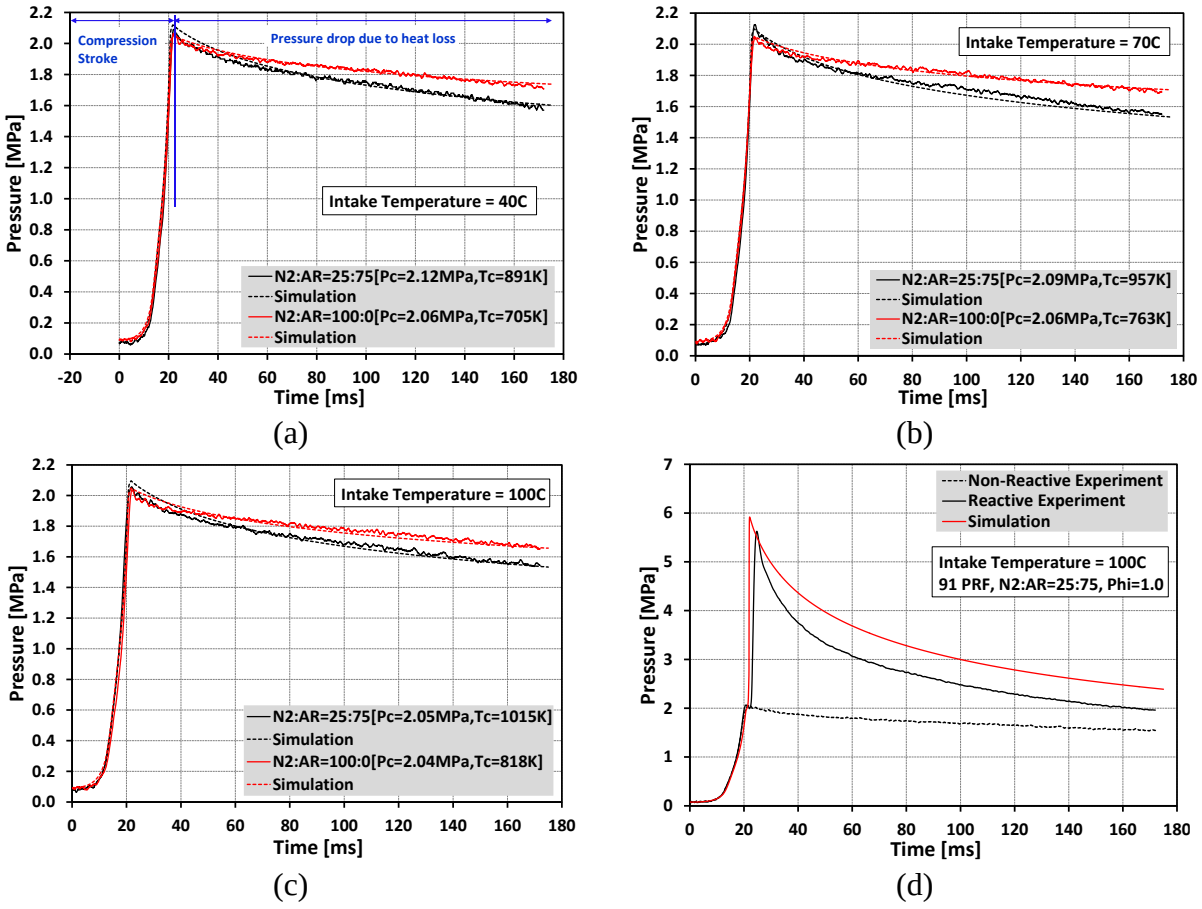

Figure B-3: Non-reacting pressure trace comparisons using 91 PRF fuel at (a) 40C (b)70C and (c) 100C intake temperatures. (d) Reacting pressure trace comparison between experiment and simulation using 91 PRF fuel

The experiment in Figure B-3d shows two-stage combustion, even though the time interval between the first and second stage combustion is very small. The first stage of combustion was achieved by the end of the compression stroke, whereas the second stage was achieved by the fuel burning. The heat loss in Figure B-3d was greatly under-predicted in the simulation even when an unrealistically low wall temperature of 300K was used, showing the importance of considering blow-by. Therefore, in this study instead focus was placed on modeling HCCI engine experimental data to validate the EHN mechanism.

Appendix C EHN Mechanism

The EHN Mechanism developed as part of the present study is summarized below. New reactions related to NOx interactions with lower level hydrocarbons are also mentioned, as those reactions were introduced to predict appropriate NOx emissions from the presence of EHN. The thermodynamic properties of some of the intermediate species were calculated using the Reaction Mechanism Generator [RMG, MIT].

1.	ehn=eho+no2	1.00E+16	0.0	39000.0
2.	ehn=echo+hono	1.00E+16	0.0	34000.0
3.	ehn+h=ehoh+no2	2.00E+13	0.0	4200.0
4.	ehn+h=eho+hono	2.00E+13	0.0	4200.0
5.	ehn+h=echo+h2+no2	2.00E+13	0.0	4200.0
6.	ehn+o=ehoo+no2	6.00E+12	0.0	1000.0
7.	ehn+o=ecooh+hono	6.00E+12	0.0	1000.0
8.	ehn+o=echo+oh+no2	6.00E+12	0.0	1000.0
9.	ehn+oh=ehooh+no2	1.40E+12	1.0	0.0
10.	ehn+oh=ehoo+hono	1.40E+12	1.0	0.0
11.	ehn+oh=echo+h2o+no2	1.40E+12	1.0	0.0
12.	ehn+ho2=ehoo+oh+no2	1.25E+13	0.0	6000.0
13.	ehn+ho2=ecooh+oh+hono	1.25E+13	0.0	6000.0
14.	ehn+ho2=echo+h2o2+no2	1.25E+13	0.0	6000.0
15.	ehn+o2=ecooh+oh+no2	1.00E+19	0.0	36300.0
16.	ehn+o2=eho2+oh+hono	1.00E+19	0.0	36300.0

17. ehn+o2=echo+ho2+no2	1.00E+19	0.0	36300.0
18. ehoh=c7h15-2+ch2oh	2.00E+13	0.0	15000.0
Reverse Arrhenius coefficients:	1.00E+11	0.0	0.0
19. eho=c7h15-2+ch2o	2.00E+13	0.0	15000.0
Reverse Arrhenius coefficients:	1.00E+11	0.0	0.0
20. ehoo=c7h15-2+hco+oh	2.00E+13	0.0	15000.0
Reverse Arrhenius coefficients:	1.00E+11	0.0	0.0
21. eho2=c7h15-2+co2	2.00E+13	0.0	15000.0
Reverse Arrhenius coefficients:	1.00E+11	0.0	0.0
22. ecooh=c7h15-2+co+oh	2.00E+13	0.0	15000.0
Reverse Arrhenius coefficients:	1.00E+11	0.0	0.0
23. ehooh=eho+oh	2.00E+13	0.0	15000.0
Reverse Arrhenius coefficients:	1.00E+11	0.0	0.0
24. echo=c7h15-2+hco	2.00E+13	0.0	15000.0
Reverse Arrhenius coefficients:	1.00E+11	0.0	0.0
25. hno2+h=no2+h2	2.40E+08	1.5	5087.0
26. hno2+o=no2+oh	1.70E+08	1.5	3020.0
27. hno2+oh=no2+h2o	1.20E+06	2.0	-596.0
28. hno2+ch3=no2+ch4	8.10E+05	1.9	4838.0
29. hno2=hono	1.30E+29	-5.5	52814.0
30. hono+ch3=no2+ch4	8.10E+05	1.9	5504.0
31. hono+oh=no2+h2o	1.26E+10	1.0	135.0
32. hono+o=no2+oh	1.21E+13	0.0	5962.0

33. hono+h=no2+h2		1.21E+13	0.0	7353.0
34. hono+hono=no+no2+h2o		1.02E+13	0.0	8540.0
35. no+oh(+m)=hono(+m)		2.00E+13	0.0	0.0
Low pressure limit:		0.233E+24	-0.24E+01	0.0
36. ch2oh(+m)=ch2o+h(+m)		2.80E+14	-0.7	32820.0
Low pressure limit:		0.601E+34	-0.539E+01	0.362E+05
TROE centering:	0.96	67.6	1855.0	7543.0
37. ic8h18+no2=ic8h17+hono		6.50E+14	0.0	41400.0
38. nc7h16+no2=c7h15-2+hono		6.50E+14	0.0	41400.0
39. mch+no2=mchrad+hono		6.50E+14	0.0	41400.0
40. c8h16+no2=c8h15+hono		6.50E+14	0.0	41400.0
41. c10h22+no2=c10h21+hono		6.50E+14	0.0	41400.0
42. no2+co=no+co2		4.76E+13	0.0	23600.0
43. no2+h2=no+h2o		4.76E+13	0.0	23600.0
44. no+hco=hno+co		6.90E+12	0.0	0.0
45. no+ch2oh=hno+ch2o		1.30E+12	0.0	0.0
46. no+ch3o=hno+ch2o		7.53E+12	0.0	2017.0
47. no+ch3o(+m)=ch3ono(+m)		5.99E+14	-0.6	0.0
Low pressure limit:		0.814E+26	-0.28E+01	0.0
TROE centering:		0.10E+01	0.10E-29	0.90E+03
48. no+ch3o2=no2+ch3o		1.40E+12	0.0	-715.0
49. no2+ch3=no+ch3o		4.00E+13	-0.2	0.0
50. no2+hco=no+co2+h		2.30E+13	0.0	0.0

51. no2+hco=hono+co	4.95E+12	0.0	0.0
52. no2+hco=no+co+oh	4.95E+12	0.0	0.0
53. no2+ch2o=hono+hco	1.42E-07	5.6	9220.0
54. no2+ch2o=hno2+hco	1.07E-01	4.2	19850.0
55. no2+ch2oh=hono+ch2o	5.00E+12	0.0	0.0
56. no2+ch3o=hono+ch2o	6.00E+12	0.0	2285.0
57. no2+ch3o(+m)=ch3ono2(+m)	2.19E+15	-0.9	0.0
Low pressure limit:	0.291E+24	-0.174E+01	0.0
TROE centering:	0.60E+00	0.10E-29	0.10E+31
58. no2+c2h6=hono+c2h5	6.50E+14	0.0	41400.0
59. no2+c2h6=hno2+c2h5	6.00E+14	0.0	33200.0
60. hno+ch3=no+ch4	2.30E+14	0.0	8400.0
61. hno+hco=no+ch2o	5.83E-01	3.8	115.0